
Electronic Thesis and Dissertation Repository

7-27-2023 9:30 AM

ASSESSING THE SPATIO-TEMPORAL BEHAVIOURS OF INCOMPLETE SURFACE TEMPERATURES USING THERMAL REMOTE SENSING AND GIS

Derrick Kessie, *Western University*

Supervisor: Dr James A Voogt, *The University of Western Ontario*

A thesis submitted in partial fulfillment of the requirements for the Master of Science degree in
Geography and Environment

© Derrick Kessie 2023

Follow this and additional works at: <https://ir.lib.uwo.ca/etd>



Part of the [Environmental Health and Protection Commons](#)

Recommended Citation

Kessie, Derrick, "ASSESSING THE SPATIO-TEMPORAL BEHAVIOURS OF INCOMPLETE SURFACE TEMPERATURES USING THERMAL REMOTE SENSING AND GIS" (2023). *Electronic Thesis and Dissertation Repository*. 9438.
<https://ir.lib.uwo.ca/etd/9438>

This Dissertation/Thesis is brought to you for free and open access by Scholarship@Western. It has been accepted for inclusion in Electronic Thesis and Dissertation Repository by an authorized administrator of Scholarship@Western. For more information, please contact wlsadmin@uwo.ca.

Abstract

This study aimed to better understand the spatiotemporal behaviors of "incomplete" surface temperatures, a subset of all the active surfaces in urban areas, that are relevant for outdoor thermal comfort assessments.

This study answered the following questions:

1. What is the temperature of "incomplete surfaces" that are most relevant in urban thermal comfort assessments, and what is its spatiotemporal behavior in different urban neighborhoods?
2. How are the relevant incomplete temperatures related to nadir view remotely sensed surface temperatures (T_{plan})?

By combining distributions of wall temperatures from TUF-3D, an urban energy balance model, and horizontal surface temperatures from airborne remotely observed data with building polygons, the study defines and estimates the pedestrian temperature (T_{ped}), an application-relevant incomplete surface temperatures for four Local Climate Zones (LCZ 5,6,7, and 8) in Phoenix, USA for both daytime and nighttime. The results show that T_{ped} can be up to 8°C less than T_{plan} . The results also show that T_{ped} varies within different sub areas of a large study area, and also it varies between different study areas. For daytime T_{plan} , LCZ 6 recorded the highest temperature value while LCZ 8 recorded the lowest temperature value, even though the difference between the two temperatures is very small.

Keywords;

Pedestrian temperature, plan temperature, thermal remote sensing, thermal comfort, Local Climate Zone

Keywords;

Pedestrian temperature, plan temperature, thermal remote sensing, thermal comfort, Local Climate Zone

Summary for Lay Audience

Urbanization significantly impacts the temperatures in urban areas. This transformation leads to an increase in temperatures, a phenomenon known as the "urban heat island" effect. This effect can present potential heat-related challenges for city inhabitants, such as health issues related to overheating and the increased energy consumption associated with cooling demands.

Traditionally, remote sensing technologies like satellites have been employed by many researchers to study urban climates and monitor surface temperatures. However, viewing an urban area using remote sensing leads to a discrepancy between the surfaces observed by satellites, which preferentially view rooftops and ground areas, and the surfaces that are most relevant for specific urban heat applications. In the case of outdoor thermal comfort, these surfaces consist of the combination of wall and ground temperatures that emit heat directly to pedestrians. This combination of surfaces is "incomplete" with respect to the full three-dimensional urban surface as is the (different) combination of surfaces seen by remote sensing. The study was designed to understand the behavior of these relevant "incomplete" surface temperatures in urban areas, especially how they vary in time and space across different neighborhoods. To accomplish this, the study utilized a combination of airborne thermal remote sensing, which provided high-resolution thermal images, and LiDAR-derived building data, which offered detailed information about building characteristics. An energy balance model known as TUF-3D was used to generate wall temperatures of buildings in the study areas because these surfaces are not otherwise 'seen' by most remote sensing instruments.

The focus of the study was to answer two main questions: What is the temperature of these incomplete surfaces that are most relevant to urban thermal comfort, and how do they vary across different parts of the city? Furthermore, how are these temperatures related to the temperatures seen in the straight-down view provided by remote sensing satellites?

To answer these questions, the study focused on four Local Climate Zones in Phoenix, USA, using high-resolution thermal imagery captured between July 12-15, 2011. Through

a combination of wall temperatures from the TUF-3D model and horizontal surface temperatures from the airborne remote sensing data, the study defined and estimated the application-relevant incomplete surface temperatures.

The results of the study reveal that researchers who depend solely on satellite view surface temperatures tend to overestimate the temperatures experienced by pedestrians by more than 8 degrees Celsius. This discrepancy has significant implications for understanding and mitigating urban heat challenges. Furthermore, the study developed first-of-their-kind multiple regression models that can be used by researchers to predict pedestrian-level temperatures. This model uses information about the plan temperatures, the cumulative wall areas in their research zone, and the ratio of plan to area, offering a promising predictive tool for future urban climate studies. Other results from the study show that heat load on pedestrian varies with the geometry of buildings in an area, with areas with buildings closely packed together being more thermally comfortable.

Co-Authorship Statement

1. **Derrick Kessie**, as the principal author, is responsible for conducting the main body of the research work. The contributions include developing the GIS methods used to create the incomplete temperature estimates, running the TUF-3D model, undertaking a comprehensive analysis of the data, constructing and interpreting graphical representations of the research findings, and the preparation of the manuscript of the thesis. Derrick took the lead role in articulating the analysis and interpretation of the results, thereby ensuring that the thesis effectively addresses the research questions posed.
2. James A. Voogt, in his role as the graduate supervisor, suggested the initial thesis topic and helped to formulate the research questions that guided the study. He sourced and provided the primary data that formed the basis of the research. His role involved supervision, guidance, and constructive criticism, ensuring the research maintained a high standard of academic rigor. His involvement also included reviewing and suggesting edits to the manuscript of the thesis.

Acknowledgments

I would like to express my sincere gratitude and appreciation to all those who have contributed to the completion of this thesis. Without their support, guidance, and encouragement, this work would not have been possible.

First and foremost, I am deeply grateful to my supervisor, James A. Voogt, for his invaluable guidance, patience, and expertise throughout the entire process. His unwavering support and insightful feedback have been instrumental in shaping this thesis and my growth as a researcher in the field of urban climatology.

I extend my heartfelt thanks to the faculty members of The University of Western Ontario, Department of Geography, for their valuable insights and for creating an enriching academic environment. Their lectures, discussions, and academic resources have significantly contributed to my understanding and development in the field of urban climatology.

I would like to acknowledge the assistance of my colleagues and friends, whose continuous encouragement and intellectual exchange have been a source of motivation and inspiration. Their willingness to lend a helping hand, offer suggestions, and engage in stimulating discussions have enriched the quality of this work.

I would like to express my deep gratitude to my family for their unwavering love, encouragement, and understanding. Their constant support and belief in my abilities have been a driving force throughout this journey. I am eternally grateful for their sacrifices and the opportunities they have provided me.

Table of Contents

<i>Abstract</i>	i
<i>Summary for Lay Audience</i>	ii
<i>Co-Authorship Statement</i>	iv
<i>Acknowledgments</i>	v
<i>List of Tables</i>	x
<i>List of Figures</i>	xii
<i>List of Symbols and Abbreviations</i>	xx
<i>List of Appendices</i>	xxii
Chapter 1.....	1
1 Introduction.....	1
1.1 The Urban Thermal Environment.....	2
1.2 Surface temperatures and urban heat assessments.....	4
1.3 Limitations of Thermal Remote Sensing in Urban Areas.....	7
1.4 Spatio-Temporal Behaviors of Surface Temperatures: Implications for Outdoor Thermal Comfort and Urban Planning.....	9
1.5 Research Questions and Objectives.....	13
1.6 A Potential Approach to Estimate the Temperatures of Surfaces Unseen by Satellites.....	15
1.7 Thesis Organization.....	16
Chapter 2.....	17
2 Study area.....	17
2.1 Site Selection.....	17
2.2 Airborne Remotely Sensed Data.....	19

2.3 Assessing Thermal Comfort in Select Local Climate Zones of Phoenix Metropolitan Area.....	27
2.4 LiDAR-Derived Building Database.....	29
2.5 Meteorological Data Sites.....	30
2.6 Sub-LCZ Spatial Variabilities.....	30
Chapter 3.....	36
3 Methods.....	36
3.1 Conceptual Approach.....	36
3.2 Numerical Modelling of Wall Temperatures.....	38
3.3 Urban Surface Set-up.....	40
3.3.1 Meteorological Model forcing.....	40
3.4 Model Simulation Procedure.....	41
3.4.1 Calculating the Shaded Areas of Modelled Sunlit Walls.....	44
3.4.2 Calculating Incomplete Surface Temperatures.....	46
3.4.3 Estimating T_{ped} and T_{plan} for Different Spatial Domains.....	47
Chapter 4.....	51
4 Model Evaluation and Sensitivity Analysis.....	51
4.1 Sensitivity Test on the Important Parameters that Affect Modelled Surface Temperatures.....	52
4.1.1 Sensitivity Analysis of the Cardinal Direction of Walls.....	53
4.1.2 Sensitivity Analysis for Different H/W Ratio.....	57
4.1.3 Sensitivity Analysis to Roughness Length and Wind Speed.....	59
4.1.4 Sensitivity Analysis for wind Speed.....	61
4.1.5 Sensitivity Analysis for Wall Thermal Admittance and Albedo.....	63
4.2 TUF-3D Model Evaluation for Phoenix.....	68
4.3 Summary.....	73

Chapter 5.....	75
5 Results.....	75
5.1 Comparisons between T_{ped} and T_{plan} for LCZ 6 at the 50m x 50m spatial scale. ..	75
5.1.1 $T_{plan} - T_{ped}$ Comparisons at Larger Spatial Scales.....	90
5.2 Comparisons Between T_{ped} and T_{plan} for Different LCZ.....	94
5.3 Multiple Regression Modelling for the Study Areas.....	96
5.4 A Unified Multiple Regression Model for all LCZ.....	104
5.5 Advancing T_{ped} Predictions with Versatile Multiple Regression Models.....	107
5.6 Comparative Analysis of a Unified Multiple Regression Model for All LCZs and Versatile Multiple Regression Models for Advancing T_{ped} Prediction.....	111
5.7 Multiple Regression Models from Vancouver LI Area.....	113
5.8 Discussion.....	128
5.8.1 Comparing the Multiple Regression Models from Phoenix with Regression Models from Other Study Areas.....	129
5.8.2 How T_{ped} Relates to More Advanced Measures of Pedestrian Thermal Comfort.....	135
Chapter 6.....	138
6 Summary and Recommendations.....	138
6.1 Thesis Summary.....	138
6.1.1 Understanding the Relationship between T_{plan} and T_{ped} for both Day and Night.....	140
6.1.2 Daytime and Nighttime Regression Models to Predict T_{ped}	141
6.2 Limitations Encountered.....	142
6.2.1 Temporal Limitations.....	143
6.2.2 Lack of Observed Wall Temperature Data.....	143
6.3 Future recommendations.....	144
6.4 Conclusion.....	147

<i>References</i>	149
<i>Appendices</i>	159
<i>Curriculum Vitae</i>	192

List of Tables

Table 2. 1. The dates and times that the thermal data were collected for each study	25
Table 3. 1. The step sizes and number of downward and rightward movements for each domain size.	49
Table 3. 2. The number of individual cells within the three domains for all the LCZ.	49
Table 4. 1. The range of differences in wall temperatures (in °C) with 11.25 degrees variation from the 4 cardinal points.	56
Table 4. 2. TUF3d model self-calculated H/W ratios.....	58
Table 4. 3. Differences in temperature values from H/W sensitivity analysis	59
Table 4. 4. Input parameters for wall temperature sensitivity test and their corresponding output wall temperatures. TA - thermal admittance ($\text{J m}^{-2} \text{s}^{-1/2} \text{K}^{-1}$) ; h1 and c1 means the hottest and coldest walls, respectively.	65
Table 4. 5. The range of values for the daytime wall temperatures of LCZ 6 SA1. All values are in °C.	67
Table 4. 6. The range of values for the nighttime wall temperatures of LCZ 6 SA1	67
Table 4. 7. Pixel counts (roofs) for the chosen sub areas	69
Table 4. 8. Pixel counts (roads) for the chosen sub areas	69
Table 4. 9. R^2 values from roof and road surface temperature evaluation.	72
Table 5. 1. Amount of vegetation in each LCZ	76

Table 5. 2. Average daytime and nighttime T_{ped} and T_{plan} values for the four LCZ.	95
Table 5. 3. Measures of variability for each LCZ for daytime T_{ped}	95
Table 5. 4. Measures of variability for each LCZ for nighttime T_{ped}	96
Table 5. 5. Regression model statistics for daytime and nighttime for 100m x 100m spatial domain of each LCZ; Int = intercept.	101
Table 5. 6. Regression model statistics for daytime and nighttime for 100m x 100m spatial domain of all LCZ.	106
Table 5. 7. Regression model statistics for daytime and nighttime from TUF-3D.....	110
Table 5. 8. Comparisons of regression model based on observed data (Table 5. 6) and the regression model based on numerical data (Table 5. 7).....	112
Table 5. 9. Regression model statistics for each flight.	126
Table 5. 10. Regression model statistics for the combined flight data.	128
Table 5. 11. Regression statistics from linear regression models for Phoenix and Vancouver LI	130
Table A. 1. Variations of T_{ped} and T_{plan} temperatures for both daytime and nighttime for all SA, in LCZ 5.....	167
Table A. 2. Variations of T_{ped} and T_{plan} temperatures for both daytime and nighttime for all SA, in LCZ 6.....	167
Table A. 3 Variations of T_{ped} and T_{plan} temperatures for both daytime and nighttime for all SA, in LCZ 7.....	168
Table A. 4 Variations of T_{ped} and T_{plan} temperatures for both daytime and nighttime for all SA, in LCZ 8.....	168

List of Figures

Figure 1. 1. Relationship between air and surface temperatures on a clear day and night (Oke et al., 2017)	3
Figure 1. 2. Complete and incomplete surface temperatures (Stewart et al., 2021).	7
Figure 1. 3. Graphical visualization of the difference in application specific incomplete surface temperatures from plan view surface temperatures based on TUF-3D modelling for three Local Climate Zones in a hot dry desert climate showing the differences between between (left panel) T_{bldg} and T_{plan} and (right panel) T_{ped} and T_{plan} (Stewart et al., 2021).	10
Figure 1. 4. Local climate zone classification system (Stewart and Oke, 2012).	12
Figure 2. 1. Imagery showing Phoenix Metropolitan area.....	18
Figure 2. 2. Solar radiation observed during the period of daytime airborne remote sensing flights.	21
Figure 2. 3. Air temperature observed during the period of airborne remote sensing flights.	22
Figure 2. 4. Relative humidity observed during the period of airborne remote sensing flights.	23
Figure 2. 5. Wind speed observed during the period of airborne remote sensing flights.	24
Figure 2. 6. Local climate zone map of Phoenix. Modified after Wang et al. 2018.....	28
Figure 2. 7. Satellite visible wavelength images of a) LCZ 5 Study area, b) LCZ 6 Study area, c) LCZ 7 Study area, d) LCZ 8 Study area (Google Earth, 2022).	29
Figure 2. 8. The different sub areas within LCZ 5.....	32

Figure 2. 9. The different sub areas within LCZ 6.....	33
Figure 2. 10. The different sub areas within LCZ 7.....	34
Figure 2. 11. The different sub areas within LCZ 8.....	35
Figure 3. 1. Surface temperatures of a simple building array represented by TUF-3D (Image provided by Prof. E.S. Krayenhoff).....	37
Figure 3. 2. Individual cells that represent a building in TUF-3D (Krayenhoff and Voogt, 2007).	39
Figure 3. 3. Ground temperature (in °C) from 7 m x 7 m airborne thermal imagery over a 100 m x 100 m domain.	42
Figure 3. 4. Wall temperatures (°C) obtained from TUF-3D	43
Figure 3. 5. Combined ground and wall temperatures (°C).....	44
Figure 3. 6. The initial 100m x 100m grid position on LCZ 6.	48
Figure 3. 7. Conversion of results from the spatially shifted grids. a) Point shapefiles representing 100m x 100m polygons. b) 20m x 20m cells (polygons) converted from the points.....	50
Figure 4. 1. Histograms showing the distribution of wall orientations in a) LCZ 5, b) LCZ 6, c) LCZ 7, d) LCZ 8.	54
Figure 4. 2. Model sensitivity of LCZ 5 SA8 roof surface temperature to three different momentum roughness lengths for roofs.....	60
Figure 4. 3. Model sensitivity of LCZ 5 SA8 roof surface temperature to wind speed....	62
Figure 4. 4. the sensitivity of East wall temperatures to albedo and thermal admittance. 66	
Figure 4. 5. Model evaluation of day (red) and nighttime (blue) roof temperatures for a) LCZ 5 SA8 b) LCZ 6 SA1, c) LCZ 7 SA1. Dotted line represents the 1:1 line.	71

Figure 4. 6. Model evaluation of day (red) and nighttime (blue) temperatures of four roads, one from each SA.....	72
Figure 5. 1. Images of daytime T_{plan} for 50m x 50m domains of LCZ 6 constructed at 10 m spatial resolution.....	77
Figure 5. 2. Images of daytime T_{ped} for 50m x 50m domains of LCZ 6 constructed at 10 m spatial resolution.....	78
Figure 5. 3. Images of nighttime T_{plan} for 50m x 50m domains of LCZ 6 constructed at 10 m spatial resolution.....	79
Figure 5. 4. Images of nighttime T_{ped} for 50m x 50m domains of LCZ 6 constructed at 10 m spatial resolution.....	80
Figure 5. 5. Building heights within LCZ 6.....	82
Figure 5. 6. Histogram plot for daytime T_{plan} and T_{ped} for 50m x 50m domain of LCZ 6.....	83
Figure 5. 7. Histogram plot for nighttime T_{plan} and T_{ped} for 50m x 50m domain of LCZ 6.....	84
Figure 5. 8. Scatterplot for daytime T_{plan} and T_{ped} for 50m x 50m spatial domain of LCZ 6 at 10 m spatial resolution.....	85
Figure 5. 9. Scatterplot for nighttime T_{plan} and T_{ped} for 50m x 50m spatial domain of LCZ 6 at 10 m spatial resolution.....	85
Figure 5. 10. The effects of λ_p on T_{plan} and T_{ped} values. Larger circles represent larger λ_p	88
Figure 5. 11. The effects of wall areas on T_{plan} and T_{ped} values. Larger circles represent larger wall area within the domain.....	89

Figure 5. 12. The effects of building heights on T_{plan} and T_{ped} values. Larger circles represent larger building heights within the domain.....	90
Figure 5. 13. Images of daytime a) T_{plan} and b) T_{ped} for 100m x 100m domains of LCZ 6 constructed at 10 m spatial resolution.....	91
Figure 5. 14. Images of nighttime a) T_{plan} and b) T_{ped} for 100m x 100m domains of LCZ 6 constructed at 10 m spatial resolution.....	91
Figure 5. 15. Histogram plots for a) daytime T_{plan} and T_{ped} and b) nighttime T_{plan} and T_{ped} for 100m x100m domain of LCZ 6.....	92
Figure 5. 16, Images of daytime a) T_{plan} and b) T_{ped} for 200m x 200m domains of LCZ 6 constructed at 20 m spatial resolution.....	92
Figure 5. 17. Images of nighttime a) T_{plan} and b) T_{ped} for 200m x 200m domains of LCZ 6 constructed at 20 m spatial resolution.....	93
Figure 5. 18. Histogram plots for a) daytime T_{plan} and T_{ped} and b) nighttime T_{plan} and T_{ped} for 200m x200m domain of LCZ 6.....	93
Figure 5. 19. Regression model for predicted and calculated a) daytime T_{ped} and b) nighttime T_{ped} for 100m x 100m spatial domain of LCZ 5. The dashed red line is the 1:1 line.....	97
Figure 5. 20. Regression model for predicted and calculated a) daytime T_{ped} and b) nighttime T_{ped} for 100m x 100m spatial domain of LCZ 6. The dashed red line is the 1:1 line.....	98
Figure 5. 21. Regression model for predicted and calculated a) daytime T_{ped} and b) nighttime T_{ped} for 100m x 100m spatial domain of LCZ 7. The dashed red line is the 1:1 line.....	99

Figure 5. 22. Regression model for predicted and calculated a) daytime T_{ped} and b) nighttime T_{ped} for 100m x 100m spatial domain of LCZ 8. The dashed red line is the 1:1 line.....	100
Figure 5. 23. Regression model for predicted and calculated a) daytime T_{ped} and b) nighttime T_{ped} for 100m x 100m spatial domain of all LCZ combined. The dashed red line is the 1:1 line.....	105
Figure 5. 24. Regression model predicted and calculated a) daytime T_{ped} and b) nighttime T_{ped} from TUF-3D simulation based on data from Stewart et al. (2021). The dashed red line is the 1:1 line.....	109
Figure 5. 25. Image of daytime T_{plan} for 101m x 101m domains flight 1 of Vancouver LI area.....	116
Figure 5. 26. Image of daytime T_{ped} for 101m x 101m domains flight 1 of Vancouver LI area.....	117
Figure 5. 27. a) Scatter plot and b) Histogram showing T_{ped} and T_{plan} for 101m x 101m domains flight 1 of Vancouver LI area.....	118
Figure 5. 28. Image of daytime T_{plan} for 101m x 101m domains flight 2 of Vancouver LI area.....	119
Figure 5. 29. Image of daytime T_{ped} for 101m x 101m domains flight 2 of Vancouver LI area.....	120
Figure 5. 30. a) Scatter plot and b) Histogram showing T_{ped} and T_{plan} for 101m x 101m domains flight 2 of Vancouver LI area.....	121
Figure 5. 31. Image of daytime T_{plan} for 101m x 101m domains flight 3 of Vancouver LI area.....	122
Figure 5. 32. Image of daytime T_{ped} for 101m x 101m domains flight 3 of Vancouver LI area.....	123

Figure 5. 33. a) Scatter plot and b) Histogram showing T_{ped} and T_{plan} for 101m x 101m domains flight 3 of Vancouver LI area.	124
Figure 5. 34. Regression model predicted and calculated daytime T_{ped} 101m x 101m spatial domain of Vancouver LI area (Flight1). The dashed red line is the 1:1 line.	125
Figure 5. 35. Regression model predicted and calculated daytime T_{ped} 101m x 101m spatial domain of Vancouver LI area (Flight 2). The dashed red line is the 1:1 line. ...	125
Figure 5. 36. Regression model predicted and calculated daytime T_{ped} 101m x 101m spatial domain of Vancouver LI area (Flight 3). The dashed red line is the 1:1 line. ...	126
Figure 5. 37. Regression model predicted and calculated daytime T_{ped} 100m x 100m spatial domain of Vancouver LI area (Flight 3). The dashed red line is the 1:1 line. ...	127
Figure A. 1. Building heights within LCZ 5.	169
Figure A. 2. Building heights within LCZ 7.	170
Figure A. 3. Building heights within LCZ 8.	171
Figure A. 4. Images of a) Daytime T_{plan} and b) Daytime T_{ped} for 50m x 50m domains of LCZ 5.	172
Figure A. 5. Images of a) Nighttime T_{ped} and b) Nighttime T_{plan} for 50m x 50m domains of LCZ 5.	173
Figure A. 6 Histogram plots for a) Daytime T_{plan} and T_{ped} and b) Nighttime T_{plan} and T_{ped} for 50m x 50m domain of LCZ 5.	173
Figure A. 7. Scatter plots for a) Daytime T_{plan} and T_{ped} and b) Nighttime T_{plan} and T_{ped} for 50m x 50m domain of LCZ 5.	174
Figure A. 8. Images of a) Daytime T_{ped} and b) Daytime T_{plan} for 100m x 100m domains of LCZ 5.	174

Figure A. 9. Images of a) Nighttime T_{ped} and b) Nighttime T_{plan} for 100m x 100m domains of LCZ 5.....	175
Figure A. 10. Images of a) Daytime T_{ped} and b) Daytime T_{plan} for 200m x 200m domains of LCZ 5.....	176
Figure A. 11. Images of a) Nighttime T_{ped} and b) Nighttime T_{plan} for 200m x 200m domains of LCZ 5.	176
Figure A. 12. Images of a) Daytime T_{ped} and b) Daytime T_{plan} for 50m x 50m domains of LCZ 7.....	177
Figure A. 13. Images of a) Nighttime T_{ped} and b) Nighttime T_{plan} for 50m x 50m domains of LCZ 7.....	177
Figure A. 14. Images of a) Daytime T_{ped} and b) Daytime T_{plan} for 100m x 100m domains of LCZ 7.....	178
Figure A. 15. Images of a) Nighttime T_{ped} and b) Nighttime T_{plan} for 100m x 100m domains of LCZ 7.	178
Figure A. 16. Images of a) Daytime T_{ped} and b) Daytime T_{plan} for 200m x 200m domains of LCZ 7.....	179
Figure A. 17. Images of a) Nighttime T_{ped} and b) Nighttime T_{plan} for 200m x 200m domains of LCZ 7.	179
Figure A. 18. Images of a) Daytime T_{ped} and b) Daytime T_{plan} for 50m x 50m domains of LCZ 8.....	180
Figure A. 19. Images of a) Nighttime T_{ped} and b) Nighttime T_{plan} for 50m x 50m domains of LCZ 8.....	180
Figure A. 20. Images of a) Daytime T_{ped} and b) Daytime T_{plan} for 100m x 100m domains of LCZ 8.....	181

Figure A. 21. Images of a) Nighttime T_{ped} and b) Nighttime T_{plan} for 100m x 100m domains of LCZ 8.	181
Figure A. 22. Images of a) Daytime T_{ped} and b) Daytime T_{plan} for 200m x 200m domains of LCZ 8.	182
Figure A. 23. Images of a) Nighttime T_{ped} and b) Nighttime T_{plan} for 200m x 200m domains of LCZ 8.	182
Figure A. 24. Albedo for LCZ 5.	185
Figure A. 25. Albedo for LCZ 6.	186
Figure A. 26. Albedo for LCZ 7.	187
Figure A. 27. Albedo for LCZ 8.	188

List of Symbols and Abbreviations

Symbol	Unit	Property
e_a	hPa	water vapor pressure
H/L	-	Building height to length ratio
H/W or λ_s	-	building height to street width
K_{\downarrow}	Wm^{-2}	downward shortwave flux density
LAST	-	Local Apparent Solar Time
LCZ	-	Local Climate Zone
LiDAR	-	Light Detection and Ranging
L_{\downarrow}	Wm^{-2}	downward longwave flux density
λ_p	-	Plan to area ratio
NDVI	-	Normalized Difference Vegetation Index
PASS	-	Phoenix Area Social Survey
Q^*	Wm^{-2}	net radiation flux density
Q_h	Wm^{-2}	convective sensible heat flux density
QUAC	-	Quick Atmospheric Correction

SA	-	Sub Area of an LCZ
σ	$5.67 \times 10^{-8} \text{ W m}^{-2} \text{ K}^{-1}$	Stefan-Boltzmann constant
SVF	-	Sky View Factor
T_{air}	$^{\circ}\text{C}$	Air temperature
T_{blg}	$^{\circ}\text{C}$	Building surface temperature
T_{c}	$^{\circ}\text{C}$	Complete temperature
TA	$\text{J m}^{-2} \text{ s}^{-0.5} \text{ K}^{-1}$	Thermal admittance
T_{inc}	$^{\circ}\text{C}$	Incomplete temperature
T_{ped}	$^{\circ}\text{C}$	Pedestrian temperature
T_{plan}	$^{\circ}\text{C}$	Plan temperature
TUF-3D	-	Temperatures of Urban Facets in 3 Dimensions
UHI	-	Urban Heat Island
Z_0	-	Momentum roughness length
Z_{ref}	m	Reference height for forcing data
Z_h	m	mean building height

List of Appendices

- A1. Horizontal Boundary Conditions Set-up
- A2. Vertical Boundary Conditions Set-up
- A3. Sub-LCZ Spatial Variabilities
- A4. Daytime and Nighttime T_{plan} and T_{ped} Estimations for Sub-Areas.
- A5. Images of Building Heights in Each Study Area.
- A6. Images of T_{ped} and T_{plan} for LCZ 5, 7 and 8
- A7. Determining Shaded and Sunlit Walls for the Study Areas using Azimuth Angles and Overhang Calculations
- A8. Graphical visualizations of albedo in each study area.
- A9. Input Parameters for LCZ 5 SA 1

Chapter 1

1 Introduction

The alteration of the natural land covers to build houses, roads, and industries increases urban surface temperatures. Urban areas are characterized by important spatial and temporal patterns of temperature that have implications for humans (e.g., heat stress in a city varies spatially). With increasing populations in urban areas and expanding urban development, there is a need for a deeper understanding of how to estimate the relevant temperature of specific surfaces of the urban environment that contribute to urban heat problems, along with their spatiotemporal behavior in space (neighborhood type) or time (day and night).

Remote sensing technologies have been used to study environmental hazards, understand urban climate changes, and monitor surface temperatures in cities for many years (Poursanidis and Chrysoulakis, 2017). The complete surface temperature of a 3-Dimensional urban area includes horizontal and vertical surface temperatures. Horizontal surface temperatures (T_{plan}) include rooftops, treetops, and ground surface temperature. Vertical surface temperatures include walls of buildings. An incomplete surface temperature may therefore be defined as the temperature of any subset of the complete 3D urban area. Even though remote sensing provides a potentially attractive way to assess heat in cities, it has limitations. This is because surface temperatures are different from air temperatures and because the surfaces seen by remote sensors do not match the surfaces that are of relevance to different urban heat applications. For example, the surfaces that contribute to the heat load on pedestrians include walls, the ground, and the area below treetops, and thus, they are the relevant surfaces for outdoor thermal comfort. Nadir-view satellites and airborne remote sensors, however, see primarily rooftops, the ground, and treetop surface temperatures (i.e. T_{plan}). This leads to a mismatch between the combination of surfaces observed by remote sensors and the surfaces that are relevant to particular applications.

1.1 The Urban Thermal Environment

Humans have always altered the environment to improve their standards of living. The continuous alteration of lands has created urban and rural areas. The rapid urbanization of the earth, mass migration to cities, and congestion in urban areas, coupled with the already known health issues in these urban areas have made cities a hotspot for sustainability studies (Zhu et al., 2019).

One of the most notable differences in climate between an urban area and a rural area is temperature. In urban areas, both air and surface temperatures are warmer than the nearby rural areas due to alteration of the natural land cover which transforms the surface energy balance (defined as the energy input and output from a surface) of different surfaces, and the urban area in general. Our understanding of urban air temperature is vast and detailed, and goes back to the 1800s. Luke Howard (1810) was the first person to realize that air temperatures are slightly higher in urban areas than in rural areas. In his book, *The Climate of London*, Howard compared the mean air temperature of London to the nearby rural areas and noticed that the air temperature in London was higher than those in the rural areas (Howard, 2007). The term “Urban Heat Island (UHI)” was later coined to explain Howard’s discovery (Oke, 1995). Air temperature UHI shows a temperature increase from the edges of the city to the center of the urban area, especially at night, generating a profile like a dome-shaped island.

Urban surface temperature studies, however, are more recent and an interesting field of research as surface temperatures are a driver of urban air temperature heat islands. Figure 1.1 shows the relationship between surface temperature (black line) and air temperature (red line) during clear weather conditions across a hypothetical city.

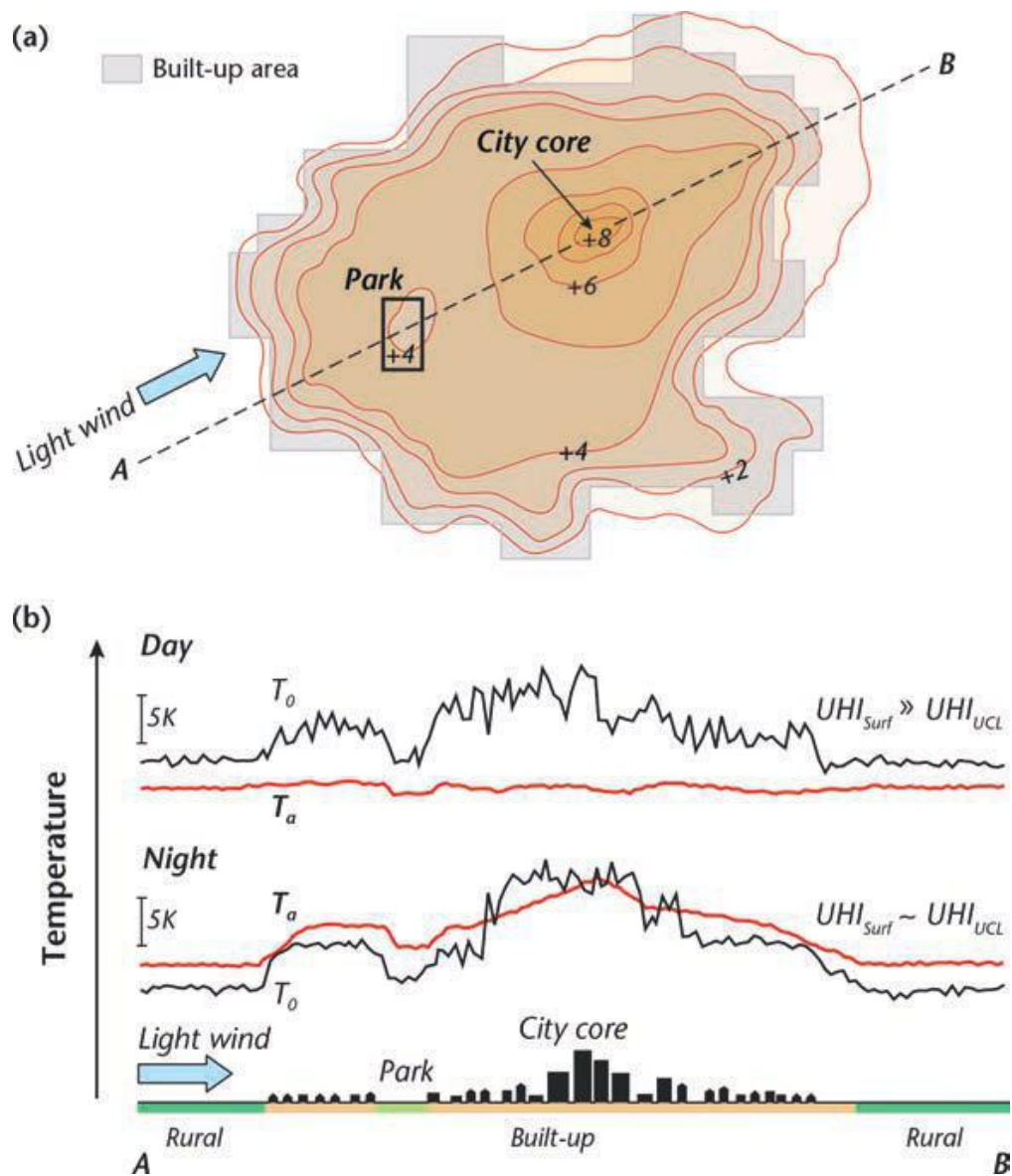


Figure 1. Relationship between air and surface temperatures on a clear day and night (Oke et al., 2017)

A close relationship exists between surface and air temperatures and their respective urban heat island effects at nighttime. From the edges of the city to the center of the urban area, there is an increase in the alteration of the natural land and the use of different materials to build houses. At nighttime, the different surfaces from the built environment release the absorbed daytime radiation as heat into the atmosphere more slowly than that from the surrounding rural regions. Under clear and calm conditions at nighttime, with low advection (horizontal transport by winds) of heat out of the city, the heat remains in the city, creating the UHI effect. Anthropogenic activities, which release more heat into the city, removal of vegetation, the thermal and radiative properties of the materials that help them absorb and store heat, and the reduced sky view factor (SVF) arising from the 3D surface structure of the city, all contribute to the UHI effect (Oke et al. 2017). SVF is a quantitative measure used in urban and environmental studies to describe the proportion of the visible sky hemisphere from a specific location on the ground (Oke et al. 2017).

1.2 Surface temperatures and urban heat assessments

Excessive heat stress can be fatal, especially to children and older people. With warming due to large scale climate change, combined with urban climate effects there has been a recent increase in interest in understanding intra-urban variations in urban temperature, as a contributor to heat stress (Cao et al. 2022; Top et al. 2020).

Urban heat assessments play a crucial role in our assessment of thermal comfort and thermal hotspots in urban areas. Various approaches are employed to assess different variables or parameters that affect urban heat. One commonly used method involves monitoring air temperatures using thermometers placed at different meteorological stations throughout an urban area. These stations are strategically positioned to capture temperature variations across the city and provide data on local heat conditions. By analyzing this data, researchers and urban planners can identify areas experiencing higher temperatures, commonly known as heat spots.

Humidity, which is the amount of water content in the air is also an important variable in urban heat assessments. The approach to assess humidity in urban areas involve the use of hygrometers or psychrometers to measure humidity or relative humidity, respectively. These devices are placed at selected sites across the city to gather enough data to identify areas with high humidity levels that may contribute to increased heat stress. Researchers also assess urban wind speed, as wind disperses and transfers heat from one location to another. Researchers measure wind speed using anemometers, which quantities direction and velocity of wind. By knowing the areas with low wind speed, researchers can estimate heat accumulation and the resulting heat stress in those locations.

Some researchers have used more advanced thermal indices such as the Mean Radiant Temperature (MRT) and Universal Thermal Climate Index (UTCI) to gain a more comprehensive understanding of urban heat phenomena. These techniques, while complex, offer more nuanced insights into thermal behavior and human comfort. Mean Radiant Temperature (MRT) is a method that quantifies the impact of radiant energy on perceived temperature in urban settings (Tan et al. 2014). This energy is derived from sources like the sun, buildings, and other objects, which absorb, store, and radiate heat. The MRT is a critical element in thermal comfort studies as it accounts for the asymmetrical and angular impacts of radiant heat, which are common in urban environments with diverse surfaces and structures (Kong et al. 2022). This methodology involves the use of sophisticated sensors or computational models to calculate the weighted average of all radiant temperatures within a given field of view.

Universal Thermal Climate Index (UTCI), is a comprehensive heat assessment tool that reflects the physiological response of the human body to the surrounding climatic conditions (Bröde et al. 2012). The index incorporates a complex set of variables, including air temperature, radiant temperature, humidity, and wind speed. It uses advanced biometeorological models to simulate the human body's thermal responses to these environmental parameters and estimates the equivalent air temperature at which these responses would occur in an idealized reference environment (Błażejczyk et al. 2013). The outcome is a single, easily interpretable index that represents the "feels like" temperature, making it a practical tool for urban planners and public health officials.

Despite the insightful data that MRT and UTCI methodologies provide, they come with inherent complexities. These techniques require specialized equipment, advanced computational models, and significant technical expertise to implement effectively. For example, measurement of the MRT requires monitoring the radiation fluxes in three separate planes, and can only sample a relatively small number of locations for a given time period (e.g. Middel and Krayenhoff, 2019). Similarly, the UTCI demands substantial inputs that require either extensive measurements or high resolution modeling. The complexity and cost of these methodologies may pose challenges for some researchers, particularly in low-resource settings.

Another approach to assessing urban heat involves the use of thermal remote sensing technologies. This approach is favored by numerous researchers due to its comparative simplicity and the ease with which results can be acquired. Thermal remote sensing allows for the measurement of surface temperatures, which directly influence air temperature (Figure 1. 1). Surface temperatures are driven by factors such as building materials, vegetation cover, and the urban heat island effect. By capturing surface temperature data, remote sensing provides valuable insights into localized heat patterns and helps identify areas where interventions may be necessary to mitigate heat stress.

With the invention of satellites, it became possible to monitor surface temperatures over large areas regularly. Remote sensing of surface temperatures initially focused on monitoring ocean surface temperatures (McClain et al., 1985) that provide expansive, homogeneous surfaces that are easily observed. Later, satellite thermal remote sensing was used to monitor urban surfaces. For example, Roth et al. (1989) monitored the surface temperature of Vancouver, Seattle, and Los Angeles with the use of NOAA AVHRR satellite data. Many modern researchers have also used Landsat 8 satellite to assess urban heat (e.g. Seletković et al. 2023; Matuzko & Yakubailik, 2018; Sagris & Sepp, 2017, Tsou et al. 2017).

1.3 Limitations of Thermal Remote Sensing in Urban Areas

The 3D structure of an urban area, together with the heterogeneous materials and properties of these surfaces, makes monitoring surface temperatures of urban areas more difficult than horizontal ocean surfaces or homogenous land surfaces with low surface cover, such as deserts or grassland.

Roth et al. (1989) made explicit the conceptual limitations of the application of thermal remote sensing in urban areas. The active surfaces of the 3D urban area include the surfaces of the ground, rooftops, walls of buildings, and tree crowns, all of which emit radiation. Figure 1. 2 shows all the active surfaces of a typical urban area. To get a complete estimate of the thermal conditions of an urban area, temperatures of all the active surfaces can be measured (or estimated) to compute an “area-weighted temperature” (Voogt, and Oke, 1997). This temperature is known as the complete urban surface temperature (Figure 1. 2a).

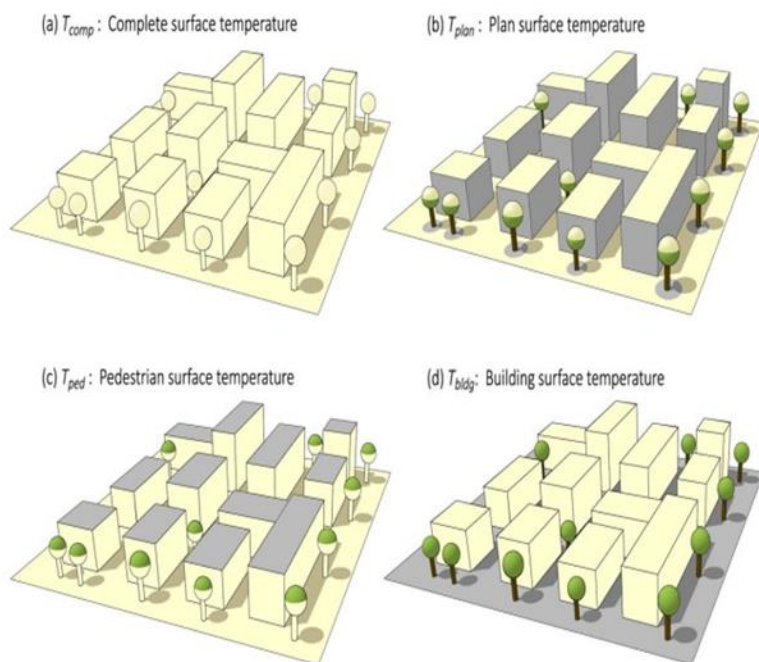


Figure 1. 2. Complete and incomplete surface temperatures (Stewart et al., 2021).

Satellite thermal remote sensing, however, only measures the temperatures that are within the direct line of sight of the sensor (Figure 1. 2b), so it most often measures rooftops, tree crowns, and the ground, excluding areas under crowns of trees and walls of buildings, producing data that are an *incomplete* and biased representation of the complete thermal conditions of the urban area (Stewart et al., 2021). Although satellite thermal data are themselves a type of incomplete surface temperature, their sampling of surfaces is different from the combination of surfaces used to define outdoor thermal comfort (Figure 1. 2c) or the exterior heat loading on buildings (Figure 1. 2d). Thus, incomplete surface temperature data from a satellite is not necessarily representative of the incomplete surface temperatures for urban thermal comfort assessments, although assessments of this agreement are generally lacking.

The complete urban surface temperature is a conceptually useful measure, but a more application-driven assessment of urban surface temperatures would combine components of the complete urban surface that are relevant for specific applications. Outdoor thermal comfort (Lindberg et al., 2014), indoor building energy use (Gustin et al., 2020), and sensible heat flux observation and modeling (Voogt and Grimmond 2000) all depend on relevant incomplete surface temperatures, and not the complete urban surface itself, or the view-direction dependent incomplete surface temperatures seen by a satellite.

For example, to assess the pedestrian comfort of an urban area requires the relevant component surface temperatures, which are primarily walls and ground surface temperatures, along with the underside of tree crowns (Figure 1. 2c), as they are the direct contributors to the thermal radiative heat load on a pedestrian (Middel and Krayenhoff, 2019), assuming flat rooftops that do not emit or reflect radiation into the street canyon. Thus, rooftop temperatures seen by remote sensors are not directly relevant in the assessment of outdoor pedestrian thermal comfort, while wall temperatures and the undersides of tree canopies, unseen by remote sensors, are relevant in this application. Wall temperatures are also important in the assessment of indoor climates. Walls and rooftops transmit heat inside buildings and are thus the surfaces of relevance to this application (Figure 1.2d), but again remote sensors do not directly see this combination of surfaces.

1.4 Spatio-Temporal Behaviors of Surface Temperatures: Implications for Outdoor Thermal Comfort and Urban Planning

“What is the spatio-temporal behavior of incomplete surface temperatures that are relevant for applications such as outdoor thermal comfort (wall and ground surface temperatures)?” This question arose from recent studies, such as Yang et al. (2021) who showed that surface geometries including SVF, building height, building density, and time of day affect urban surface temperature intensities. Very few studies have been completed that examine the spatio-temporal behavior of complete surface temperatures (Allen et al. 2018, Adderley et al., 2015, Jiang et al., 2018) in contrast to the vast number of studies that examine incomplete surface temperatures as most-often seen by remote sensors (i.e., rooftop and ground surfaces; Bechtel et al. 2019).

A first attempt to answer the question above is the simple modeling-based study of Stewart et al. (2021). They attempted to estimate the diurnal behavior of relevant incomplete surface temperature for both outdoor and indoor thermal comfort for different neighborhoods and climates, with the use of a numerical model.

Figure 1. 3 below shows some of the results from their study. The figure panels show the results from simulations of diurnal temperature differences between incomplete surface temperatures relevant to indoor thermal comfort (T_{bldg}) and incomplete surface temperatures as seen by a satellite (T_{plan}) in the left panel, and the diurnal temperature differences between incomplete surface temperatures for outdoor thermal comfort (T_{ped}) and incomplete surface temperatures as seen by a satellite (T_{plan}) in the right panel, for three local climate zones (LCZ) of a hot desert climate.

While T_{ped} is the weighted average temperature of all surfaces that a pedestrian at street level would encounter, which includes roads, walls, ground surfaces, T_{bldg} symbolizes the heat absorbed by a building's exterior (i.e. the weighted average of wall and roof surface temperature). T_{bldg} has implications for the thermal discomfort felt by people inside the building and consequently, the energy necessary for heating or cooling the interior of buildings (Stewart et al. 2021).

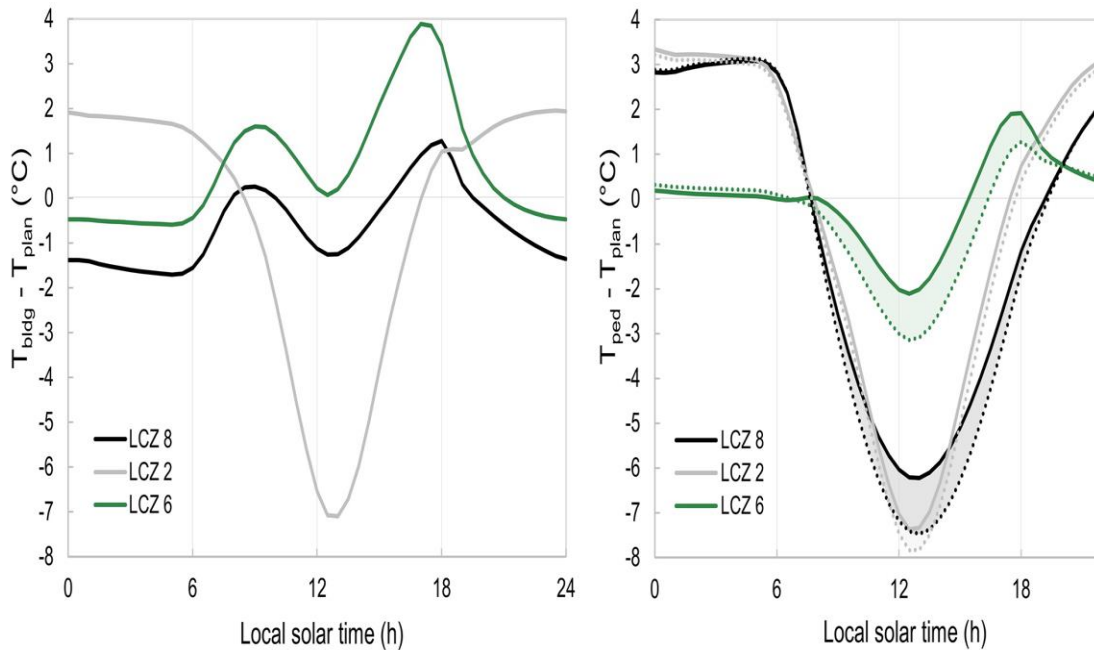


Figure 1. 3. Graphical visualization of the difference in application specific incomplete surface temperatures from plan view surface temperatures based on TUF-3D modelling for three Local Climate Zones in a hot dry desert climate showing the differences between between (left panel) T_{bldg} and T_{plan} and (right panel) T_{ped} and T_{plan} (Stewart et al., 2021).

These results show substantial differences in the application-specific incomplete surface temperatures and those typically measured by nadir-viewing remote sensors.

The Local Climate Zones (LCZ) system (Figure 1. 4) is a land cover classification system designed to separate areas that are expected to have different near-surface air temperatures (Stewart and Oke, 2012). It contains 17 different surface covers and surface structures that can represent the full spectrum of urban, rural, and natural surface types over spatial scales for approximately 100 m and larger (Stewart and Oke, 2012). Even though the LCZ classification was created to study urban near-surface air temperatures, other researchers such as Bechtel et al. (2019) have classified different neighborhoods with the LCZ

classification in their urban surface temperature studies and shown that most LCZs are also characterized by differences in remotely observed nadir-viewing surface temperature (T_{plan}). The spatiotemporal behavior of relevant incomplete temperatures as shown in Stewart et al. (2021) is also limited to a few select LCZ neighborhoods, and thus needs to be broadened to include a broader range of LCZs.

TABLE 2. Abridged definitions for local climate zones (see electronic supplement for photographs, surface property values, and full definitions). LCZs 1–9 correspond to Oke's (2004) urban climate zones.


















Built types	Definition	Land cover types	Definition
 <p>1. Compact high-rise</p>	Dense mix of tall buildings to tens of stories. Few or no trees. Land cover mostly paved. Concrete, steel, stone, and glass construction materials.	 <p>A. Dense trees</p>	Heavily wooded landscape of deciduous and/or evergreen trees. Land cover mostly pervious (low plants). Zone function is natural forest, tree cultivation, or urban park.
 <p>2. Compact midrise</p>	Dense mix of midrise buildings (3–9 stories). Few or no trees. Land cover mostly paved. Stone, brick, tile, and concrete construction materials.	 <p>B. Scattered trees</p>	Lightly wooded landscape of deciduous and/or evergreen trees. Land cover mostly pervious (low plants). Zone function is natural forest, tree cultivation, or urban park.
 <p>3. Compact low-rise</p>	Dense mix of low-rise buildings (1–3 stories). Few or no trees. Land cover mostly paved. Stone, brick, tile, and concrete construction materials.	 <p>C. Bush, scrub</p>	Open arrangement of bushes, shrubs, and short, woody trees. Land cover mostly pervious (bare soil or sand). Zone function is natural scrubland or agriculture.
 <p>4. Open high-rise</p>	Open arrangement of tall buildings to tens of stories. Abundance of pervious land cover (low plants, scattered trees). Concrete, steel, stone, and glass construction materials.	 <p>D. Low plants</p>	Featureless landscape of grass or herbaceous plants/crops. Few or no trees. Zone function is natural grassland, agriculture, or urban park.
 <p>5. Open midrise</p>	Open arrangement of midrise buildings (3–9 stories). Abundance of pervious land cover (low plants, scattered trees). Concrete, steel, stone, and glass construction materials.	 <p>E. Bare rock or paved</p>	Featureless landscape of rock or paved cover. Few or no trees or plants. Zone function is natural desert (rock) or urban transportation.
 <p>6. Open low-rise</p>	Open arrangement of low-rise buildings (1–3 stories). Abundance of pervious land cover (low plants, scattered trees). Wood, brick, stone, tile, and concrete construction materials.	 <p>F. Bare soil or sand</p>	Featureless landscape of soil or sand cover. Few or no trees or plants. Zone function is natural desert or agriculture.
 <p>7. Lightweight low-rise</p>	Dense mix of single-story buildings. Few or no trees. Land cover mostly hard-packed. Lightweight construction materials (e.g., wood, thatch, corrugated metal).	 <p>G. Water</p>	Large, open water bodies such as seas and lakes, or small bodies such as rivers, reservoirs, and lagoons.
 <p>8. Large low-rise</p>	Open arrangement of large low-rise buildings (1–3 stories). Few or no trees. Land cover mostly paved. Steel, concrete, metal, and stone construction materials.	VARIABLE LAND COVER PROPERTIES	
 <p>9. Sparsely built</p>	Sparse arrangement of small or medium-sized buildings in a natural setting. Abundance of pervious land cover (low plants, scattered trees).	Variable or ephemeral land cover properties that change significantly with synoptic weather patterns, agricultural practices, and/or seasonal cycles.	
 <p>10. Heavy industry</p>	Low-rise and midrise industrial structures (towers, tanks, stacks). Few or no trees. Land cover mostly paved or hard-packed. Metal, steel, and concrete construction materials.	<p>b. bare trees</p> <p>s. snow cover</p> <p>d. dry ground</p> <p>w. wet ground</p>	<p>Leafless deciduous trees (e.g., winter). Increased sky view factor. Reduced albedo.</p> <p>Snow cover >10 cm in depth. Low admittance. High albedo.</p> <p>Parched soil. Low admittance. Large Bowen ratio. Increased albedo.</p> <p>Waterlogged soil. High admittance. Small Bowen ratio. Reduced albedo.</p>

Figure 1. 4. Local climate zone classification system (Stewart and Oke, 2012).

1.5 Research Questions and Objectives

The initial work of Stewart et al. (2021) provided some first estimates of application-relevant incomplete surface temperatures based on numerical modeling. However, their work did not extend to the use of real-world observational data and there are no assessments of application-relevant incomplete surface temperatures at scales beyond individual study sites in the literature. Observed thermal data is preferred in the estimation of incomplete surface temperatures as they better represent the real-world thermal conditions - and its inherent spatial variability - of urban areas. Stewart et al. (2021) also is restricted in the number of LCZs it represents and does not represent the temperature variability within an LCZ. Estimating incomplete surface temperatures at smaller scales within an LCZ (sub-LCZ scale) shows the spatial variability of incomplete surface temperatures that characterize an LCZ and can provide more location-specific information to users.

In addition to variable building heights and street canyon widths, varying vegetation cover and different surface radiative and thermal properties values at different parts of an LCZ can affect the surface temperatures at different parts of the LCZ. It is hypothesized that, the varying heights, H/W, vegetation and other parameters at the sub-LCZ scale level may affect the incomplete temperatures so that they differ from the estimated overall incomplete temperatures at the LCZ scale. Thus, estimating incomplete surface temperatures at sub-LCZ scale will help us to understand the sensitivity of incomplete surface temperatures to different vertical and horizontal surface temperatures and this will also help us to understand the different heat loads on pedestrians at different parts of the LCZ. Because many researchers continue to depend on satellites to assess urban heat, there is a need to create a methodology that relates the surface temperatures seen by satellites and the relevant surface temperatures for thermal comfort assessments. This methodology will help researchers accurately estimate urban heat and thermal comfort in different parts of different urban areas.

Therefore, this research will answer the following research questions:

1. What is the temperature of "incomplete surfaces" that are most relevant in urban thermal comfort assessments, and what is their observed spatio temporal behavior in different neighborhoods of an urban area?
2. How are the relevant incomplete temperatures related to nadir view remotely sensed thermal images, and can the relevant incomplete temperatures be predicted by nadir view temperatures?

This study will be the first attempt to define and estimate application-relevant outdoor incomplete surface temperatures (T_{ped}) using observed data as an attempt to expand on the study by Stewart et al (2021), which used a full model approach to estimate the diurnal behavior of incomplete temperatures. This will give a more accurate and real world understanding of incomplete temperatures.

Answers to the second question will help find the relationship between nadir view plan temperatures (ie, rooftop, ground and treetop temperatures) and incomplete temperatures for outdoor thermal comfort (wall, ground and area below tree canopies), It is hypothesized that T_{ped} may be cooler than plan temperatures (T_{plan}) during the day as building walls and vegetation will make a huge difference for T_{ped} relative to the inclusion of roof temperatures in T_{plan} . At nighttime, it is hypothesized that T_{ped} may be hotter than T_{plan} as roof temperatures cool rapidly during the night because of their insulation properties.

An applied goal of the research is to develop relations that can be used to predict T_{ped} from the commonly measured T_{plan} to help researchers who depend on nadir view satellite images and to make them more application relevant.

1.6 A Potential Approach to Estimate the Temperatures of Surfaces Unseen by Satellites

If satellites see rooftops and ground temperatures, but they miss wall temperatures and the area below tree crowns, even though wall temperatures are relevant for both urban indoor and outdoor climates, then how do we generate wall temperatures to help us estimate the relevant incomplete surface temperatures? One potential way to answer this question is to estimate the temperatures of walls from numerical models. Mesoscale and microscale models have been used by researchers to simulate the real-world effects of the urban environment. For example, computational fluid dynamics models have long been used in engineering to simulate how air flows around obstacles. Recently, they have been used to understand airflow, and dispersal of heat through advection, in and out of urban areas (Baik et al., 2003). Also, energy balance models can simulate the surface energy balance of an urban area with the use of the thermal, geometric, and radiative properties of surfaces within the canopy layer. Some of the current energy balance models include the microscale urban surface energy balance model (MUSE; Lee and Lee, 2020), the three-dimensional urban canopy model (3DUCM: Conigliaro et al., 2021), the ENVI-MET model (Huttner and Bruse, 2009), the temperature for urban facets in 3D (TUF-3D; Krayenhoff and Voogt, 2007) and Vegetated Temperatures of Urban Facets (VTUF-3D; Nice et al., 2018).

In summary, my thesis builds upon the work of Stewart et al. (2021) by estimating the application-driven (relevant) incomplete surface temperatures at the LCZ neighborhood scale and sub-LCZ scale with the use of thermal airborne observational data.

1.7 Thesis Organization

The opening chapter provides a broad overview of the topic, outlining the importance of understanding urban surface temperatures in the context of growing urbanization. It introduces the use of remote sensing technologies to study these patterns, discussing their strengths and limitations. The chapter sets the Phoenix metropolitan area as the study area and highlights the need to assess temperature variations in various urban surfaces. Chapter 2 introduces the concept of Local Climate Zones (LCZ) and describes the specific LCZs in Phoenix that are central to this study. It explores how different LCZs contribute to the variations in surface temperature due to their unique physical and structural characteristics. The chapter includes a comparative analysis of these LCZs, focusing on their thermal behaviors. Chapter 3 discusses the blend of numerical modeling and real-world observational data used to assess pedestrian level temperatures (T_{ped}). It elaborates on the strategies for gathering data, processing it, and the calculations and models employed to evaluate surface temperatures in Phoenix's urban landscape. Chapter 4 presents an evaluation of the performance of the numerical models against real-world observations. It also addresses the limitations of the study, especially the lack of observed wall temperature data. Sensitivity analysis is conducted to gauge the reliability of the model predictions and to identify crucial parameters affecting the model outputs. Chapter 5 presents the results derived from the models and data analysis. Using graphical representations like scatter plots and multiple regression plots, it explores the relationship between T_{ped} and T_{plan} . The chapter also focuses on the comparisons between T_{ped} and T_{plan} for LCZ 6 at a 50m x 50m spatial scale, and its findings are discussed in relation to the broader context of urban heat patterns.

Chapter 2

2 Study area

The Phoenix metropolitan area is known for its warm and sunny climate, making it a prime location to study human thermal comfort. This chapter discusses the data sources utilized in this research, including the airborne remotely sensed data obtained from a 5-day campaign in 2011, which encompassed daytime and nighttime airborne remote sensing flights over the Phoenix metropolitan area. The data collected includes surface temperatures, albedo, surface reflectance, and the Normalized Difference Vegetation Index (NDVI).

However, because only select neighborhoods in the metropolitan area were selected in the original study to have fully processed and georeferenced thermal data, this study is limited to four select neighbourhoods that have LCZ classifications of LCZ 5, 6, 7, and 8. The thesis refers to these neighbourhoods by their LCZ label (e.g. “LCZ 5” is used as the ‘name’ for the study neighbourhood that has that LCZ classification. The chapter also highlights the LiDAR-derived building data used in this study, which provided detailed 3D representations of buildings in the study areas, including their heights and footprints. Finally, the chapter addresses the assessment of spatial variabilities of similar radiative and thermal properties within the LCZ study areas, as buildings within the same LCZ may have different radiative and thermal properties affecting surface temperatures.

2.1 Site Selection

The study area for this research is the Phoenix metropolitan area (Figure 2. 1), the largest metropolitan area in the southwestern part of the United States of America. The area is commonly referred to as the “Valley of the Sun,” as it experiences warm and sunny climates for most of the year (Cotton, 2019). The climate of the metropolis is moderately hot; a sub-tropical desert climate denoted as BWh on the Koppen Climate classification (Stone, 2012).

Study Area: Phoenix, AZ



LCZ graphics from
Stewart & Oke, (2012)

Figure 2. 1. Imagery showing Phoenix Metropolitan area.

According to World Population Review (2023), the last 2020 census recorded a population of 1,608,139 residents. The city also has a population density of 3201 people living in every square mile. Many researchers have previously studied the climate of the city to find ways to improve the thermal comfort of the ever-growing population of the Phoenix metro area (e.g. Middel et al. 2014; Li et al. 2016) especially given the frequency of heat events and the expected impacts of climate change.

The Phoenix metropolitan area was chosen as the study site for three main reasons: First, is the availability of pre-existing very high resolution (7m/pixel) airborne thermal data, that

covers 41 select parts of the urban area. Such datasets with a spatial resolution sufficient to resolve the urban surface components (e.g. building roofs) needed to construct the various application-relevant incomplete surface temperatures of interest to this thesis are rare. Second, the airborne dataset collected is spatially extensive enough to assess multiple different neighborhoods or LCZs. This attribute is necessary in order to understand the spatial behavior of the relevant incomplete surface temperatures across neighborhoods (and to examine variability within LCZs). Thirdly, there is an available LiDAR data set for the entire metropolitan area. These data are needed to provide building information such as building height, width, length, and footprint information required to estimate the area weightings that are part of incomplete surface temperatures.

2.2 Airborne Remotely Sensed Data

Airborne thermal images that were used for surface temperature analysis in this thesis were obtained from a 5-day airborne data collection campaign conducted in July, 2011, jointly funded by the Urban Vulnerability to Climate Change project (UVCC) and the Central Arizona – Phoenix Long-Term Ecological Research project (CAP LTER, NSF Grant No. BCS-1026865). The MODIS/ASTER Simulator (MASTER) was mounted on a Beechcraft B-200 aircraft to collect daytime and nighttime airborne data for the Greater Phoenix metropolitan area (Stefanov et al. 2015). The data includes daytime and nighttime surface temperatures, albedo, surface reflectance, and normalized difference vegetation index (NDVI). Daytime flights were conducted on July 12th and July 13th 2011 from 10:00 to 13:00 local time (Mountain Standard Time). Nighttime flights were also conducted on July 15th and July 16th, from 00:30 to 03:00 local time. The flight times were intentionally selected to represent mid-day and mid-night periods, respectively, when surface temperatures are more constant with time and to avoid the strong heating/cooling periods associated with sunrise and sunset (Jenerette et al. 2016). Even though the full dataset has already been processed to at-sensor radiance, only 41 spatially discrete Phoenix Area Social Survey (PASS) neighborhoods had been georeferenced to make a study on the

relationship between surface temperatures and land cover and residential heat impact in the selected PASS neighborhoods (Jenerette et al. 2016).

The MASTER instrument collects data in 50 spectral bands in the visible and infrared parts of the electromagnetic spectrum (Hook et al., 2001). The sensors were set only in the nadir view, thus only horizontal surface information, including the ground and rooftops, was obtained. The quick atmospheric correction (QUAC) algorithm found in the ENVI/IDL image processing software was used to perform atmospheric corrections to generate apparent surface emissivity, surface temperature, and NDVI, and reflectance. Even though the airborne data does not represent vertical surface temperatures, its coverage of the different parts of the metropolitan area produced horizontal surface thermal data for large areas with different neighborhoods at a spatial resolution that allows the separation of component parts of the urban surface (roofs, roads etc).

The data set therefore provides the real-world spatial behavior of different neighborhoods and the ability to extract relevant components of the urban surface that are part of application relevant incomplete surface temperatures. The high spatial resolution dataset also provides the ability to estimate the plan temperatures of different neighborhoods in the metropolitan area, and to degrade the 7m per pixel scale of the plan temperatures from the airborne data to match the scale of satellite sensors (e.g. 100m per pixel for Landsat 8). This provides the potential to assess the relationship between a satellite scale view of nadir temperatures and the different application-dependent definitions of ‘incomplete’ urban surface temperatures calculated from the high-resolution airborne remote sensing data for different neighborhoods of the urban area.

A limitation of the airborne data is the temporal restriction to one daytime and one nighttime overflight. This is because the thermal data for each LCZ was captured at just one time during the day and one time during the night (Table 2.1). This means that, even though we can estimate the spatial behavior of the relevant incomplete surface temperatures of different neighborhoods, we can only estimate their behaviour for two times of the day. Because of the time it took to acquire the airborne data for the entire Phoenix area, the individual study areas represent slightly different times and/or days.

Figure 2. 2 shows the diurnal cycle of solar radiation (in Wm^{-2}) for the two daytime flights in Table 2. 1 using data from the Phoenix Encanto station. It can be seen that the amount of solar radiation received for the study sites for the two days is very similar.

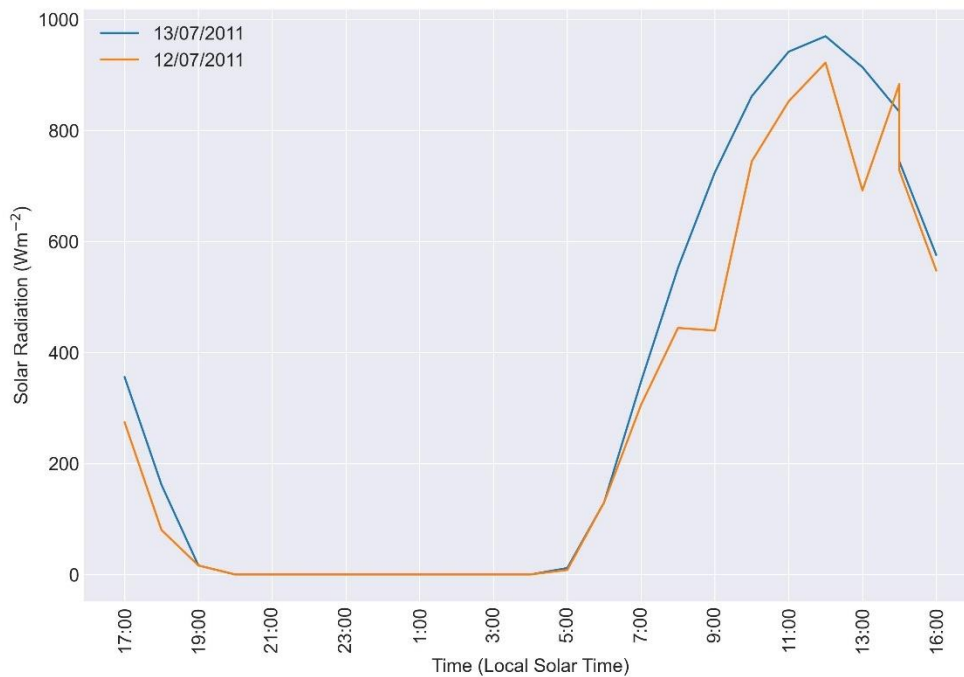


Figure 2. 2. Solar radiation observed during the period of daytime airborne remote sensing flights.

Figure 2. 3 and Figure 2. 4 show the diurnal cycle of air temperature ($^{\circ}\text{C}$) and relative humidity (%) respectively, for the two daytime flights in Table 2. 1.

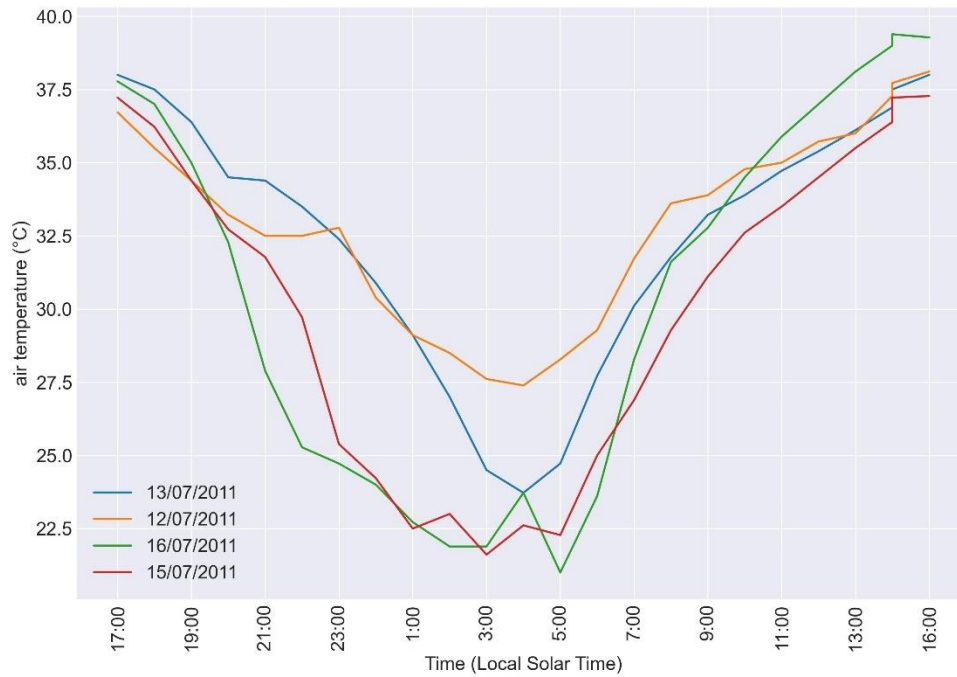


Figure 2. 3. Air temperature observed during the period of airborne remote sensing flights.

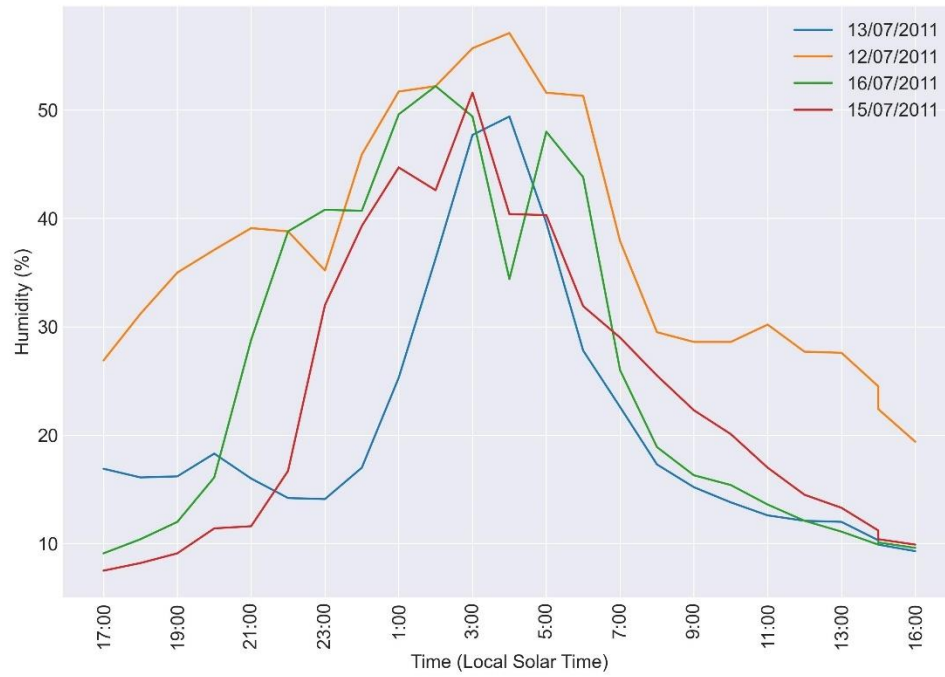


Figure 2. 4. Relative humidity observed during the period of airborne remote sensing flights.

Figure 2. 5 show the diurnal cycle of wind speed, for the daytime and nighttime flights in Table 2. 1.

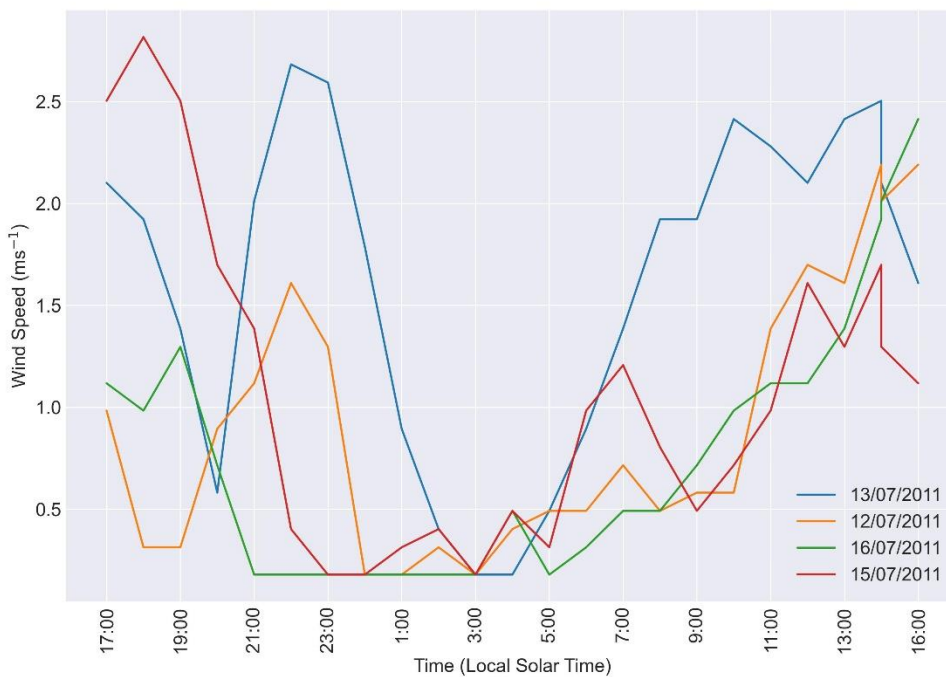


Figure 2. 5. Wind speed observed during the period of airborne remote sensing flights.

In order to approximate the time that thermal data for each LCZ was taken, the flight path data of the MASTER PROJECT (Stefanov, 2022) were obtained from the NASA/JPL website. These data contain the geographical coordinates and the start and end time of each flight path. The geographic coordinates were plotted in Google Earth Desktop to obtain the date and time in local apparent (mean) solar time (LAST) of the thermal data for each neighborhood selected for study (Table 2. 1).

Table 2. 1. The dates and times that the thermal data were collected for each study

Study Area	Total Plan area (m ²)	Daytime (LAST)	Daytime Elevation Angle (°)	Daytime Azimuth Angle (°)	Nighttime (LAST)
LCZ 5	501564	13/07/2011; 11:00	71.7	125.4	16/07/2011; 1:00
LCZ 6	1202006	12/07/2011; 13:00	73.1	230.6	15/07/2011; 3:00
LCZ 7	1674658	12/07/2011; 12:00	78.4	175.4	15/07/2011; 2:00
LCZ 8	718445	12/07/2011; 13:00	73.1	230.6	15/07/2011; 3:00

Comparing the graphs in Figure 2. 2 to Figure 2. 5 and the data from Table 2. 1 **Error! Reference source not found.**, it becomes evident that the weather conditions, especially the temperature between the 12th and 13th of July, as well as the 15th and 16th of July, are strikingly similar. The clear skies indicated by the solar radiation data further accentuate this observation. Thus, the data from the MASTER sensor can be confidently employed in this study. The analysis of the diurnal cycle reveals distinctive patterns typical of urban areas during the summer season:

Air Temperature

Daytime temperatures, as recorded on the 12th and 13th of July, ranged between 34.72°C to 36.11°C across the LCZs, emblematic of the summer heat. Contrastingly, the nights of the 15th and 16th witnessed a dip in temperatures, spanning from 24.50°C to 29.11°C, showcasing the natural cooling post-sunset.

Humidity

A complementary pattern emerges in humidity levels. All four days show similar patterns even though the difference between humidity for two days could reach as high as 10%

Solar Radiation

Solar radiation data underscores the clear skies during the data collection period. With daytime values fluctuating between 914.12 Wm⁻² and 969.94 Wm⁻², the intense sunlight of the summer season is evident.

Wind Speed

The wind speed shows similar patterns on each of the airborne flight days; the winds were a little stronger on July 13, 2011 but otherwise the wind speeds were similar on most of the days.

Uniformity of Weather Conditions

The weather conditions during the specific flight times resonate with the broader diurnal patterns. Daytime flights on the 12th and 13th were marked by higher temperatures, lower humidity levels, significant solar radiation, and moderate wind speeds, representing typical mid-day weather. Conversely, the nighttime flights on the 15th and 16th are characterized by cooler temperatures, higher humidity, an absence of solar radiation, and diverse wind speeds. In the context of the study conducted on the nights of July 15 and 16, 2011, METARs (Meteorological Aerodrome Reports) were obtained from Phoenix Sky Harbor

International Airport (KPHX) from (Ogimet, n.d.). The analysis focused on the time intervals corresponding to the nighttime flights used for the study area (Table 2. **Error! Reference source not found.**).

Nighttime Observations

The METARs for the specified nights were decoded to characterize the meteorological conditions during the flights. One of the most crucial aspects of the METARs is the consistent indication of clear skies (CLR) during the time of the overflights. This observation is consistent across the reports for both nights, as might be anticipated for the region's typical weather patterns during the summer months.

The confirmation of clear skies during the nighttime observations has significant implications for the study. The absence of clouds ensures uniformity in the weather conditions across different dates at night. This uniformity facilitates the comparison of airborne imagery and other data for different dates without the interference of varying cloud cover. The information gleaned from the METARs adds an additional layer of confidence to the study and aligns with other meteorological conditions characterized during the flight. It further reinforces the decision to utilize the MASTER sensor data for the comprehensive analysis of urban surface temperatures and related climatic phenomena in the Greater Phoenix metropolitan area.

2.3 Assessing Thermal Comfort in Select Local Climate Zones of Phoenix Metropolitan Area

Wang et al. (2018) conducted studies to classify different neighborhoods of Phoenix and Las Vegas metropolitan areas into LCZs (Figure 2. 6).

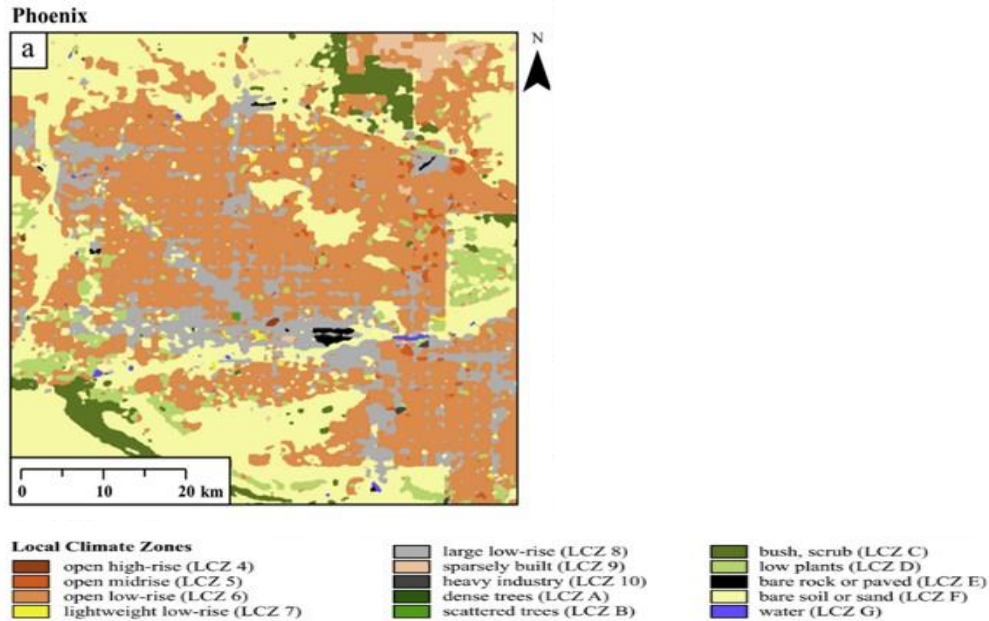


Figure 2. 6. Local climate zone map of Phoenix. Modified after Wang et al. 2018.

They found LCZ 4 to LCZ 10 in Phoenix. They used aerial photographs, basic definition, and surface geometry values for different LCZs by Stewart and Oke (2012), and the World Urban Database and Access Portal Tools (WUDAPT), a methodology for LCZ classification, proposed by Bechtel et al. (2015) to classify the LCZs. Their output for each LCZ included mean impervious surface fraction, mean pervious surface fraction, mean SVF and mean building surface fraction.

Even though the available LiDAR and LCZ data cover the entire Phoenix region, the available thermal data limits this study to LCZ 5, 6, 7 and 8, as none of the 41 discrete PASS neighborhoods fall within the other LCZ neighborhoods. Thus, study is limited to the assessment of incomplete surface temperatures in LCZ 5, LCZ 6, LCZ 7 and LCZ 8 (Figure 2. 7).



Figure 2. 7. Satellite visible wavelength images of a) LCZ 5 Study area, b) LCZ 6 Study area, c) LCZ 7 Study area, d) LCZ 8 Study area (Google Earth, 2022).

2.4 LiDAR-Derived Building Database

Light detection and ranging (LiDAR) is a modern remote sensing technology that can measure heights and distances of objects and create a very detailed 3D representation of those objects, through the use of laser remote sensing (Reutebuch et al. 2005).

The LiDAR data used for this study was obtained from the Data and Geospatial Hub of Arizona State University (Arizona State University, 2014). The data has already been processed into 3D building footprint polygon layers, which include the heights of buildings and the area of their footprints.

A limitation of the difference in the acquisition dates of the thermal data and the LiDAR data is that the LiDAR data shows some building rooftops as ground areas in the thermal data, as the LiDAR data were not obtained until three years after the thermal acquisition date (see Appendix A.1 for more information).

2.5 Meteorological Data Sites

A limitation of the thermal data is the lack of vertical surface temperatures. This required use of a numerical urban energy balance model to generate vertical surface temperature (see Chapter 3). The model requires a number of meteorological parameters including solar radiation, humidity and air temperature as part of the input forcing data. These parameters are measured at meteorological stations throughout the Phoenix metropolitan area. Phoenix Encanto and Phoenix airport weather stations were chosen as the meteorological stations for this study. Phoenix Encanto station is located at 33.478443°N 112.098046°W and an elevation of 334 m above sea level. Phoenix Encanto is the closest meteorological station to the study areas so is used as the source for all parameters except barometric pressure, which is taken from the Phoenix airport station. The measured parameters at the time of the aircraft over flight were used for this study (see Appendix A.2 for more information).

2.6 Sub-LCZ Spatial Variabilities

Even though the LCZ system classifies neighborhoods with similar characteristics including building heights and plan to area ratio, there are many other important factors that need to be considered in surface temperature studies. Different buildings within one LCZ with similar building heights may have different radiative and thermal parameters, which will result in varying surface temperatures. For example, buildings with the same height but different wall radiative properties (albedo and emissivity) or different thermal properties (thermal conductivity and heat capacity) may have different wall surface temperatures. Thus, these parameters need to be taken into consideration in order to

generate more accurate surface temperatures of buildings. To fully characterize the wall temperature variability in the four study areas would require simulating the model for each building with individualized thermal and radiative parameters. However, the number of buildings in each study area limits the viability of this approach, so a simpler approach is taken for this study. This involved further dividing each LCZ study area into sub-regions that have relatively homogeneous characteristics, termed here as “sub areas (SA).”

One characteristic of a SA (see Appendix A.3) within an LCZ is similar building type. For example, an SA may include primarily commercial buildings (warehouses, offices and other institutions), high density residential buildings (multi-storey buildings and apartments with few open spaces in between the building), or low-density residential buildings (smaller private homes with more open spaces between buildings). Further characteristics used to define an SA include: similar height of buildings, presence of roof overhangs, building plan to area ratio, and visual appearance of buildings including colors of rooftops and walls, and estimated thermal and radiative parameters. The identification of SAs permits a finer scale representation of urban structure for assessing wall temperatures from numerical modeling (see Section A.3) Multiple model runs at the SA scale provide a simple approach to obtaining some spatial variation in wall temperatures for use in incomplete surface temperature calculations..

Figure 2. 8 to Figure 2. 11 show all the SAs that exist in the study area. There were 15 SAs found in LCZ 5, 14 SAs in LCZ 6, 15 SAs in LCZ 7 and 12 SAs in LCZ 8.

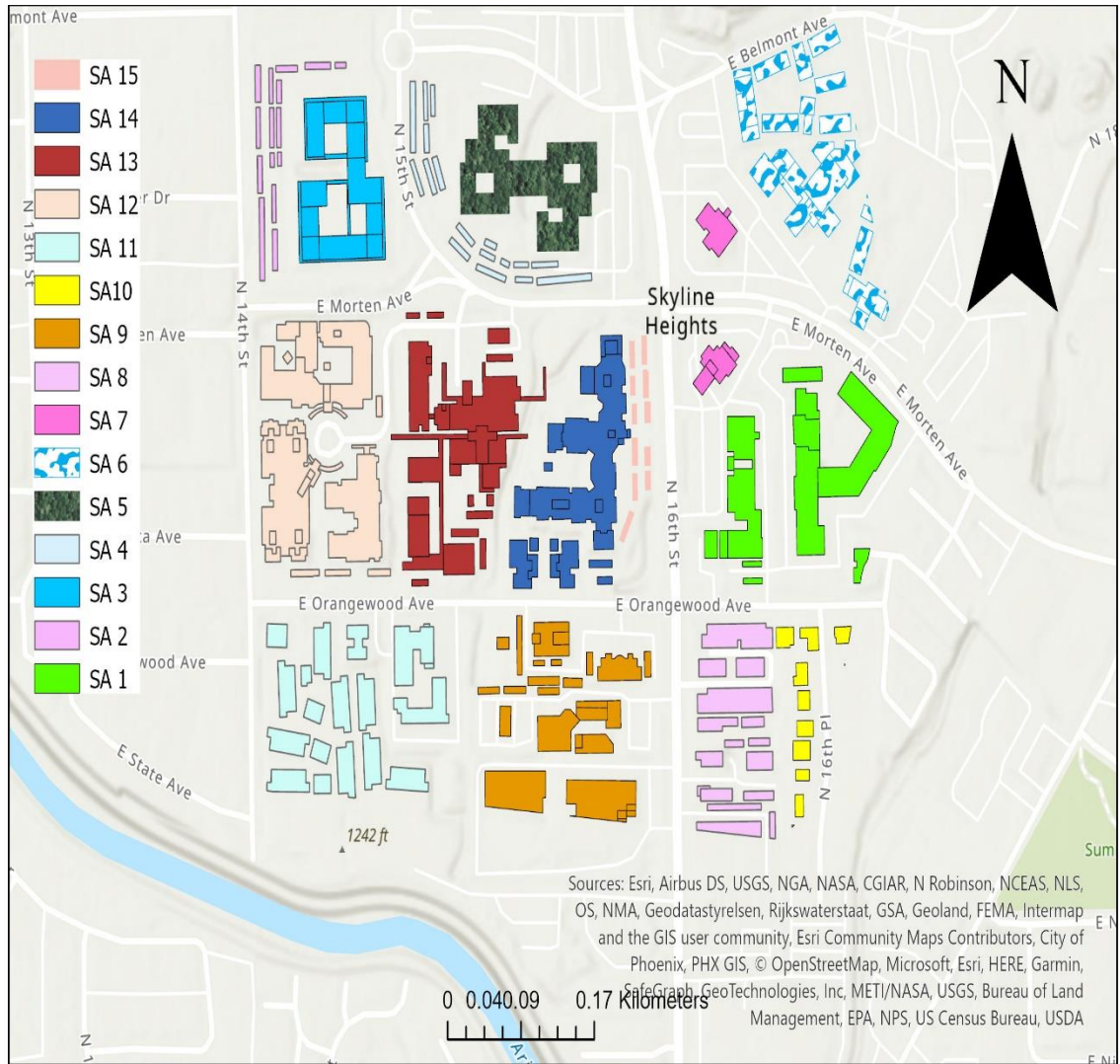


Figure 2. 8. The different sub areas within LCZ 5.

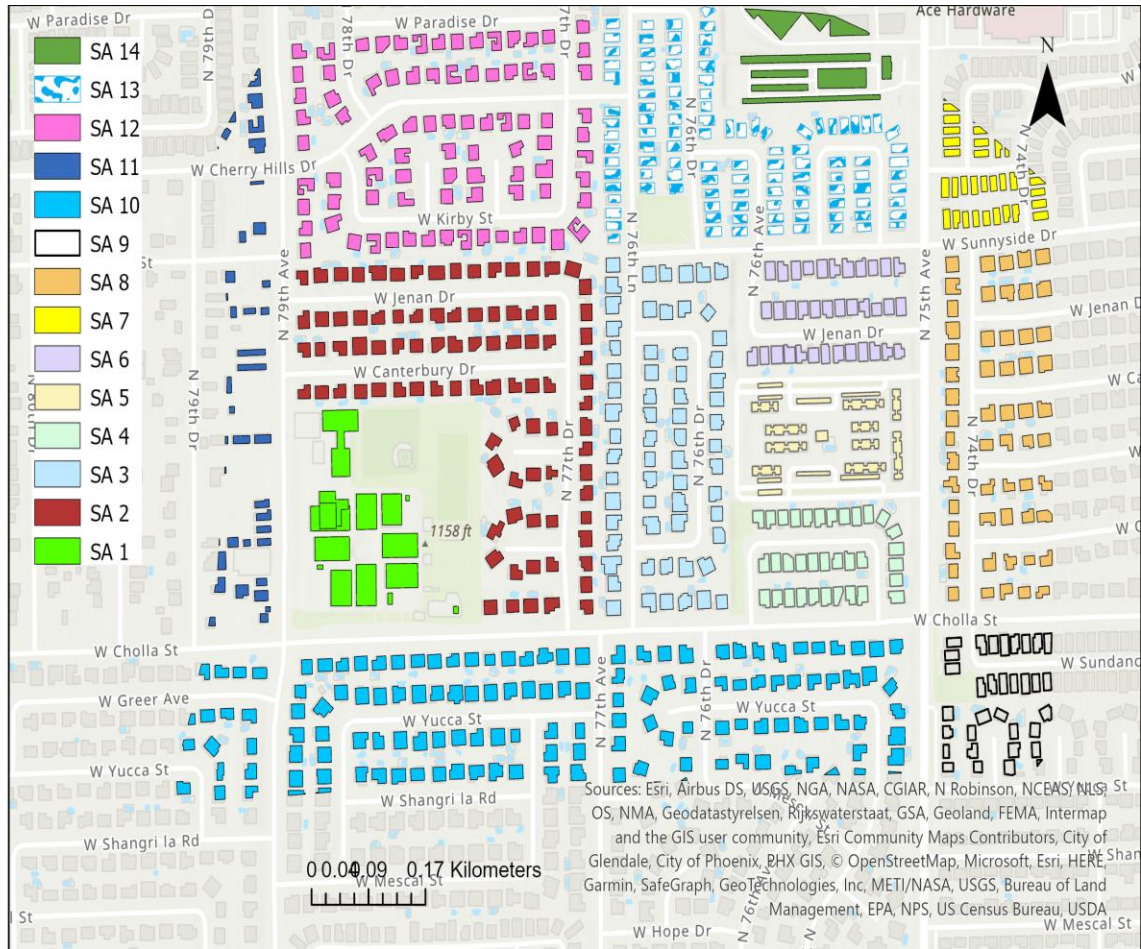


Figure 2. 9. The different sub areas within LCZ 6.



Figure 2. 10. The different sub areas within LCZ 7.

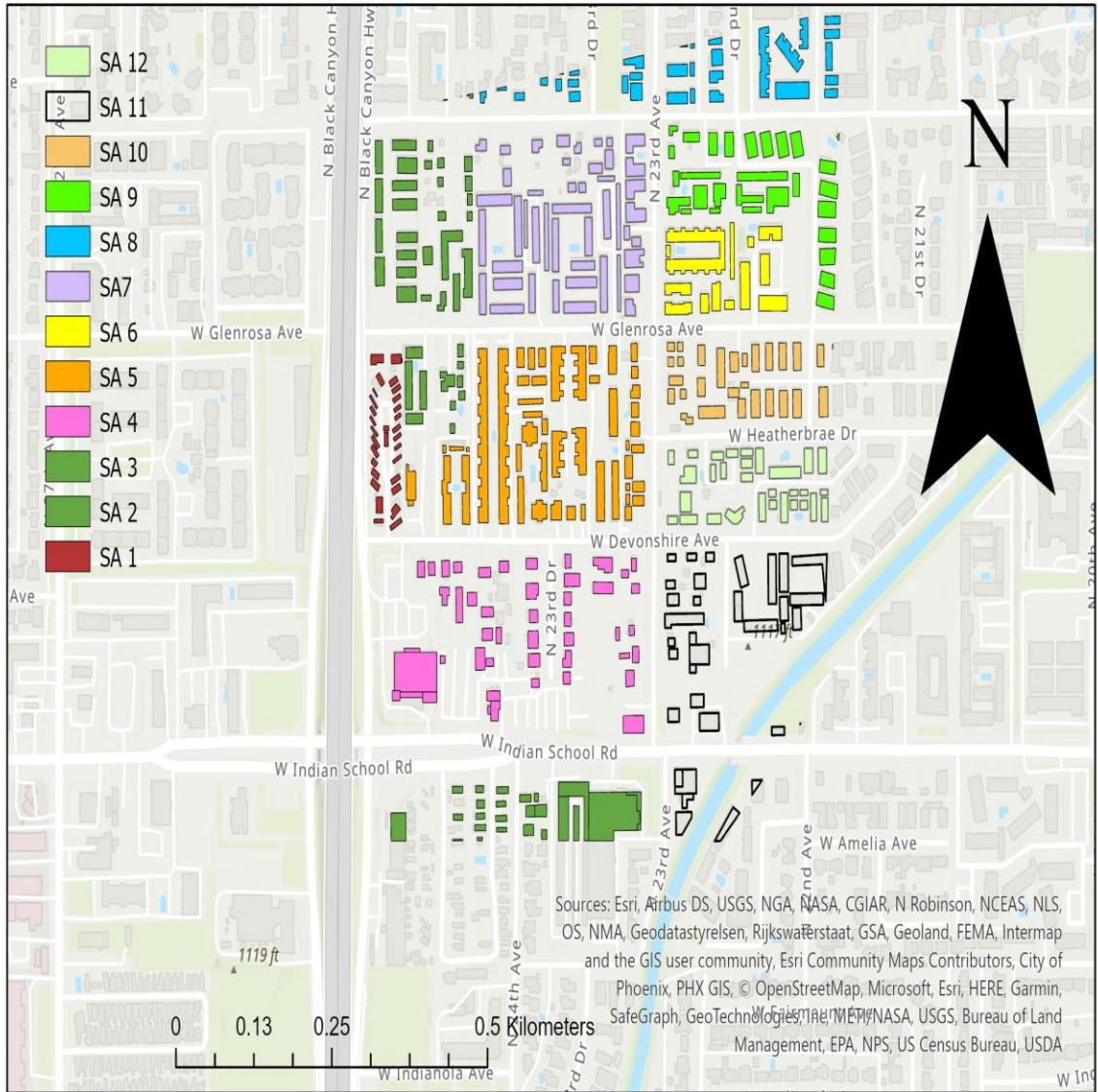


Figure 2. 11. The different sub areas within LCZ 8.

Chapter 3

3 Methods

Stewart et al (2021) assessed T_{ped} for select cities and neighborhoods using a numerical modeling approach. This thesis combines numerical modelling and real world observational data to assess T_{ped} . This chapter will explain the methods used to calculate T_{ped} from the combination of observational and modeling data.

3.1 Conceptual Approach

The best method to answer the research questions posed in Chapter 1 is a full observational data approach. This involves the use of observational data from remote sensing of an urban area with all neighborhoods in the LCZ classification. The thermal data must provide daytime and nighttime temperatures at a spatial resolution that resolves both the horizontal and vertical surfaces of all the LCZ neighborhoods in the urban area. This way, the component temperatures that are needed to estimate daytime and nighttime incomplete surface temperatures for both outdoor and indoor thermal comfort for each neighborhood can be extracted. A problem with this approach is the inability to get remote sensing data that contain horizontal and vertical component temperatures over a large area. Previous airborne thermal remote studies that combine nadir and off-nadir sensor views have generated horizontal and vertical surface temperatures (e.g. Voogt & Oke, 1997; Lagouarde et al. 2004) and some tower-based studies provide the ability to sample temperatures in a limited spatial domain (e.g. Adderley et al. 2015), but these are rare and the data typically provide a limited sampling of LCZs.

Most data available from airborne thermal remote sensing that covers larger areas include only the horizontal surface temperature. Thermal images from satellites also have an additional problem of not clearly resolving the temperatures of different horizontal surfaces, thereby limiting their use in estimating incomplete surface temperatures such as T_{ped} that do not include all horizontal surfaces. Another approach is to generate vertical and

horizontal surface temperatures from 3D numerical models and use them to estimate the relevant incomplete surface temperatures. This fully model-based approach was employed by Stewart et al. (2021). A major limitation of numerical modeling is its inability to mimic the real-world nature of urban areas. For example, models may use simple plane parallel cubes to represent buildings, which does not represent the actual geometries of different buildings and vegetation in an urban area and often simplify the thermal and radiative properties of materials that create important surface temperature variability (e.g. Figure 3. 1).

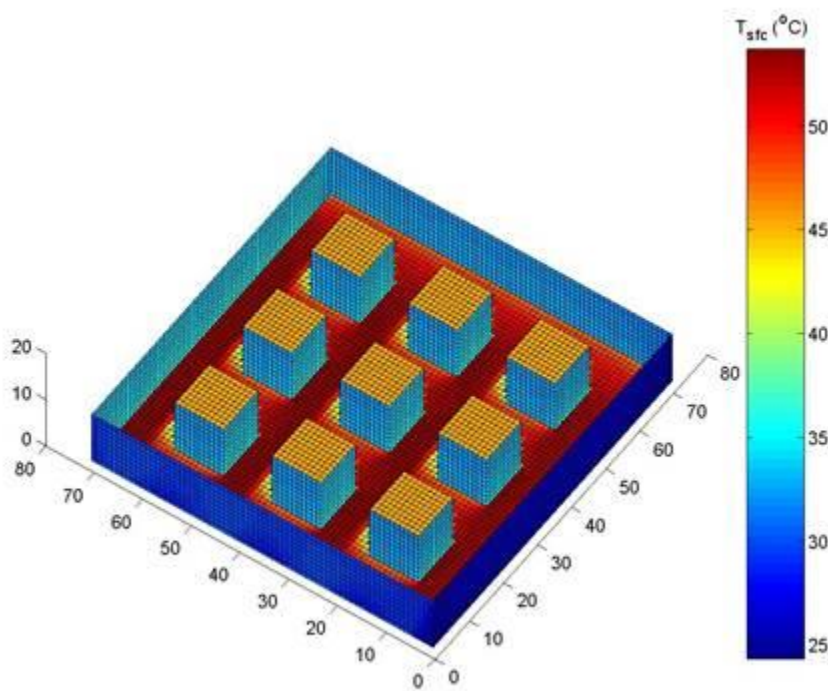


Figure 3. 1. Surface temperatures of a simple building array represented by TUF-3D (Image provided by Prof. E.S. Krayenhoff).

The next best solution after a full observational data approach is a hybrid of high-resolution observational data and a 3D model to generate temperatures for the missing surfaces. Using observed horizontal surface temperatures shows the real-world spatial behavior of these temperatures. This will help us to estimate accurately the spatial behaviors of T_{ped} .

3.2 Numerical Modelling of Wall Temperatures

The model selected for use in modeling the wall surface temperatures in this thesis is the Temperature for Urban Facets in 3D (TUF-3D) model (Krayenhoff and Voogt 2007). TUF-3D can simulate the surface energy balance and associated surface temperatures of a 3-D urban area with a focus on radiation exchanges as the sub-facet scale. This makes it a suitable model for this study. The use of TUF-3D provides a cheap method of estimating surface temperatures, as compared with airborne remote sensing, and outputs from TUF-3D do not need atmospheric or geometric corrections, unlike remote sensing data.

TUF-3D is designed to simulate the urban energy balance, and to generate urban facet temperatures for different surface properties (such as surface albedo), surface geometries (such as building height, vertical and horizontal surfaces), weather conditions (such as clear sky conditions) and solar angles. The model defines the 3D urban area as a simple plane parallel grid array of cubic cells (Figure 3. 2), with x and y coordinates of a cell defining the horizontal, and the z coordinate at the center of the cell, defining the vertical. Thus, the facets are further divided into identical square-sized sub-facets or patches. For example, a wall facet consists of identical square-sized cells (or patches). Patches can exchange longwave and shortwave radiation with the sky (e.g., radiation exchange with rooftop patches with the sky) or with other patches (e.g., radiation exchanges between walls and the ground). Patches can also exchange sensible heat by conduction with underlying street and building, and sensible heat by convection with the atmosphere (Aliabadi et al. 2017).

The simple plane parallel description of the model means that surfaces are not inclined. For example, in a typical urban area, some surfaces such as roofs or the ground may be sloped. TUF-3D assumes that all angles between two surfaces are 90 degrees. These cubic cells contain either ambient air, building interior (to define building facet surfaces), or street layers (to define street facet surfaces).

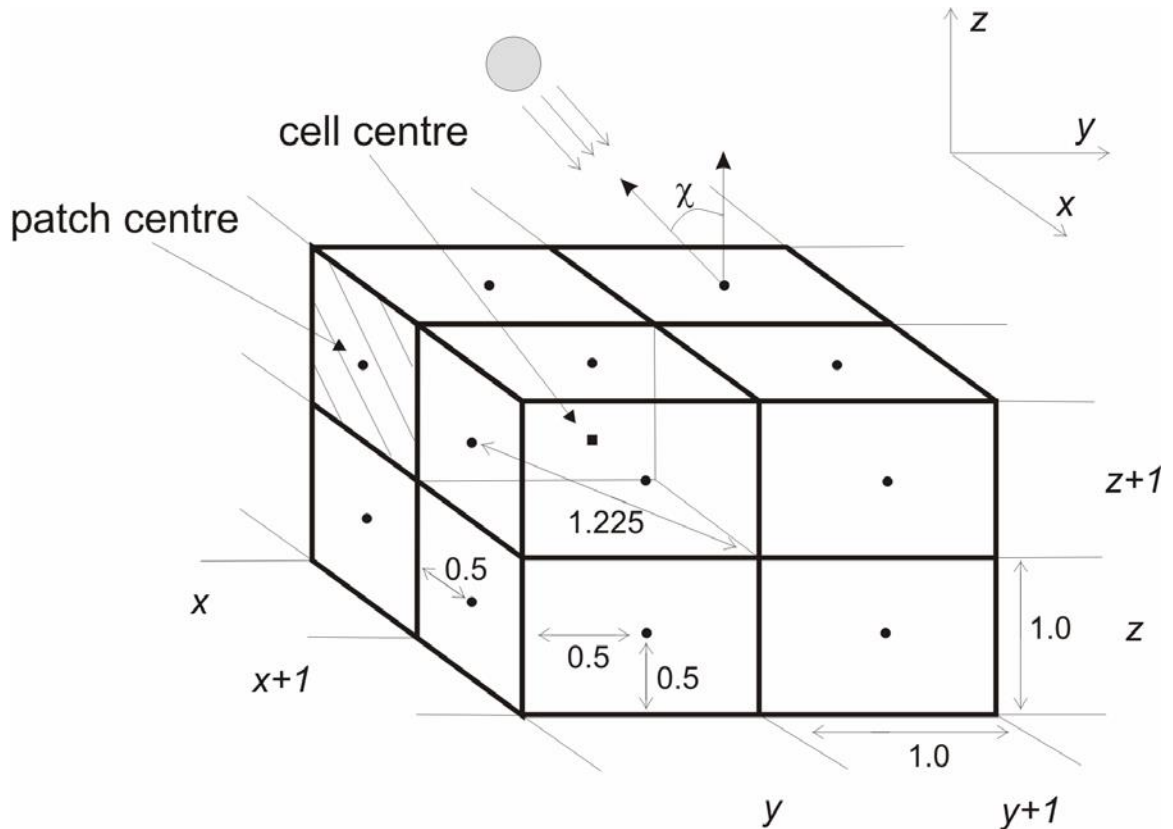


Figure 3. 2. Individual cells that represent a building in TUF-3D (Krayenhoff and Voogt, 2007).

The model also groups cells to form buildings with equal heights and rectangular footprints, with a test building in the middle of nine array buildings arrangement as the default arrangement of buildings (i.e. default horizontal boundary conditions). A user can set the domain to have different building heights or different street widths; all buildings in the array of 9 must have the same height, and all streets must have the same width. This is a limitation, as the real-world urban area has different building heights and widths.

The model requires atmospheric forcing from above the model; these are referred to here as vertical boundary conditions (see Appendix A.2). The forcing data, including short and longwave radiation, air temperature, humidity, pressure, wind speed and direction, can be provided from available observations or another larger scale model.

3.3 Urban Surface Set-up.

The horizontal boundary conditions for the model were set for each SA in each LCZ. The neighborhoods are classified based on the popular LCZ classification system, as this classification has been adopted by many previous researchers including Stewart et al. (2021).

The mean building height and footprints for each SA were generated from the LiDAR data and used to define the building geometry in the TUF-3D simulations. The radiative and thermal parameters of buildings of each neighborhood were set in the model (see Appendix A.1). Data sources used to specify these input parameters include: Shaffer et al. (2015), Stewart et al. (2014) Jackson et al. (2010), and Oke et al. (2017).

3.3.1 Meteorological Model forcing.

TUF-3D requires meteorological forcing data to generate surface temperatures (see Appendix A.2). These include barometric pressure, water vapor pressure, air temperature, wind speed, and incoming shortwave (solar) radiation ($K \downarrow$) and longwave radiation ($L \downarrow$). Two meteorological stations in Phoenix were chosen to provide these inputs, as no single station provides all the necessary input parameters for the simulations.

Phoenix Encanto weather station is the first station chosen for this study. This station was chosen because it is the closest station to all the LCZ neighborhoods. The station measures air temperature, relative humidity, and solar radiation. Air temperature in the inertial sub-layer of each LCZ neighborhood were estimated from measured air temperature values from this station. Solar radiation values from the station were also used for all the study areas. Longwave radiation for each study area were estimated with air temperature and relative humidity values from this station using the Prata (1996) longwave radiation equation for clear sky conditions. The second station is Phoenix Airport meteorological station. This station was chosen because it measures altimeter pressure, which can be used

to estimate actual barometric pressure values for the simulation. More information on all the required equations needed for each input parameter is found in Appendix A8.

3.4 Model Simulation Procedure

Vegetation in each neighborhood was not modeled in TUF-3D for two main reasons. The first reason is that surface temperatures of vegetation from a nadir view are already measured and included in the airborne thermal data set, and treetop temperatures for this analysis are assumed to be similar to the temperatures of areas below the treetops. The current approach also assumes that there is no shading by vegetation on building walls in any neighborhood, and so the walls of buildings with no roof overhangs are fully sunlit (in the real world, shading by trees on a building reduces the wall temperatures of the building). This assumption is assisted by the timing of the daytime airborne flights that were intentionally selected to represent a mid-day period when solar zenith angle and thus projected shadow areas are small and more likely affecting horizontal surfaces (Jenerette et al. 2016).

The TUF-3D model was run to simulate each sub-LCZ neighborhood or SA (see Section 3.2). Solving the energy inputs and outputs from individual patches through convection, conduction, and radiation modeling, with horizontal and vertical boundary conditions of each SA forced into the model, TUF-3D provided temporally (daytime and nighttime) resolved facet temperatures applicable to the time matching that of the airborne remotely sensed temperatures.

The model was simulated multiple times with the number of wall colours (albedo) present in each SA to generate a temperature distribution of different temperatures for each orientation. This was done to reflect the variability of wall temperatures within the SA. The output wall temperatures were then randomly selected from the distribution. Thus, two north walls within an SA, would have different wall temperatures, according to the temperature distribution of north wall temperatures. Wall temperatures were imported into the LiDAR shapefile and rasterized as 1m x1m building walls. The wall raster data

were then combined with the ground temperatures from the airborne data to estimate T_{ped} for different spatial domains. Ground temperature raster images were obtained by masking out rooftop temperatures from the thermal data Figure 3. 3 to Figure 3. 5 visualizes temperature inputs needed to estimate T_{ped} for a 100m x 100m domain in LCZ

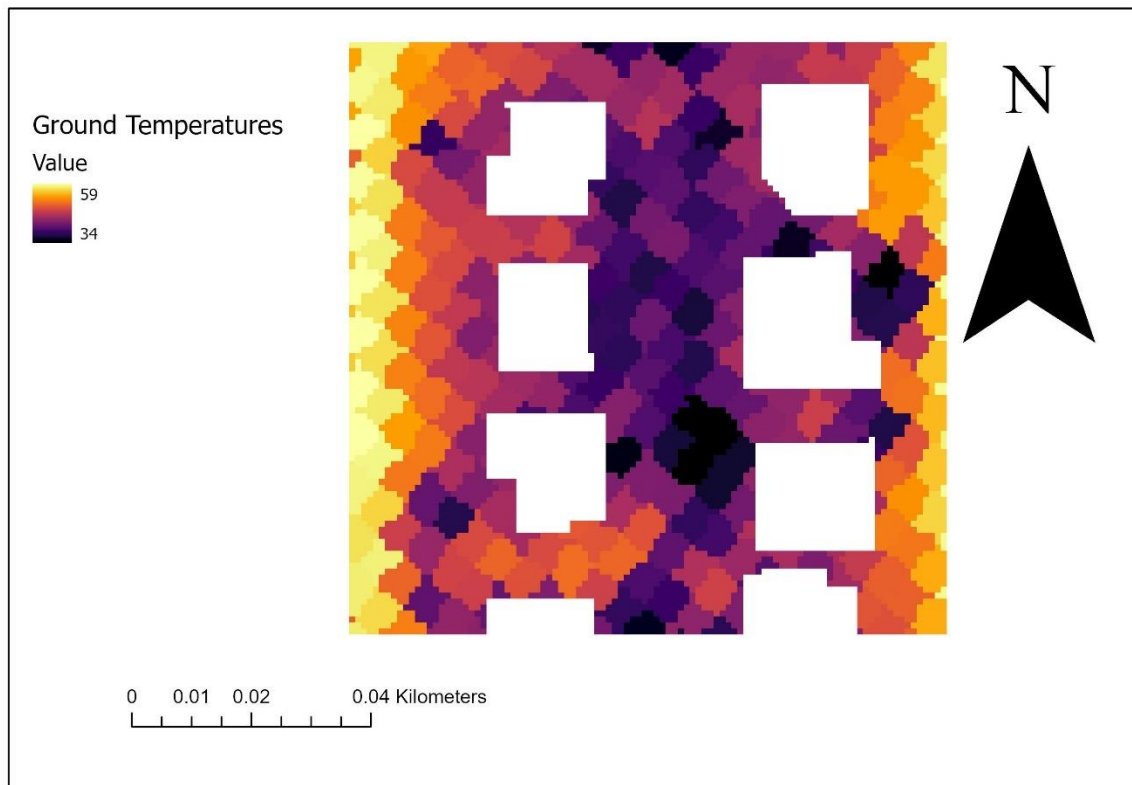


Figure 3. 3. Ground temperature (in °C) from 7 m x 7 m airborne thermal imagery over a 100 m x 100 m domain.

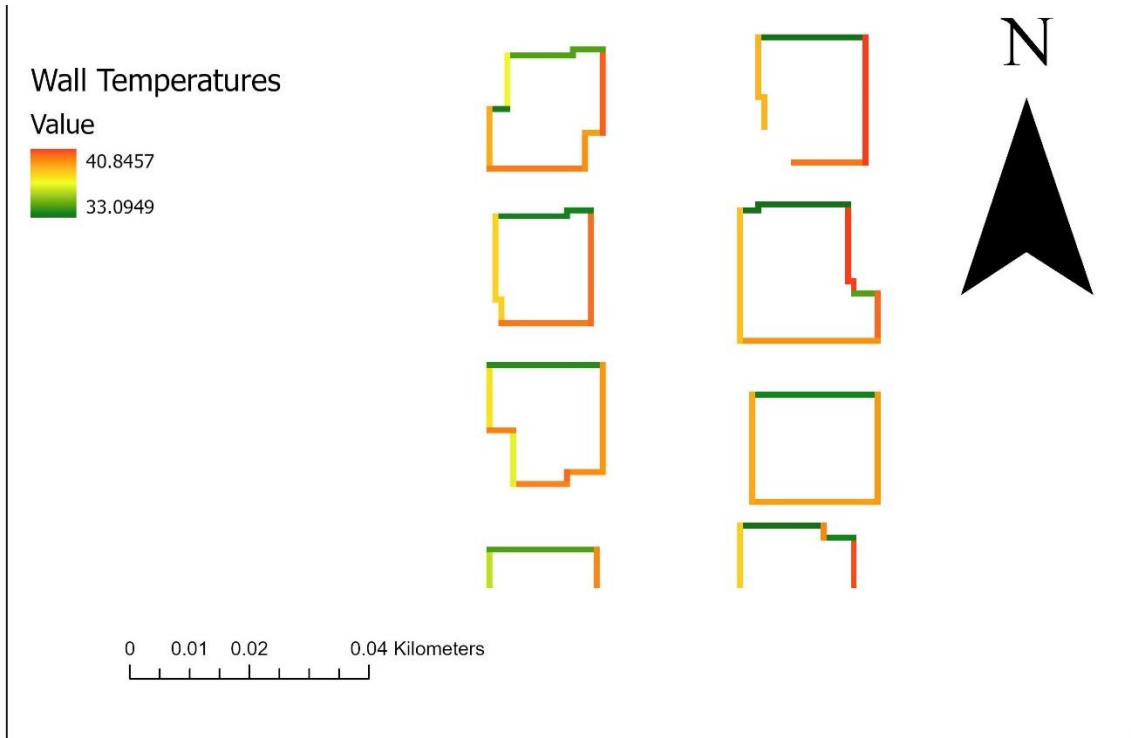


Figure 3. 4. Wall temperatures (°C) obtained from TUF-3D

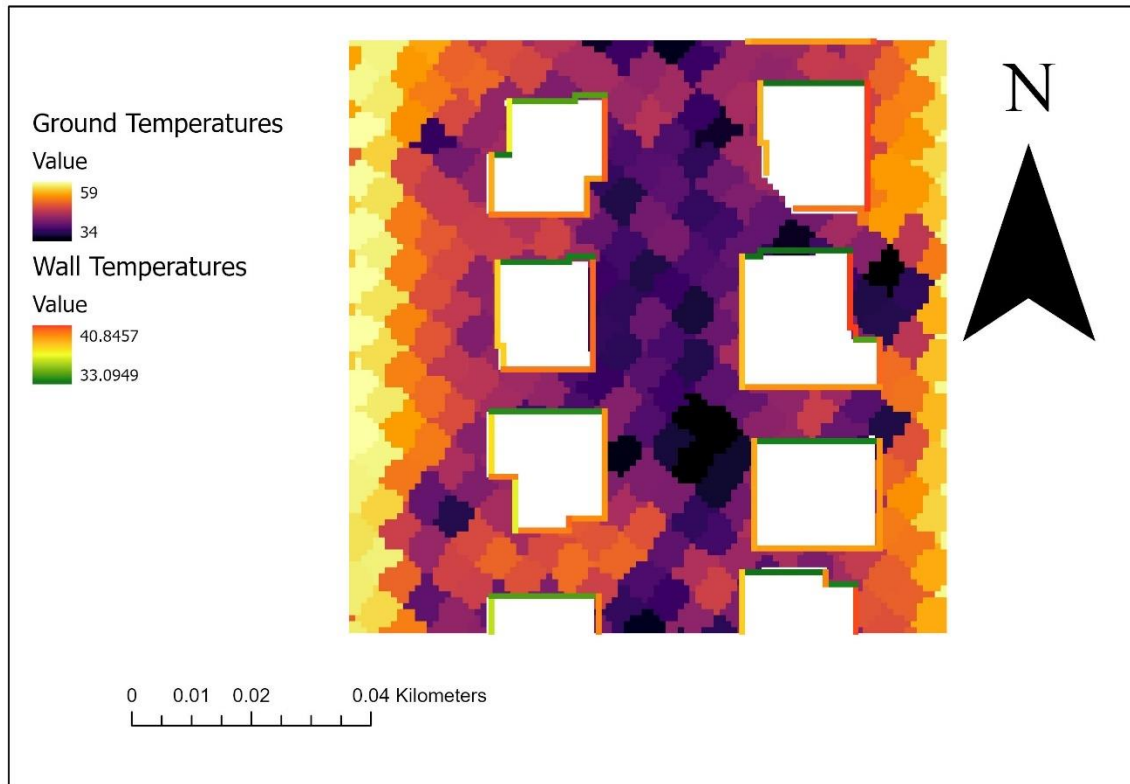


Figure 3. 5. Combined ground and wall temperatures ($^{\circ}\text{C}$).

3.4.1 Calculating the Shaded Areas of Modelled Sunlit Walls

The TUF-3D model used in this study can estimate the average temperatures of each of the four walls of the test building and incorporates shading effects that arise from the presence of surrounding buildings in the model array when they obstruct direct solar radiation (Figure 3. 1).

When buildings are widely separated, shading on the test building from the neighbouring buildings is unlikely except near sunrise and sunset when the solar zenith angle is large. However, buildings with roof overhangs can have parts of their walls (near the roof overhang) shaded. That is, a roof overhang can cast shadows to parts of the walls, even

when the wall is otherwise expected to be sunlit. Observations of buildings in the Phoenix study areas based on Google Street View images show that substantial numbers of buildings have such roof overhangs and that representing these effects in the model simulation is potentially important to avoid over-estimating the wall temperatures. Thus, there was a need to recalculate the wall temperatures from the model to incorporate shaded areas of the walls arising due to roof overhangs. The LiDAR data cannot be used to estimate the length of roof overhangs, so these values were estimated from Google Street View. The geometry of a roof overhang, the position of the sun (time of day) and the orientation of the building determine when and how much solar radiation can be received by the wall, and the areas of the shaded and sunlit parts of the wall. Knowing the position of the sun (solar elevation and azimuth angles) helped determine walls that are shaded and sunlit in Phoenix. Table 2.1 shows the solar angles at the time the thermal data was obtained for each LCZ.

The TUF-3D model used in this study can estimate the average temperatures of each of the four walls of the test building and incorporates shading effects that arise from the presence of surrounding buildings in the model array when they obstruct direct solar radiation (Figure 3. 1).

When buildings are widely separated, shading on the test building from the neighbouring buildings is unlikely except near sunrise and sunset when the solar zenith angle is large. However, buildings with roof overhangs can have parts of their walls (near the roof overhang) shaded. That is, a roof overhang can cast shadows to parts of the walls, even when the wall is otherwise expected to be sunlit. Observations of buildings in the Phoenix study areas based on Google Street View images show that substantial numbers of buildings have such roof overhangs and that representing these effects in the model simulation is potentially important to avoid over-estimating the wall temperatures. Thus, there was a need to recalculate the wall temperatures from the model to incorporate shaded areas of the walls arising due to roof overhangs. The LiDAR data cannot be used to estimate the length of roof overhangs, so these values were estimated from Google Street View. The geometry of a roof overhang, the position of the sun (time of day) and the orientation of the building determine when and how much solar radiation can be received by the wall,

and the areas of the shaded and sunlit parts of the wall. Knowing the position of the sun (solar elevation and azimuth angles) helped determine walls that are shaded and sunlit in Phoenix. Table 2.1 shows the solar angles at the time the thermal data was obtained for each LCZ

3.4.2 Calculating Incomplete Surface Temperatures.

An incomplete surface temperature (T_{inc}) is an area-weighted temperature, where the component surface temperatures are combined in proportion to the areal fraction of the incomplete surface. The pedestrian temperature (T_{ped}) is defined as the area-weighted incomplete surface temperature for a spatial domain that incorporates ground and wall areas (but not roofs). The spatial domain needs to be sufficiently large to incorporate wall and ground areas (so is most relevant at spatial scales larger than that used to define the plan area fraction (i.e. building length + inter-building spacing). In this thesis, T_{ped} is calculated for both daytime and nighttime by weighting the temperature for each component surface within the domain with its areal fraction using spatial domains with length scales of 50, 100 and 200 m. The equation for the area weighted T_{ped} for a 100m x 100m spatial domain is:

$$T_{ped} = \frac{(A_g \cdot T_g) + \sum_{i=1}^n (A_w \cdot T_w)}{A_g + \sum_{i=1}^n A_w} \dots \quad \dots \text{Equation 3. 1}$$

where

A_g = total ground area. This is the total horizontal area excluding the building footprint (i.e. roof) area. This value was obtained by subtracting the total building footprint area from the grid area (e.g. 10000m² for 100x100 spatial domain).

T_g = average temperature of the ground area. This was obtained by dividing the total sum of all the pixel values covering the total ground area by the total number pixels covering the ground.

A_w = the area of a wall. The length of each polyline that represents a wall area was multiplied by its building height to calculate the area of the wall.

T_w = the temperature of a wall area. The temperature of a wall will be multiplied by its wall area to get $A_w \cdot T_w$.

3.4.3 Estimating T_{ped} and T_{plan} for Different Spatial Domains.

Estimating T_{ped} requires the specification of a spatial domain from which to combine the component areas and temperatures. The main spatial domain assessed in this study to calculate T_{ped} was 100m x 100m, as this matches the spatial resolution of the thermal sensor for Landsat 8 and 9 satellites that is commonly used in urban heat assessment studies. However, 50m x 50m and 200m x 200m domains are also considered in order to assess the spatial variability of T_{ped} in smaller and larger domains. This section describes the procedures used to estimate T_{ped} for 100m x 100m domains within an LCZ; this procedure is applied similarly to other spatial domains and LCZs.

A grid, containing 100m x 100m domain was overlaid on the plan area of LCZ 6 (Figure 3.4). The individual grid cells define the spatial domain for the calculation of T_{ped} . Grids with area less than 100m x 100m were excluded from the analysis. To ensure that all parts of the study area are assessed for T_{ped} calculations, the grid was moved across the entire study area in both the x and y directions in a manner analogous to a spatial filtering operation using a step size of 20m. for each position, T_{ped} and T_{plan} were calculated for each 100m x 100m domain.

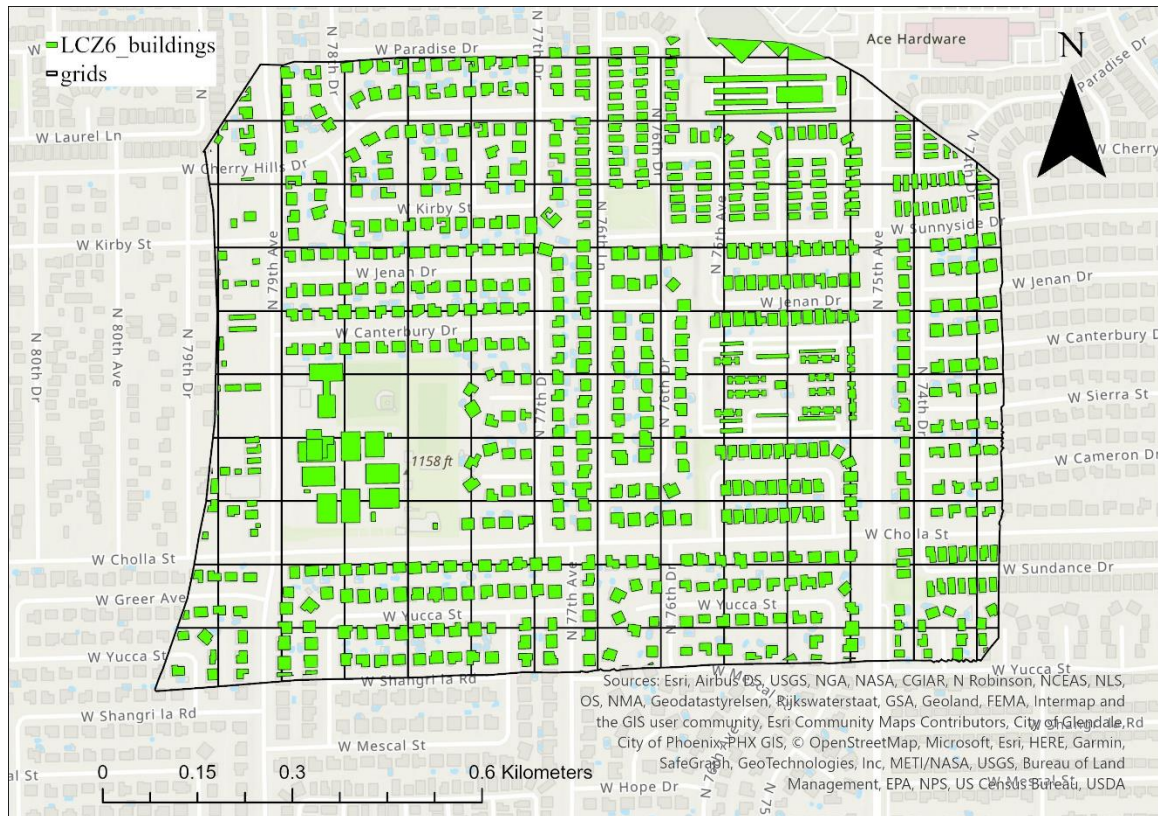


Figure 3. 6. The initial 100m x 100m grid position on LCZ 6.

For a grid size of 100m x 100m, a total of 2315 domains were obtained for the LCZ 6 study area. A step size, amounting to 20% of the domain's length, was chosen for each domain. For instance, in the case of a 100m x 100m domain, the domain was shifted 20m to the right and 20m downward. These step sizes were selected primarily for two reasons: firstly, a smaller step size would lead to less variation in the T_{ped} temperature with each domain movement, and secondly, given that the spatial resolution of the thermal data was 7m/pixel, a step size larger than 7m was required to ensure variations in different pixels with each domain movement. The domain was moved four times in both rightward and downward directions. The grid step size for all the other domains and study areas are shown in Table 3. 1 and Table 3. 2

Table 3. 1. The step sizes and number of downward and rightward movements for each domain size.

Domain (m)	Size	step size (m)	Number of steps
50 x 50		10	4
100 x 100		20	4
200 x 200		40	4

Table 3. 2. The number of individual cells within the three domains for all the LCZ.

Study area	Number of 50m x 50m cells	Number of 100m x 100m cells	Number of 200m x 200m cells
LCZ 5	3496	740	87
LCZ 6	10515	2315	419
LCZ 7	14807	3172	632
LCZ 8	5874	1147	158

Each 100m x 100m cell was converted to points (Figure 3. 7a). Each point was placed at the exact center of the cell, and therefore, there was 20m space between adjacent points following the movement of the grids in the x and y directions. The points were then converted to 20m x 20m cells (Figure 3. 7b). These polygons were then converted to two raster files, with pixels representing T_{plan} and T_{ped} , respectively. In a domain where there were no building walls, T_{ped} was equal to T_{plan} .

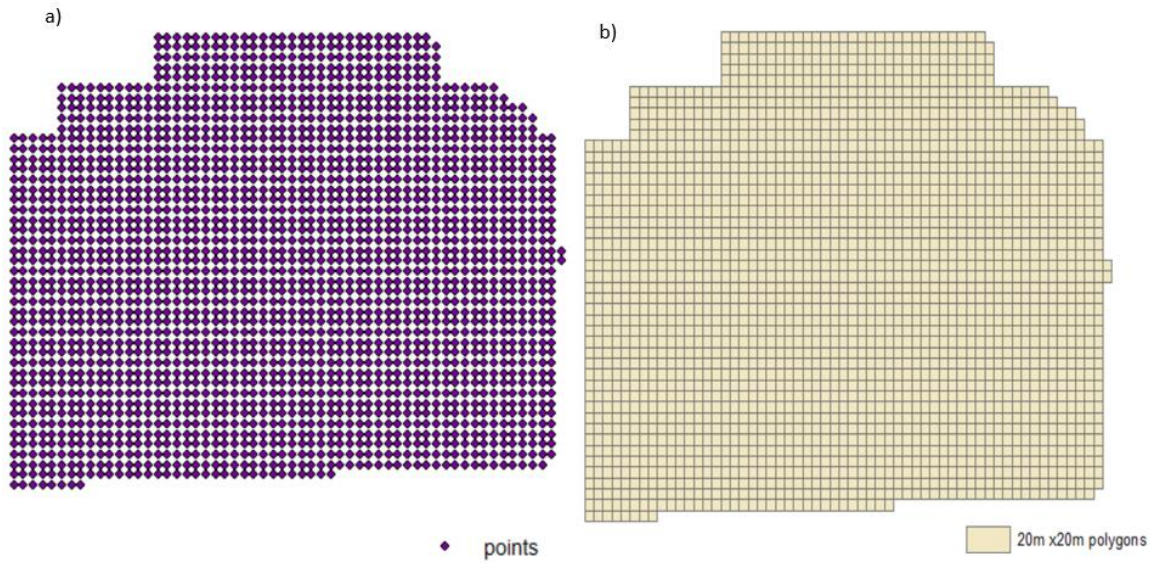


Figure 3. 7. Conversion of results from the spatially shifted grids. a) Point shapefiles representing 100m x 100m polygons. b) 20m x 20m cells (polygons) converted from the points.

4 Model Evaluation and Sensitivity Analysis

Normally, outputs from numerical models need to be compared graphically and statistically with real-world observations to provide a model evaluation (Krayenhoff et al. 2021). The performance of TUF-3D in generating surface temperatures was previously assessed by Krayenhoff and Voogt (2007) when they simulated the energy balance of two study sites: Vancouver Light Industrial and Basel-Sperrstrasse and compared the model output with real-world observations of the energy balance and surface temperatures. The model performed well against these real-world observations (for statistics and graphical comparisons of the model, see Krayenhoff and Voogt (2007)).

The present study permits evaluation of horizontal (ground and roof) surface temperatures but lacks observed wall temperature data in the Phoenix study sites thereby limiting the ability to undertake a model evaluation for wall surfaces. Here, an evaluation of the modelled horizontal (roof and road) surface temperatures is performed, with the assumption that if the model performs well in simulating horizontal surface temperatures (where the range of temperatures is expected to be much larger than for walls) for the given vertical boundary conditions, then, based on past evaluations, we can anticipate reasonable performance in modeling the wall temperatures assuming good estimations of the thermal and radiative properties of the walls in each sub area (SA). The model evaluation for this study is also compared with the model evaluation by Krayenhoff and Voogt (2007) on Vancouver Light Industrial.

4.1 Sensitivity Test on the Important Parameters that Affect Modelled Surface Temperatures.

Since horizontal surface albedo and incoming solar radiation above the buildings (the two most important parameters for surface temperatures) are constrained from the remotely sensed data and the meteorological station respectively, the sensitivity of model output likely arises from other secondary parameters required by the model. These parameters are assessed. These parameters include momentum roughness length for roofs and roads, wall orientation, H/W, thermal and radiative parameters and wind speed. Aerodynamic (momentum) roughness length is an important parameter in Monin Obukhov Similarity Theory (MOST) and boundary layer meteorology. It is defined as a “lower boundary condition to the averaged properties of atmospheric flow in the surface layer” (Malhi, 1996), a region that extends from the urban surface to a height of 100m. As the transfer of heat from horizontal surfaces in TUF-3D follows the MOST theory, values of momentum roughness length for roofs and roads are required by the model to simulate horizontal surface temperatures. These values were obtained from the literature (Lachappelle et al. 2022, Stewart et al. 2021) as they are difficult to calculate for each SA. The results from the sensitivity analysis of momentum roughness length for roof was assumed to be similar to the results from momentum the sensitivity analysis roughness length for road. The model was allowed to calculate its own thermal roughness length for roof and road surfaces, and thus they are not included the sensitivity analysis. A sensitivity test was also performed to assess the effects of wind speed on the model’s predicted roof temperatures in the model evaluation studies. Sensitivity analyses for thermal admittance, H/W and wall orientations were done to assess the modelled wall temperatures sensitivity to variations of these input parameters.

4.1.1 Sensitivity Analysis of the Cardinal Direction of Walls

One characteristic of TUF-3D is its ability to estimate temperatures of walls with different street orientations. However, the many different orientations of walls in all the four study areas required walls to be classified into groups of orientations to be able to simulate the model for those groups, as opposed to simulating each individual building and its specific wall orientations. A frequency distribution table, and a histogram with a 1-degree variation was created for each study area to understand the arrangement of buildings in different orientations.

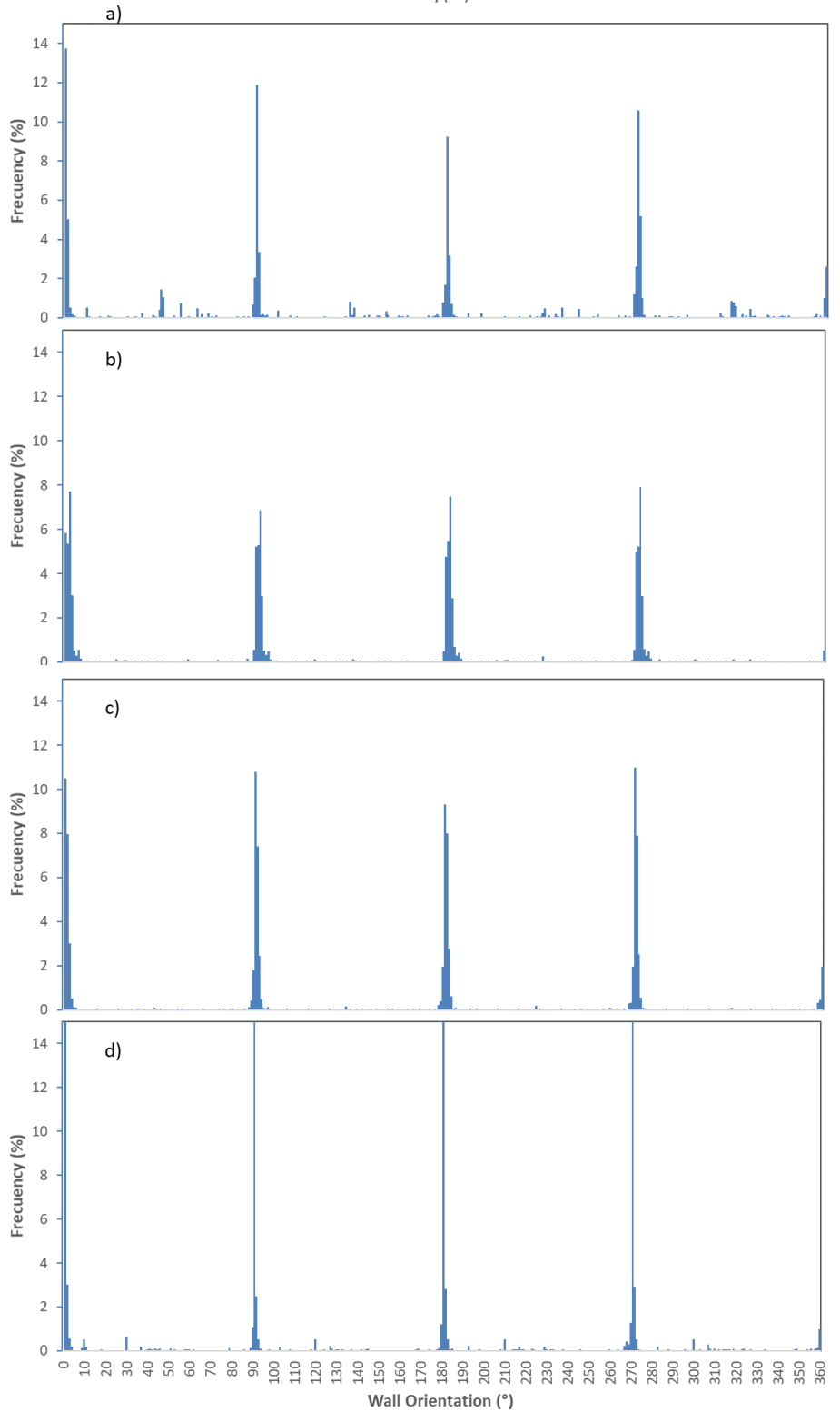


Figure 4. 1. Histograms showing the distribution of wall orientations in a) LCZ 5, b) LCZ 6, c) LCZ 7, d) LCZ 8.

It can be seen from Figure 4. 1 that most of the walls in all four study areas are oriented in the North (0° or 360°), South (180°), East (90°) and West (270°) directions with few walls oriented in other directions.

TUF-3D requires the specification of a street orientation, which sets the orientation of the four building walls to be simulated. It is not practical to simulate all possible building orientations, but if the wall temperatures are relatively insensitive to small changes in wall orientations, then TUF-3D can be used to simulate street orientation for a select number of orientations.

A sensitivity test was performed to assess the error associated with grouping walls with $\pm 11.25^\circ$ variation in orientation, to represent the few walls oriented in other directions. The $\pm 11.25^\circ$ orientation represents a 22.5° sector, corresponding to a subdivision of the cardinal orientations by 4, associated with the nomenclature of, for example: N, NNE, NE, ENE, E for north, north-northeast, northeast, east-northeast, and east street orientations. The model was run for LCZ 5 SA8 for N, S, E and W orientations (base orientations) along with orientations $\pm 11.25^\circ$ to the base orientation. Wall temperature differences at select times from their corresponding base orientations were recorded. The resulting range of temperature differences (in $^\circ\text{C}$) are shown in Table 4. 1. Only the temperature differences at the time period of the MASTER data observations are considered.

Table 4. 1. The range of differences in wall temperatures (in °C) with 11.25 degrees variation from the 4 cardinal points.

TIME	N (+-)11.25	E (+-)11.25	S (+-)11.25	W (+-)11.25
0.0	0.05-0.14	0.07-0.02	0.02-0.07	0.01-0.07
1	0.03-0.12	0.02-0.07	0.025-0.08	0.02-0.08
2	0.013-0.13	0.032-0.09	0.03-0.09	0.026-0.09
3	0.012-0.01	0.02-0.09	0.02-0.09	0.018-0.09
4	0-0.12	0.03-0.1	0.03-0.1	0.023-0.1
TIME				
12	0.11-0.41	0.24-0.05	0.4-0.57	0.02-0.32
13	0.09-0.32	0.12-0.16	0.066-0.18	0.387-0.42
14	0.18-0.28	0.05-0.11	0.614-0.78	0.33-0.40

Table 4. 1 shows that none of the temperature differences reached 1°C and almost all are <0.5°C. This demonstrates that grouping the walls with 11.25°-variations will have negligible effects on the wall temperature prediction.

4.1.2 Sensitivity Analysis for Different H/W Ratio

As already explained, SAs were grouped according to similar radiative and geometric parameters. This allows separate model simulations to represent some of the variability within an LCZ. However, variations in street width and building heights exist within an SA and so require a sensitivity analysis to know the variability of wall temperatures associated with different H/W ratios. The model, however, requires inputs of plan to area ratio (λ_p) and building height to length (H/L) ratios and then calculates the building height to street width (H/W) ratio internally.

A sensitivity test was performed to assess how the model's calculated H/W affects wall temperatures. The sensitivity test involved model simulations with three different λ_p for LCZ 5 SA8. A λ_p of 0.44 was set as the reference value. This value is derived by making a buffer around the edges of the streets of the SA and using this as the plan area. The buffer extended from the buildings around the boundaries of the SA to 2m of the ground.

From the base case, λ_p is altered by increasing and decreasing the plan area of the SA by a factor of 0.2, yielding λ_p of 0.24 and 0.64 respectively. The large change to plan area ratio does not represent the uncertainty associated with the SA study area; rather it is used in order to generate the variability of H/W that is known to exist within the study area based on the LiDAR building database. A H/L ratio of 0.18, calculated from the LiDAR database for this SA that represents the building dimensions was maintained for all three simulations.

The model uses the equation below to calculate the H/W

$$H/W = \sqrt{(\lambda_p)} \cdot \frac{\frac{H}{L}}{(1 - \sqrt{(\lambda_p)})} \dots\dots \quad \text{Equation 4. 1}$$

Table 4. 2 shows the H/W values calculated by the model from the input λ_p and H/L values.

Table 4. 2. TUF3d model self-calculated H/W ratios

λ_p	H/L	H/W
0.24	0.18	0.17
0.44	0.18	0.35
0.64	0.18	0.72

Table 4. 3 shows that the difference in the modelled surface temperature output for south, north and west walls with different H/W is negligible, although the model output shows a very small increase in south wall temperature outputs with a change of λ_p . and a 0.5-1 °C increase in east wall temperatures with an increase in H/W.

The sensitivity tests show that modelled wall temperatures are relatively insensitive to the difference in H/W ratios at the times that the thermal data were captured, as all the walls were very hot from the sun angle positions during that time period. This means that the approach for creating boundaries for SA's, and the decision to apply the modelled wall temperature outputs to buildings at the boundaries of each building, does not largely underestimate or overestimate wall temperatures.

Table 4. 3. Differences in temperature values from H/W sensitivity analysis

TIME (Night)	N(0.44 -0.24)	N(0.44- 0.64)	S(0.44- 0.24)	S(0.44- 0.64)	E(0.44- 0.24)	E(0.44- 0.64)	W(0.44- 0.24)	W(0.44 -0.64)
0	0.12	-0.16	0.11	-0.14	0.12	-0.15	0.1	-0.1
1	0.2	-0.27	0.18	-0.26	0.19	-0.26	0.18	-0.22
2	0.26	-0.37	0.25	-0.36	0.25	-0.36	0.24	-0.32
3	0.3	-0.44	0.3	-0.44	0.3	-0.44	0.29	-0.41
4	0.35	-0.48	0.35	-0.48	0.35	-0.48	0.34	-0.45
Day								
12	-0.1	0	0.14	-0.15	0.44	-0.57	0.05	-0.09
13	0	-0.13	0.27	-0.37	0.48	-0.71	0.2	-0.36

4.1.3 Sensitivity Analysis to Roughness Length and Wind Speed

A sensitivity test performed was to assess the impact of different momentum roughness lengths of roofs on roof surface temperature. The model was simulated with three different momentum roughness lengths for LCZ 5 SA8 roofs. The diurnal cycle of the three simulations is plotted in Figure 4. 2

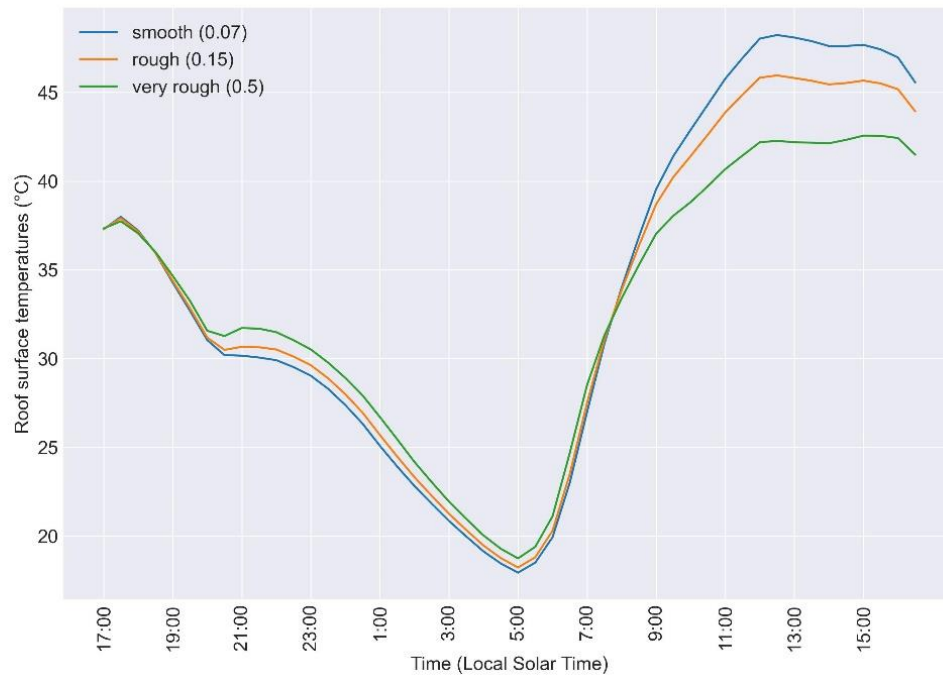


Figure 4. 2. Model sensitivity of LCZ 5 SA8 roof surface temperature to three different momentum roughness lengths for roofs.

Figure 4. 2 shows that the modelled roof surface temperatures from 09:00 to 17:00 varies substantially with different roughness lengths. Comparing Figure 4. 2 with **Table 2. 1**, it can be seen that, a 0.2 change in the roughness length for roof can cause up to 6 °C change in roof surface temperature, at the daytime flight times, and up to 1 °C for nighttime flight times.

A higher momentum roughness length, such as 0.5, indicates a very rough surface. This enhanced roughness promotes greater turbulence in the air layer just above the roof. During the day, this turbulence facilitates the efficient mixing of cooler ambient air with the warmer air immediately above the roof surface, promoting convective heat transfer away from the roof. As a result, the roof surface temperature tends to decrease. The effect is more pronounced during the day because of the higher temperature gradients between the roof surface and the ambient environment.

During the night, the primary mode of heat loss from the roof is through radiative cooling. A roof with a higher roughness length might retain more air in its immediate vicinity due to the increased turbulence and drag. This trapped air acts as a thin insulating layer, slightly reducing the rate of radiative heat loss from the roof to the sky. Consequently, a very rough roof surface might experience a slight increase in surface temperature during nighttime compared to a smoother roof. On the contrary, a lower momentum roughness length, such as 0.07, indicates a smoother surface. Such a surface induces less turbulence in the boundary layer above the roof. This leads to reduced mixing of cooler ambient air with the warmer layer above the roof during the daytime, causing the roof to retain more heat and hence, exhibit a higher surface temperature. A smoother roof allows for more direct radiative cooling during the night, without the interference of a turbulent layer of air acting as an insulating barrier. Thus, smoother roofs may cool more efficiently at night, leading to slightly lower nighttime temperatures.

4.1.4 Sensitivity Analysis for wind Speed

Another parameter that can impact the modelled surface temperature is wind speed. TUF-3D is an energy balance model and therefore requires the wind speed and wind direction at different time steps to be able to simulate the energy balance and the surface temperature of facets. Surface temperature is sensitive to wind speed since it affects the convection coefficient that controls the convective sensible heat flux from surfaces. A lack of meteorological stations within each sub area makes it difficult to accurately estimate the local wind speed for each SA. Additionally, while it is known that smaller scale factors such as topography can affect local wind speed values, there were no data to show the effects of these factors on wind speed in each SA. A sensitivity test was performed to check the modelled roof surface temperature sensitivity to the wind speed. A 2m s^{-1} wind speed increment was added, and deducted from the calculated wind speed, and the results were plotted in Figure 4. 3.

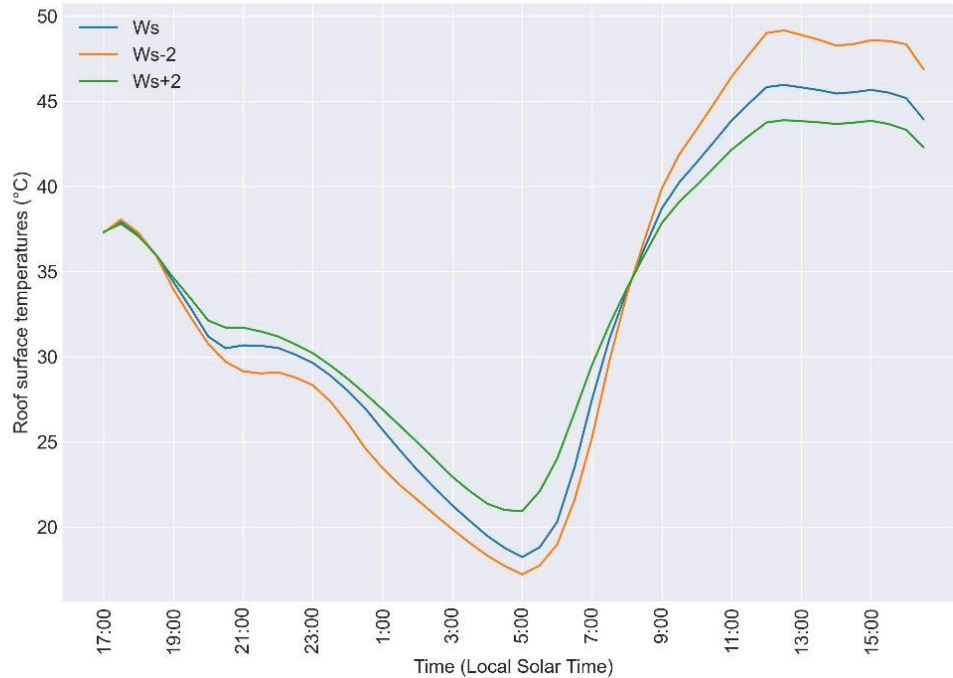


Figure 4. 3. Model sensitivity of LCZ 5 SA8 roof surface temperature to wind speed.

Figure 4. 3 shows the effects of wind speed on surface temperatures. During the day, the sun heats the surface of the roof, raising its temperature. Normally, wind would facilitate convective heat transfer, mixing heat away from the roof surface (increasing Q_H) and cooling it. When the wind speed is reduced, convection decreases, meaning less heat is removed from the roof. Therefore, the roof's surface temperature increases. At night, the roof radiates heat back into the cooler night sky, lowering its temperature. If the wind speed decreases, radiation heat loss dominates, and the low thermal admittance of the roof surface allows it to cool, sometimes below the ambient air temperature, reversing the temperature profile. Convection is weak and the roof becomes cooler than in situations with greater wind speed. This slows down the rate of heat loss by radiation, which makes the roof warmer than it would be with a higher wind speed.

It can also be seen from Figure 4. 3 that variations in wind speed result in a 2 to 6°C difference in roof temperature from 9:00 to 14:00 (time period for daytime observations from the MASTER data), and from 00:00 to 04:00 (time period for nighttime observations from the MASTER data). Comparing Figure 4. 3 with **Table 2. 1**, a 2 ms⁻¹ change in the wind speed can cause up to 7 °C change in roof surface temperature, at the daytime flight times, and up to 2 °C for nighttime flight times.

The sensitivity analyses highlight that the momentum roughness length and wind speed significantly affect the modeled rooftop temperature. However, determining which factor has a more substantial impact can be difficult. When looking at the roughness length, its effect is more apparent during times of maximum solar radiation, leading to rooftop temperature differences of up to 10°C. This considerable variation implies that an incorrect the roughness length could result in substantial inaccuracies in predicting the surface temperature. In contrast, the influence of wind speed is steady, both during the day and at night, causing a 2 to 6°C shift in roof temperature. Even though the temperature variation attributed to wind speed is less than that due to roughness length, its constant presence over longer durations highlights its vital role in surface temperature predictions.

4.1.5 Sensitivity Analysis for Wall Thermal Admittance and Albedo

The estimation of T_{ped} depends partly on wall temperatures and because wall temperatures were simulated from a model, it is necessary to assess the sensitivity of wall temperatures to the thermal properties of walls, including heat capacity, conductivity and albedo, to know their effects on the output wall temperatures. The data generated for these tests were derived using LCZ 6 SA1 forcing data.

The wall thermal and radiative properties were manipulated in eight distinct but interconnected ways, selecting two vastly different albedos (0.2 and 0.8) and testing four thermal parameter combinations for each albedo. An albedo of 0.2 corresponds to a very dark-colored (e.g. dark grey) wall, whereas an albedo of 0.8, on the other hand, is close to the reflectivity of a freshly painted bright white wall.

For each of the two albedos, eight combinations of thermal parameters were applied (Table 4. 4). The thermal properties of the walls were approximated based on empirical understanding and informed estimates and are chosen to represent walls that vary in properties from those that are well insulated, with a relatively low thermal admittance, to those that represent more massive construction (e.g. thick concrete). The thermal admittance (TA), which combines conductivity and heat capacity into a single parameter, was calculated for each layer of the four-layered surface. These parameters were then used to calculate the weighted thermal admittance for the entire wall, accounting for the depth of each layer. The TA of the uppermost (surface) layer was also calculated recognizing it might have a more significant influence on the surface temperature than the depth weighted TA of the entire wall. The sensitivity analysis was performed on the Phoenix LCZ 6 study site .

Table 4. 4. Input parameters for wall temperature sensitivity test and their corresponding output wall temperatures. TA - thermal admittance ($\text{J m}^{-2} \text{s}^{-1/2} \text{K}^{-1}$) ; h1 and c1 means the hottest and coldest walls, respectively.

Test	albedo	TA (depth weighted)	TA (outer layer)	Ranking - E wall	Ranking S wall	Ranking W Wall
1	0.2	721	1918	h3	h3	h3
2	0.2	1105	1774	h2	h2	h2
3	0.2	619	980	h1	h1	h1
4	0.2	2011	2075	h4	h4	h4
Test	albedo	TA (depth weighted)	TA (outer layer)	Ranking E Wall	Ranking S wall	Ranking W wall
5	0.8	721	1918	c2	c2	c2
6	0.8	1105	1774	c3	c3	c3
7	0.8	619	980	c4	c4	c4
8	0.8	2011	2075	c1	c1	c1

An assessment of the resulting wall temperatures highlighted that the hottest walls were associated with low albedo and low overall wall thermal admittance, whereas the coldest walls corresponded to the greatest thermal admittance and highest albedo.

The analysis confirmed that albedo exerts a powerful influence over the wall temperature, as compared to the thermal properties of the wall. For example, for East walls (Figure 4.4), there was a temperature difference of up to 10 °C between walls with lower albedos, and walls with higher albedos.

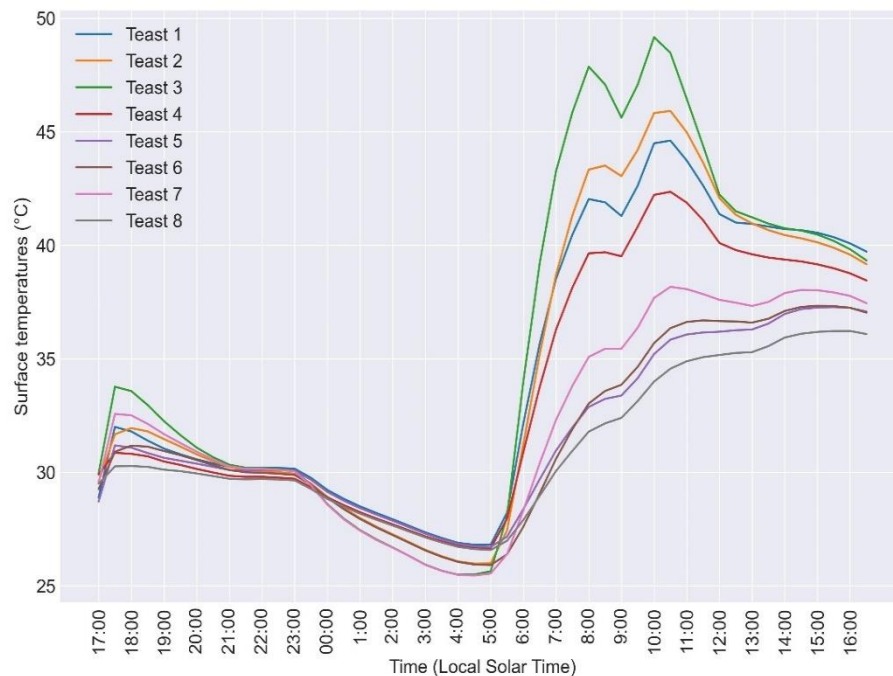


Figure 4.4. The sensitivity of East wall temperatures to albedo and thermal admittance.

This suggests that accurate estimation of albedo is more critical for determining wall temperature, which in turn feeds into the pedestrian temperature (T_{ped}). The choice of albedos here was based on visual assessments of the study areas' walls, and the model was simulated based on a range of albedos determined by the observed wall colors, which

represents some uncertainty in the actual albedo values. However, the range of 0.2 to 0.8 was chosen for this sensitivity test to show the widest range the temperatures of walls might have. The variabilities of wall albedo inferred from observed wall colours for most SA were smaller than the range used in this test, and therefore, the wall temperature variabilities for most SA were minimal. For example, with albedo values from 0.35 to 0.45, Table 4. 5 and Table 4. 6. Walls with higher range show walls higher temperature differences.

Table 4. 5. The range of values for the daytime wall temperatures of LCZ 6 SA1. All values are in °C.

N	S	E	W	NE	SW	SE	NW
0.2	0.3	0.4	0.3	0.3	0.3	0.4	0.3
NNE	SSW	ESE	WNW	ENE	WSW	SSE	NNW
0.2	0.4	0.4	0.3	1.23	2.5	1.3	2.4

Table 4. 6. The range of values for the nighttime wall temperatures of LCZ 6 SA1

N	S	E	W	NNE	SSW	ESE	WNW
0.1	0.1	0.1	0.1	0.1	0.1	0.1	0.01
NE	SW	SE	NW	ENE	WSW	SSE	NNW
0.1	0.0	0.1	0.1	1.39	1.5	1.4	1.5

4.2 TUF-3D Model Evaluation for Phoenix

The TUF-3D model evaluation was performed for both daytime and nighttime periods on selected roofs and roads from the Phoenix study areas. To provide a good match between model assumptions and real-world characteristics, flat roofs were chosen to ensure that each part of the roof surface received an equal amount of sunlight. Moreover, roads with no median or bordering vegetation were chosen, as the version of the model used for this study cannot predict vegetation temperatures. Because wide roads that have few buildings bordering them were selected, the plan area ratio for each SA was reduced for the road simulations to ensure that the model accurately predicts open roads with no shading from buildings onto the roads. The plan area ratio for each SA remained fixed for rooftop simulations.

Three SAs, one from LCZ 5, 6 and 7 were chosen for the model evaluation. Within each SA, four large, flat roofs were selected for further analysis. This was done to assess how the model performs against the calculated vertical boundary conditions from the meteorological stations for an SA. The following process further explains the model evaluation procedures for the daytime roof temperatures of LCZ 5 SA1. This process was repeated for the other SAs for both daytime and nighttime roof surface temperature evaluation.

The MASTER data include estimated roof and ground albedo values for all the study areas. The LiDAR polygons (representing roofs) for LCZ 5 SA1 were used to select and estimate the mean and standard deviation of the albedo values of the four chosen roofs in the SA. Three TUF-3D simulations were performed for each building roof. The first simulation used the mean albedo values for each roof. The second and third simulations use the mean roof albedo plus and minus the standard deviation of the albedo respectively. The thermal properties and roughness length of the roof were held fixed at the estimated values for all

three simulations. The plan area ratio and building height to building length ratio was calculated for each building.

The rooftop temperatures of the three simulations were then combined to find the mean rooftop temperature for the SA, which was then plotted against the mean rooftop temperature of the SA from the airborne thermal data. Table 4. 7 and Table 4. 8 shows the number of pixels obtained for roof and road temperatures respectively for the model evaluation.

Table 4. 7. Pixel counts (roofs) for the chosen sub areas

LCZ 5		LCZ 6		LCZ 7	
Building 1	858	Building 1	548	Building 1	636
Building 2	781	Building 2	554	Building 2	490
Building 3	562	Building 3	513	Building 3	308
Building 4	562	Building 4	514	Building 4	281

Table 4. 8. Pixel counts (roads) for the chosen sub areas

ROADS	COUNT
LCZ 5	4695
LCZ 6	3923
LCZ 7	12712
LCZ 8	11886

Vertical error bars representing the maximum and minimum temperatures of the three-model simulation were added to each point, while horizontal error bars represent standard deviation of the pixel temperature values from the thermal data. The results for both daytime and nighttime analysis are plotted on the same graph. Selected linear regression metrics for each graph were calculated to assess how the model output compares to the observed data.

The procedure for daytime and nighttime model evaluation of the roads is similar to the evaluation procedure for the roofs. Here, four large roads were chosen; one from each of the study areas. Figure 4. 5 and

Figure 4. 6 show the scatter plots obtained plotting the mean rooftop and road temperatures respectively with the thermal data. Table 4. 9 shows the performance metrics. R^2 values across different LCZs for roof temperatures are impressively high, hovering close to 1 for LCZ 5 SA8, LCZ 6 SA1, and LCZ 7 SA1. This indicates that the model's predictions for roof temperatures in these zones align remarkably well with the observed data. Such a strong correlation suggests that the TUF-3D model is performing well at predicting roof surface temperatures. However, the roads present a different story. With an R^2 value of 0.78, there is a noticeable drop in the ability of the model to predict road temperatures. The MSE and RMSE values across LCZs provide tangible evidence of the model's prediction accuracy. LCZ 6 SA1, with its notably low MSE and RMSE, shows high model precision for that particular zone. In contrast, the higher MSE and RMSE values for roads hint at a larger discrepancy between the model's predictions and the observed temperatures.

The MAPE values offer a relative measure of the model's prediction accuracy. For instance, LCZ 6 SA1's low MAPE of 4.3% showcases the model's remarkable accuracy in predicting roof temperatures for that LCZ. However, the higher MAPE values observed for LCZ 7 SA1 and roads point towards more significant relative errors in predictions.

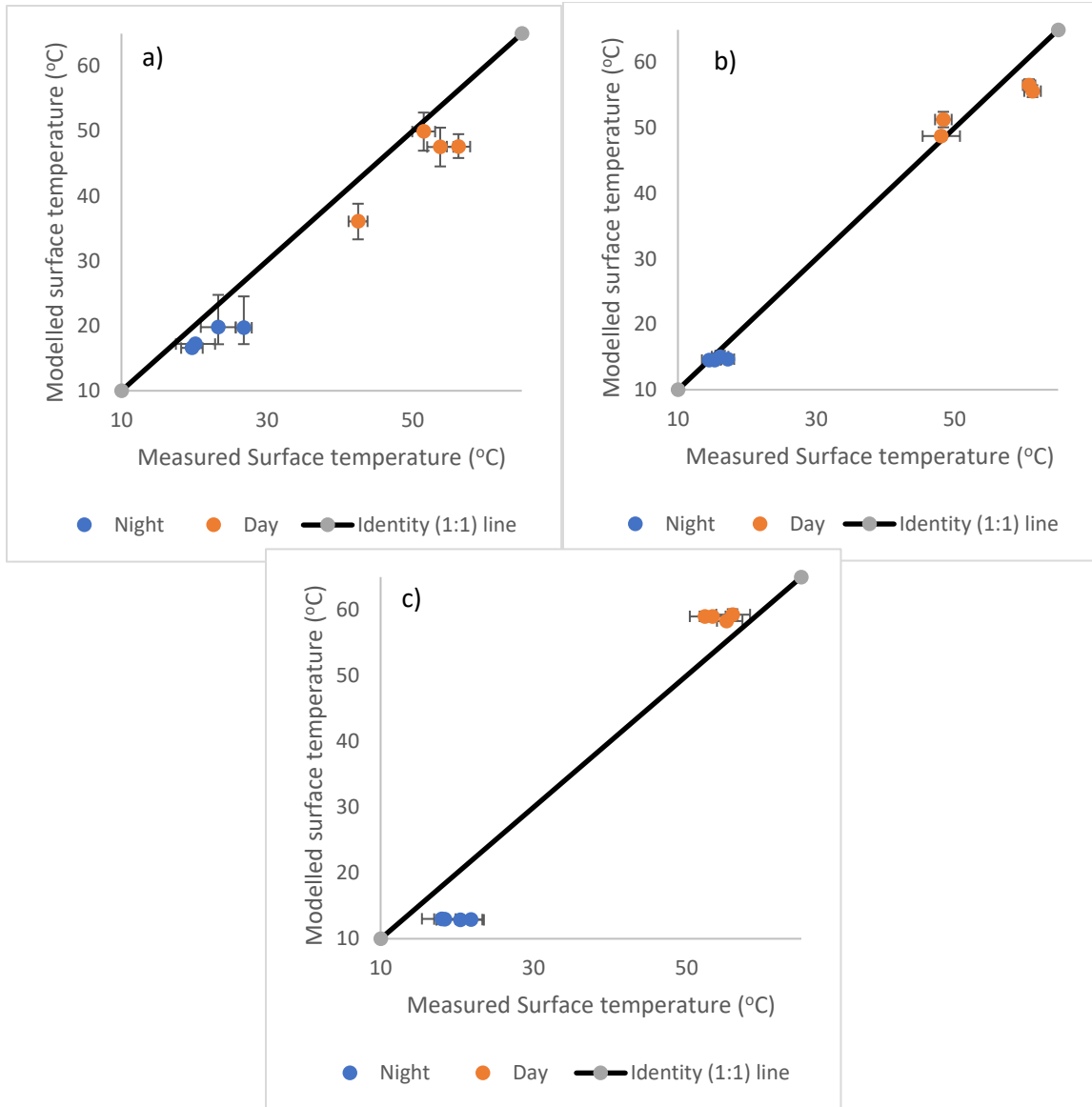


Figure 4. 5. Model evaluation of day (red) and nighttime (blue) roof temperatures for a) LCZ 5 SA8 b) LCZ 6 SA1, c) LCZ 7 SA1. Dotted line represents the 1:1 line.

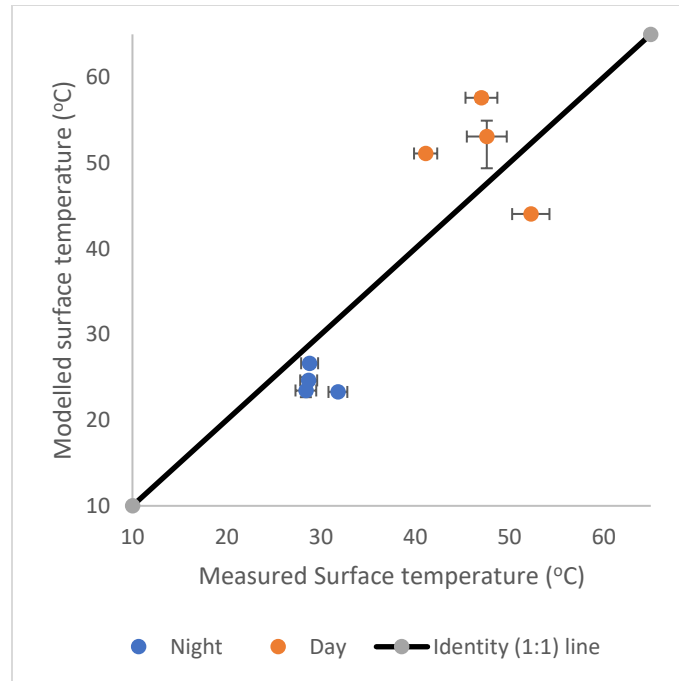


Figure 4. 6. Model evaluation of day (red) and nighttime (blue) temperatures of four roads, one from each SA.

Table 4. 9. R² values from roof and road surface temperature evaluation.

Study area	R ²	MSE (°C ²)	RMSE (°C)	MAPE (%)
LCZ 5 SA8	0.98	29.9	5.47	14.7
LCZ 6 SA 1	0.98	8.39	2.90	4.3
LCZ 7 SA1	0.99	35.70	5.98	21.2
Roads	0.78	53.47	7.31	17.5

In summary, the plots show that the model predicts very well the daytime and nighttime temperatures for the roofs and roads in the chosen sub areas with a difference of up to 2°C. The high R^2 and the other values showed that the model performed well in predicting the surface temperatures.

4.3 Summary

Model evaluation and sensitivity analysis are very steps in assessing the performance of numerical models in predicting surface temperatures. Model evaluation involves comparing the model outputs with observed data. This is done both graphically and statistically. Evaluation an energy balance model helps to identify the strengths and weaknesses of the model and its ability to simulate surface temperatures accurately. By comparing the model outputs with real-world observations, researchers can determine the level of agreement between the two and identify areas where the model needs improvement. Sensitivity analysis, on the other hand, helps to identify the most influential input parameters in the model and their impact on the output. This information can be used to improve the model's performance by adjusting the input parameters or improving the accuracy of the input data.

With regards to model evaluation, the lack of observed wall temperature data in the Phoenix study sites limited the ability to undertake a model evaluation for wall surfaces. Thus evaluation of the model was performed on comparing the roof temperatures from the model with the roof temperatures from the observed data from Phoenix, with the assumption that, if the model performs well for generating similar roof temperatures, then it would perform well for generating wall temperatures. It was also shown that the model was previously evaluated by Krayenhoff and Voogt (2007) in two study sites, Vancouver Light Industrial and Basel-Sperrstrasse. The regression statistics, and graphs for their

evaluations for Vancouver were shown in this study. Their results also showed that the model performs well in generating surface temperatures.

In addition to model evaluation, sensitivity analysis was also conducted to identify the most influential input parameters in the model and their impact on the output. The sensitivity analysis focused on parameters such as momentum length for roofs and roads, wall orientation, H/W, albedo, thermal and radiative parameters, and wind speed. The results of the sensitivity analysis showed that the most influential parameters were momentum length for roofs and roads and wind speed. The sensitivity test on H/W ratio showed that, the difference in H/W ratios did not have a significant impact on the modelled wall temperatures during the time when the thermal data were captured. This is because all the walls were already very hot due to the sun angle positions during that time period. The sensitivity test on albedo and thermal admittance showed that, the model is highly sensitive to albedo inputs, with wall temperature differences reaching as high as 10 °C when albedo is decreased from 0.8 to 0.2. The sensitivity test on wall orientations showed that, grouping walls with a variation of $\pm 11.25^\circ$ in orientation have less than 1°C potential error. overall, the sensitivity tests showed that the the input parameters used in simulating the model were not largely underestimated or overestimated in generating accurate wall temperatures.

Chapter 5

5 Results

This chapter presents the results of T_{ped} calculations plotted as gridded data in map form for both daytime and night results to allow assessment of the spatial variation in T_{ped} . Scatter plots are used to visualize the difference between T_{ped} and T_{plan} . A multiple regression approach is developed and tested to assess the ability to predict T_{ped} using T_{plan} and select measures of the urban surface structure.

5.1 Comparisons between T_{ped} and T_{plan} for LCZ 6 at the 50m x 50m spatial scale.

This section presents the spatial pattern of T_{ped} and compares it to that of T_{plan} for LCZ 6. Results for the other LCZ, which show similar patterns, are included in Appendix A.6.

Figure 5. 1 to Figure 5. 4 show the spatial patterns of the calculated daytime and nighttime T_{ped} and, for comparison, T_{plan} using a 50m x 50m domain for LCZ 6 . Areas with higher temperatures (hotspots) for T_{plan} are areas with warmer roof and ground surface temperatures (Figure 5. 1) or (T_{ped}) areas with warmer wall and ground surface temperatures (Figure 5. 2) The hotspot patterns in the 50m x 50m domains show that T_{plan} and T_{ped} temperatures are similar on wider streets where the low fraction of building walls limits the impact of wall temperature effects on T_{ped} estimation. In parts of the study area where buildings are more closely spaced, there is both more shading from walls on the ground and a greater contribution of wall temperatures that are typically cooler than roof temperatures to T_{ped} . This helps to make narrower streets (large H/W ratio street canyons) more thermally comfortable in terms of T_{ped} . Areas with vegetation are relatively cool in maps of both T_{ped} and T_{plan} . Where vegetation occurs in the vicinity of buildings, the use of T_{ped} further reduces the temperature because walls are colder than roof temperatures. Table 5. 1 shows the estimated vegetation plan fraction and tree canopy fraction for each LCZ.

Those values are calculated to assess the amount of vegetation, that are calculated as part of T_{ped} , and they are assumed to be areas under tree canopies.

Table 5. 1. Amount of vegetation in each LCZ

LCZ	Vegetation plan fraction	Tree Canopy fraction
5	0.1	0.09
6	0.15	0.12
7	0.06	0.05
8	0.04	0.02

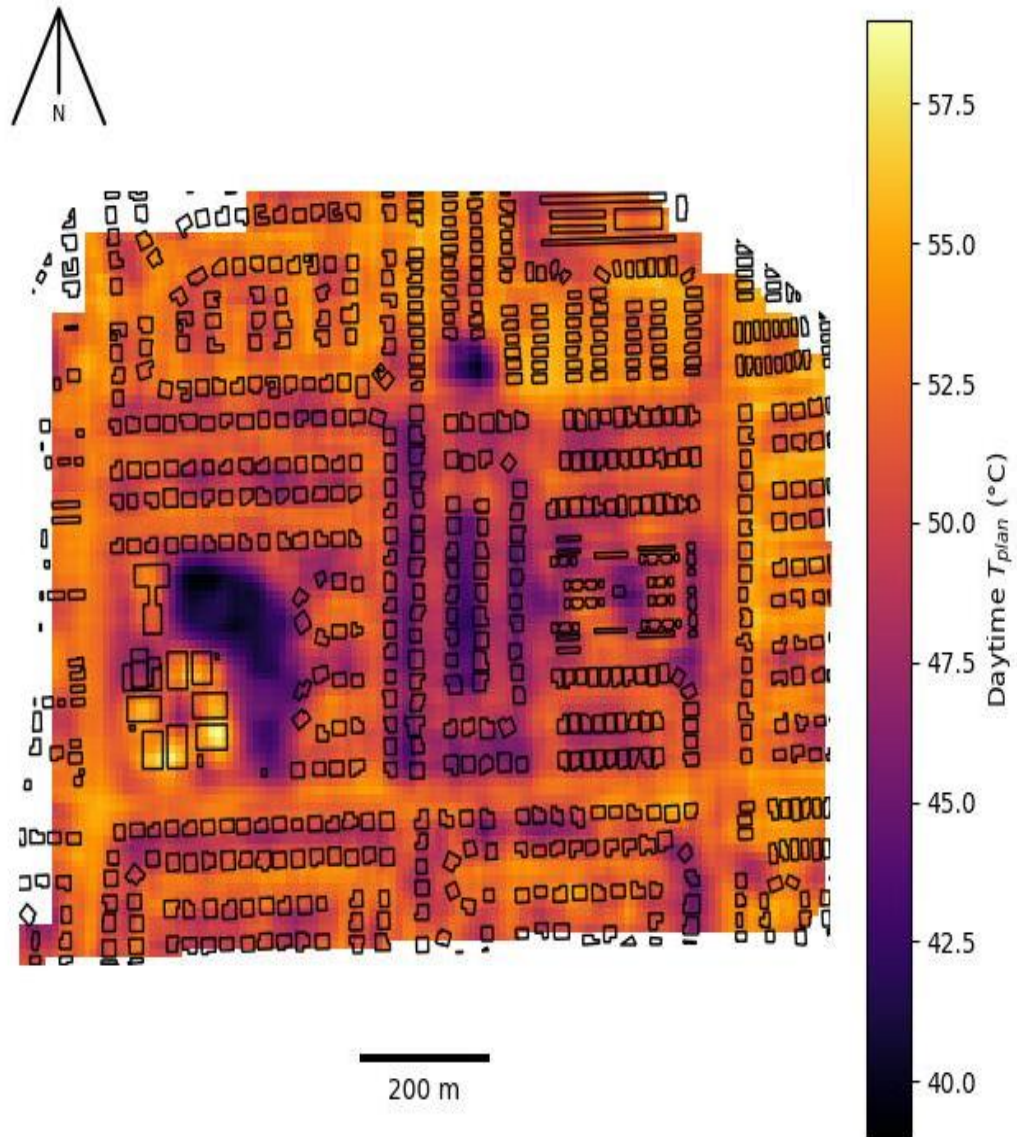


Figure 5. 1. Images of daytime T_{plan} for 50m x 50m domains of LCZ 6 constructed at 10 m spatial resolution.

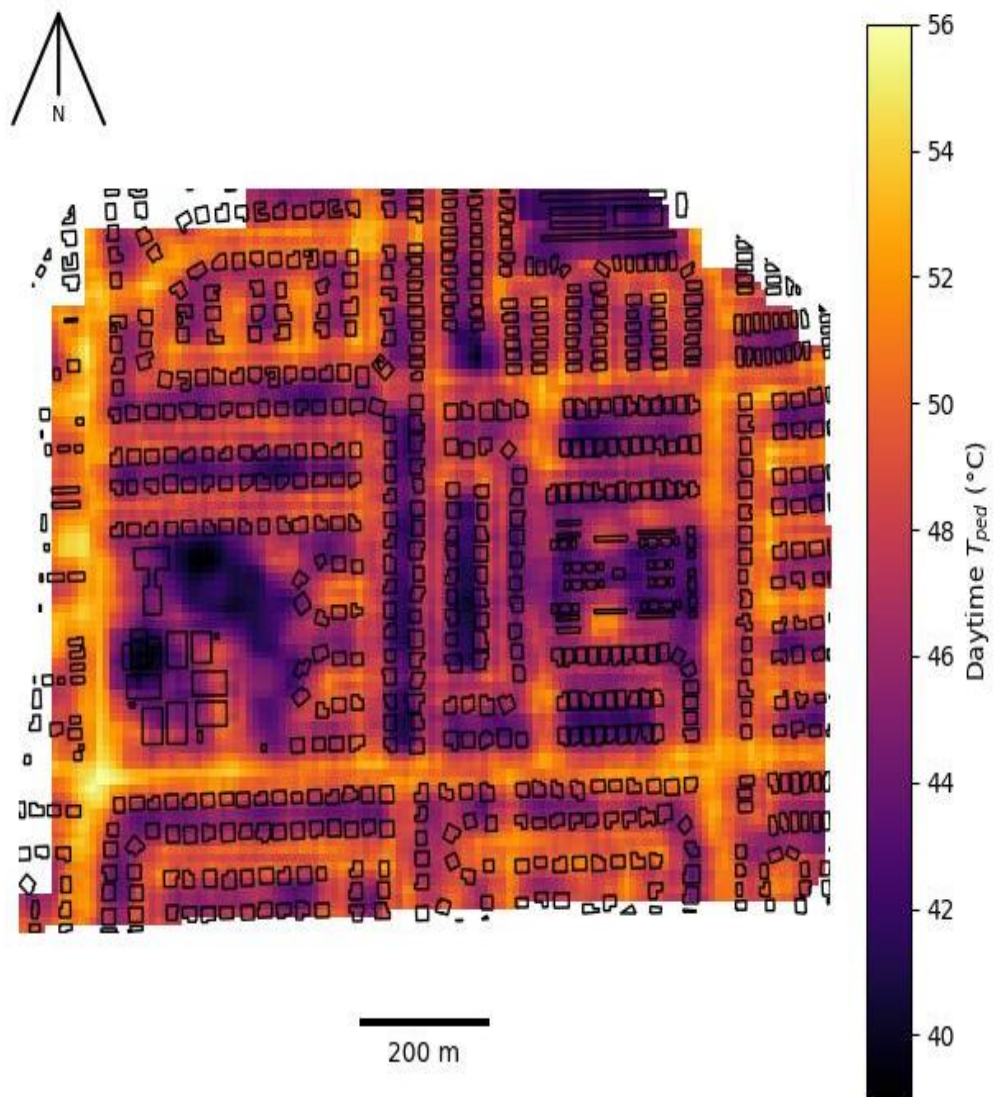


Figure 5. 2. Images of daytime T_{ped} for 50m x 50m domains of LCZ 6 constructed at 10 m spatial resolution.

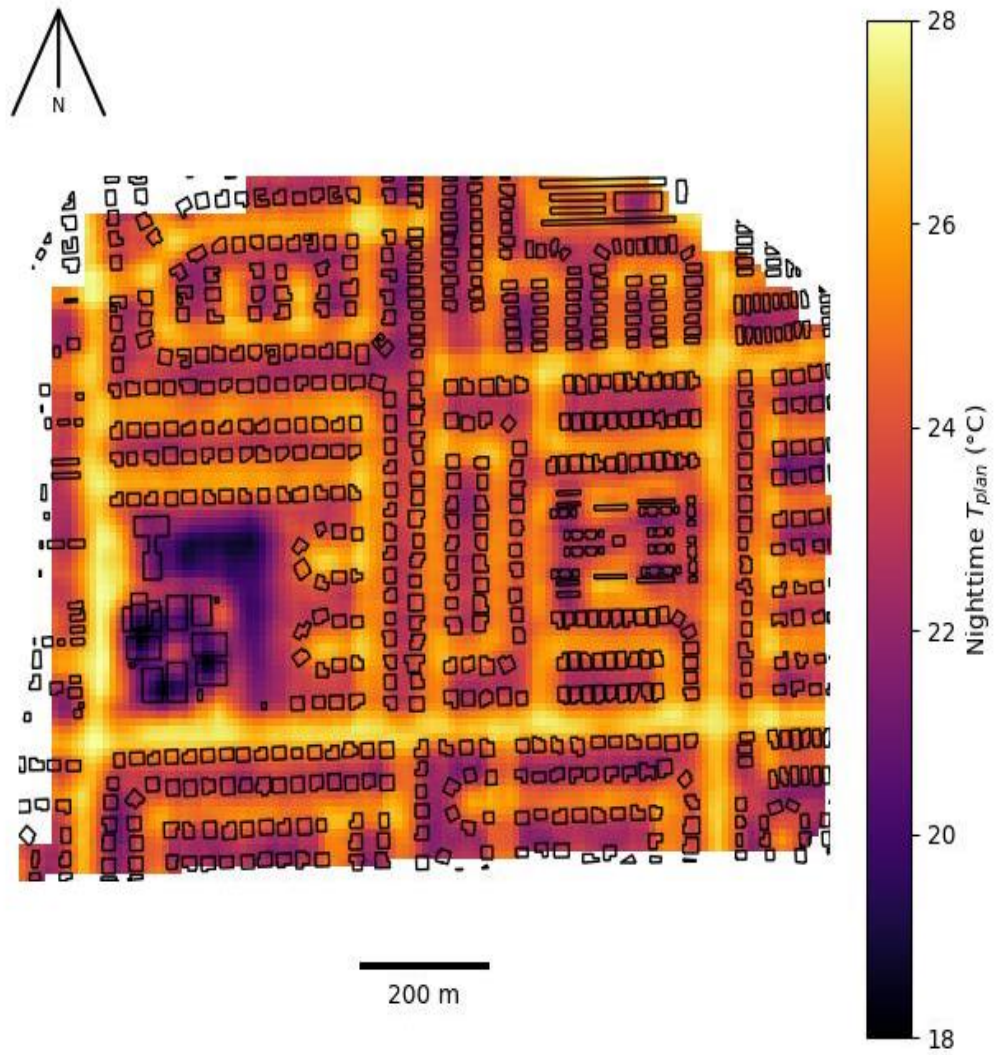


Figure 5. 3. Images of nighttime T_{plan} for 50m x 50m domains of LCZ 6 constructed at 10 m spatial resolution.

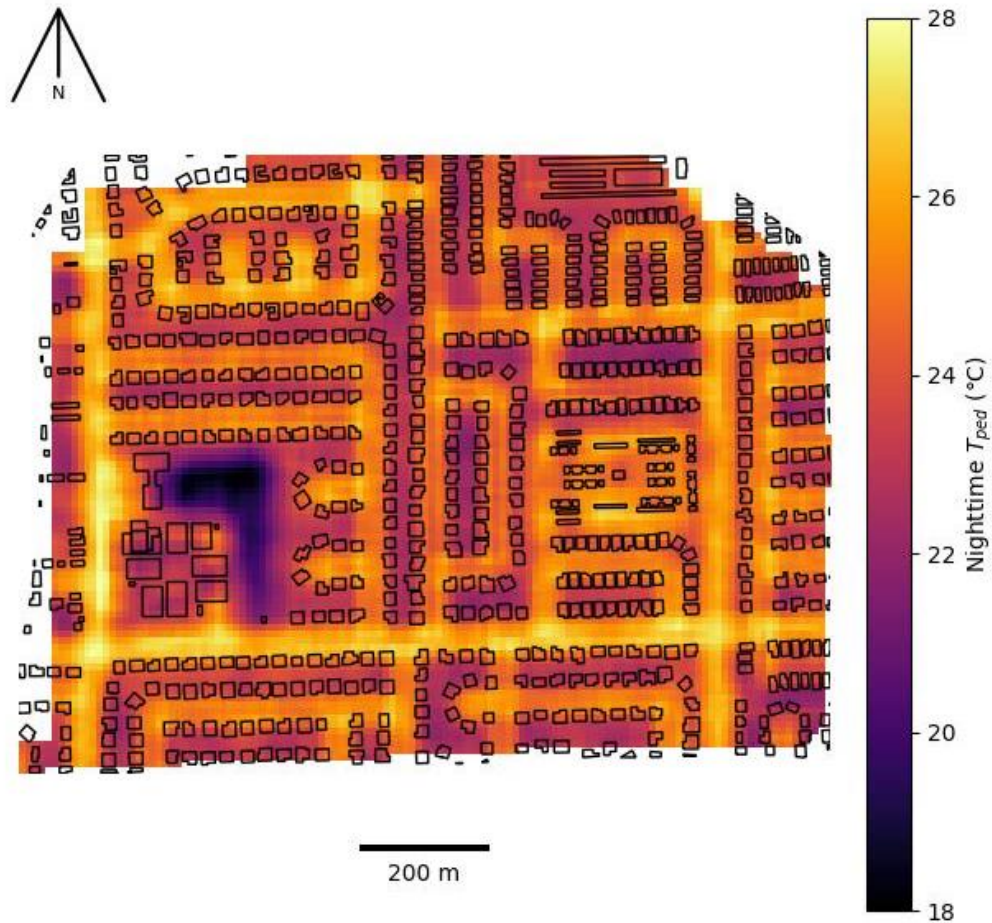


Figure 5. 4. Images of nighttime T_{ped} for 50m x 50m domains of LCZ 6 constructed at 10 m spatial resolution.

The difference in temperatures for T_{plan} and T_{ped} is largely explained by the different combination of surfaces that define each incomplete temperature. T_{plan} is the combination of ground and rooftop temperatures. T_{ped} however, is the combination of ground and wall temperatures. Roofs are commonly the hottest facet at midday. The solar zenith angle is small during the summer. This means the angle of incidence between the sun's rays and the roof surface is close to perpendicular providing a strong solar loading on the roof. In contrast, the angle of incidence between wall surfaces and the sun's rays is smaller due to the vertical orientation of the walls. Another factor is the insulation properties of rooftops. Rooftops are generally designed to have high insulation, which prevents more heat from

conducting through the roofs as compared to other built surfaces (e.g. ground pavements and walls) during the day. Thus, during daytime, high roof insulation leads to strong heat convergence at the roof surface, and makes roof surface temperatures higher than the other built surfaces. At night, well insulated roof surfaces lack a store of heat to replenish heat loss from the roof surface and thus roofs lose heat faster than other built surfaces during the night and are likely to become the coldest facet (Oke et al. 2017).

Figure 5. 5 shows the height of buildings in LCZ in meters. It can be seen that there are some wider spaces between buildings. These areas, where there are no building walls. These areas will show T_{ped} being the same as T_{plan} . Moreover, comparing Figure 5. 5 with Figure 5. 1 and Figure 5. 2, it can be seen that building heights have effects on T_{plan} and T_{ped} differences. Areas with taller buildings normally show lower T_{ped} . This is because taller buildings normally have wider wall areas, and these reduces T_{ped} calculations.

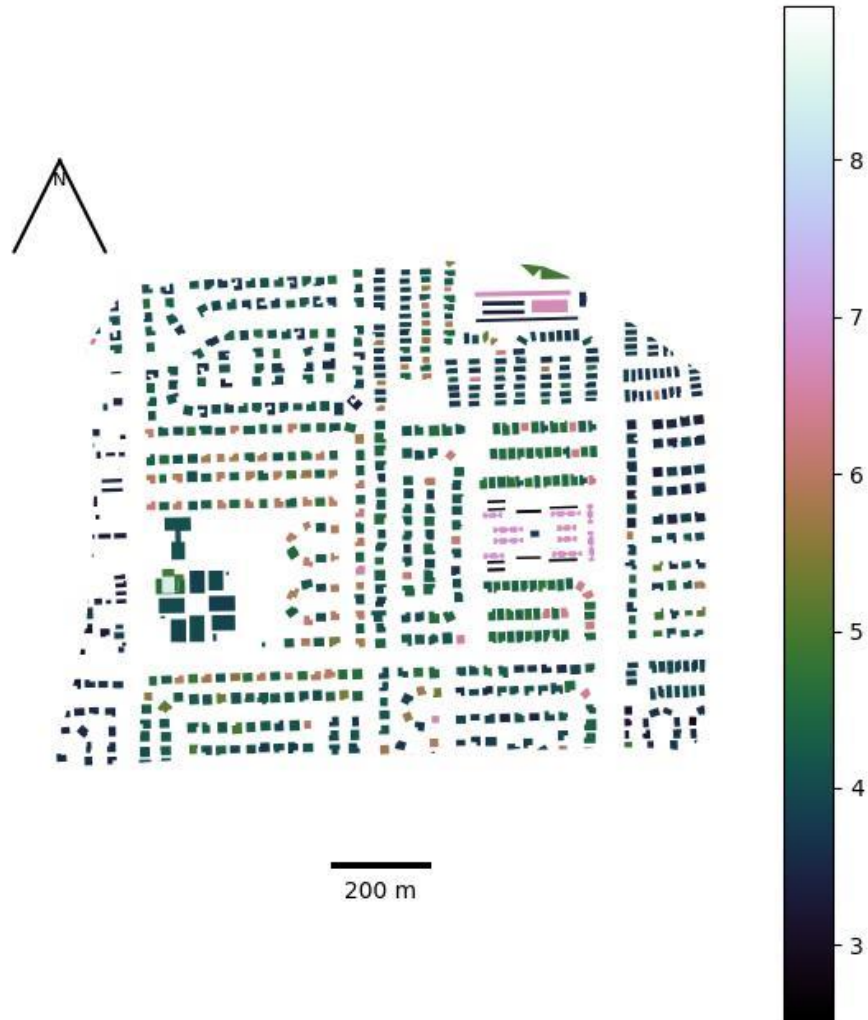


Figure 5. 5. Building heights within LCZ 6

Figure 5. 6 and Figure 5. 7 show the distribution of daytime and nighttime T_{plan} and T_{ped} . These plots confirm that during the day T_{plan} temperatures are higher than T_{ped} , but T_{ped} values are a little higher than T_{plan} values at night

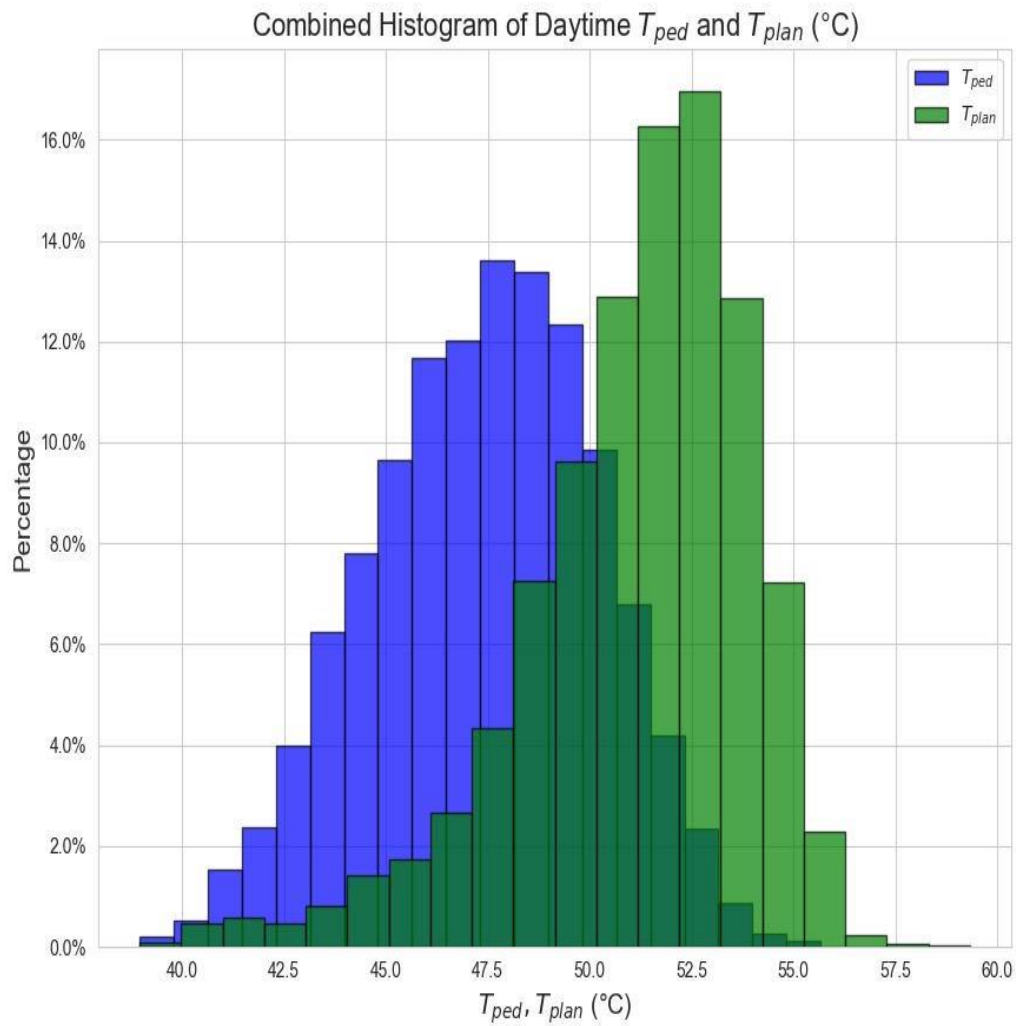


Figure 5. 6. Histogram plot for daytime T_{plan} and T_{ped} for 50m x 50m domain of LCZ 6.

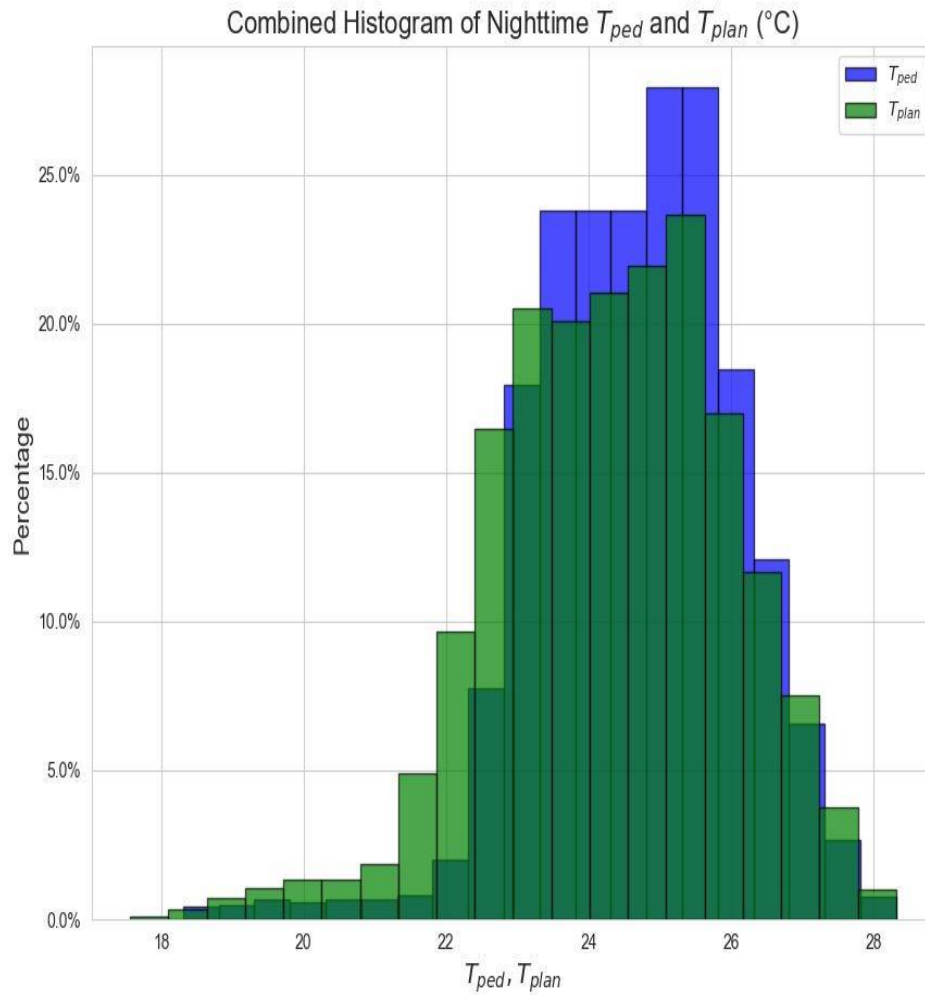


Figure 5. 7. Histogram plot for nighttime T_{plan} and T_{ped} for 50m x 50m domain of LCZ 6.

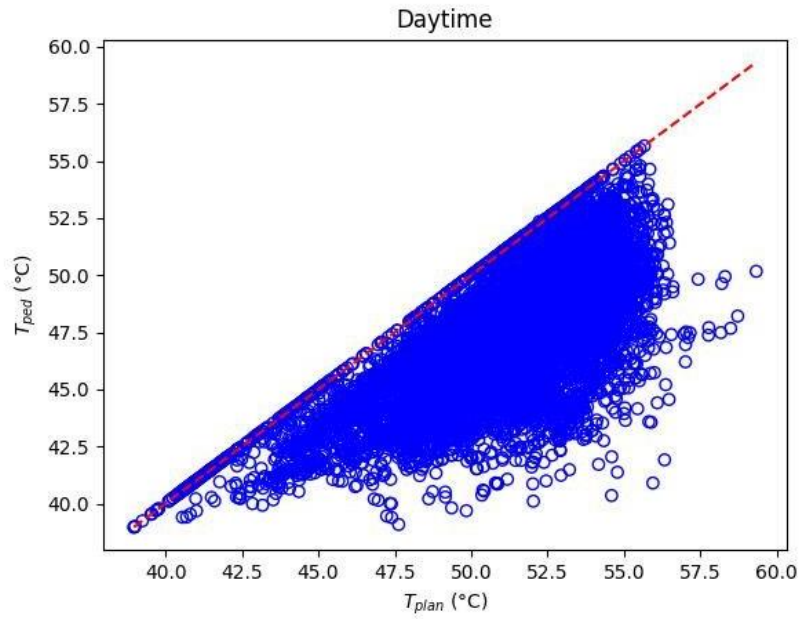


Figure 5. 8. Scatterplot for daytime T_{plan} and T_{ped} for 50m x 50m spatial domain of LCZ 6 at 10 m spatial resolution.

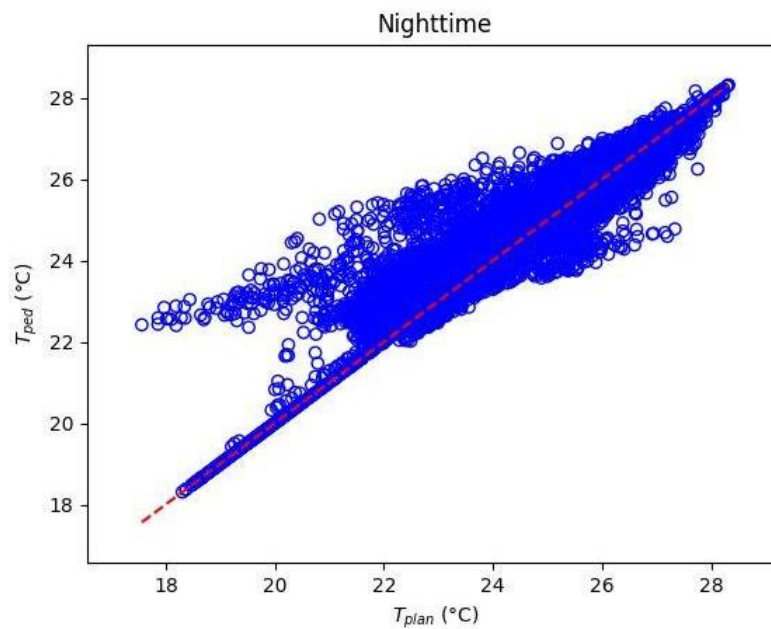


Figure 5. 9. Scatterplot for nighttime T_{plan} and T_{ped} for 50m x 50m spatial domain of LCZ 6 at 10 m spatial resolution.

Figure 5. 8 and Figure 5. 9 plot the relation between T_{plan} and T_{ped} as scatterplots for daytime and nighttime periods respectively. In the analysis of daytime temperatures (T_{plan} and T_{ped}) within the study area, both histogram plots and scatterplots were used to represent the data. The histogram plots presented the frequency distribution of T_{plan} and T_{ped} across all test grids (spatial domains) throughout the entire study area, while the scatterplots depicted the relationship between T_{plan} and T_{ped} for individual grid cells.

The histograms of T_{plan} and T_{ped} show how often specific temperature values occur across all spatial domains in the study area. As a result, the histograms provide an overview of the general tendencies of the entire dataset. By day, the histograms show a distinct separation of T_{ped} and T_{plan} distributions across the LCZ 6 study area, with the peak of the distribution indicating T_{ped} are most often cooler than T_{plan} . A tail towards cooler temperatures exist, especially for T_{plan} , that may be related to specific roof characteristics (anomalous roof emissivity or perhaps high albedo). At night the T_{ped} and T_{plan} distributions are very similar with a very slight shift of T_{ped} towards warmer temperatures. Unlike histograms, scatterplots provide a more detailed perspective by representing the relationship between T_{plan} and T_{ped} on a grid-cell basis. Each point on the scatterplot corresponds to a single spatial domain (grid cell) within the study area, where T_{plan} and T_{ped} values are matched for that specific location. In Figure 5. 8, the scatterplot for daytime T_{plan} and T_{ped} reveals that, at the grid-cell level, T_{ped} is always less than or equal to T_{plan} during the day.

In Figure 5. 8, the points on and around the identity line shows areas where are few to no buildings, which makes T_{ped} similar to T_{plan} . Also, the points deviate substantially below (and only below) the 1:1 line by day, showing that T_{ped} is always cooler than T_{plan} with the likelihood of large differences increasing for values of high T_{plan} . No values of T_{ped} exist above the 1:1 line, which marks spatial domains that consist entirely of ground or (less likely) roof surfaces with no walls present.

The larger differences arise because the hottest surfaces in the mid-day period are usually roofs. Where a spatial domain incorporates buildings characterized by both high roof temperatures and large wall area, the potential for a substantially reduced T_{ped} is increased.

That is, a larger roof will increase T_{plan} estimation while a larger wall area will decrease T_{ped} . At night (Figure 5. 9), the points in the scatterplot are mostly above the 1:1 line for spatial domains that incorporate buildings but unlike the daytime case, T_{ped} can be both warmer and cooler than T_{plan} . The difference of T_{ped} from T_{plan} is largest at values of low T_{plan} . This pattern arises because the walls cool more slowly at night relative to the roofs, especially if the roofs are well insulated and they have a low albedo. The walls thus become relatively warmer than the roofs. There is a small area of points that lie below the 1:1 line at higher values of T_{plan} , with points arranged in a linear pattern with a slope similar to that which characterizes T_{ped} values at low T_{plan} . In this part of the scatterplot, $T_{\text{ped}} < T_{\text{plan}}$ with an increase of T_{ped} that is less than that of T_{plan} (i.e. a trend to increasing difference of T_{ped} from T_{plan} , where T_{ped} is cooler). These points contradict the expectation that nighttime T_{ped} should be warmer than T_{plan} . They may arise because a grid cell is mostly occupied by ground surfaces, which can be much better stores of heat at night, with some adjoining building walls. Overall, in comparison to the daytime scatterplot, T_{ped} is more similar to T_{plan} with the variability of T_{ped} showing about half the size of the temperature differences observed during the day. The smaller night time differences are related to the smaller surface temperature variability that occurs in the absence of daytime solar forcing.

To further assess the scatter demonstrated by the T_{plan} vs T_{ped} relations, an analysis is undertaken to show how the potential controlling factors of wall areas and λ_p affect T_{plan} and T_{ped} values. Twenty points from Figure 5. 8 were chosen for analysis. The points are taken to represent a variety of $T_{\text{plan}}-T_{\text{ped}}$ differences over the large range that characterizes higher values of T_{plan} . These points are plotted in Figure 5. 10 and Figure 5. 11 for the λ_p and sum of wall areas respectively, with the size of the symbol corresponding to points with higher values of λ_p , and the sum of wall areas. There is a direct relationship between λ_p and the T_{plan} vs T_{ped} scatterplot, as seen in Figure 5. 10.

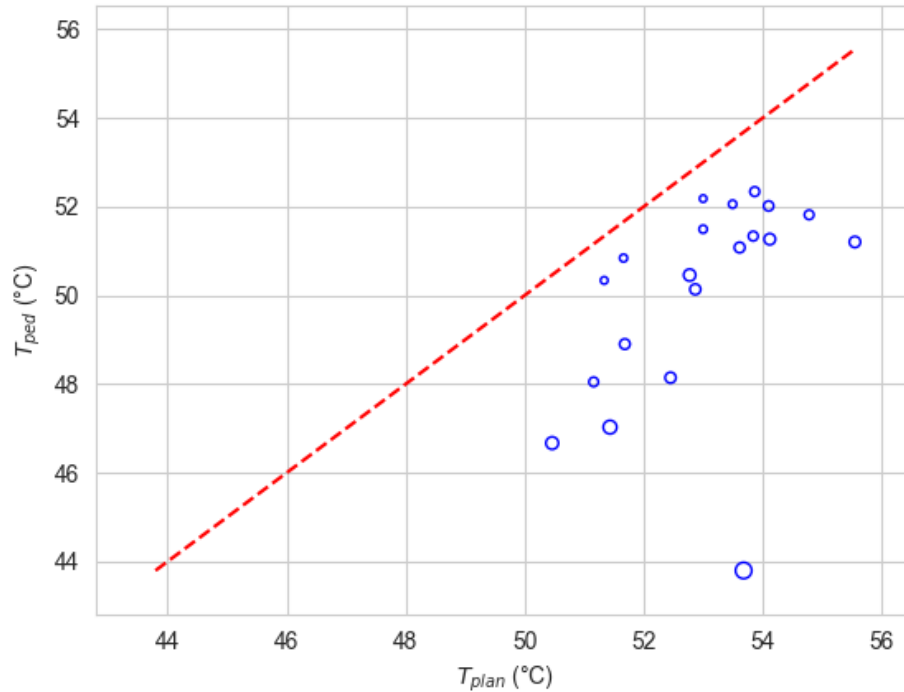


Figure 5. 10. The effects of λ_p on T_{plan} and T_{ped} values. Larger circles represent larger λ_p .

Areas with lower λ_p also have lower T_{plan}/T_{ped} differences. Higher λ_p values represent more buildings per domain area grid. This decreases the building spacing (increases H/W) and increases the likelihood of more shading on the building walls, reducing their temperatures, which in turn decreases T_{ped} , as compared to the hotter rooftop and ground temperatures in T_{plan} temperatures. A direct relationship also exists for wall areas and T_{plan}/T_{ped} differences (Figure 5. 11). The differences between T_{plan} and T_{ped} are higher if there are more wall areas. A domain with more building walls will likely reduce T_{ped} by increasing the amount of wall surface area and recognizing these surfaces are typically cooler than plan surfaces. Such domains are also likely to have a smaller building spacing with greater likelihood of wall shading that could further reduce the wall temperature and decrease T_{ped} .

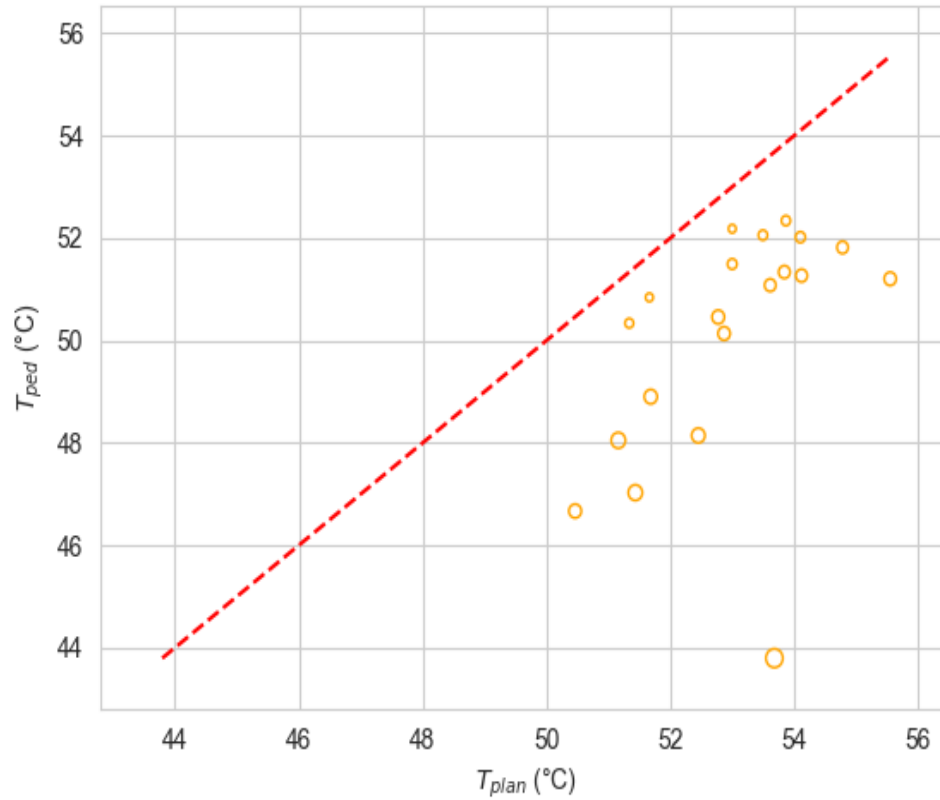


Figure 5. 11. The effects of wall areas on T_{plan} and T_{ped} values. Larger circles represent larger wall area within the domain.

With regard to the effects of building wall heights on T_{ped} , Figure 5. 12 shows a similar direct relationship between building heights and T_{plan}/T_{ped} differences.

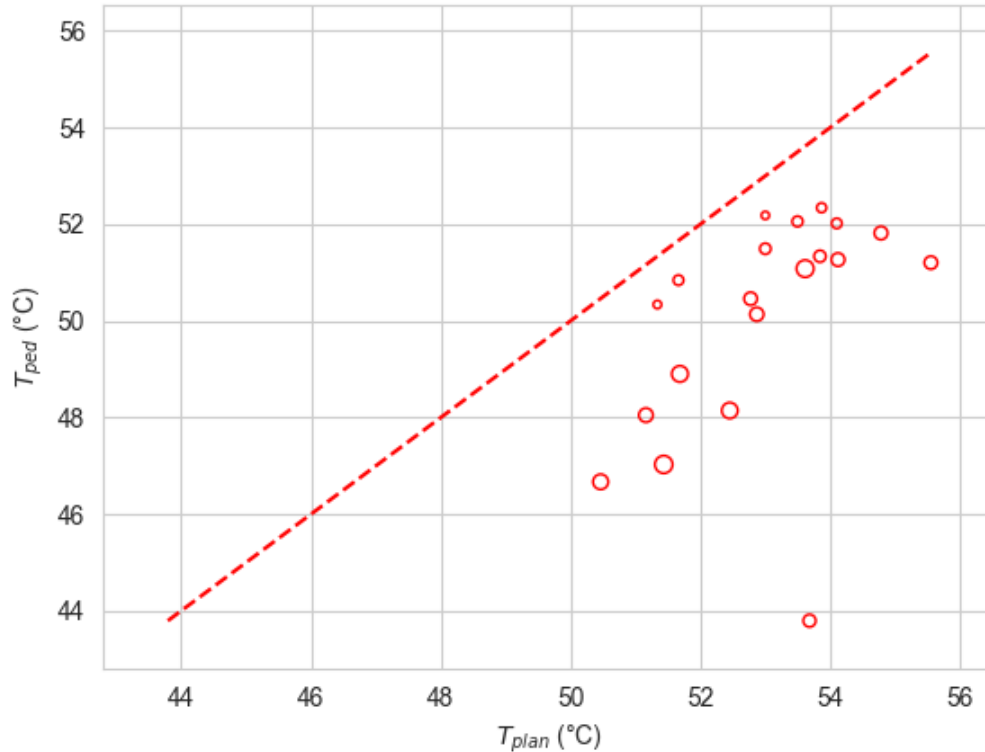


Figure 5. 12. The effects of building heights on T_{plan} and T_{ped} values. Larger circles represent larger building heights within the domain.

5.1.1 $T_{plan} - T_{ped}$ Comparisons at Larger Spatial Scales.

Figure 5. 13 to Figure 5. 18 show T_{plan} and T_{ped} plotted at 100m x 100m and 200m x 200m domain sizes for daytime and nighttime with their corresponding histograms. Comparing these figures to Figure 5. 1 to Figure 5. 4, the hotpot patterns are most clearly seen in the 50m x 50m domains. The spatial patterns become less distinct as the domain size increases, as seen in the 200m x 200m domains. To better assess the spatial variability of T_{ped} , researchers and urban planners should perform these calculations on smaller spatial domains (see Section 6 Summary and).

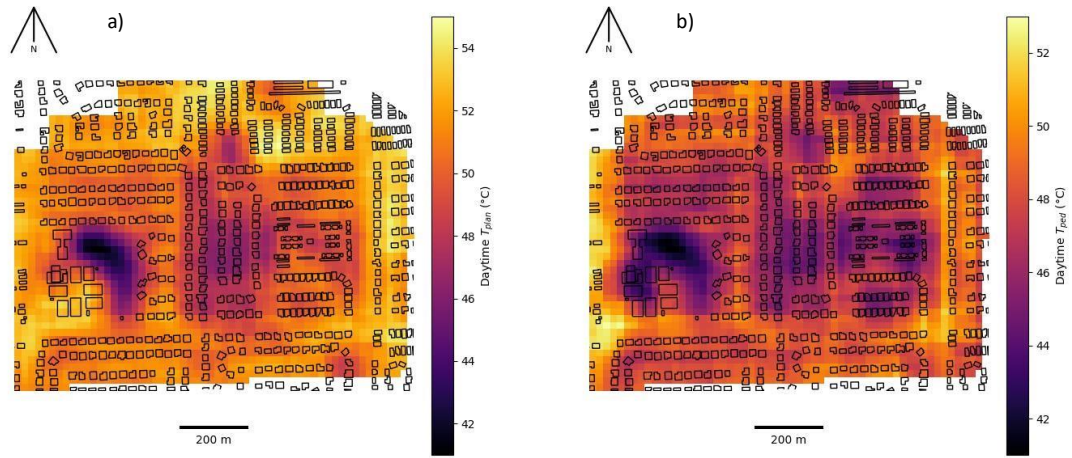


Figure 5. 13. Images of daytime a) T_{plan} and b) T_{ped} for 100m x 100m domains of LCZ 6 constructed at 10 m spatial resolution.

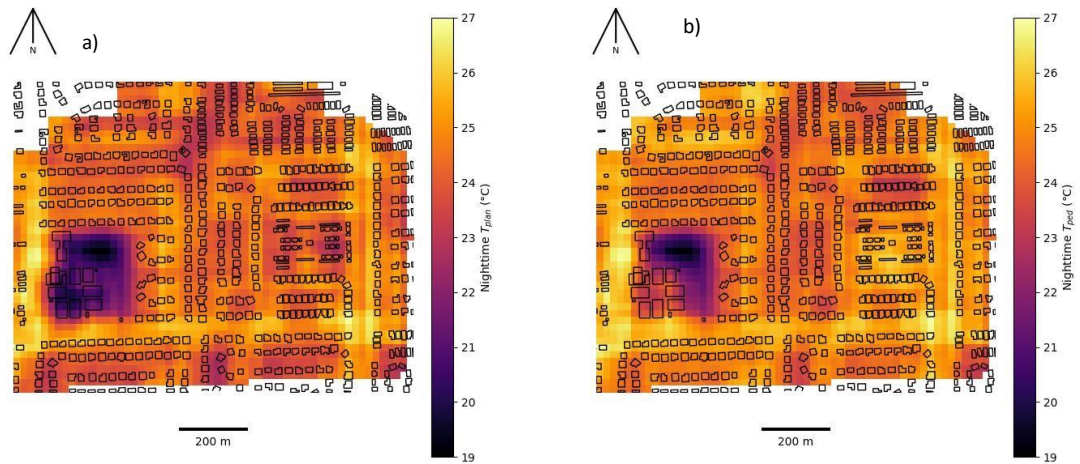


Figure 5. 14. Images of nighttime a) T_{plan} and b) T_{ped} for 100m x 100m domains of LCZ 6 constructed at 10 m spatial resolution

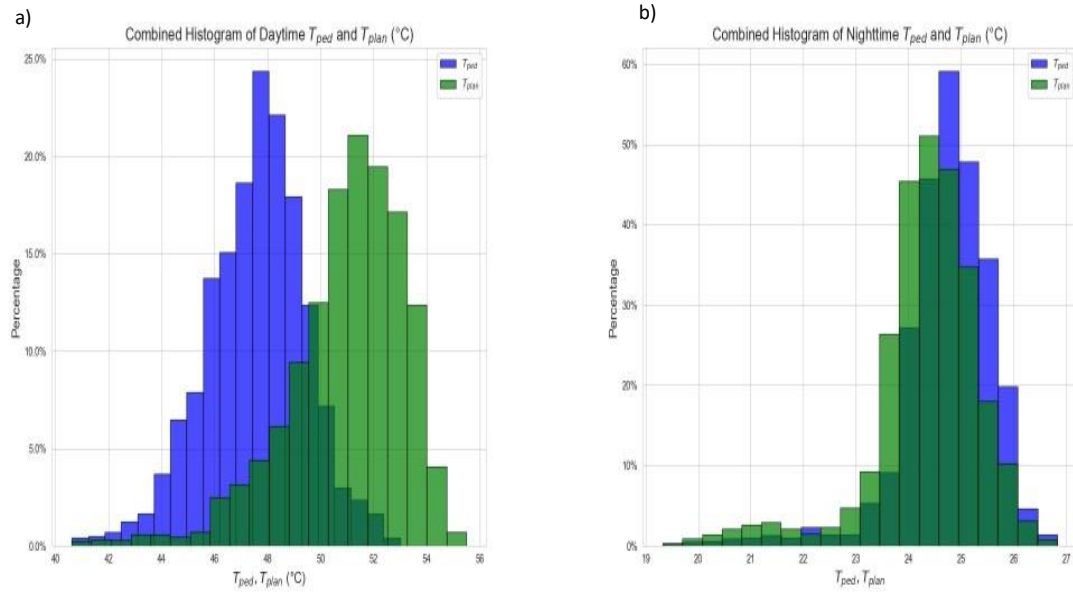


Figure 5. 15. Histogram plots for a) daytime T_{ped} and T_{plan} and b) nighttime T_{ped} and T_{plan} for 100m x100m domain of LCZ 6.

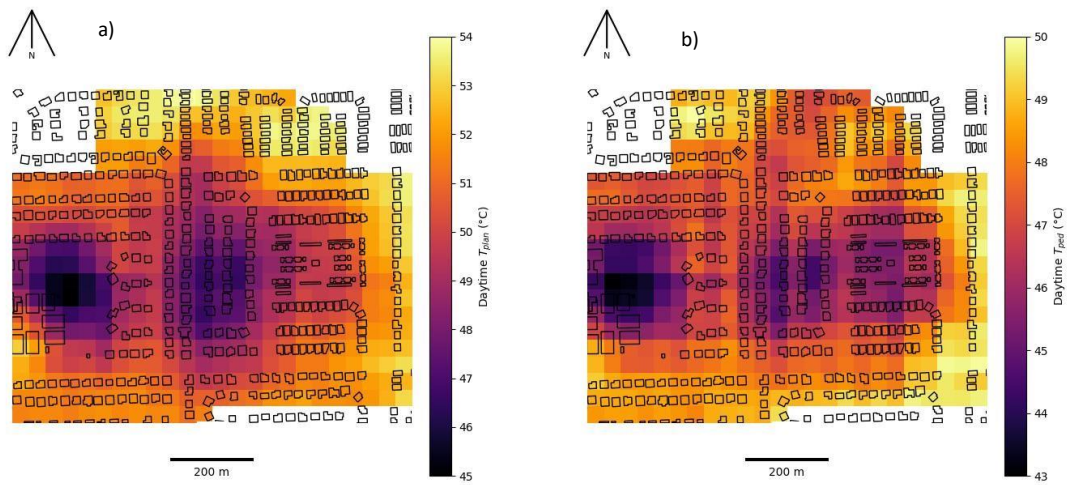


Figure 5. 16, Images of daytime a) T_{plan} and b) T_{ped} for 200m x 200m domains of LCZ 6 constructed at 20 m spatial resolution.

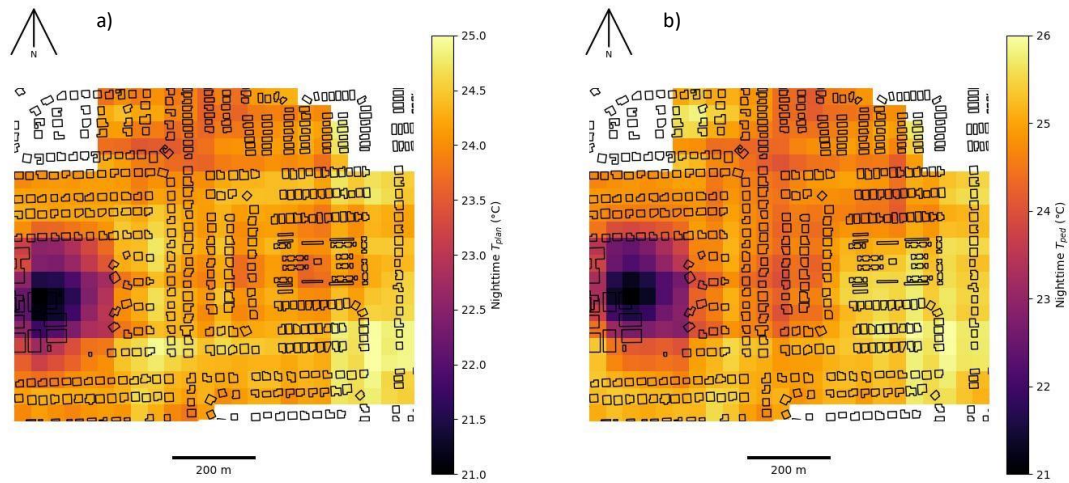


Figure 5. 17. Images of nighttime a) T_{plan} and b) T_{ped} for 200m x 200m domains of LCZ 6 constructed at 20 m spatial resolution.

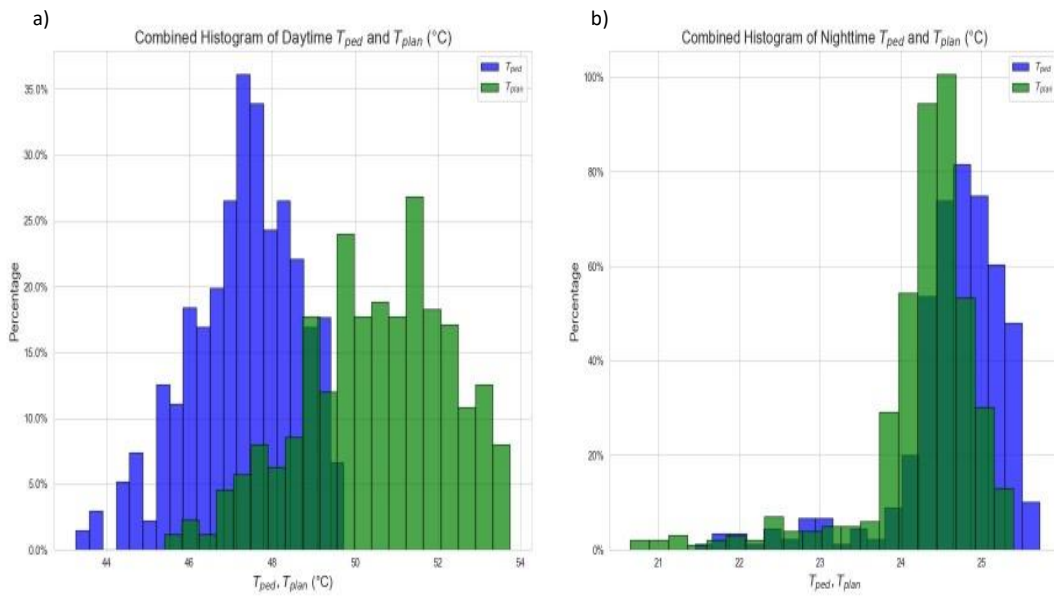


Figure 5. 18. Histogram plots for a) daytime T_{ped} and T_{plan} and b) nighttime T_{ped} and T_{plan} for 200m x200m domain of LCZ 6.

5.2 Comparisons Between T_{ped} and T_{plan} for Different LCZ

Table 5. 2 shows the study area average daytime and nighttime T_{plan} and T_{ped} values for the different LCZ study areas. For daytime T_{plan} , LCZ 6 recorded the highest temperature value while LCZ 8 recorded the lowest temperature value, even though the difference between the two temperatures is very small. Studies from other researchers have shown that LCZ 8 typically has higher surface temperatures than other LCZ (e.g. Betchel et al. 2019; Mushore et al. 2022; Chen et al. 2020). Since T_{plan} is obtained directly from the observed thermal data, the lower T_{plan} for LCZ 8 in this study may be due to the material properties of the roofs and ground, and the amount of vegetation on the ground relative to other cities. For example, very high albedo values for roofs in LCZ 8, due to implementation of ‘cool’ roof technologies in this desert city, as compared to roofs in LCZ of other study areas, may decrease in T_{plan} values for LCZ 8 in this study area relative to those in other studies.

The higher T_{plan} temperature value for LCZ 6 may result from the lower albedo value (A.8) and the material properties of the rooftops in LCZ 6, which makes them absorb and retain more heat than the other LCZ. LCZ 5 recorded the lowest daytime T_{ped} , possibly due to the amount of vegetation on the ground surfaces, which reduced T_{ped} . LCZ 7 recorded the highest daytime T_{ped} values.

At night, differences in the temperatures for T_{ped} and T_{plan} for all LCZ are minimal. The absence of solar radiation at night means that surface temperature variations are much reduced, making large differences between T_{ped} and T_{plan} less likely than during daytime. The smaller differences between T_{ped} and T_{plan} at night are analogous to the smaller difference between remotely observed T_{plan} and T_{air} that are commonly noted in cities (Song et al. 2017).

Table 5. 2. Average daytime and nighttime T_{ped} and T_{plan} values for the four LCZ.

LCZ	Average Daytime T_{plan} (°C)	Average Daytime T_{ped} (°C)	Average Nighttime T_{plan} (°C)	Average Nighttime T_{ped} (°C)
5	50.13	45.3	27.94	27.68
6	51.35	48.24	24.27	24.76
7	51.19	49.58	25.8	26.13
8	49.59	47.54	25.62	25.92

Table 5. 3 and Table 5. 4 show the number of SAs, and their minimum, maximum, and mean temperatures and the standard deviation within each LCZ for both daytime T_{ped} and nighttime T_{ped} . This shows the variabilities that exist within each LCZ. Further results for each SA are found in Appendix A.4.

Table 5. 3. Measures of variability for each LCZ for daytime T_{ped}

LCZ	SA count	Min (°C)	Max (°C)	Mean (°C)	Std (°C)
5	15	39.62	48.02	43.94	2.89
6	14	45.43	50.83	47.57	1.56
7	15	45.27	51.02	49.13	1.52
8	12	45.91	48.96	47.07	0.93

Table 5. 4. Measures of variability for each LCZ for nighttime T_{ped}

LCZ	SA count	Min (°C)	Max (°C)	Mean (°C)	Std (°C)
5	15	25.28	29.5	27.01	1.28
6	14	23.07	25.52	24.51	0.69
7	15	23.99	27.9	25.77	1.24
8	12	23.77	26.12	25.06	0.79

5.3 Multiple Regression Modelling for the Study Areas.

The dependence of the T_{ped} temperature difference from T_{plan} by day on some basic measures of the urban surface structure described in Section (5.1) suggests that these measures may be used to derive an empirically based method of estimating T_{ped} from T_{plan} . As they affect T_{plan}/T_{ped} differences. These measures are λ_p (Figure 5. 10) and the sum of wall areas (Figure 5. 11). Such a model would help researchers who use satellite-based measurements of T_{plan} to assess pedestrian comfort in urban areas by providing a more relevant measure of surface temperature for these assessments. In this section, multiple regression models for both daytime and nighttime were performed for each 100m x 100m domain of each LCZ. The 100m x 100m scale is chosen for analysis because this is the resolution of Landsat satellite thermal data that is widely available and often used for intra-urban thermal analysis.

Table 5. 5 shows the multiple regression statistics for each LCZ, both for daytime and nighttime. Figure 5. 19 to Figure 5. 22 show the multiple regression plots for each LCZ, both for daytime and nighttime. These figures plot the results of the predicted regression model output against the actual calculated T_{ped} for each of the LCZs.

Taking the general equation for a multiple regression, which is

$$Y = b_0 + b_1x_1 + b_2x_2 + \dots \dots b_kx_k\dots \quad \text{Equation 5. 1}$$

where

Y = The dependent value

b_0 = the intercept

b_1, b_2, b_k = slope coefficients,

We can generate the multiple regression equation for each LCZ in Table 5. 5. The multiple regression model for each LCZ was created by training on half of the points, and testing the trained data on the remaining half of the points. Values of R^2 , adjusted R^2 , MAPE, RMSE and MAE are used to assess the performance of the model on the test data.

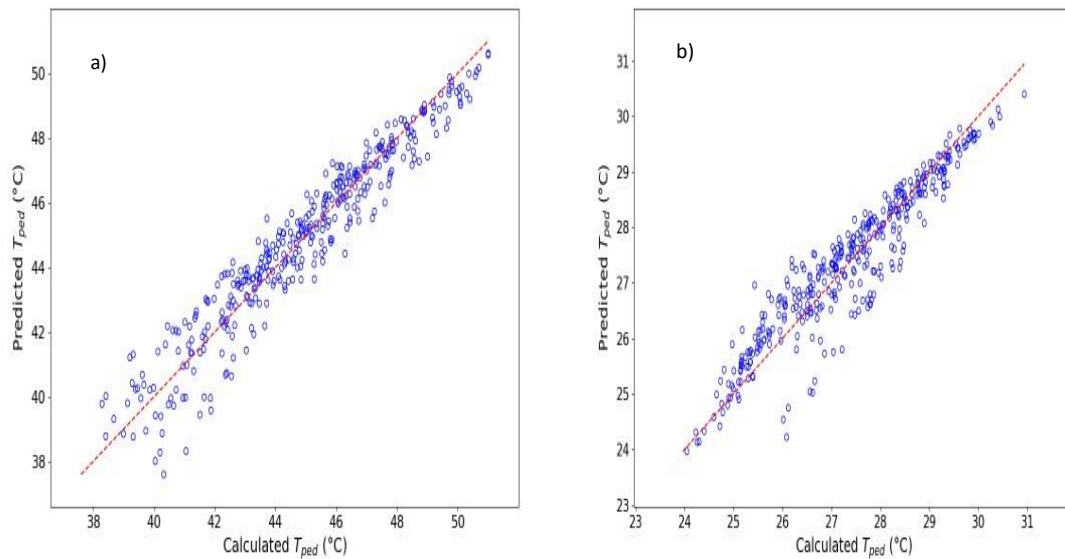


Figure 5. 19. Regression model for predicted and calculated a) daytime T_{ped} and b) nighttime T_{ped} for 100m x 100m spatial domain of LCZ 5. The dashed red line is the 1:1 line.

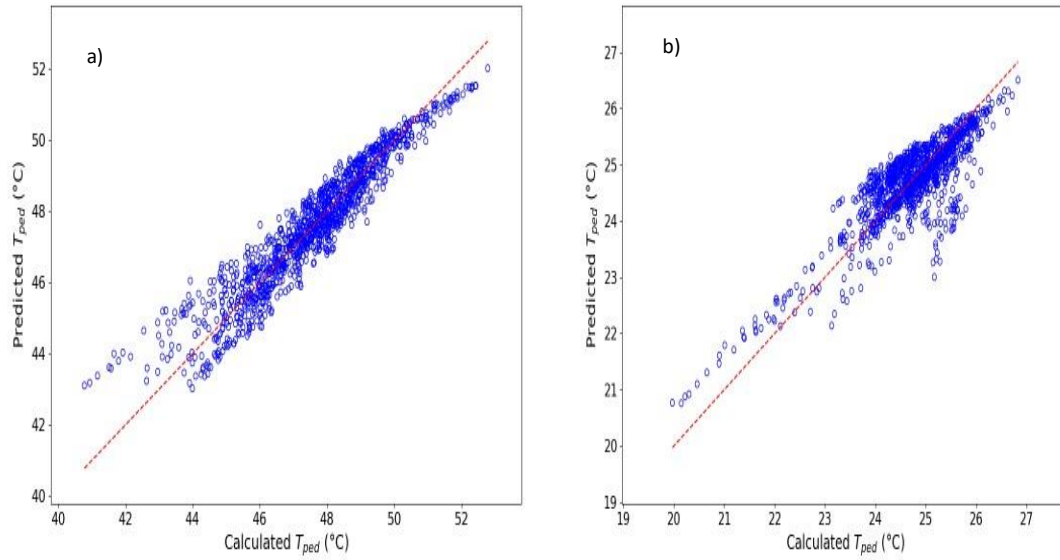


Figure 5. 20. Regression model for predicted and calculated a) daytime T_{ped} and b) nighttime T_{ped} for 100m x 100m spatial domain of LCZ 6. The dashed red line is the 1:1 line.

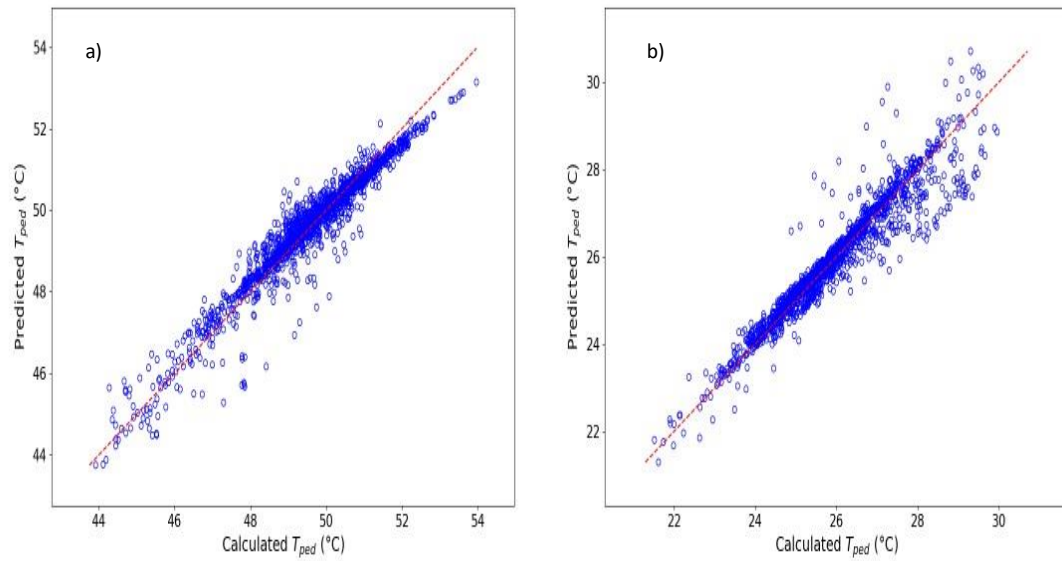


Figure 5. 21. Regression model for predicted and calculated a) daytime T_{ped} and b) nighttime T_{ped} for 100m x 100m spatial domain of LCZ 7. The dashed red line is the 1:1 line.

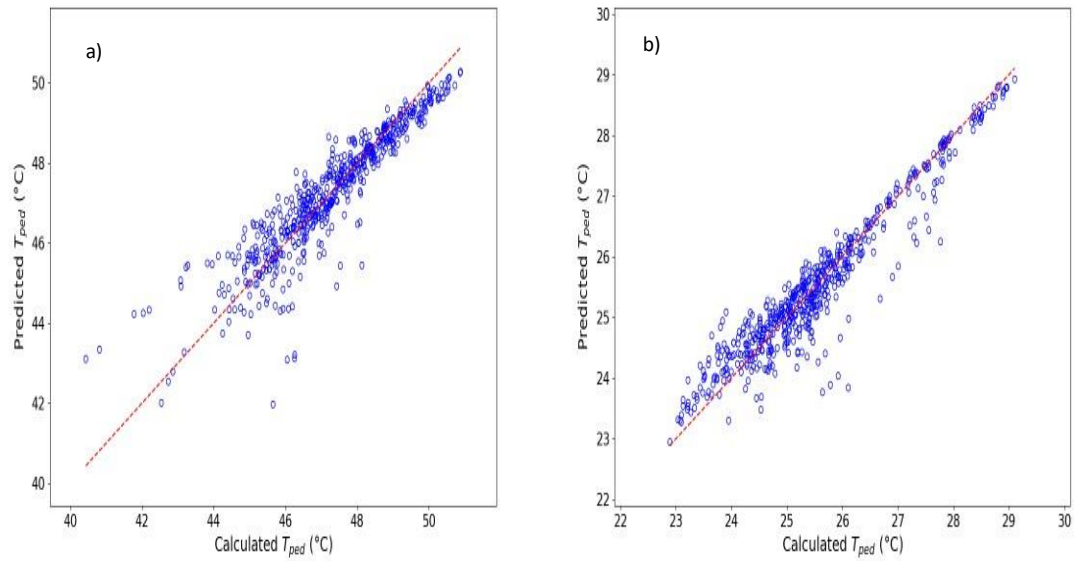


Figure 5. 22. Regression model for predicted and calculated a) daytime T_{ped} and b) nighttime T_{ped} for 100m x 100m spatial domain of LCZ 8. The dashed red line is the 1:1 line.

Table 5. 5. Regression model statistics for daytime and nighttime for 100m x 100m spatial domain of each LCZ; Int = intercept.

LCZ 5	R²	Adj. R²	RMSE	MAPE	MAE	Int.	λ_p	Wall area	T_{plan}
Daytime	0.92	0.92	0.81	1.44	0.63	22.23	-7.28	-0.0008	0.58
Nighttime	0.9	0.9	0.49	1.38	0.37	6.81	3.56	-0.0004	0.76
LCZ 6									
Daytime	0.896	0.895	0.6	0.99	0.46	14.4	-6.99	-0.0007	0.71
Nighttime	0.77	0.77	0.46	1.39	0.34	4.5	3.67	-0.0002	0.82
LCZ 7									
Daytime	0.932	0.932	0.41	0.6	0.29	9.23	-2.84	-0.0008	0.8
Nighttime	0.911	0.91	0.42	0.98	0.26	0.43	5.8	-0.0003	0.99
LCZ 8									
Daytime	0.81	0.81	0.68	0.99	0.46	18.57	-1.89	-0.008	0.63
Nighttime	0.89	0.89	0.4	1.12	0.28	2.59	6.18	-0.0005	0.92

Table 5. 5 outlines the statistics of the regression models used for the 100m x 100m spatial domains of each Local Climate Zone (LCZ) for both daytime and nighttime. Metrics such as R², Adjusted R², RMSE, MAPE, MAE, and intercepts for λ_p , wall area, and T_{plan} are included, offering a comprehensive understanding of the models' performance.

Coefficient of Determination (R^2) and Adjusted R^2 :

In LCZ 5, during daytime, we observe that the R^2 and Adjusted R^2 values are identical at 0.92. This suggests that the model is capable of explaining 92% of the variance in T_{ped} , indicating robust predictive performance. Moving into nighttime, these values are 0.9, showcasing a slight reduction, but still maintaining strong predictive capabilities. Moving to LCZ 6, the also model exhibits different performances under daytime nighttime conditions. For the daytime condition, R^2 and Adjusted R^2 values are 0.896 and 0.895 respectively. For the nighttime condition, these values are slightly lower at 0.77, indicating a reduction in the model's predictive capability under these specific conditions. LCZ 7 displays impressive model performance, with R^2 and Adjusted R^2 values reaching 0.932 during daytime, the highest across all LCZs. This indicates a highly effective model in this zone under daytime conditions. At nighttime, the values drop slightly to 0.911, but still exhibit robust predictive capability. Finally, in LCZ 8, the model performance shows R^2 and Adjusted R^2 values of 0.81 during daytime, the lowest in the daytime comparisons but still illustrating a substantial predictive power. During nighttime, however, the model's predictive power increases, with R^2 and Adjusted R^2 values of 0.89.

These findings demonstrate a high level of predictive power in our models across various local climate zones and times of the day. However, it also emphasizes the subtle influences of different conditions on model performance, with some variability in R^2 and Adjusted R^2 values under different settings. This highlights the importance of considering time-specific and spatial factors when evaluating model performance and emphasizes the importance of context-specific modeling in climate science.

Root Mean Square Error (RMSE), Mean Absolute Percentage Error (MAPE), Mean Absolute Error (MAE):

The regression model statistics presented in Table 5. 5 for different Local Climate Zones (LCZs) provide essential insights into the model's performance during daytime and nighttime. The error metrics including RMSE, MAPE, and MAE play a significant role in assessing the model's accuracy across different LCZs and times of the day.

Starting with LCZ 5, the RMSE values for daytime and nighttime are 0.81 and 0.49, respectively, signifying an average deviation between the model predictions and actual values. This informs us about the typical error magnitude and is a particularly crucial measure when larger deviations result in more significant problems. Shifting to LCZ 6, daytime has an RMSE of 0.6, whereas the nighttime has an RMSE of 0.46. The lower RMSE value for the 'Night' indicates a slightly better model performance during the night for LCZ 6.

For LCZ 7, we can see an impressive improvement in RMSE values, particularly during the day, with the RMSE being 0.41. The lower this value, the closer the fit of the model to the data. At nighttime, the RMSE remains almost the same as during the daytime, signifying consistent performance of the model across different times of the day for LCZ 7. In LCZ 8, there's a noticeable increase in the RMSE value during the day, reaching 0.68. Despite the increase, this value still indicates a fairly good model fit to the data. The RMSE value improves during the nighttime to 0.40, implying a better model performance. The MAE and MAPE values further provide additional insights into the model's accuracy, reflecting the average absolute error and the average percentage error respectively. The variation in these values across different LCZs and times of the day points to the varying performance of the model. While some LCZs show consistent model performance across daytime and nighttime (like LCZ 7), others show variations (like LCZ 6 and LCZ 8), indicating that the model's predictive capability might be influenced by the time of the day (Table 2. 1).

5.4 A Unified Multiple Regression Model for all LCZ

The comprehensive analysis of the daytime and nighttime multiple regression models used for the various study areas demonstrates striking similarities among them. This conclusion is based on the statistical comparison of these models, which are intended to be representative of each respective LCZ study area. The uniformity of these justifies combining them into a singular, more versatile model to represent daytime and nighttime conditions to universally apply across all study areas. This concept involves creating a master multiple regression model for daytime and nighttime that retains the accuracy and predictive power of the individual models and yet generalizes across the distinct study areas. Such a consolidated model could have numerous benefits for researchers. A primary advantage lies in its potential for streamlining predictive analysis. Currently, to predict the T_{ped} value for multiple study areas, individual LCZ-specific multiple regression models are required. However, with the proposed unified regression model, T_{ped} values are predicted for a range of LCZs using the same model. This would increase efficiency and also enhance the overall predictability. It will also simplify the analytical process. The process of creating these models involved using machine learning to train half of the

Figure 5. 23 show the results of single regression models for both daytime and nighttime study periods respectively, for all LCZ study areas used in Phoenix.

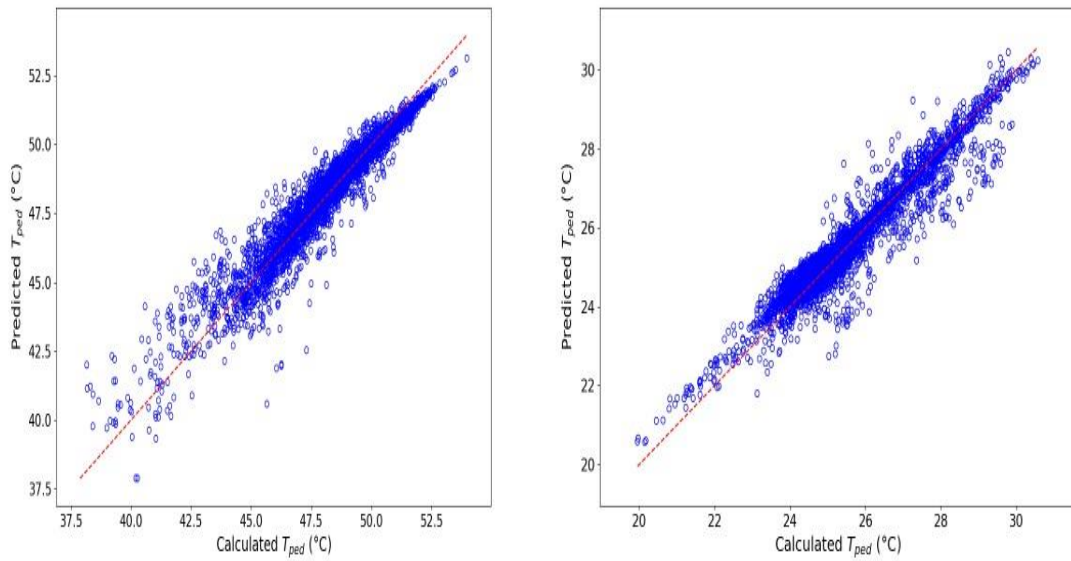


Figure 5. 23. Regression model for predicted and calculated a) daytime T_{ped} and b) nighttime T_{ped} for 100m x 100m spatial domain of all LCZ combined. The dashed red line is the 1:1 line.

These models were created by combining all the predictor variables in all four study areas. The resulting predicted T_{ped} were then plotted with the combined calculated T_{ped} from all the study areas. The higher R^2 values in Table 5. 6 shows that the models perform well in predicting T_{ped} .

Table 5. 6. Regression model statistics for daytime and nighttime for 100m x 100m spatial domain of all LCZ.

-	R ²	Adjusted R ²	RMSE	MAPE	MAE	Int.	λ_p	Wall area	T _{plan}
Daytime	0.92	0.92	0.67	0.99	0.47	14.1	-4.5	-0.0009	0.73
Nighttime	0.9	0.9	0.45	1.2	0.31	3.1	4.7	-0.0002	0.89

Comparing Table 5. 5 to Table 5. 6 provides an opportunity to assess the performance and differences between the unified multiple regression model presented in Table 5. 6 and the LCZ-specific regression models outlined in Table 5.6. By critically examining the statistics presented in both tables, we can gain insights into the effectiveness of the unified model and its advantages over the LCZ-specific models. Starting with the coefficient of determination (R²), we observe that the R² values in Table 5. 6 for both daytime and nighttime are slightly lower compared to the R² values in Table 5. 5 for the LCZ-specific models. This indicates that the LCZ-specific models explain a slightly higher proportion of the variance in T_{ped} within their respective study areas compared to the unified model. However, the differences in R² values are relatively small, suggesting that the unified model still captures a substantial amount of the variance in T_{ped} across multiple study areas.

Examining the root mean square error (RMSE) values, we find that the RMSE values in Table 5. 6 for both daytime and nighttime are comparable to or slightly higher than the RMSE values in Table 5. 5. This implies that the unified model has similar or slightly higher average deviations between the predicted and actual T_{ped} values compared to the LCZ-specific models. However, the differences in RMSE values are relatively small, suggesting that the unified model still provides accurate predictions of T_{ped} across multiple study areas.

In terms of MAPE, we find that the MAPE values in Table 5. 6 for both daytime and nighttime are generally lower compared to the MAPE values in Table 5. 5. This indicates

that the unified model has a smaller average percentage deviation between the predicted and actual T_{ped} values compared to the LCZ-specific models. This suggests that the unified model provides more accurate predictions in terms of percentage deviation across multiple study areas.

While the unified model may have slightly lower R^2 values and comparable or slightly higher RMSE values compared to the LCZ-specific models, it demonstrates the ability to generalize predictions across multiple study areas. These advantages make the unified model a more versatile and efficient approach for predicting T_{ped} , considering the broader context of urban areas.

5.5 Advancing T_{ped} Predictions with Versatile Multiple Regression Models.

The two multiple regression models that have been developed for predicting daytime and nighttime pedestrian temperature, across different Local Climate Zones as shown in Figure 5. 24 and their regression statistics in Table 5. 6 certainly provide beneficial insights. However, they are not without their limitations. For example, these models are strictly applicable to the four LCZs used in this study because the thermal data used for this study is constrained to these four LCZs. Therefore, the ability to use these models to predict T_{ped} does not extend beyond these areas. This limits its generalizability and application for other LCZ. Furthermore, the models are also time-restricted. They can only predict T_{ped} at the specific times of the day when the thermal data for these four LCZs was gathered, as indicated in Table 2. 1 . This inability to project beyond the time frame of data collection further limits the models' versatility and usefulness for other important times, especially during the day. In light of these limitations, data are needed that can represent a more comprehensive range of hours during both daytime and nighttime. This would enable prediction of T_{ped} at various times throughout the day and night, enhancing the temporal scope. While remotely observed surface temperatures, especially using high resolution airborne remote sensing, provide valuable insights into

the spatial variability of surface temperatures, it inherently only offers a snapshot view of the surface temperature at the precise moment the data is collected. This transient nature of thermal data limits our understanding of the diurnal cycle. On the other hand, a numerical model has the capacity to generate surface temperatures consistently throughout the day, providing a more holistic picture of the diurnal cycle. This allows regression models to be developed for a wider range of times in a day, or times across a year. In this section, data is extracted from the numerical modeling of surface temperatures conducted by Stewart et al. (2021) for Phoenix. Stewart et al. (2021) charted the disparities between T_{ped} and T_{plan} for LCZ 2, 6, and 8, as depicted in Figure 1. 3. Their groundbreaking research offered the first intensive studies on relevant incomplete temperatures for thermal comfort. From their input conditions and modelled outputs, T_{plan} , λ_p , the sum of wall areas, and the solar zenith angle are extracted. Their T_{ped} calculated from numerically modelled surface temperatures for walls and ground surfaces are also extracted. The solar zenith angle was incorporated in the regression to account for the influence of time, which influences surface temperatures and the relative differences between vertical and horizontal surface temperatures through the diurnal variation of incident solar radiation. To ensure we were capturing the most pertinent times of the day for our study, our selection of zenith angles was synchronized with the crossing times of the MODIS and Landsat 8 satellites. This decision was primarily influenced by the fact that T_{plan} is a vital variable in predicting T_{ped} . Among the various methods of estimating T_{plan} , in urban areas, the use of data from MODIS, and Landsat 8 and 9 satellites is most prevalent among researchers due to the spatial resolution and frequency of data acquisition these satellites provide.

Landsat satellites have a local overpass time of approximately 10:00 (+/- 15 min), while MODIS-Terra has a crossing time around 10:30, though this can drift towards earlier times and MODIS-Aqua has a crossing time of 13:30 (Earthdata. (n.d.); NASA. (n.d.), USGS. (n.d.)). For nighttime, Landsat satellites generally have a crossing time about 12 hours after their daytime crossing, or a local time of approximately 22:00. The MODIS-Terra and Aqua overpass times are also 12 hours after their daytime overpass, 22:30 and 01:30 respectively.

Consequently, the zenith angles for daytime were chosen to correspond with solar times from 10:00 to 14:00, while the nighttime zenith angles were selected to align with solar times from 22:00 to 02:00. The choice of extending the zenith angle range in daytime until 14:00 accounts for any potential variations from the standard 13:30 crossing time for MODIS-Terra. A similar extension is applied at nighttime until 02:00.

Figure 5. 24 shows the results from applying single regression models for both daytime and nighttime to the numerically modeled data.

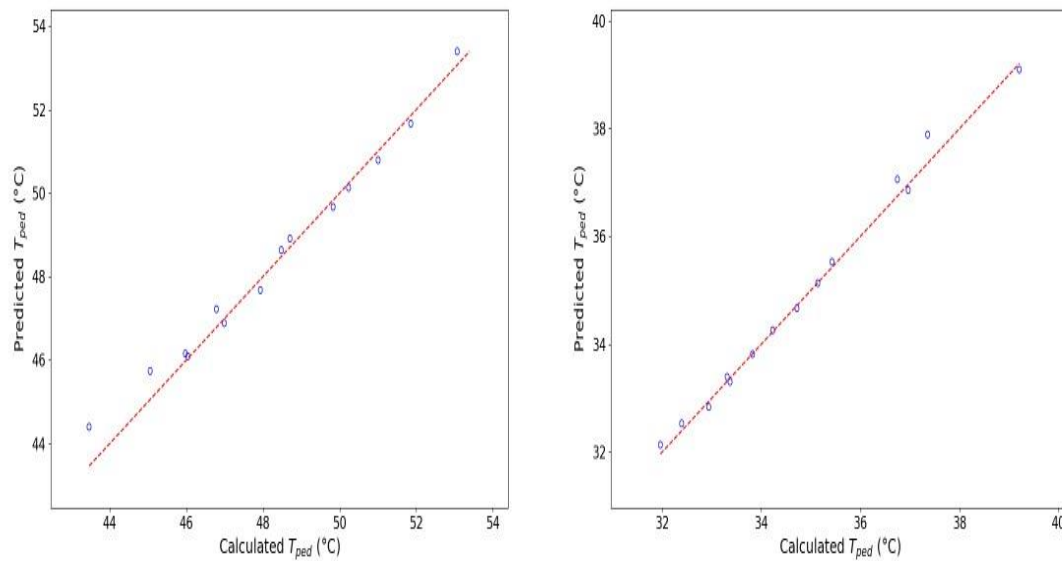


Figure 5. 24. Regression model predicted and calculated a) daytime T_{ped} and b) nighttime T_{ped} from TUF-3D simulation based on data from Stewart et al. (2021). The dashed red line is the 1:1 line.

Table 5. 7. Regression model statistics for daytime and nighttime from TUF-3D

-	R ²	Adj. R ²	RMSE	MAPE	MAE	Int.	λ_p	Wall area	T _{plan}	Zenith Angles
Daytime	0.995	0.993	0.37	0.61	0.29	8.47	-8.01	-0.0015	0.8	0.08
Nighttime	0.998	0.997	0.18	0.37	0.13	-0.42	4.63	0.002	0.98	-0.005

presents the regression model statistics for predicting daytime and nighttime pedestrian temperature (T_{ped}) using data from the TUF-3D simulation. These statistics provide crucial insights into the performance and accuracy of the regression models developed based on the numerical modeling of surface temperatures. The coefficient of determination (R^2) values for both daytime and nighttime models in Table 5. 7 are exceptionally high. The daytime model achieves an R^2 of 0.995, indicating that it explains 99.5% of the variance in T_{ped} . Similarly, the nighttime model achieves an R^2 of 0.998, indicating an explanation of 99.8% of the variance. These high R^2 values signify that the regression models capture a significant portion of the variability in T_{ped} and exhibit a strong linear relationship with the predictor variables. The adjusted R^2 values in Table 5. 7 further support the models' performance. The adjusted R^2 values are slightly lower than the R^2 values but remain close, indicating that the models' explanatory power is not inflated by including excessive predictors. These adjusted R^2 values, 0.993 for daytime and 0.997 for nighttime, suggest that the models are robust and provide reliable predictions of T_{ped} . Examining the root mean square error (RMSE) values, we observe that both daytime and nighttime models exhibit exceptionally low values. The RMSE for the daytime model is 0.37, while for the nighttime model, it is even lower at 0.18. These low RMSE values indicate that, on average, the predicted T_{ped} values from the regression models deviate from the actual values by a small margin. The low RMSE values signify the accuracy of the models in capturing the true T_{ped} values and their ability to provide precise predictions. Mean absolute percentage error (MAPE) values in Table 5. 7 shed light on the percentage deviation between predicted and

actual T_{ped} values. Both the daytime and nighttime models exhibit impressively low MAPE values. The daytime model achieves a MAPE of 0.61%, while the nighttime model achieves an even lower MAPE of 0.37%. These low MAPE values indicate that the regression models have a high level of accuracy in predicting T_{ped} , with minimal percentage deviations.

5.6 Comparative Analysis of a Unified Multiple Regression Model for All LCZs and Versatile Multiple Regression Models for Advancing T_{ped} Prediction

The essence of multiple regression modeling is to establish an empirical relationship between multiple independent variables and a dependent variable. Two sections, Section 5.4 and 5.5 in the thesis introduce two distinct but interconnected approaches to modeling. The former addresses the creation of a singular, comprehensive model, while the latter elaborates on the establishment of versatile models that account for more extensive spatial and temporal variabilities.

Both sections fundamentally deal with the prediction of T_{ped} from T_{plan} using multiple regression models. Also, both sections utilize the same variables, such as T_{plan} , the sum of wall areas, and λ_p in their multiple regression models. Aside from that, both models from the two Sections 5.4 and 5.5 show high predictive power.

Table 5. 8. Comparisons of regression model based on observed data (Table 5. 6) and the regression model based on numerical data (Table 5. 7)

-	R ²	Adj. R ²	Int.	λ_p	Wall area	T _{plan}	Zenith Angle
Table 5. 6							
Daytime	0.92	0.92	10.45	14.1	-4.5	0.0009	-
Nighttime	0.9	0.9	3.1	4.7	-0.0002	0.39	-
Table 5. 7							
Error! Reference source not found.							
Daytime	0.995	0.993	8.47	8.01	0.0015	0.8	0.8
Nighttime	0.998	0.997	-0.42	4.63	0.002	0.98	-0.005

A major difference between models in the two sections lie in the data source. The observed data model in Section 5.4 is built on a combination of observed thermal data and numerical model, while the regression model in Section 5.5 incorporates data from the full numerical modeling of surface temperatures conducted by Stewart et al. (2021) for Phoenix. Another difference is the existence of spatial variabilities of surface temperatures in the observed data used to create the multiple regressions in Section 5.4. This made it possible to predict T_{ped} across 100m x 100m grids within the study areas. This generated more estimates of T_{ped} and T_{plan} that vary spatially. However, the full numerical model approach, (Section 5.5 does not incorporate any spatial variability, as

the model represents the average conditions expected at the scale of an LCZ and thus T_{ped} predictions apply to the LCZ scale only. This means that regression models in Section 5.4 can be used to predict T_{ped} for 100 x 100m domain of LCZ 5, 6 7 and 8, while the regression models in Section 5.5 can be used to predict T_{ped} for the whole of LCZ 2, 6 and 8. Another difference is that only the regression models in section 5.5 include the solar zenith angle, accounting for the influence of time and the diurnal variation of incident solar radiation. This addition to the models aims to enhance the temporal scope, making it applicable for a broader range of hours during both daytime and nighttime. Thus, while the regression models in section 5.4 can be used to predict T_{ped} for 100 x 100m domain of LCZ 5, 6 7 and 8, their applicability are only favorable for the time of the thermal data acquired for each LCZ in Table 2. 1. Regression models in section 5.5 can be used to predict T_{ped} for the whole of LCZ 2, 6 and 8 from 10am to 2pm (daytime) and 10pm to 2am (nighttime) periods.

5.7 Multiple Regression Models from Vancouver LI Area

The development of regression models, as presented in Sections 5.4 and 5.5 of the thesis, offers promising ways of predicting T_{ped} across a variety of Local Climate Zones (LCZs). In Section 5.4, the unified multiple regression model was combined from regression models for LCZ 5, LCZ 6, LCZ 7 and LCZ 8 to deliver a single, generalized model. While these models show accurate predictive capacity within the LCZs involved in its formulation, their performance has not yet been compared with models created from observed data from other distinct geographic and climatic contexts. This lack of comparative analysis leaves uncertainty regarding the model's ability to perform well in different regions, leaving its claim to universality untested. Therefore, the inability to ascertain statistical similarities with regressions from other areas calls into question the robustness and transferability of the model. Similarly, the regression models presented in Section 5.5 show accurate regression statistics, yet their dependence on specific input parameters, such as the T_{plan} derived from the TUF-3D urban energy balance model,

introduces another layer of complexity. Numerical models, while proficient in their capacity to generate consistent surface temperatures throughout the day, often lack the inherent spatial variability that actual field measurements present. Therefore, there is also the need to compare their regression statistics with the regression statistics of real world data. The multiple regression models in Figure 5. 24 and their regression statistics in **Error! Reference source not found.**, developed for predicting daytime and nighttime T_{ped} have been shown to work well. However, to help assess the applicability of these models more broadly, there is a need to test the models with predictor variables from other study areas not included in the model development.

The availability of data with the required characteristics – a spatial resolution able to resolve individual buildings and streets, and ideally, observations of wall surface temperatures along with the 3D building structural information – needed to calculate T_{ped} are rare. One such data set was collected by Voogt and Oke (1997) who studied the complete surface temperatures of three primary areas within the city of Vancouver, British Columbia, Canada. These areas included a light industrial area (LI) with warehouses and workshops, a downtown office/commercial zone with tall buildings (D), and a suburban residential neighborhood (R) with single-family dwellings. To test the regression models, data from the LI study region is used, which is available with the necessary ancillary information.

The study used two thermal remote sensing methods to collect thermal data from the three study areas. An airborne infrared thermal scanner (AGEMA 880 LWB) operating in the 8–14 mm waveband was mounted in a helicopter and used to obtain thermal images over each of the study areas from nadir and 45-degree off-nadir sensor angles. Three flights were made over the study area: mid-morning (1000 - 1100 Pacific Daylight Time), slightly after solar noon (1345 – 1430 PDT), and in the late afternoon (1705 – 1745 PDT) for the north-south and east-west street orientations of the LI area. The thermal imagery has a ground spatial resolution of approximately 1m x 1m for an individual pixel. Individual thermal images are composited into a single 1m spatial resolution image that covers the maximum extent of the study area possible based on the available images.

Wall temperatures were obtained using two observational approaches. Ground-based observations were made by an infrared thermometer mounted on a vehicle that traversed all streets of the study area. Measurements were made at a spatial interval of approximately 4.76 m (Voogt and Oke 1998). The non-scanning infrared radiometers used provide an integrated sample of the wall temperature over the instrument field of view; the distribution of temperatures is assessed to remove samples where the field of view is contaminated by ‘sky’ and/or when it is known to be in a location where measurements are not needed (e.g. intersections or open areas) and then provides an average value for each of the four wall-orientations in the study area. Wall temperatures from select buildings were also extracted from the off-nadir airborne thermal data by averaging the temperatures from digitized wall polygons. These temperatures are assigned to their respective buildings, providing some measure of spatial variability in the temperatures of a particular wall orientation. A 3D building database is also available for the study area, derived from digitizing building footprints from aerial photos and assigning building heights from inspection of the number of building floors and assigning heights as 3.7 m per floor. Datasets are available as 1 m spatial resolution raster datasets. Thus, these datasets provide suitable real world predictor variables to test the daytime regression model.

To calculate T_{ped} and T_{plan} for the three flight times from the LI area, a spatial filtering operation over the raster data layers with a 101m x 101m domain (user-defined spatial filters required use of an odd-numbered dimension), at a step size of 20m, was performed using Idrisi GIS software. Spatial filtering to obtain T_{plan} simply used the composite nadir thermal image for each flight as input. To obtain T_{ped} , the rasterized building database is used to link the wall temperature information to wall surface area. The rasterized building database is also used to specify the wall areas and λ_p inputs required in the regression modelling. Mask files are employed to remove surfaces (e.g. roofs) not part of the pedestrian surface definition from the analysis. The overall approach is consistent with the methods used to generate T_{plan} and T_{ped} values of the four study areas in Phoenix, as described in “Methods”

The results of the analysis in the form of plotted images, scatter plots and histograms for each flight time are shown from Figure 5. 25 to Figure 5. 33. These images confirm the

findings explained in Section 5.1, that is T_{plan} is higher than T_{ped} during the day. Also, wider spaces show higher T_{plan} while buildings closer together have lower T_{ped} . Moreover, the images from the three flights provide additional insights on the variations of T_{plan} and T_{ped} through time. For example, the maximum T_{plan} temperature value for the first flight was 34 °C while T was 29 °C. These temperatures increased to 44 °C and 37 °C respectively (flight 2). However, the maximum temperatures reduced to 38 °C and 34 °C respectively in flight 3.

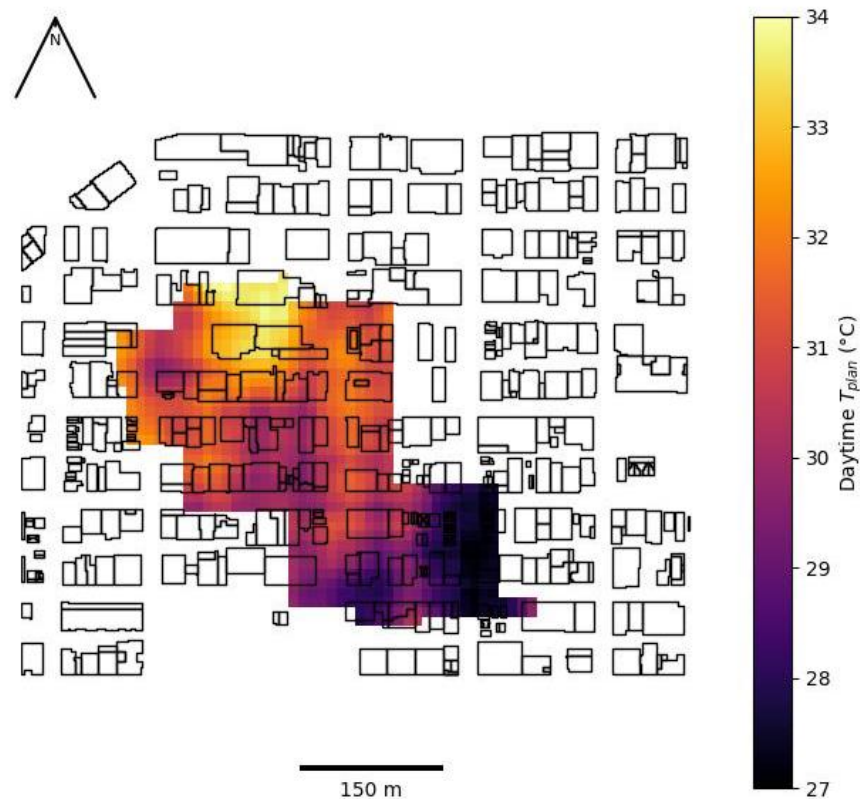


Figure 5. 25. Image of daytime T_{plan} for 101m x 101m domains flight 1 of Vancouver LI area.

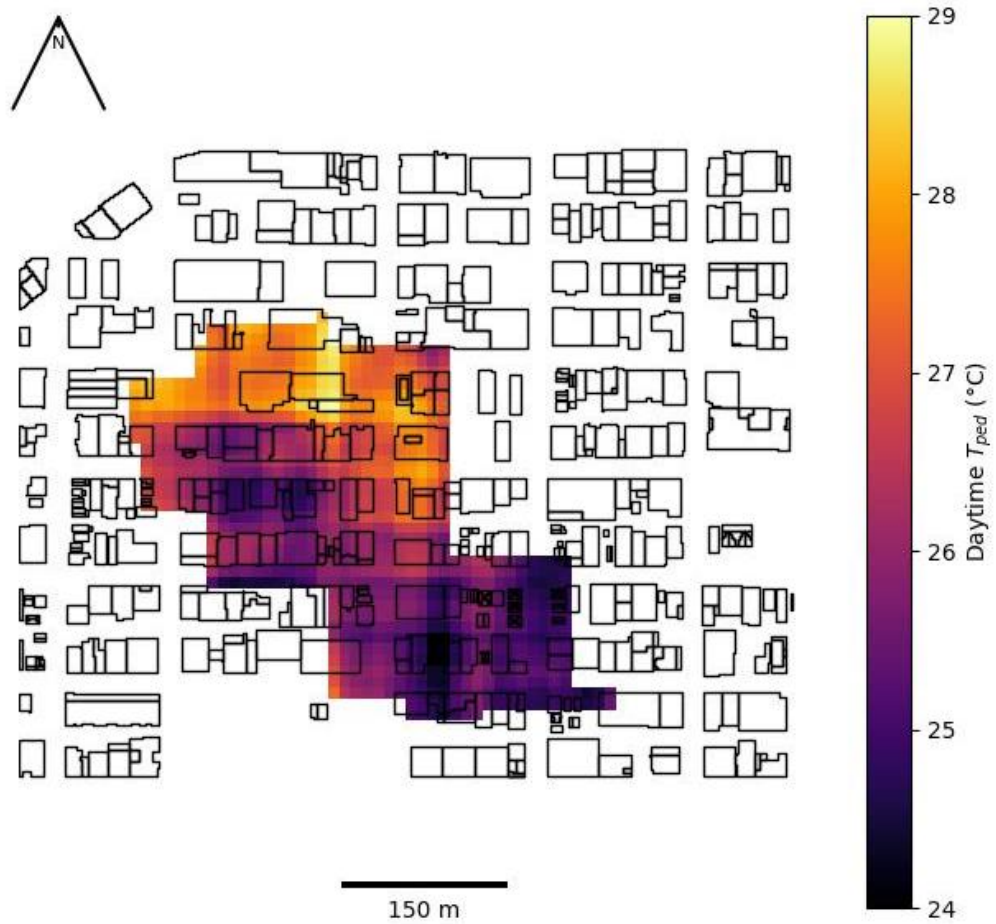


Figure 5. 26. Image of daytime T_{ped} for 101m x 101m domains flight 1 of Vancouver LI area.

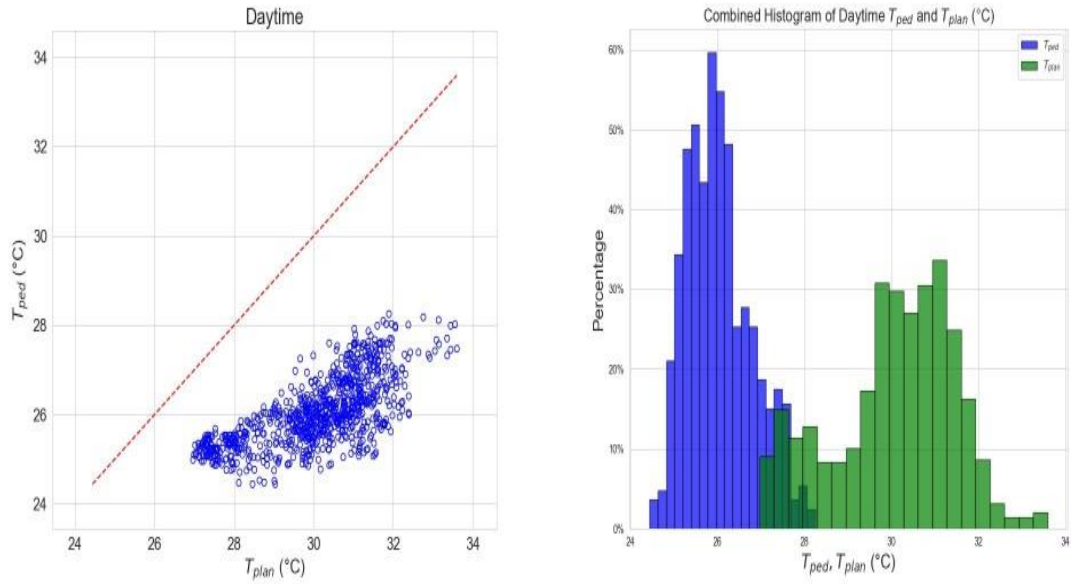


Figure 5. 27. a) Scatter plot and b) Histogram showing T_{ped} and T_{plan} for 101m x 101m domains flight 1 of Vancouver LI area.

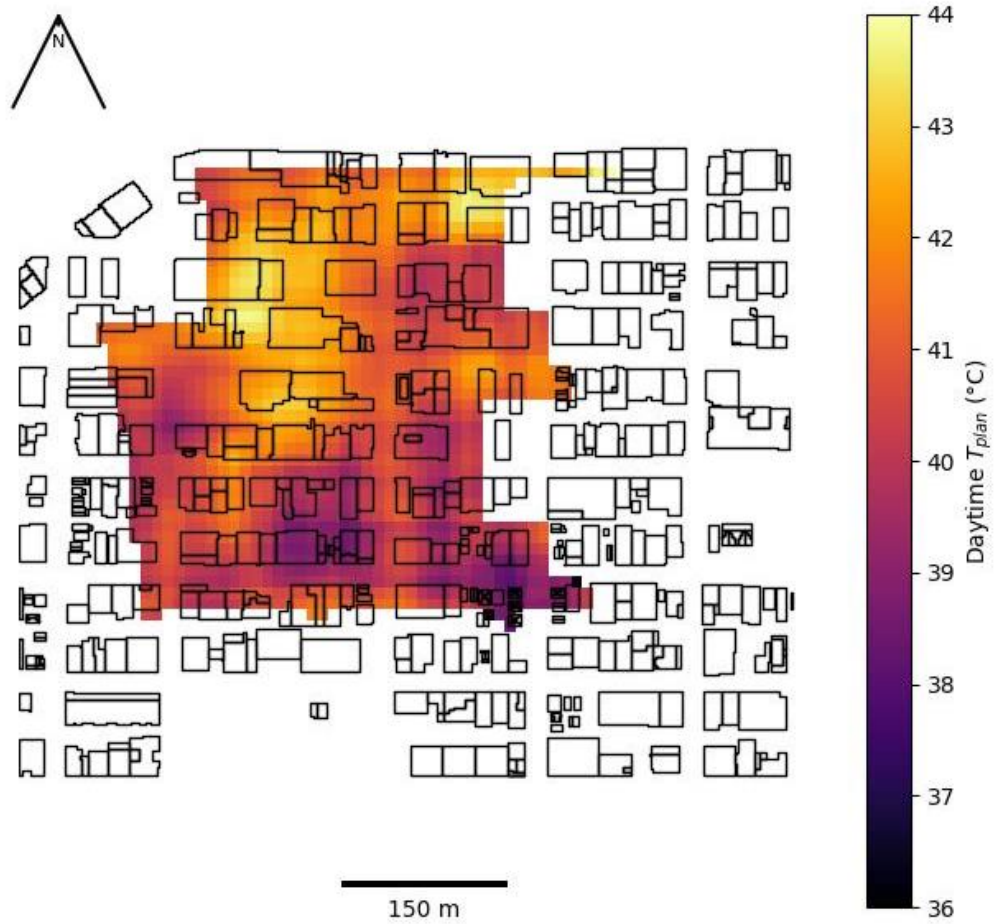


Figure 5. 28. Image of daytime T_{plan} for 101m x 101m domains flight 2 of Vancouver LI area.

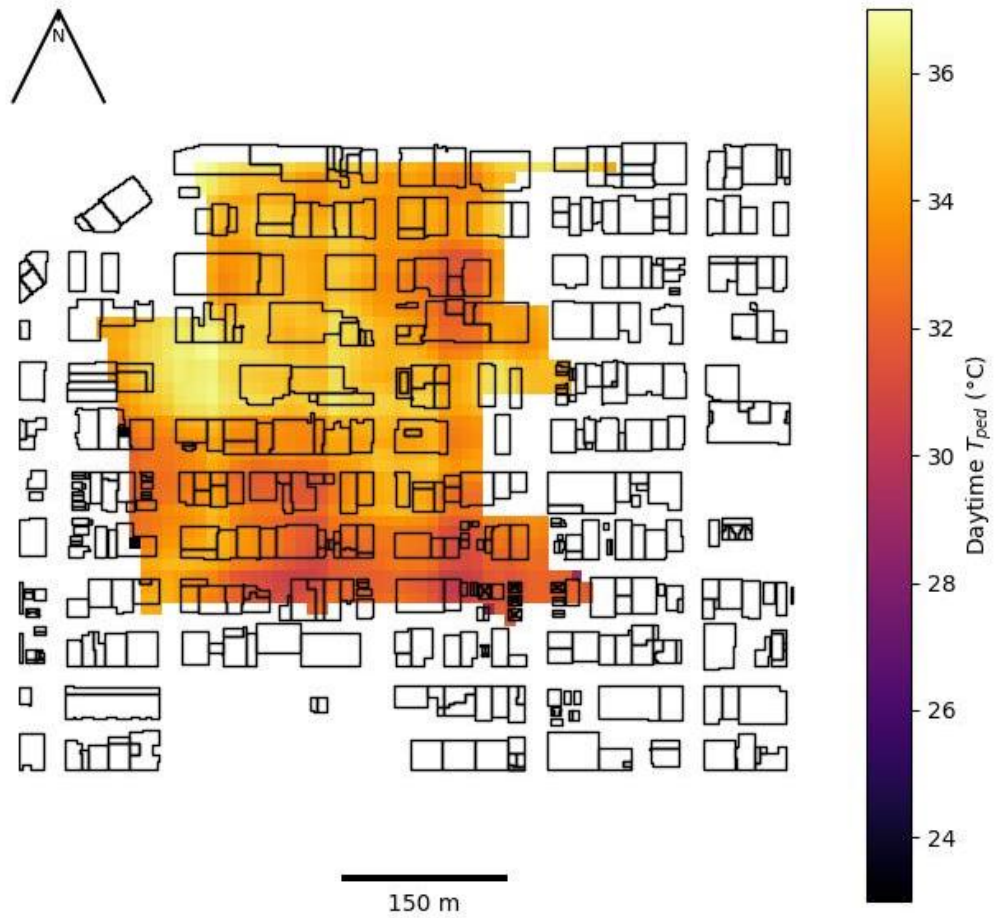


Figure 5. 29. Image of daytime T_{ped} for 101m x 101m domains flight 2 of Vancouver LI area.

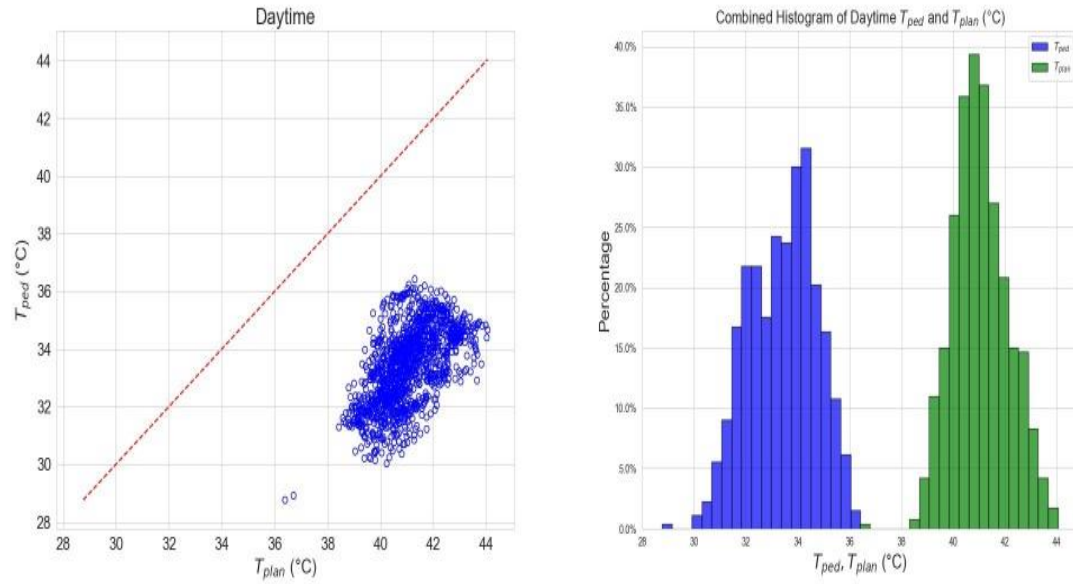


Figure 5. 30. a) Scatter plot and b) Histogram showing T_{ped} and T_{plan} for 101m x 101m domains flight 2 of Vancouver LI area.

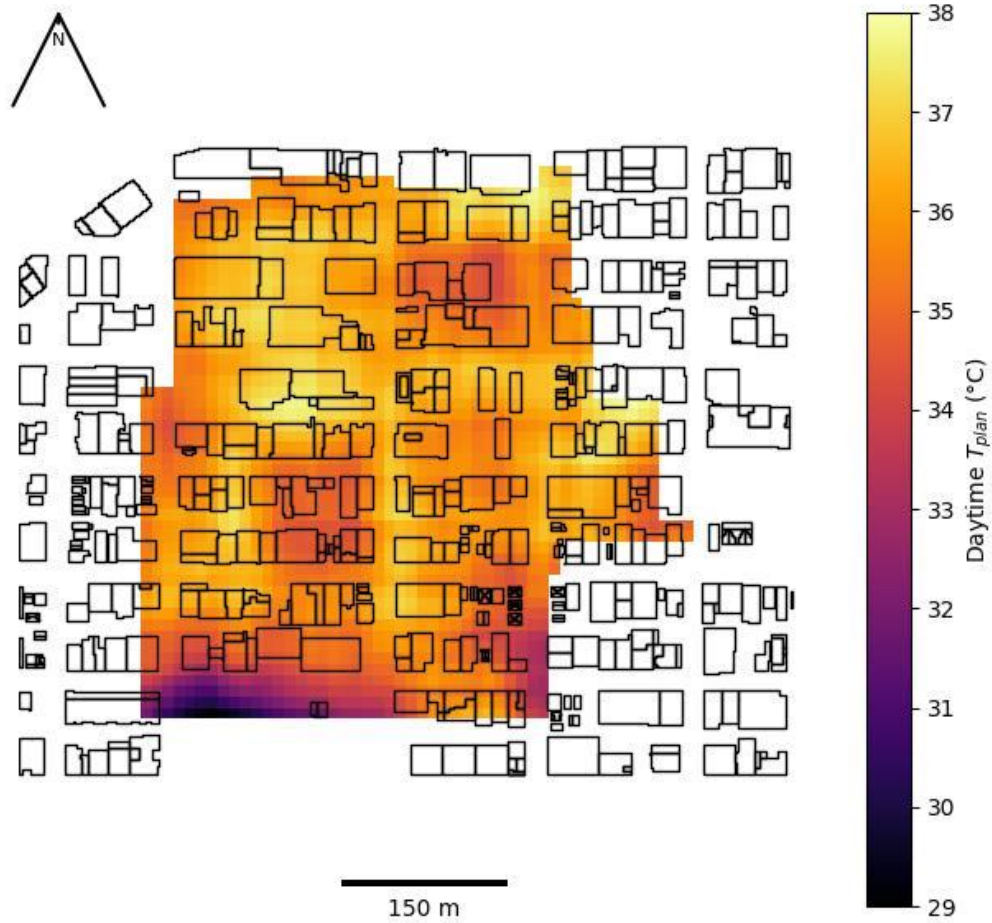


Figure 5. 31. Image of daytime T_{plan} for 101m x 101m domains flight 3 of Vancouver LI area.

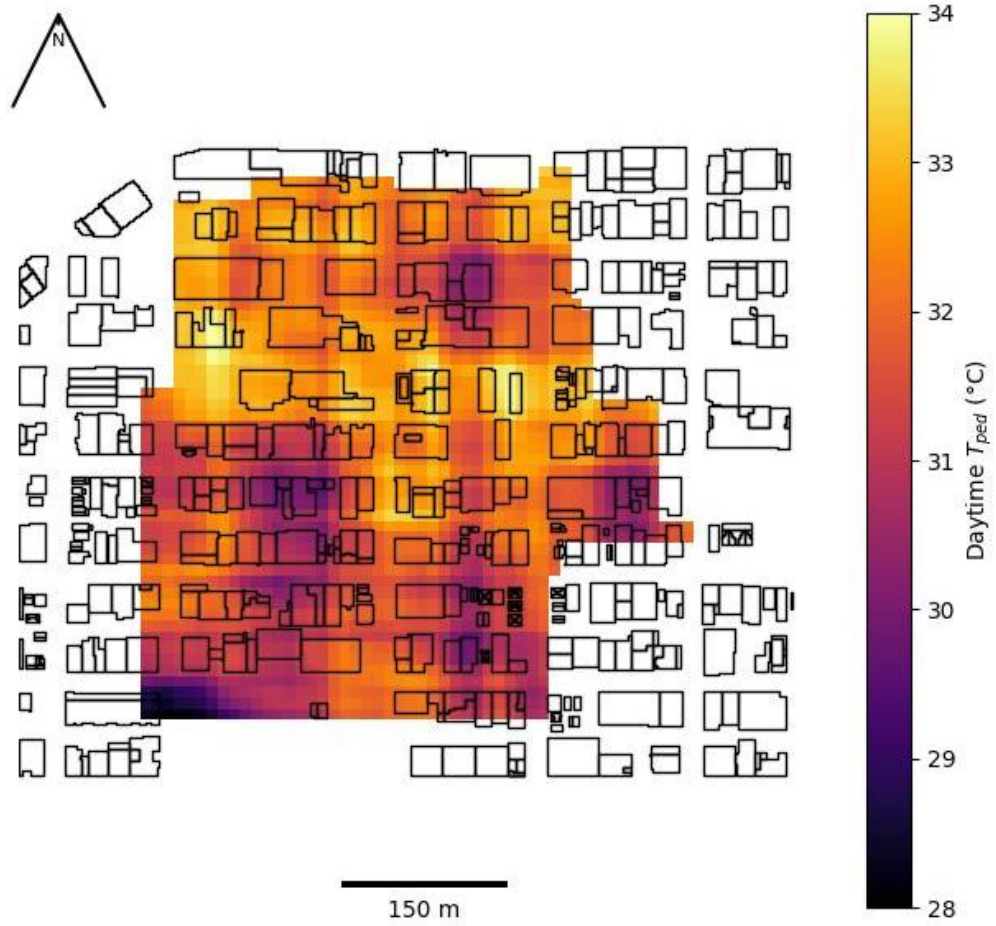


Figure 5. 32. Image of daytime T_{ped} for 101m x 101m domains flight 3 of Vancouver LI area.

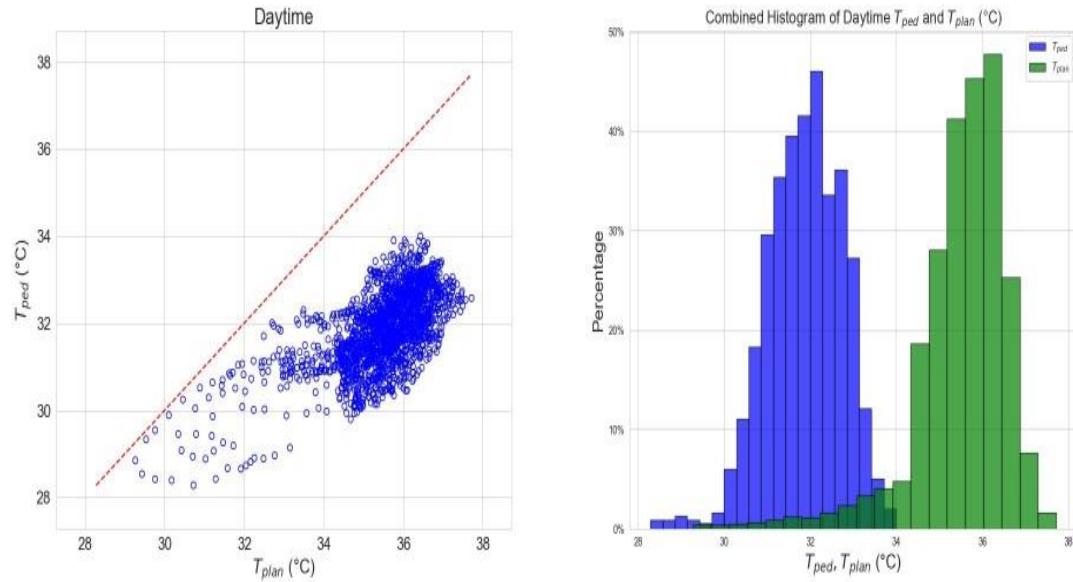


Figure 5. 33. a) Scatter plot and b) Histogram showing T_{ped} and T_{plan} for 101m x 101m domains flight 3 of Vancouver LI area.

Figure 5. 34 to Figure 5. 36 shows the linear regression plots for each flight, while Table 5. 9 shows the statistics for each flight

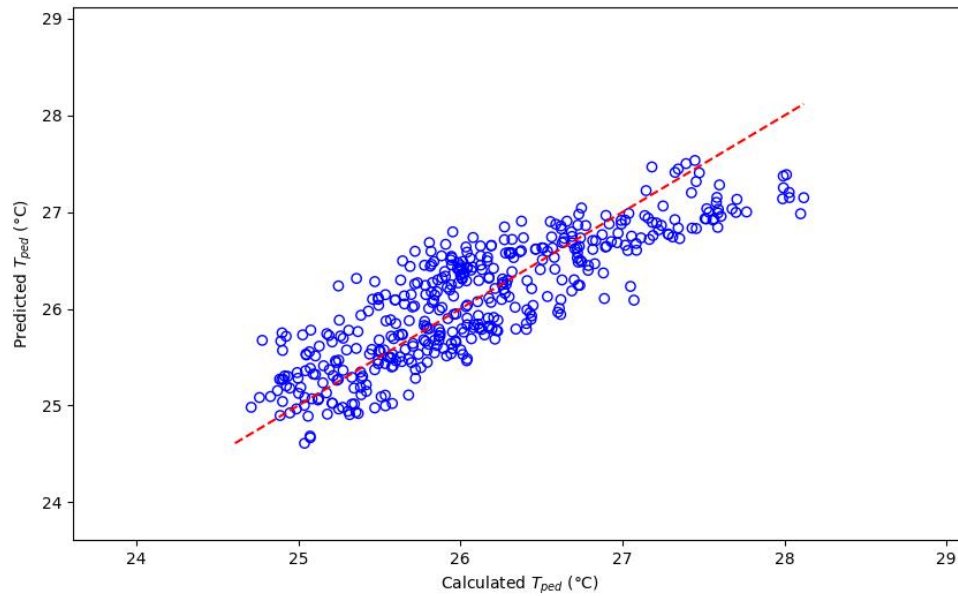


Figure 5. 34. Regression model predicted and calculated daytime T_{ped} 101m x 101m spatial domain of Vancouver LI area (Flight1). The dashed red line is the 1:1 line.

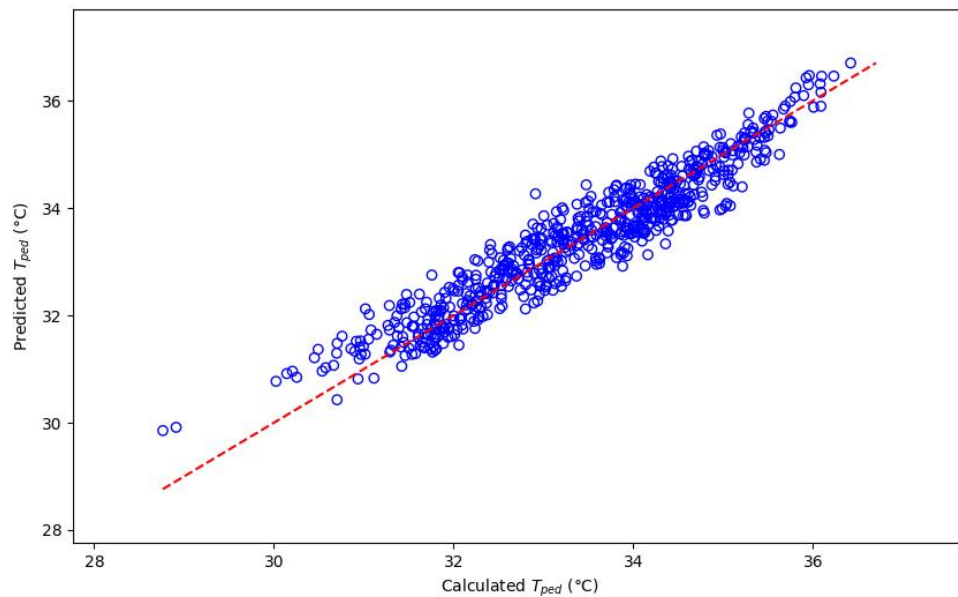


Figure 5. 35. Regression model predicted and calculated daytime T_{ped} 101m x 101m spatial domain of Vancouver LI area (Flight 2). The dashed red line is the 1:1 line.

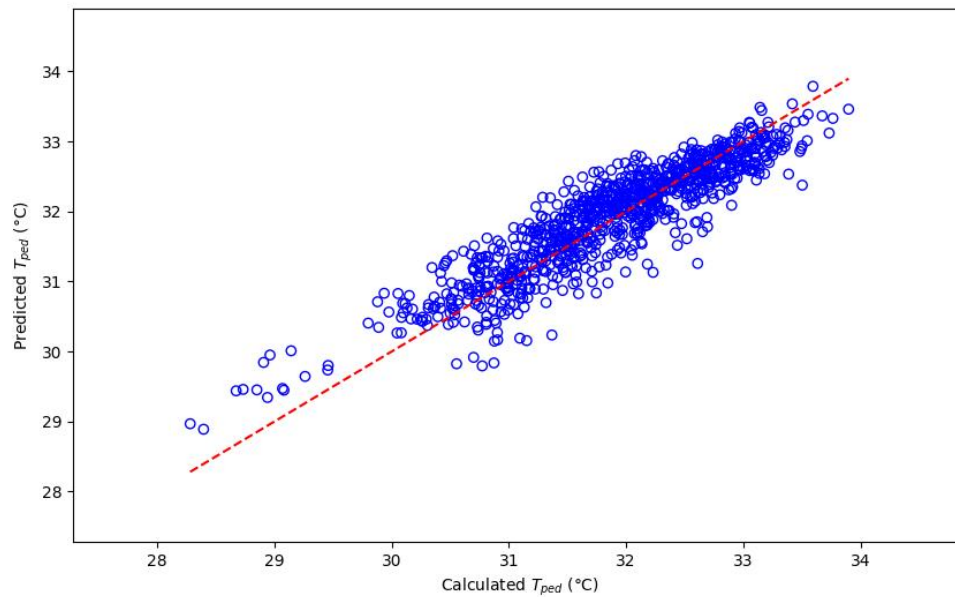


Figure 5. 36. Regression model predicted and calculated daytime T_{ped} 101m x 101m spatial domain of Vancouver LI area (Flight 3). The dashed red line is the 1:1 line.

Table 5. 9. Regression model statistics for each flight.

Flight	R^2	Adj. R^2	RMSE	MAPE	MAE	Int	λ_p	Wall area	T_{plan}	Zenith angle
Flight 1	0.7	0.7	0.4	1.26	0.33	0	-5.41	-0.0001	0.48	0.13
Flight 2	0.9	0.91	0.41	0.99	0.33	0	-8.93	-0.0009	0.6	0.19
Flight 3	0.8	0.81	0.36	0.9	0.29	0	-6.57	-0.0001	0.81	0.12

Flight 2 demonstrates the highest R^2 and adjusted R^2 values, indicating the strongest relationship between the predictor variables and T_{ped} . This flight also exhibits the lowest RMSE and MAPE values, suggesting the smallest prediction errors and highest accuracy among the flights. Flight 3 follows closely, with slightly lower R^2 and adjusted R^2 values, but still performs well overall. Flight 1 shows relatively lower statistics compared to the other flights, implying a slightly weaker relationship between the predictor variables and T_{ped} . There were no intercept values in each model. This may imply that the models do not exhibit any inherent bias.

Data from all three flights were combined to also create a single linear regression model, which is shown in Figure 5. 37 and its regression statistics in Table 5. 10. The discontinuity in the points in Figure 5. 37 from 28 °C to 30 °C suggests that there were no T_{ped}/T_{plan} pixel values with those temperatures.

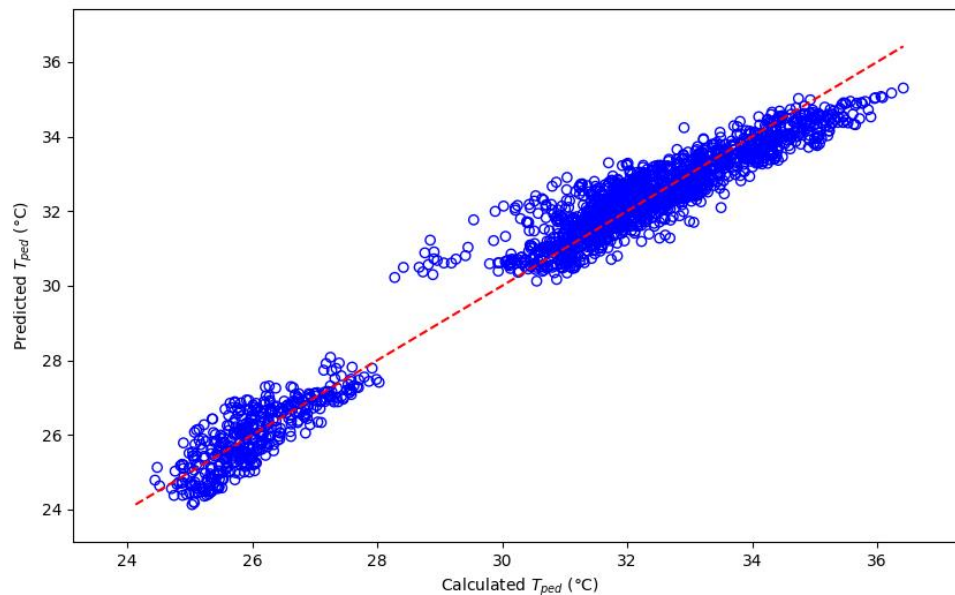


Figure 5. 37. Regression model predicted and calculated daytime T_{ped} 100m x 100m spatial domain of Vancouver LI area (flight 3). The dashed red line is the 1:1 line.

Table 5. 10. Regression model statistics for the combined flight data.

-	R ²	Adj. R ²	RMSE	MAPE	MAE	Int	λ_p	Wall area	T _{plan}	Zenith angle
Daytime	0.97	0.97	0.4	1.26	0.33	17.9	-6.38	-0.0003	0.57	-0.05

Comparing Table 5. 9 to Table 5. 10 reveals important insights into the performance of the regression models. The individual flight models (Table 5. 9) demonstrate good performance, with each flight exhibiting satisfactory R² values and relatively low prediction errors. However, the combined flight model (Table 5. 10) outperforms the individual flight models. The R² and adjusted R² values in the combined model increase significantly to 0.97, indicating a stronger relationship between the predictor variables and T_{ped}. The RMSE value remains consistently low, suggesting small prediction errors. However, it is worth noting that the MAPE value in the combined model is slightly higher compared to the individual flights, indicating a moderate level of accuracy.

5.8 Discussion

Many linear regression models have been developed for many areas in this study. All these regression models can be used to predict T_{ped} in each of their study areas. This section discusses the similarities and differences between these models, and the comparisons of these models to more advanced methods of pedestrian thermal comfort assessments.

5.8.1 Comparing the Multiple Regression Models from Phoenix with Regression Models from Other Study Areas

The comparative analysis of **Error! Reference source not found.** and Table 5. 10, as shown in Table 5. 11, highlights the strengths and characteristics of regression models for predicting T_{ped} . The regression models developed from the TUF-3D simulations performed by Stewart et al. (2021) demonstrate exceptional performance in capturing the temporal variability in T_{ped} , providing highly accurate predictions. On the other hand, the regression models based on real-world data exhibit strong relationships and reasonable accuracy, considering the inherent spatial variability of field measurements. However, when comparing the coefficients and intercepts from both models, they are very different, and therefore the model Phoenix is not transferrable to Vancouver.

Table 5. 11. Regression statistics from linear regression models for Phoenix and Vancouver LI

LCZ 5	R2	Adj. R2	RMSE	MAPE	MAE	Inter.	λ_p	Wall area	T_{plan}	Zenith Angles
Daytime	0.92	0.92	0.81	1.44	0.63	22.23	-7.28	-0.0008	0.58	
Nighttime	0.9	0.9	0.49	1.38	0.37	6.81	3.56	-0.0004	0.76	
LCZ 6										
Daytime	0.896	0.895	0.6	0.99	0.46	14.4	-6.99	-0.0007	0.71	
Nighttime	0.77	0.77	0.46	1.39	0.34	4.5	3.67	-0.0002	0.82	
LCZ 7										
Daytime	0.932	0.932	0.41	0.6	0.29	9.23	-2.84	-0.0008	0.8	
Nighttime	0.911	0.91	0.42	0.98	0.26	0.43	5.8	-0.0003	0.99	
LCZ 8										
Daytime	0.81	0.81	0.68	0.99	0.46	18.57	-1.89	-0.008	0.63	
Nighttime	0.89	0.89	0.4	1.12	0.28	2.59	6.18	-0.0005	0.92	
Phoenix (TUF-3D)										
Daytime	0.995	0.993	0.37	0.61	0.29	8.47	-8.01	-0.002	0.8	0.08
Vancouver										
Daytime	0.97	0.97	0.4	1.26	0.33	17.9	-6.38	-3.00E-04	0.57	-0.05

Similarly, when comparing the combined model for daytime for Phoenix, and the combined model for daytime Vancouver, they also show different intercepts. However, comparing the daytime scatter plots for LCZ 6 (Figure 5. 8) and the scatter plots for the three flights for Vancouver (Figure 5. 27, Figure 5. 30, and Figure 5. 37) give us an exciting insights on the spatio temporal behaviours of T_{ped} . The points on Figure 5. 8 extends upwards from closer to T_{plan} (x axis) towards the identity line. This means that T_{plan}/T_{ped} differences reduces as the points move towards the identity line. As already explained, the points are nearer to the identity line shows areas where there were little to no buildings. Thus the amount of shading on the grounds and cooler wall temperatures were little to none, making T_{ped} behaving like T_{plan} . However, when compared with (Figure 5. 27, Figure 5. 30, and Figure 5. 37, very few points in Figure 5. 37 were a bit closer to the identity line. This means that the buildings are more tightly packed together in Vancouver LI area. This shows that spatially, areas with wider spaces in between will have lower number of T_{plan}/T_{ped} differences at different parts of the larger area, while areas with their buildings tightly packed will have high T_{plan}/T_{ped} differences at different part of the larger area. Thus, areas with building more tightly packed together are more thermally comfortable. In addition, comparing Figure 5. 27, Figure 5. 30, and Figure 5. 37, provies us some additional insights to the temporal behaviour of T_{ped} . It can be seen from Figure 5. 27 that, at lower temperatures, some points were a bit closer to the identity line. However, these points went further away from the identity line in Figure 5. 30. These points became more closer to the identity line in Figure 5. 37. This shows that, in the early morning, T_{plan}/T_{ped} differences are smaller. However, these differences increase rapidly with T_{plan} becoming hotter during the afternoon. However, these differences reduces rapidly closer to the evening.

Moreover, comparing the intercepts and coefficients of each model in Table 5. 11 it can be seen that none of them are similar to each other, even though they all perform very well in predicting T_{ped} for their study areas, according to the RMSE, MAE and the other performance metrics. This means that it is difficult to transfer the model from one study area to another.

There could be several reasons for the non transferability of the model. Below are some possible reasons:

Differences in the geometry of buildings in different study areas: The differences in the geometries of buildings in different study areas affect the models created for that area. For example, The model in **Error! Reference source not found.** was originally developed from outputs from TUD-3D. these outputs in turn came from specific inputs for each in Phoenix. It is possible that this may have resulted in the differences of intercept and coefficients as compared to the regression from Vancouver.

Phoenix, located in the Sonoran Desert, has a hot desert climate. It is characterized by extremely high summer temperatures, a high degree of sunlight, low humidity, and minimal precipitation. The urban infrastructure in Phoenix is designed and built to cope with these conditions. For example, materials used in construction might be chosen for their ability to withstand intense sun and heat, buildings may be designed with cooling in mind. As all these may have impacted the input parameters used for each LCZ simulations by Stewart et al (2021). Vancouver, in contrast, has an oceanic climate. It experiences mild, often damp winters and warm to hot, dry summers. Its climate is heavily influenced by its proximity to the Pacific Ocean and the North Shore Mountains. Vancouver's urban development, including its building designs, materials, vegetation cover, have all adapted to these specific climatic conditions. Comparing a model developed in the context of Phoenix's hot desert climate to Vancouver's significantly different climate environment could yield inaccurate predictions. A model's predictive capabilities are inherently tied to the conditions for which it was developed. Variables important in Phoenix, like the type and color of building materials, the amount of shade provided by vegetation, might not have the same level of impact in Vancouver. Thus, the unique climatic and environmental conditions of Vancouver could mean that the patterns and relationships captured by the model in Phoenix do not hold true in Vancouver, contributing to the model's poor predictive performance.

This also holds true when the models from the observed data for each LCZ are compared with each other, and the models created for Vancouver. Each study area has its own building geometry.

Existence of spatial variabilities in observed data:

Indeed, the difference in spatial resolution between the observed data for Vancouver and TUF-3D model used to create the regression model might have contributed significantly to the differences in the coefficients of both models. The observed data for Vancouver had a high spatial resolution of 1 meter per pixel, which provided highly detailed and localized information about temperatures across different surface types, such as roofs, ground, and vegetation. In contrast, the numerical model from which the regression model was derived, had inherent limitations in its spatial capabilities. Firstly, TUF-3D is not capable of predicting vegetation temperatures. Secondly, the output parameters such as T_{plan} and T_{ped} from TUF-3D were calculated for the entire LCZs (ie, LCZ 2, 6, and 8), rather than specific, localized areas. As a result, the model lacked the high spatial variability present in the observed data. For instance, T_{plan} and other input parameters that were used to train the regression model, were calculated for each 100m x 100m domain for each flight area in the observed data. This level of granularity was not reflected in the numerical model. Therefore, the predictive performance of the model may have been negatively impacted by this disparity. It suggests that a regression model derived from a numerical model that calculates temperatures for entire LCZs may not be well-suited to predicting temperatures at a more localized scale (100m x 100m domains) in a distinct environment like Vancouver. The specificities of local climate and environment, which are captured in the observed high-resolution data, may not be fully accounted for in the regression model, leading to its observed poor performance.

Influence of unaccounted variables: Urban energy balance models, like TUF-3D, simulate the energy exchanges between different urban surfaces (such as buildings, streets, and vegetation) and the atmosphere. These models consider factors such as solar radiation, longwave radiation, sensible heat, latent heat, and heat stored in and released by urban surfaces. To accurately represent these energy exchanges, the model needs to be based on

certain assumptions and parameters that reflect the characteristics of the urban area being simulated. This includes factors like making assumptions on input parameters including λ_p , thermal and radiative parameters, albedo, and emissivity. However, these parameters and assumptions are unlikely to perfectly represent any real-world urban area. There will always be some level of error or uncertainty introduced due to factors like measurement error, simplifications made in the model, or temporal and spatial variability in the urban area's characteristics. For example, as shown in Figure 3. 1, TUF-3D assumes a simple array of 9 buildings for an urban structure, which is very different from the real world.

This discrepancy between the model's assumptions and reality could lead to inaccuracies in the model's intercept and coefficients. The regression model's assumptions and relationships, based on the energy balance model's outputs, might not accurately represent the energy exchanges happening in Vancouver's urban environment.

Differences in input LCZ.

The incorporation of multiple LCZs into a model may introduce a broader range of variability, leading to differences in the regression model's intercept and coefficients. For instance, each LCZ's unique microclimate dynamics could influence the model's calculations, leading to different intercepts and coefficients for the prediction of T_{ped} . Conversely, a model built predominantly on a single LCZ, like the Vancouver LI model, might exhibit a narrower range of variability and result in different coefficients and intercepts as it is tailored to represent the specific conditions of that LCZ. While it is true that the Phoenix model was also designed to predict T_{ped} for LCZ 6, the inclusion of LCZ 2 and LCZ 8 in the model's creation introduces additional parameters and influences. These added layers of complexity and variables likely result in differing coefficients and intercepts compared to a model based on a singular LCZ. Similarly, when the model for Vancouver had Zenith angles included in its creation, while the combined model, and also the models for the individual LCZ did not have Zenith angles included.

Differences in Meteorological conditions.

The meteorological conditions are also critical in determining the relationship between T_{plan} and T_{ped} . For example, it has already been explained in Section 4.1.4 that wind speed can affect surface temperatures. For instance, wind speed can significantly influence the energy balance of urban areas, affecting roof temperatures and potentially altering the relationship between T_{plan} and T_{ped} . If the wind speed in one area is different from another, it might affect the heat transfer between different urban surfaces and the atmosphere. As such, if the meteorological conditions, including wind speed, humidity, and air temperature, differ between the areas where data were collected, it would likely result in differences in the intercepts and coefficients of the regression models.

5.8.2 How T_{ped} Relates to More Advanced Measures of Pedestrian Thermal Comfort

Urbanization will continue to progress globally, and urban thermal comfort research will continue to advance improve the thermal comfort of urban residents. The building of urban environments, using concrete and steel in city environments, combined with anthropogenic heat production often results in rapid increase in urban temperatures, creating what are known as urban heat islands (Roth, 2012). Because climate change expected to increase the frequency and severity of heatwaves in cities, these urban heat islands pose serious health risks for city-dwelling populations (Kelbaugh, 2019). The thermal comfort of residents is a critical aspect in urban planning and design, and academic research studies.

In the assessment of outdoor thermal comfort in cities, many researchers have used a simple approach: the use of remotely sensed “plan” temperatures, or T_{plan} , derived from nadir view satellites and airborne data. This method is practical and cost-effective, providing large-scale temperature data for extensive urban areas. However, reliance on T_{plan} for thermal comfort analysis has its limitations. This study has indicated that this approach may lead to a significant overestimation of pedestrian thermal comfort by more than 8 °C. This discrepancy arises because T_{plan} includes the temperatures of rooftops, which tend to be

much warmer than pedestrian-level temperatures. This overestimation of pedestrian thermal comfort can distort our understanding of urban heat phenomena and impact the effectiveness of urban heat mitigation strategies.

To provide better estimates of outdoor thermal comfort in urban settings various indices and methods have been developed . The Universal Thermal Climate Index (UTCI) (Błażejczyk et al. 2013) and Mean Radiant Temperature (MRT) (Naboni et al. 2017) are two advanced measures commonly used in this field. These tools incorporate multiple weather variables to provide a holistic understanding of human thermal comfort in the urban environment. While these advanced measures provide valuable insights, there are logistical and economic challenges associated with their application, such as the need for specialized equipment and detailed meteorological data. The assessment of MRT and UTCI from observations are, however, a complex and time-consuming process. For instance, to determine the MRT for an individual in a street canyon via observations, a researcher must measure the total radiative heat load on the individual from all six surrounding surfaces, i.e., front, back, left, right, up, and down.

Hence, numerous researchers employ numerical models to forecast MRT. For example, many rely on the Solar and Longwave Environmental Irradiance Geometry (SOLWEIG; Lindberg et al. 2008) model to estimate the mean radiant temperature (MRT), as seen in the works of Aminipouri et al. (2019), Buo et al. (2023), Li, (2021), Lindberg & Grimmond (2011). Yet, the application of SOLWEIG is a difficult and lengthy process. The model requires meteorological forcing data including shortwave radiation, air temperature, and relative humidity. Urban geometry (typically from a Digital Surface Model - DSM), geographical information (latitude, longitude, and elevation), and continuous maps of sky view factors are also required to provide the surface characteristics. estimate MRT. Furthermore, to enhance the accuracy of the model, the researcher has to include both vegetation and ground cover information in the model (Lindberg et al. 2008).

In contrast, T_{ped} , while simpler than advanced measures like UTCI and MRT, could potentially improve urban thermal comfort assessments. The refinement of the T_{plan} approach offered by this research provides a pragmatic solution for researchers aiming to

maintain cost-effectiveness while ensuring a higher level of accuracy in their analysis. While it does not match the complexity and comprehensiveness of advanced measures like UTCI and MRT, this methodology represents an important step forward in the use of satellite-derived data for urban thermal comfort studies. By facilitating a more precise understanding of urban heat dynamics, it can better inform urban planning strategies and contribute to creating healthier, more comfortable urban spaces in an era of climate change.

6 Summary and Recommendations

This final chapter presents a conclusion and summary of the significant findings of this research, elucidates the responses to the research questions delineated in Section 1.5, discusses the relevance of this study, highlights the limitations of this study, and offers recommendations for future work .

6.1 Thesis Summary

One of the key challenges for cities as they face climate change is the higher urban temperatures that pose a present and future hazard for urban residents and infrastructure (Heaviside et al. 2017). Remotely sensed surface temperatures are a valuable data source for characterizing thermal conditions in cities. To improve the ability of using thermal remote sensing methods for understanding urban heat two areas of research need have been identified: First, is to critically study the relationship between surfaces seen by satellites and surfaces that are most relevant to human health. This is very important as many researchers depend on the use of T_{plan} measured from satellites including Landsat 8 and MODIS , to monitor heat patterns in urban areas (e.g. Sidiqi et al. 2016; Kaplan et al. 2018; Sagris & Sepp, 2017). However, the standard combination of rooftop and ground temperatures seen by these satellites from nadir represented in T_{plan} , are not the most appropriate combination of surfaces that should be used in assessing urban heat. In contrast, T_{ped} , the combination of walls and ground surface temperatures are a better match for the application of outdoor thermal comfort in urban areas. When T_{plan} is used instead of T_{ped} in daytime pedestrian thermal comfort analysis, researchers may be overestimating T_{ped} up to 8°C by day during the mid and late afternoons. This research was undertaken to study the spatio temporal variation of T_{ped} , the relevant incomplete temperature that affects

pedestrian thermal comfort. Another objective was to study how T_{ped} relates to T_{plan} , and the controls on that relation.

This research also aimed to create daytime and nighttime multiple regression models. These models were designed to incorporate T_{plan} , λ_p and the sum of wall areas to accurately predict T_{ped} . In essence, these models serve as practical tools through which researchers can generate more precise insights about urban heat while still leveraging the cost-effectiveness of T_{plan} data. By providing a systematic and robust method to predict T_{ped} from T_{plan} , this research offered a significant contribution to the urban climate study. Researchers can maintain the cost-effectiveness of their studies while ensuring a higher level of accuracy in their analysis. The outcomes of this research might also serve as a stepping stone for future studies aimed at refining these models further or incorporating additional variables for an even more comprehensive understanding of urban heat phenomena.

Acknowledging the practicality and economic factors of research, this study recognizes that many researchers will continue to rely on T_{plan} temperatures rather than on advanced measures of thermal comfort such as T_{mrt} or UTCI. T_{plan} data, predominantly derived from satellites like Landsat 8, are more accessible and cost-effective compared to other data sources, whereas the calculation of advanced measures of thermal comfort often require complex numerical models with high resolution characterization of surface structure and extensive input data. However, as demonstrated by this thesis, the reliance on T_{plan} potentially leads to an overestimation of pedestrian heat. This misrepresentation can skew our understanding of urban heat phenomena and, consequently, the strategies devised to mitigate them. To address this concern, the primary objective of this research was to provide a means for researchers to predict T_{ped} , a more accurate measure of urban heat for outdoor thermal comfort applications, from T_{plan} and some basic urban surface structure measures. This novel approach aimed to reconcile the cost-effective accessibility of T_{plan} data with the more accurate depiction of outdoor urban heat offered by T_{ped} .

6.1.1 Understanding the Relationship between T_{plan} and T_{ped} for both Day and Night.

At the start of this research, hypotheses were established in Section 5.1 on the relationship between T_{plan} and T_{ped} . It was postulated that during the day, pedestrian level temperatures (T_{ped}) should be cooler than plan temperatures (T_{plan}), attributing this to the cooling effects of building walls, building geometry, and vegetation, which significantly alter T_{ped} , in contrast to the inclusion of high roof temperatures in T_{plan} . Conversely, it was theorized that at night, T_{ped} should be warmer than T_{plan} due to the rapid cooling of roof temperatures, a result of their strong radiative cooling, insulation properties and lack of heat storage. The results show support for the hypothesis related to daytime conditions, as seen in Figure 5.8. During the day, T_{ped} is consistently cooler than T_{plan} . This observation was evident in the scatter plot, where data points deviate significantly below the 1:1 line. The likelihood of large differences increases with high values of T_{plan} . This phenomenon occurs because the hottest surfaces during mid-day are usually roofs. Hence, a spatial domain incorporating buildings with high roof temperatures and a large wall area could substantially reduce T_{ped} . In simpler terms, a larger roof area increases T_{plan} estimation, while a larger wall area decreases the T_{ped} calculation. However, at night, the results differed as illustrated in Figure 5.9. Most scatter plot points are above the 1:1 line for spatial domains that incorporate buildings. In this scenario, T_{ped} could be either warmer or cooler than T_{plan} , contradicting the initial hypothesis. Walls, especially compared to well-insulated and low albedo roofs, cool more slowly, thus becoming relatively warmer, drive the expectation for $T_{\text{ped}} > T_{\text{plan}}$ at night and this is observed for many, but not all points. The case of T_{ped} cooler than T_{plan} is also observed for a significant number of points. This situation could occur due to a grid cell being predominantly occupied by ground surfaces, which store heat better at night, along with some adjoining building walls, or from building roofs that may be anomalously warm. These findings challenge the initial assumption that nighttime T_{ped} would generally be warmer than T_{plan} , underscoring the complexity of urban thermal dynamics.

6.1.2 Daytime and Nighttime Regression Models to Predict T_{ped} .

By combining T_{ped} calculations for the four study areas in Phoenix, namely LCZ 5, LCZ 6, LCZ 7, and LCZ 8, the research created multiple regression models for daytime and nighttime (Figure 5. 23), providing researchers with statistical tools in Table 5. 6 to predict T_{ped} for any 100m x 100m domain within those specific LCZs. This prediction method relies on utilizing T_{plan} data obtained from satellite imagery, along with the parameters λ_p (a coefficient representing the influence of roof area on T_{ped}) and the sum of wall areas within the 100m x 100m domain.

It is important to note that the regression models used to create the predictive statistics were developed based on the observed data collected during the study. As a result, researchers can only reliably predict T_{ped} using these regression models within their specific study areas and within the time range covered by the observed data, as detailed in Table 2. 1. The predictive capability offered by these regression models and statistical tools represents a significant advancement in understanding and estimating T_{ped} in urban data and information about the local wall characteristics. This knowledge enables a more comprehensive assessment of pedestrian-level thermal comfort and can inform urban planning efforts to assess thermal comfort in urban environments. Researchers now have a framework to model T_{ped} values for various 100m x 100m domains within the specific study areas, based on readily available T_{plan} data and information about the local wall characteristics. This knowledge enables a more comprehensive assessment of pedestrian-level thermal comfort and can inform urban planning and design decisions. However, it is essential to recognize the limitations of these predictive models. As the regression models were developed using observed data from the specific study areas, applying them to other LCZ or time periods may lead to less accurate predictions.

In an effort to enhance the predictive capabilities of T_{ped} for a wider range of time, this research created additional regression models using data from the full model approach conducted by Stewart et al. (2021) for LCZ 2, LCZ 6, and LCZ 8. These additional regression models, depicted in Figure 5. 24, are presented in **Error! Reference source not found.** with their respective statistical values. These regression models add zenith angle to

the other predictors used and show that regressions remain stable for 4 hour windows during day and night that correspond to the overpass times of commonly used satellite data. However, it is important to note that even with the inclusion of these additional regression models, their applicability remains limited to the specific study areas and the time intervals mentioned. Applying these regression models to other LCZs or time periods may result in reduced accuracy and reliability. Researchers should exercise caution and evaluate the suitability and generalizability of these models when utilizing them beyond the specified study areas or temporal ranges.

The regression models were compared with each other in Table 5. 11. The objective was to compare the coefficients and intercepts of the models and assess the transferability of a model from one study area to another. Having similar coefficients and intercept would mean that a model created for one study area can potentially be used to predict T_{ped} in another study area.

However, the comparisons of their coefficients and intercepts, revealed differences in intercepts and coefficients between the two models. This means that more research is needed to help obtain a single model, that can be used to predict T_{ped} in multiple study areas.

6.2 Limitations Encountered.

This research has limitations that need to be acknowledged in order to interpret the findings accurately and to provide a comprehensive understanding of its implications. These limitations, although they may impact the generalizability and validity of the study, should not discount the potential contributions and insights gained from the research.

6.2.1 Temporal Limitations

Remotely observed data only provides a snapshot of surface temperature at a specific time and multiple overflights would be required to acquire the temporal resolution to capture diurnal variations. In contrast, numerical models offer a high temporal resolution, allowing for the depiction of surface temperature fluctuations throughout the day.

However, relying on observed data also posed limitations in terms of calculating T_{ped} precisely at the exact time when the thermal data was collected. Therefore, T_{ped} calculations for the study areas were made only for the times for each LCZ as shown in Table 2. 1. The assessment of T_{ped} here is also limited to the summer season so the ability for the observed data to show variations in the relation of T_{ped} to T_{plan} for different solar geometry conditions both diurnally and seasonally is restricted.

Furthermore, the consideration of the potential variation in the observed airborne data on different days is important to the reliability of this study. In an ideal scenario, all the data would have been collected on the same day to ensure uniform weather conditions. However, due to the size of the metropolitan area, and the logistical constraints inherent in airborne data collection, this was not feasible. This discrepancy may introduce a degree of uncertainty into the comparison of measurements between different days. One important assumption underlying the analysis is that weather conditions remained similar on the observation days. Preliminary analyses, as demonstrated in Chapter 2, indicate a general similarity in weather conditions across the observation days. The METAR data, coupled with other meteorological observations, underscore the consistent clear sky conditions, particularly during the nighttime observations. While there are inherent temporal variations in weather, the uniformity witnessed in our datasets suggests that any potential disparity is likely minimal.

6.2.2 Lack of Observed Wall Temperature Data

Another significant limitation of this study was related to the nature of the observed thermal data used. Although the airborne data had sufficiently high spatial resolution to allow

calculation of T_{ped} , it was limited to nadir view measurements. This meant that the observed data only provided information on rooftop and ground temperatures, excluding crucial data on wall temperatures. Wall surfaces play a crucial role in the calculation of T_{ped} and contribute to the overall thermal dynamics of urban environments. To address this limitation, the TUF-3D urban energy balance model was used to model wall temperatures, which were then combined with the ground temperatures obtained from the observed data to estimate T_{ped} . However, relying on a modeling approach to obtain wall temperatures introduced limitations. The accuracy of the modeled wall temperatures depend on various assumptions and input parameters used in the TUF-3D model, especially the wall thermal properties and thickness. Additionally, the complexity of urban environments and the heterogeneity of building materials and orientations presented challenges in accurately representing the thermal behavior of walls due to the simplicity by which TUF-3D represents the urban structure. Subdividing each LCZ into subareas characterized by their own structural and surface properties helps to provide some spatial variability into the estimates of wall surface temperature, but the ability to represent the actual wall temperature variability remains limited in the current approach and the lack of observed wall temperature data in the study areas limits the ability to evaluate modelled wall temperatures directly.

6.3 Future recommendations.

One major area needed in pedestrian thermal comfort assessment is the creation of a single model which can predict T_{ped} at different areas. Such a model, if feasible and accurate, could have profound implications for researchers relying on thermal data from satellites to predict T_{ped} , thereby expanding our understanding of urban microclimates and informing urban planning and design strategies. However, the findings of this study show that such a model will need further research on T_{plan}/T_{plan} differences and behaviours across different study areas. The complexities of different urban environments, shaped by a multitude of geographical, climatic, and human factors, thus far make it challenging to create a universal model that can accurately predict T_{ped} across diverse settings. These are some of the reasons

for the different regression model intercepts and coefficients (see section 5.8.1) Future researchers might consider adopting a more sophisticated modeling approach that harnesses the spatial variability of observed data, thereby addressing the shortcomings identified in this study. To refine the current model or build a new one, it is crucial to recognize the limitations of the data source. The TUF-3D numerical model, which was the basis for the model in Table 5.11, inevitably has its own constraints and assumptions that affect its output. These constraints may have indirectly influenced the performance of the model, resulting in a poor fit with the observed data.

Creating a more sophisticated T_{ped} prediction model that depends solely on observed data instead of numerical modelling, and possibly entailing using machine learning algorithms that can handle complex, non-linear relationships is recommended. More spatially and temporally resolved data at the microscale would also potentially improve the model's performance. Interest in collecting high spatial and temporal resolution data at microscale level in cities has also grown. For example, Murakami et al. (2019) studied the spatio-temporal behaviors of surface temperature at the microscale level in Sumida ward, Tokyo. Part of their research included an experiment that involved mounting a thermal camera on a tower. The thermal camera captured thermal images of the study area at 10 minute intervals from 10:00 to 18:00. Morrison and Grimmond (2021) also performed a similar study by using ground-based thermography to capture very high spatial resolution (0.5 to 2.5 meters) of their study sites in Borough of Islington in London, UK, with a temporal resolution of 5 minutes. And Jiang et al. (2018) estimated complete surface temperatures from directional radiometric temperatures.

By capturing the microscale spatio-temporal behaviors of surface temperature, these approaches provide a wealth of detailed information that can be used to improve the predictive accuracy and reliability of T_{ped} prediction models. Such data can help capture the temporal changes in T_{ped} and T_{plan} over the course of a day, accurately reflecting the impacts of local weather conditions, building characteristics, vegetation, human activities, and other urban factors. This is particularly crucial as urban microclimates can show substantial variability and complexity over short distances and periods. By monitoring microscale temperature variations throughout the day and night, researchers may be able

to better determine how T_{ped} responds to changes in T_{plan} , the time lag between peaks in T_{plan} and T_{ped} , or the influence of different building materials and designs on T_{ped} and T_{plan} . The incorporation of such detailed data can address some of the limitations identified in the model developed in this study.

An alternative potential strategy for providing data to further develop T_{ped} and T_{plan} relations would be to leverage the outputs from sophisticated energy balance models, such as ENVI-Met, to predict pedestrian level temperature. ENVI-Met, as a sophisticated urban microclimate model, provides a detailed representation of urban environments, including various microclimatic factors, thus addressing the limitation of high-resolution data acquisition.

The TUF-3D model was used in this study as it has been well tested and applied in other studies (eg. Krayenhoff and Voogt, 2007, Stewart et al. 2021). However, it presents some inherent limitations. As a simplified urban energy balance model, it fails to capture the full complexity and variability of real-world conditions. It is here that more sophisticated energy balance models like ENVI-Met demonstrate their strength.

Unlike TUF-3D, ENVI-Met and other advanced models account for a wide range of urban and environmental variables, such as vegetation, buildings, and different types of surfaces, thus making them more robust in reflecting real-world variability (Faragallah & Ragheb, 2022). Their detailed simulations offer a high level of precision, enabling a more accurate analysis of urban microclimates. As such, these models provide a practical alternative to traditional data collection methods, eliminating the need for costly remote sensor operations. However, the downside of these models is the complexities in their usabilities. Users of such models have to prescribe the spatial variations of the surface characteristics, which include the albedo, thermal properties, etc. therefore, even though the use of a complex energy balance model may generate a more accurate surface temperatures for T_{ped} assessments, they are also complex in their usage.

The third option to obtain high spatial resolution data for T_{ped} studies is the method of downscaling lower resolution thermal data from a satellite to a spatial resolution that allows separation of roof and road temperatures (Stathopoulou & Cartalis, 2009; Liu & Pu 2008;

Yoo et al. 2020; Zakšek & Oštir, 2012). Once the thermal data is downscaled, an energy balance model could then be used to generate the wall temperature.

In conclusion, trying to better understand the $T_{\text{plan}} - T_{\text{ped}}$ relation in order to obtain a single model to predict T_{ped} in many areas may require:

1. Use of better models (like ENVI-Met) but with better definition of the relevant surface properties that create spatio-temporal variations of surface temperature.
2. Use of high resolution observed data that can generate more datasets of observed T_{plan} and T_{ped} for different LCZs and for temporal variation, for both daily and also seasonal variations and different weather conditions.
3. The method of downscaling satellite data to a spatial resolution that allows separation of roof and road temperatures and then using a numerical model to prescribe the wall temperatures.

6.4 Conclusion

In light of the significant challenges posed by increasing urban temperatures due to climate change, this research has provided pivotal insights into the use of remotely sensed surface temperatures for characterizing thermal conditions within cities. The critical examination of the relationship between T_{plan} , predominantly derived from satellite platforms, and T_{ped} , which better represents human thermal comfort, has revealed the potential inaccuracies in depending on T_{plan} . The study emphasizes the potential risk of overestimating T_{ped} by as much as 8°C when relying on T_{plan} during the day. Through a combination of observed data and the TUF-3D model, the research has successfully formulated regression models that enable the prediction of T_{ped} from T_{plan} for specific Local Climate Zones (LCZs) in Phoenix. This provides a potential tool for researchers aiming to gauge urban heat while still benefiting from the cost-effectiveness of T_{plan} data. However, the restricted applicability of these models due to their basis on specific study areas underscores the necessity for further research to refine and generalize these predictive tools. The inherent

temporal limitations of this study highlight the need for additional high spatio-temporal observational data or for enhanced numerical models that can accurately capture diurnal and seasonal variations. This will help better define a more universal model to predict T_{ped} for any city.

References

- Adderley, C., A. Christen, J.A. Voogt, (2015). The effect of radiometer placement and view on inferred directional and hemispheric radiometric temperatures of an urban canopy. *Atmospheric Measurement Techniques*, **8**, 2699-2714.
- Aliabadi, A. A., Krayenhoff, E. S., Nazarian, N., Chew, L. W., Armstrong, P. R., Afshari, A., & Norford, L. K. (2017). Effects of roof-edge roughness on air temperature and pollutant concentration in urban canyons. *Boundary-Layer Meteorology*, 164(2), 249-279.
- Aminipouri, M., Knudby, A. J., Krayenhoff, E. S., Zickfeld, K., & Middel, A. (2019). Modelling the impact of increased street tree cover on mean radiant temperature across Vancouver's local climate zones. *Urban Forestry & Urban Greening*, 39, 9-17.
- Arizona State University. (2014). LiDAR-Derived 3D Building Footprints - metro-Phoenix, Arizona. Retrieved from <https://geodata-asu.hub.arcgis.com/datasets/lidar-derived-3d-building-footprints-metro-phoenix-arizona-2014/explore?location=33.456655%2C-112.134799%2C11.55>
- Allen, M. A., Voogt, J. A., & Christen, A. (2018). Time-continuous hemispherical urban surface temperatures. *Remote Sensing*, 10(1), 3.
- Adderley, C., Christen, A., & Voogt, J. A. (2015). The effect of radiometer placement and view on inferred directional and hemispheric radiometric temperatures of an urban canopy. *Atmospheric Measurement Techniques*, 8(7), 2699-2714.
- Buo, I., Sagris, V., Jaagus, J., & Middel, A. (2023). High-resolution thermal exposure and shade maps for cool corridor planning. *Sustainable Cities and Society*, 93, 104499.
- Bröde, P., Fiala, D., Błażejczyk, K., Holmér, I., Jendritzky, G., Kampmann, B., ... & Havenith, G. (2012). Deriving the operational procedure for the Universal Thermal Climate Index (UTCI). *International Journal of Biometeorology*, 56, 481-494.

Bechtel, B., Alexander, P. J., Böhner, J., Ching, J., Conrad, O., Feddema, J., ... & Stewart, I. (2015). Mapping local climate zones for a worldwide database of the form and function of cities. *ISPRS International Journal of Geo-Information*, 4(1), 199-219.

Błażejczyk, K., Jendritzky, G., Bröde, P., Fiala, D., Havenith, G., Epstein, Y., ... & Kampmann, B. (2013). An introduction to the universal thermal climate index (UTCI). *Geographia Polonica*, 86(1), 5-10.

Bechtel, B., Demuzere, M., Mills, G., Zhan, W., Sismanidis, P., Small, C., & Voogt, J. (2019). SUHI analysis using Local Climate Zones—A comparison of 50 cities. *Urban Climate*, 28, 100451.

Cotton, J. S. (2019). *Phoenix*. Weigl Publishers.

Chen, Y., Zheng, B., & Hu, Y. (2020). Mapping local climate zones using ArcGIS-based method and exploring land surface temperature characteristics in Chenzhou, China. *Sustainability*, 12(7), 2974.

Cao, Q., Huang, H., Hong, Y., Huang, X., Wang, S., Wang, L., & Wang, L. (2022). Modeling intra-urban differences in thermal environments and heat stress based on local climate zones in central Wuhan. *Building and Environment*, 225, 109625.

Davenport, A. G., Grimmond, C. S. B., Oke, T. R., & Wieringa, J. (2000, May). Estimating the roughness of cities and sheltered country. In: *Proceedings 12th Conference on Applied Climatology*, Asheville, NC, American Meteorological Society, Boston (pp. 96-99).

Earthdata. (n.d.). VIIRS Instruments Become More Essential as Terra and Aqua Drift from their Traditional Orbits. Retrieved from <https://www.earthdata.nasa.gov/learn/articles/modis-to-viirs-transition>

Faragallah, R. N., & Ragheb, R. A. (2022). Evaluation of thermal comfort and urban heat island through cool paving materials using ENVI-Met. *Ain Shams Engineering Journal*, 13(3), 101609.

Gustin, M., McLeod, R. S., Lomas, K. J., Petrou, G., & Mavrogianni, A. (2020). A high-resolution indoor heat-health warning system for dwellings. *Building and Environment*, 168, 106519.

Gál, T., Bechtel, B., and Unger, L. (2015). Comparison of two different Local Climate Zone mapping methods. Extended Abstracts, 9th Int. Conf. on Urban Climate/12th Symp. on the Urban Environment, Toulouse, France, Météo-France, 6 pp., www.meteo.fr/cic/meetings/2015/ICUC9/LongAbstracts/gd2-6-1551002_a.pdf.

Google Earth. (2022). Downtown Seattle [Screenshot of Google Earth Pro]. Retrieved from [Google Earth](#)

Heaviside, C., Macintyre, H., & Vardoulakis, S. (2017). The urban heat island: implications for health in a changing environment. *Current environmental health reports*, 4, 296-305.

Hook, S. J., Myers, J. J., Thome, K. J., Fitzgerald, M., & Kahle, A. B. (2001). The MODIS/ASTER airborne simulator (MASTER)—A new instrument for earth science studies. *Remote Sensing of Environment*, 76(1), 93-102.

Jiang, L., Zhan, W., Voogt, J., Zhao, L., Gao, L., Huang, F., ... & Ju, W. (2018). Remote estimation of complete urban surface temperature using only directional radiometric temperatures. *Building and Environment*, 135, 224-236.

Jenerette, G. D., Harlan, S. L., Buyantuev, A., Stefanov, W. L., Deplet-Barreto, J., Ruddell, B. L., ... & Li, X. (2016). Micro-scale urban surface temperatures are related to land-cover features and residential heat related health impacts in Phoenix, AZ USA. *Landscape Ecology*, 31(4), 745-760.

Jackson, T. L., Feddema, J. J., Oleson, K. W., Bonan, G. B., & Bauer, J. T. (2010). Parameterization of urban characteristics for global climate modeling. *Annals of the Association of American Geographers*, 100(4), 848-865.

Kelbaugh, D. (2019). *The urban fix: Resilient cities in the war against climate change, heat islands and overpopulation*. Routledge.

- Kong, F., Chen, J., Middel, A., Yin, H., Li, M., Sun, T., ... & Ma, J. (2022). Impact of 3-D urban landscape patterns on the outdoor thermal environment: A modelling study with SOLWEIG. *Computers, Environment and Urban Systems*, 94, 101773.
- Krayenhoff, E. S., Broadbent, A. M., Zhao, L., Georgescu, M., Middel, A., Voogt, J. A., ... & Erell, E. (2021). Cooling hot cities: A systematic and critical review of the numerical modelling literature. *Environmental Research Letters*, 16(5), 053007.
- Krayenhoff, E. S., & Voogt, J. A. (2007). A microscale three-dimensional urban energy balance model for studying surface temperatures. *Boundary-Layer Meteorology*, 123(3), 433-461.
- Kusaka, H., & Kimura, F. (2004). Coupling a single-layer urban canopy model with a simple atmospheric model: Impact on urban heat island simulation for an idealized case. *Journal of the Meteorological Society of Japan. Ser. II*, 82(1), 67-80.
- Lachapelle, J. A., Krayenhoff, E. S., Middel, A., Meltzer, S., Broadbent, A. M., & Georgescu, M. (2022). A microscale three-dimensional model of urban outdoor thermal exposure (TUF-Pedestrian). *International Journal of Biometeorology*, 1-16.
- Lagouarde, J. P., Moreau, P., Irvine, M., Bonnefond, J. M., Voogt, J. A., & Sollicec, F. (2004). Airborne experimental measurements of the angular variations in surface temperature over urban areas: case study of Marseille (France). *Remote Sensing of Environment*, 93(4), 443-462.
- Li, X. (2021). Investigating the spatial distribution of resident's outdoor heat exposure across neighborhoods of Philadelphia, Pennsylvania using urban microclimate modeling. *Sustainable Cities and Society*, 72, 103066.
- Lindberg, F., Holmer, B., & Thorsson, S. (2008). SOLWEIG 1.0—Modelling spatial variations of 3D radiant fluxes and mean radiant temperature in complex urban settings. *International journal of biometeorology*, 52, 697-713.

Lindberg, F., Holmer, B., Thorsson, S., & Rayner, D. (2014). Characteristics of the mean radiant temperature in high latitude cities—implications for sensitive climate planning applications. *International Journal of Biometeorology*, 58(5), 613-627.

Lindberg, F., & Grimmond, C. S. B. (2011). The influence of vegetation and building morphology on shadow patterns and mean radiant temperatures in urban areas: model development and evaluation. *Theoretical and Applied Climatology*, 105(3), 311-323.

Libraries at Arizona State University. (2017, September 12). Robust USGS LiDAR Data for Metro Phoenix Now Available. <https://lib.asu.edu/news/robust-usgs-lidar-data-metro-phoenix-now-available>

Li, X., Li, W., Middel, A., Harlan, S. L., Brazel, A. J., & Turner II, B. L. (2016). Remote sensing of the surface urban heat island and land architecture in Phoenix, Arizona: Combined effects of land composition and configuration and cadastral–demographic–economic factors. *Remote Sensing of Environment*, 174, 233-243.

Liu, D., & Pu, R. (2008). Downscaling thermal infrared radiance for subpixel land surface temperature retrieval. *Sensors*, 8(4), 2695-2706.

Malhi, Y. (1996). The behaviour of the roughness length for temperature over heterogeneous surfaces. *Quarterly Journal of the Royal Meteorological Society*, 122, 1095–1125.

Mapsofworld.com. (n.d.). Phoenix City Map, Arizona. Retrieved from <https://www.mapsofworld.com/usa/states/arizona/phoenix-city-map.html>.

[Map of Phoenix metro area - Phoenix metro area map \(Arizona - USA\) \(maps-phoenix.com\)](https://www.maps-phoenix.com)

Masson, V., Grimmond, C. S. B., & Oke, T. R. (2002). Evaluation of the Town Energy Balance (TEB) scheme with direct measurements from dry districts in two cities. *Journal of Applied Meteorology*, 41(10), 1011-1026.

- Masson, V. (2000). A physically-based scheme for the urban energy budget in atmospheric models. *Boundary-layer meteorology*, 94, 357-397.
- Matuzko, A. K., & Yakubailik, O. E. (2018). Urban heat island effects over Krasnoyarsk obtained on the basis of Landsat 8 remote sensing data. In: *IOP Conference Series: Earth and Environmental Science* (Vol. 211, No. 1, p. 012010). IOP Publishing.
- Middel, A., & Krayenhoff, E. S. (2019). Micrometeorological determinants of pedestrian thermal exposure during record-breaking heat in Tempe, Arizona: Introducing the MaRTy observational platform. *Science of the total environment*, 687, 137-151.
- Middel, A., Häb, K., Brazel, A. J., Martin, C. A., & Guhathakurta, S. (2014). Impact of urban form and design on mid-afternoon microclimate in Phoenix Local Climate Zones. *Landscape and urban planning*, 122, 16-28.
- Murakami, D., Yamagata, Y., Yoshida, T., & Matsui, T. (2019, July). Spatiotemporal heatwave risk modeling combining multiple observations. In *IGARSS 2019-2019 IEEE International Geoscience and Remote Sensing Symposium* (pp. 5516-5519). IEEE.
- Morrison, W., Kotthaus, S., & Grimmond, S. (2021). Urban surface temperature observations from ground-based thermography: intra-and inter-facet variability. *Urban Climate*, 35, 100748.
- Mushore, T. D., Odindi, J., & Mutanga, O. (2022). Controls of land surface temperature between and within Local Climate Zones: A case study of Harare in Zimbabwe. *Applied Sciences*, 12(24), 12774.
- NASA. (n.d.). Terra & Aqua Moderate Resolution Imaging Spectroradiometer (MODIS). Retrieved from <https://ladsweb.modaps.eosdis.nasa.gov/missions-and-measurements/modis/>
- Naboni, E., Meloni, M., Coccolo, S., Kaempf, J., & Scartezzini, J. L. (2017). An overview of simulation tools for predicting the mean radiant temperature in an outdoor space. *Energy Procedia*, 122, 1111-1116.

Ogimet. (n.d.). Professional information about meteorological conditions in the world. Retrieved from <https://www.ogimet.com/metars.phtml.en>

Oke, T. R. (2002). *Boundary Layer Climates*. Abingdon: Routledge, 1992.

Oke, T. R., Mills, G., Christen, A., & Voogt, J. A. (2017). *Urban Climates*. Cambridge University Press, Cambridge UK.

Oke, T.R. (1995). The Heat Island of the Urban Boundary Layer: Characteristics, Causes and Effects. In: Cermak, J.E., Davenport, A.G., Plate, E.J., Viegas, D.X. (eds) *Wind Climate in Cities*. NATO ASI Series, vol 277. Springer, Dordrecht.

Prata, A. J. (1996). A new long-wave formula for estimating downward clear-sky radiation at the surface. *Quarterly Journal of the Royal Meteorological Society*, 122(533), 1127-1151.

Reutebuch, S. E., Andersen, H. E., & McGaughey, R. J. (2005). Light detection and ranging (LIDAR): an emerging tool for multiple resource inventory. *Journal of forestry*, 103(6), 286-292.

Roth, M. (2012). -Urban Heat Islands. In: *Handbook of environmental fluid dynamics*, Volume 2 (pp. 162-181). CRC Press.

Roth, M., Oke, T. R., & Emery, W. J. (1989). Satellite-derived urban heat islands from three coastal cities and the utilization of such data in urban climatology. *International Journal of Remote Sensing*, 10(11), 1699-1720

Sagris, V., & Sepp, M. (2017). Landsat-8 TIRS data for assessing Urban Heat Island effect and its impact on human health. *IEEE Geoscience and Remote Sensing Letters*, 14(12), 2385-2389.

Seletković, A., Kičić, M., Ančić, M., Kolić, J., & Pernar, R. (2023). The Urban Heat Island Analysis for the City of Zagreb in the Period 2013–2022 Utilizing Landsat 8 Satellite Imagery. *Sustainability*, 15(5), 3963.

Shaffer, S. R., Chow, W. T., Georgescu, M., Hyde, P., Jenerette, G. D., Mahalov, A., ... & Ruddell, B. L. (2015). Multiscale modeling and evaluation of urban surface energy balance in the Phoenix metropolitan area. *Journal of Applied Meteorology and Climatology*, 54(2), 322-338.

Sidiqui, P., Huete, A., & Devadas, R. (2016, July). Spatio-temporal mapping and monitoring of Urban Heat Island patterns over Sydney, Australia using MODIS and Landsat-8. In 2016 4th International Workshop on Earth Observation and Remote Sensing Applications (EORSA) (pp. 217-221). IEEE.

Song, J., Wang, Z. H., Myint, S. W., & Wang, C. (2017). The hysteresis effect on surface-air temperature relationship and its implications to urban planning: An examination in Phoenix, Arizona, USA. *Landscape and Urban Planning*, 167, 198-211.

Stathopoulou, M., & Cartalis, C. (2009). Downscaling AVHRR land surface temperatures for improved surface urban heat island intensity estimation. *Remote Sensing of Environment*, 113(12), 2592-2605.

Stefanov, W.L. 2022. MASTER: RSL Airborne Campaign, Heat Island Study, Phoenix, Arizona, 2011. ORNL DAAC, Oak Ridge, Tennessee, USA.

<https://doi.org/10.3334/ORNLDAAC/1975>

Stefanov, W., A. Buyantuyev, S. Harlan, and D. Jenerette. 2015. MODIS/ASTER (MASTER) imagery and derived data in select neighborhoods of the greater Phoenix metropolitan area ver 1. Environmental Data Initiative.

<https://doi.org/10.6073/pasta/f97fbfa653ff0c2c351fe40a3803023b>.

Stewart, I. D., Krayenhoff, E. S., Voogt, J. A., Lachapelle, J. A., Allen, M. A., & Broadbent, A. M. (2021). Time Evolution of the Surface Urban Heat Island. *Earth's Future*, 9(10), e2021EF002178.

- Tan, C. L., Wong, N. H., & Jusuf, S. K. (2014). Effects of vertical greenery on mean radiant temperature in the tropical urban environment. *Landscape and Urban Planning*, 127, 52-64.
- Top, S., Milošević, D., Caluwaerts, S., Hamdi, R., & Savić, S. (2020). Intra-urban differences of outdoor thermal comfort in Ghent on seasonal level and during record-breaking 2019 heat wave. *Building and Environment*, 185, 107103.
- Tsou, J., Zhuang, J., Li, Y., & Zhang, Y. (2017). Urban heat island assessment using the Landsat 8 data: a case study in Shenzhen and Hong Kong. *Urban Science*, 1(1), 10.
- USGS. (n.d.). What are the acquisition schedules for the Landsat satellites? Retrieved from <https://www.usgs.gov/faqs/what-are-acquisition-schedules-landsat-satellites>
- Voogt, J. A., & Oke, T. R. (1997). Complete urban surface temperatures. *Journal of Applied Meteorology*, 36(9), 1117-1132.
- Voogt, J. A., & Grimmond, C. S. B. (2000). Modeling surface sensible heat flux using surface radiative temperatures in a simple urban area. *Journal of Applied Meteorology*, 39(10), 1679-1699.
- Voogt, J. (2021, July). Urban Heatwaves and Thermal Remote Sensing. In 2021 IEEE International Geoscience and Remote Sensing Symposium IGARSS (pp. 938-941). IEEE.
- Wang, C., Middel, A., Myint, S. W., Kaplan, S., Brazel, A. J., & Lukasczyk, J. (2018). Assessing local climate zones in arid cities: The case of Phoenix, Arizona and Las Vegas, Nevada. *ISPRS Journal of Photogrammetry and Remote Sensing*, 141, 59-71.
- Wieringa, J. (1986). Roughness-dependent geographical interpolation of surface wind speed averages. *Quarterly Journal of the Royal Meteorological Society*, 112(473), 867-889.
- Willmott, C.J. (1984). On the Evaluation of Model Performance in Physical Geography. In: Gaile, G.L., Willmott, C.J. (eds) *Spatial Statistics and Models. Theory and Decision Library*, vol 40. Springer, Dordrecht. https://doi.org/10.1007/978-94-017-3048-8_23

World Population Review. (2023). Phoenix, AZ Population 2023. Retrieved from <https://worldpopulationreview.com/us-cities/phoenix-az-population>

Yoo, C., Im, J., Park, S., & Cho, D. (2020). Spatial downscaling of MODIS land surface temperature: Recent research trends, challenges, and future directions. *Korean Journal of Remote Sensing*, 36(4), 609-626.

Zakšek, K., & Oštir, K. (2012). Downscaling land surface temperature for urban heat island diurnal cycle analysis. *Remote Sensing of Environment*, 117, 114-124.

Appendices

ASSESSING THE SPATIO-TEMPORAL BEHAVIOURS OF INCOMPLETE SURFACE TEMPERATURES USING GIS.

A.1 Horizontal Boundary Conditions Set-up

TUF-3D requires geometric, radiative, and thermal parameters of buildings

Radiative parameters include albedo and emissivity values for roofs, roads and walls. The MASTER data provides data for albedo values of roofs and roads of each neighborhood. These data will be used to specify the albedo for roofs and roads in the model. Thermal parameters include surface layer thickness, thermal conductivity, and volumetric heat capacity of roofs and walls of buildings and the road. The model requires the thermal parameters of four layers, from the outer surface layer to the inner surface layer, each of roofs, roads and walls. Each layer were estimated from Jackson et al (2010), who compiled building information including thermal and radiative properties for layers of roofs, walls and roads of different building types in different regions around the world by studying construction data by region and country, satellite imagery and other published building types for those regions, and previous surface temperature numerical modelling studies in Phoenix by Shaffer et al. (2015), Lachapelle et al. (2022), and Stewart et al (2021). Research findings from Jackson et al (2010) have been used in numerical simulation studies by previous researchers including Stewart et al (2021). Google Earth Desktop was used to study the visual appearances of buildings and roads in each study area, and the thermal and radiative properties of each study area were approximated from the recorded values in Jackson et al (2010). For example, Google Earth Desktop was used to check the material properties roads in each study area to determine whether they are asphalt or concrete roads. Thermal and radiative values for asphalt and concrete roads are then obtained from Jackson et al (2010). One main challenge faced in this process was the requirement of TUF-3D for four layers of each material property. The thermal and radiative properties of second, third and fourth layers of materials, which could not be assessed by Google Earth Desktop were

obtained by comparing values of those layers from Jackson et al (2010) with previous urban numerical modelling research studies in Phoenix by Lachappelle et al (2022) and Stewart et al (2021).

Below are simple descriptions of the geometric parameters:

- a. Building surface/plan ratio (λ_p): this is the ratio of the building plan area to the total plan area of the LCZ neighborhoods. The values for each LCZ were obtained from LiDAR data.
- b. Mean building height (Z_h): this is the average height of buildings in the neighborhood. These data were extracted from the LiDAR data.
- c. Building height to length ratio (H/L). This is calculated from the LiDAR data. This is calculated as mean building height/ mean building width.
- d. Canyon aspect ratio (λ_s): This is the ratio of the mean building height to the street width (H/W). The model automatically calculates this from (H/L) and λ_p .
- e. Reference height of meteorological forcing data (z_{ref}). This is twice the mean building height.
- f. Roughness length at neighborhood scale (Town z_0).
- g. Roughness length for road at neighborhood scale (Road z_0)
- h. Roughness length for roofs at neighborhood scale (Roof z_0)

The roughness length for each neighborhood (town z_0) is estimated from the simple rule of thumb approach which assumes a relationship between roughness length and building height give as $z_0 \approx 0.1x$ mean building height by Oke et al. (2017).

The roughness lengths for roads and roofs are estimated from Oke et al. (2017) and Davenport et al. (2000).

A.2 Vertical Boundary Conditions Set-up

TUF-3D requires meteorological forcing data to generate surface temperatures. These include barometric pressure, water vapor pressure, air temperature, wind speed, and incoming shortwave (solar) radiation ($K\downarrow$) and longwave radiation ($L\downarrow$). These data are normally obtained from meteorological stations situated in various parts of urban areas. The ideal situation would be to get these data for each LCZ neighborhood from individual meteorological stations situated in each neighborhood. Unfortunately, because each LCZ neighborhood does not have its own meteorological station, the alternative is to obtain the data from meteorological stations in Phoenix and adjust, where necessary, each parameter for each LCZ neighborhood. This alternative is acceptable because some parameters such as solar radiation (the most important determinant for surface temperature) will be the same across all neighborhoods during the clear sky conditions experienced during the airborne remote sensing period, and air temperature and humidity may not vary much across neighborhoods, particularly at a level two times above building height. In contrast, wind speed is expected to show more variation between different neighborhoods as surface geometries affect wind speed in particular. To account for this variation, the wind speed for each neighborhood can be estimated from some governing equations, shown later in this section.

Below are short descriptions of each parameter and how it was adjusted for each LCZ neighborhood:

Solar radiation ($K\downarrow$; $W m^{-2}$): measured data from the unobstructed meteorological station (2.5m above ground surface) will be used for all neighborhoods. Phoenix Encanto station however measures solar radiation in Langley. This were converted to $W m^{-2}$ using the equation below:

$$1 \text{ Langley} = 11.6300 \text{ Wm}^{-2}$$

Incoming longwave radiation ($L\downarrow$; $W m^{-2}$): This was estimated using the incoming longwave radiation equation for clear sky conditions from Prata's (1996);

$$L\downarrow = 1 - \left(1 + 46.5 \cdot \frac{e_a}{T_{air}}\right) \cdot \exp \left[- \left(1.2 + 139.5 \cdot \frac{e_a}{T_a}\right)^{0.5} \right] \cdot \sigma \cdot T_{air}^4 \dots\dots \text{Equation A. 1}$$

where;

e_a = water vapor pressure (hPa) value at the meteorological station;

T_{air} = screen level air temperature value (K) at the meteorological station;

σ = Stefan Boltzmann's constant, which is $5.67 \times 10^{-8} \text{ Wm}^{-2}\text{K}^{-4}$

Barometric (station) pressure (hPa): adjustments were needed to correct the elevation height differences between the meteorological measurement site and each neighborhood. Google Earth Pro was used to determine the elevation height of each neighborhood. The metadata provides the elevation height of the meteorological station. The hypsometric equation was used to change the barometric pressure at the elevation height of the station to the pressure at the height of each neighborhood using:

$$P_2 = P_1 \cdot \exp\left(\frac{z_1 - z_2}{A \cdot \bar{T}_v}\right) \dots \dots \dots \text{Equation A. 2}$$

where:

P_1 = barometric pressure (kPa) at the meteorological station;

P_2 = barometric pressure (kPa) at the study area;

z_1 = elevation height (m) at the neighborhood;

$$A = 29.3 \frac{\text{m}}{\text{K}}$$

\bar{T}_v = average virtual temperature (K) between the two elevation heights.

$$\bar{T}_v = \frac{T_{v1} + T_{v2}}{2} \dots \dots \dots \text{Equation A. 3}$$

where

T_{v1} = the virtual temperature at the meteorological forcing height.

T_{v2} = the virtual temperature at the study area.

$$T_v = T(1 + 0.61 \cdot r)$$

$$\text{and } r = 0.622 \cdot \left(\frac{e}{P_1 - e} \right)$$

where r = mixing ratio

e = actual vapor pressure (mb)

P_1 = barometric (station) pressure (mb)

Because it was assumed that the air is cooling adiabatically, the dry adiabatic lapse rate equation was used to get the air temperature value at the study area height. The mixing ratio of T_{v1} was assumed to be the same in order to solve T_{v2} .

Phoenix airport measure altimeter pressure (P_a) in inch per Instead of station pressure. Thus, the altimeter pressure was converted to station pressure in millibars (mb) according to :

$$P_1 = \frac{P_a \cdot \left(\frac{288 - 0.0065 \cdot h_m}{288} \right)^{5.2561}}{0.029530} \dots \dots \dots \text{Equation A. 4}$$

where:

P_a = altimeter pressure at the meteorological station in kPa;

h_m = elevation height (m) at the meteorological station.

The unit of barometric pressure to be forced in the model is in millibars (hPa).

Air temperature (°C): the correct measurement of air temperature needs to be done in the inertial sublayer (ISL), which provides a horizontally averaged air temperature value that represents the urban surface below it. The ISL is normally found at a height of 2 to 3 times the mean building height. As measurements of the air temperature at this height are not available, the air temperature measurement from the meteorological area was adjusted to obtain the air temperature at the ISL with the use of dry adiabatic lapse rate. The tallest mean building height of the sub-LCZ neighborhood was doubled and used to obtain the air temperature at the ISL. This value was then used to force the model for the sub-LCZ neighborhood.

The equation for dry adiabatic lapse rate is written as:

$$T_{isl} = T_1 - \Gamma[(z_{ref} - z_1) + (z_s - z_2)] \dots \dots \dots \text{Equation A. 5}$$

where:

T_{isl} = air temperature in the ISL (in °C);

T_1 = air temperature from the meteorological station (°C);

z_1 = sensor height (m) at the meteorological station (m);

z_2 = the elevation height at the meteorological station;

z_s = the elevation height at the study area;

z_{ref} = the reference height, or 2 times the mean building height.

Actual water vapor pressure [mb]: This was calculated by multiplying the saturated vapor pressure by the relative humidity. It is assumed that humidity will not change with the elevation height differences between the meteorological station and the study areas for dry conditions. Thus, this parameter was not adjusted for the elevation height differences.

Saturated vapor pressure was calculated using the air temperature value from the meteorological station:

$$e = e_s \cdot RH \dots \dots \dots \text{Equation A. 6}$$

Where;

e_s = saturated water vapor pressure (mb)

$$e_s = \frac{0.611 \cdot \exp\left[5423 \cdot \left(\frac{1}{273} - \frac{1}{T}\right)\right]}{0.1} \dots \dots \dots \text{Equation A. 7}$$

RH = relative humidity,

T = air temperature at the meteorological station in °C

Wind speed (U_m ; $m s^{-1}$): different neighborhoods have different values of wind speed according to the aerodynamic roughness of each neighborhood. This roughness can be represented by the roughness length of each neighborhood. The measured wind speed at the meteorological station was converted to the wind speed in each neighborhood, using the Wieringa (1986) equation:

$$U_m = U_s \cdot \ln\left(\frac{z_{ref}}{z_0}\right) \cdot \left[\ln\left(\frac{z_1}{z_0}\right)\right]^{-1} \quad \text{Equation A. 8}$$

Where:

U_m = wind speed at each neighborhood ($m s^{-1}$)

z_0 = roughness length at each neighborhood (m)

U_s = wind speed at the meteorological station ($m s^{-1}$)

z_1 = meteorological forcing height (m).

z_{ref} = the reference height at the sub LCZ level.

Wind direction : The model also needs hourly values of wind direction for the reference height.

The unit of wind direction to be forced in the model was in degrees from the north.

A.3 Sub-LCZ Spatial Variabilities

Even though the LCZ system classifies neighborhoods with similar characteristics including building heights and plan to area ratio, there are many other important factors that need to be considered in surface temperature studies. Different buildings within one LCZ with similar building heights may have different radiative and thermal parameters, which will result in varying surface temperatures. For example, buildings with the same height but different wall colors or different thermal conductivities may have different wall surface temperatures. Thus, these parameters needed to be taken into consideration in order

to generate more accurate surface temperatures of buildings. The best way to obtain wall temperatures of all the buildings in the four study areas is to simulate the model for each building in a study area by forcing the thermal and radiative parameters of each building in the model. Unfortunately, because there are many buildings in each study area which means it will take longer to simulate the model and generate wall temperatures for each building, a simpler approach was taken for this study. This involved further dividing the LCZ study areas into spatial variabilities which we call them as “sub areas (SA).”

One distinguishing characteristic of a SA within an LCZ is similar building type. For example, a SA may include only commercial buildings (warehouses, offices and other institutions), High density residential buildings (private buildings and apartments with few open spaces in between the building), or low-density residential buildings (smaller private homes with more open spaces in between the buildings).

Further characteristics that define a SA include similar height of buildings, presence of roof overhangs, plan to area ratio, and visual appearance of buildings including colors of rooftops and walls, thermal and radiative parameters, and wall paint colors for albedo and emissivity. The values of radiative and thermal parameters of walls within an SA were obtained as follows:

Google earth desktop software was used to visualize the appearance of all walls within an SA. The estimation of the wall albedo and emissivity were partially based on the physical parameters of the walls (eg, concrete, brick, etc), and the most common color paintings of walls within the SA. This method was also used to assess the wall materials to estimate the radiative and thermal parameters of the buildings in the SA. This is because the radiative and thermal parameters of concrete walls are different from that of glass or brick walls. Values that would correctly define the thermal and radiative parameters of walls were then obtained estimated values for different building materials from Oke et al. (2017) and Jackson et al. (2010). The model was then simulated for each SA over a range of albedo values, according to the number of color wall paintings.

A.4 Daytime and Nighttime T_{plan} and T_{ped} Estimations for Sub-Areas.

The tables below shows the calculated daytime and nighttime T_{ped} and T_{plan} for each SA in each LCZ.

Table A. 1. Variations of T_{ped} and T_{plan} temperatures for both daytime and nighttime for all SA, in LCZ 5.

SA	Daytime plan (°C)	Daytime Tped (°C)	Nighttime Tplan (°C)	Nighttime Tped (°C)
SA1	51.94	46.22	28.08	26.83
SA2	50.84	48.02	30.16	29.5
SA3	48.96	39.62	26.62	26.96
SA4	49.19	46.07	29.44	28.5
SA5	49.23	40.63	25.57	26.99
SA6	49.09	39.79	26.35	25.84
SA7	50.39	47.95	29.5	29.37
SA8	49.87	43.27	26.41	26.6
SA9	49.92	44.99	27.53	26.85
SA10	50.18	46.35	25.63	25.88
SA11	50.31	43.12	26.78	26.96
SA12	50.21	42.44	25.96	25.51
SA13	46.57	43.75	25.91	26.47
SA14	49.62	40.55	26.08	25.28
SA15	48.98	46.38	28.31	27.63

Table A. 2. Variations of T_{ped} and T_{plan} temperatures for both daytime and nighttime for all SA, in LCZ 6.

SA	Daytime plan (°C)	Daytime Tped (°C)	Nighttime Tplan (°C)	Nighttime Tped (°C)
SA1	48.41	45.6	22.1	23.07
SA2	50.69	47.3	24.63	24.68
SA3	47.54	45.88	24.21	24.21
SA4	50.33	46.44	24.43	24.97
SA5	49.43	45.43	23.83	25.52
SA6	50.49	45.94	24.02	23.79
SA7	54.38	48.17	23.93	24.36
SA8	52.96	48.85	24.26	24.87
SA9	52.8	47.92	23.35	23.65
SA10	51.14	48.38	23.88	24.57
SA11	52.54	50.83	24.27	24.42
SA12	52.7	49.08	24.15	25.06
SA13	53.0	48.2	23.93	24.47
SA14	52.56	47.9	25.01	25.5

Table A. 3 Variations of T_{ped} and T_{plan} temperatures for both daytime and nighttime for all SA, in LCZ 7.

SA	Daytime plan (°C)	Daytime Tped (°C)	Nighttime Tplan (°C)	Nighttime Tped (°C)
SA1	49.27	48.3	27.86	27.9
SA2	48.38	48.34	25.28	26.61
SA3	50.33	47.41	23.56	24.07
SA4	52.54	50.71	26.14	27.47
SA5	48.67	47.86	23.95	23.99
SA6	50.72	49.28	24.82	25.06
SA7	50.54	48.68	24.08	24.48
SA8	47.95	45.27	26.88	27.81
SA9	51.63	50.2	25.74	25.7
SA10	51.23	49.56	25.61	25.68
SA11	52.74	50.31	25.58	26.15
SA12	52.91	51.02	24.77	24.99
SA13	52.61	49.58	25.05	25.39
SA14	51.96	50.36	25.3	25.49
SA15	52.09	50.08	25.32	25.82

Table A. 4 Variations of T_{ped} and T_{plan} temperatures for both daytime and nighttime for all SA, in LCZ 8.

SA	Daytime plan (°C)	Daytime Tped (°C)	Nighttime Tplan (°C)	Nighttime Tped (°C)
SA1	47.98	45.96	23.69	24.22
SA2	49.7	46.13	25.68	25.49
SA3	48.23	46.97	25.23	26.11
SA4	47.97	47.01	25.63	26.12
SA5	48.75	46.4	24.14	24.55
SA6	51.33	47.07	24.3	25.39
SA7	51.93	47.48	23.86	23.77
SA8	52.34	48.96	24.64	24.31
SA9	48.91	45.91	23.7	24.72
SA10	52.07	48.36	24.32	24.95
SA11	48.89	47.41	25.86	26.11
SA12	49.81	47.18	23.9	25.03

A.5 Images of Building Heights in Each Study Area.

The images below show the height of each building (in meters) within each LCZ.

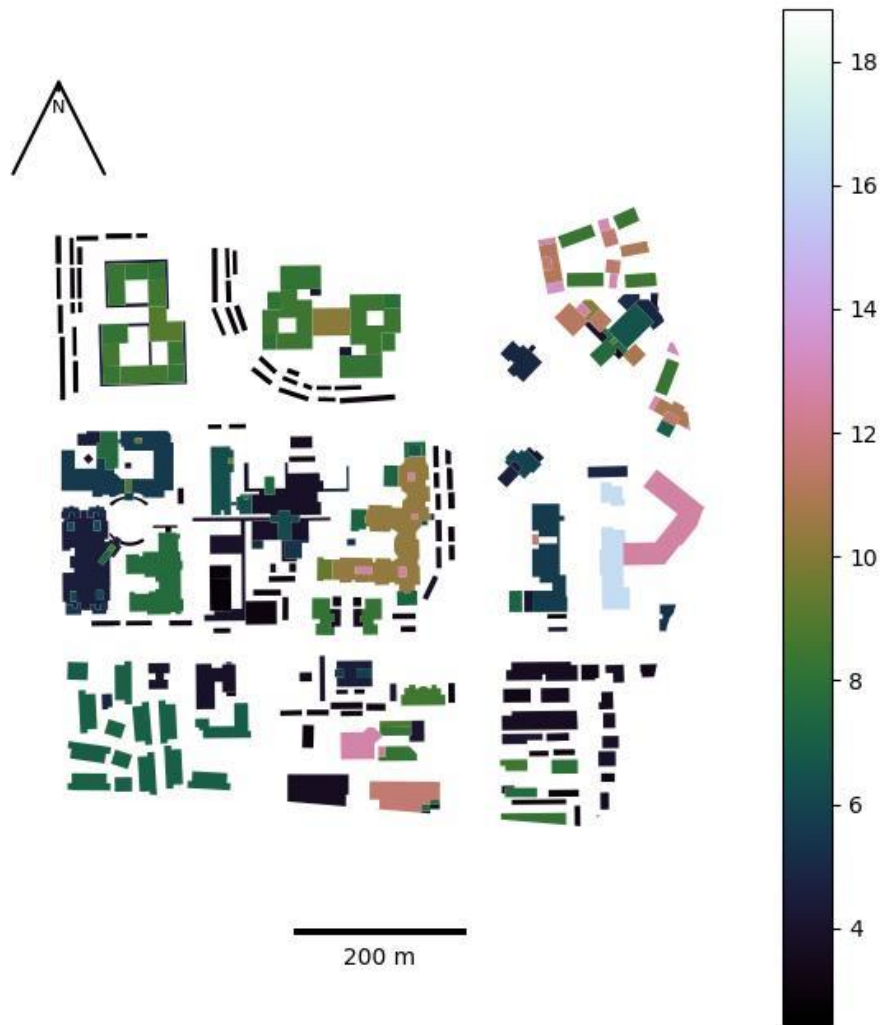


Figure A. 1. Building heights within LCZ 5.

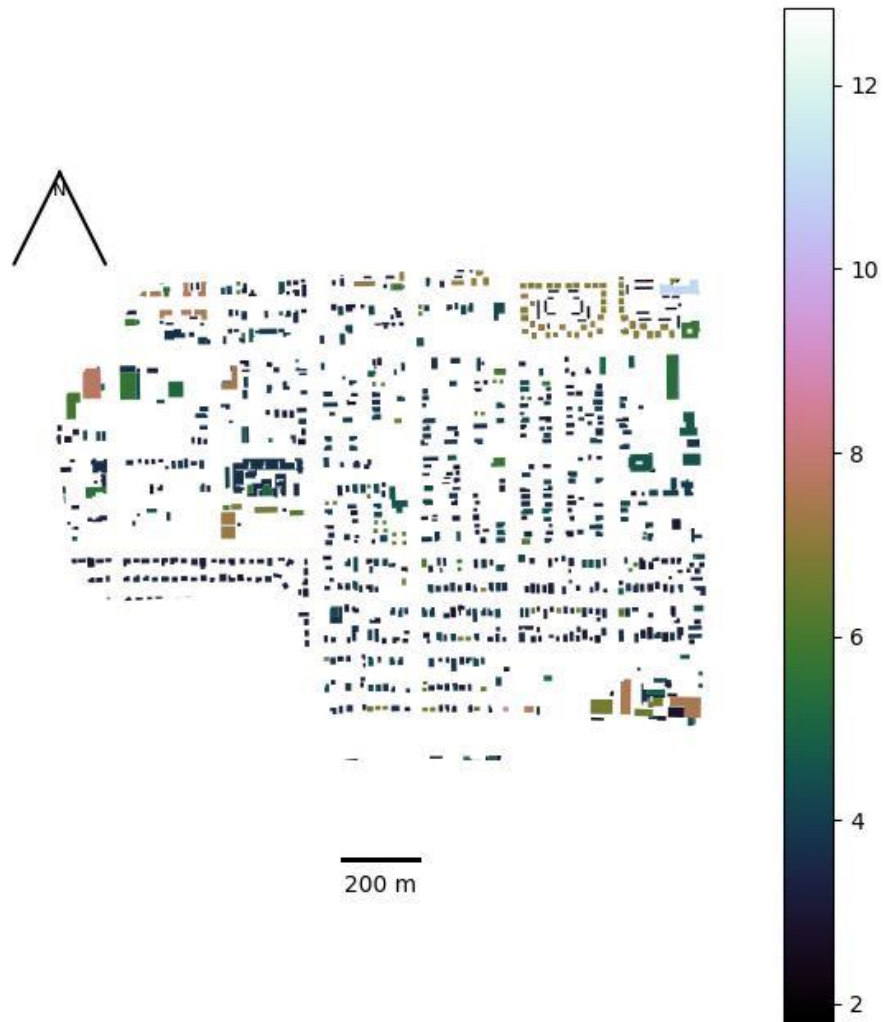


Figure A. 2. Building heights within LCZ 7.

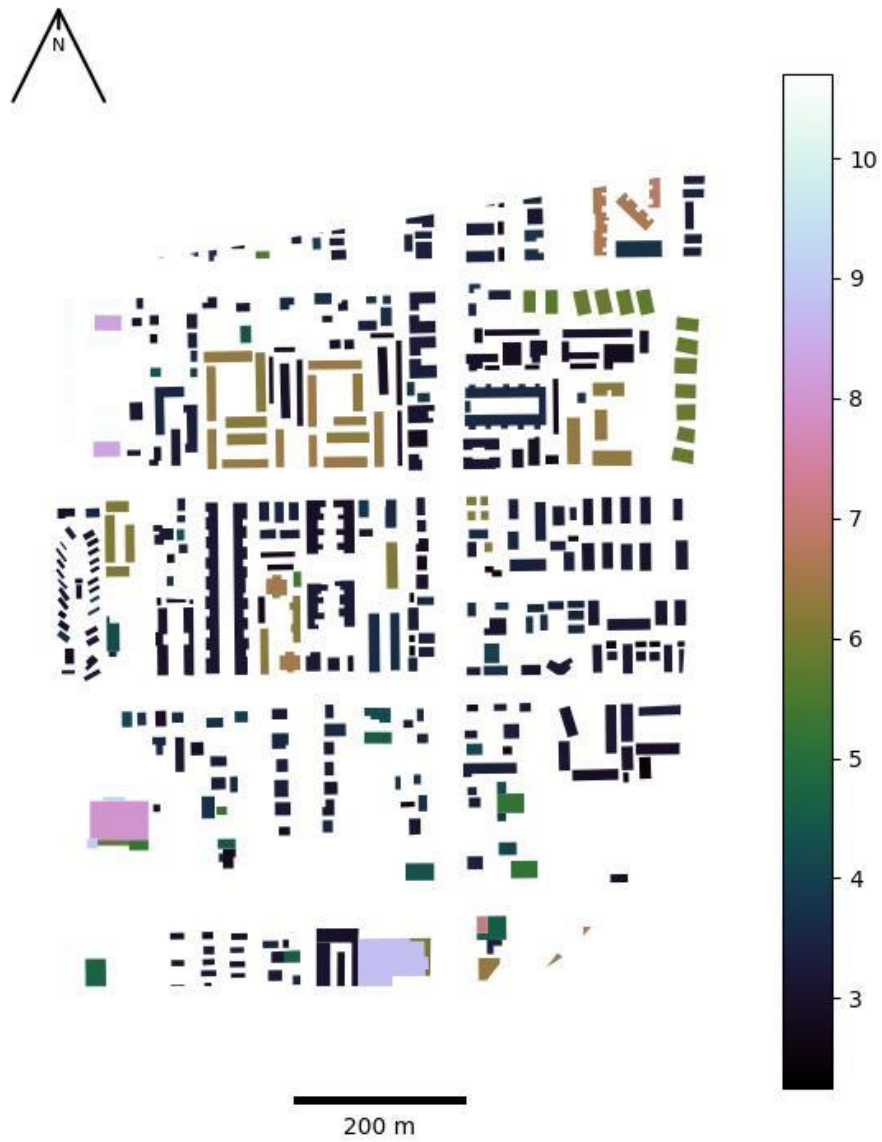


Figure A. 3. Building heights within LCZ 8.

A.6 Images of T_{ped} and T_{plan} for LCZ 5, 7 and 8

Section 5 fully concentrates on describing T_{plan} and T_{ped} using only images of daytime and nighttime T_{plan} and T_{ped} for LCZ 6, together with their scatter plots and histograms. Figure A. 4 to Figure A. 23 shows the results for LCZ 5, 7 and 8.

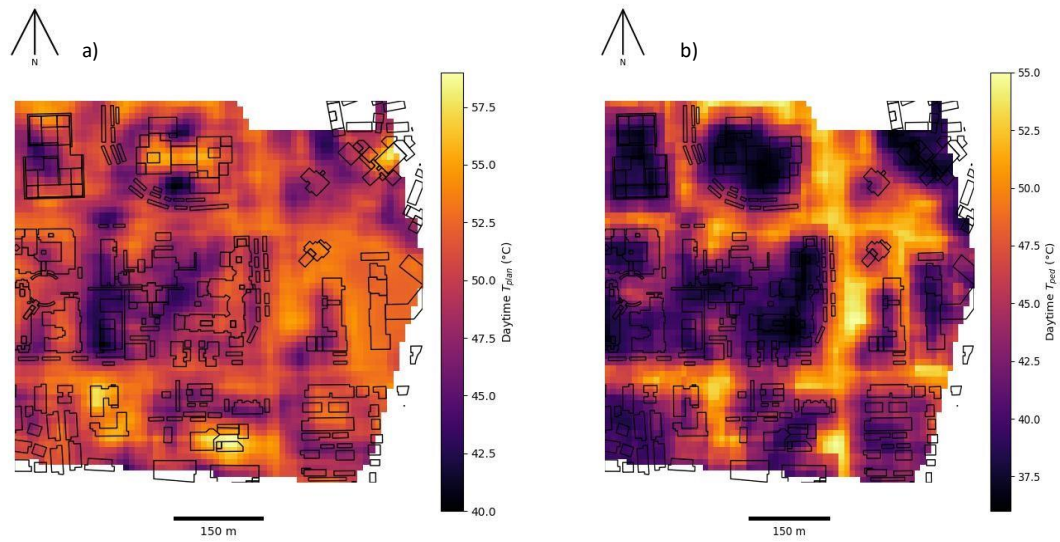


Figure A. 4. Images of a) Daytime T_{plan} and b) Daytime T_{ped} for 50m x 50m domains of LCZ 5.

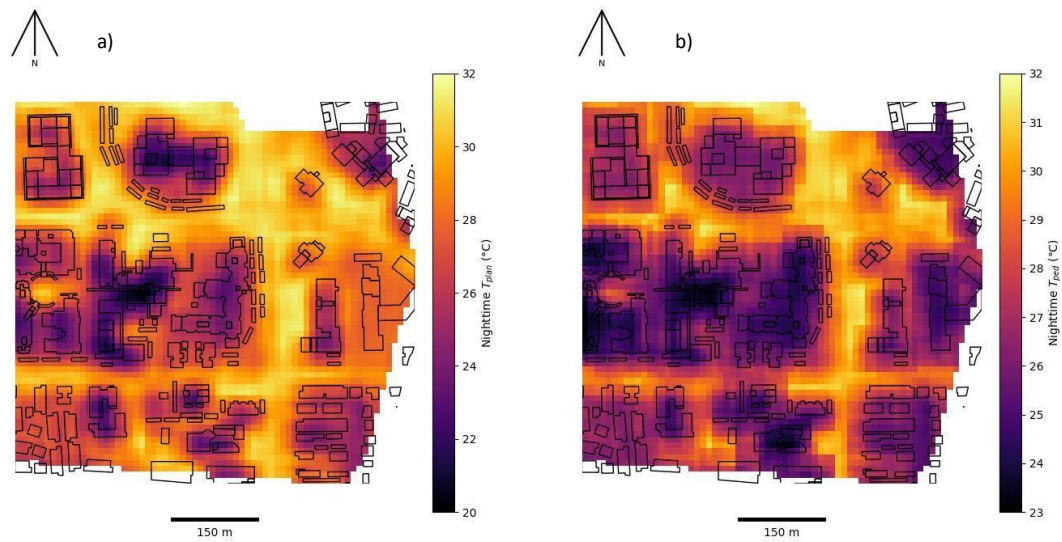


Figure A. 5. Images of a) Nighttime T_{ped} and b) Nighttime T_{plan} for 50m x 50m domains of LCZ 5.

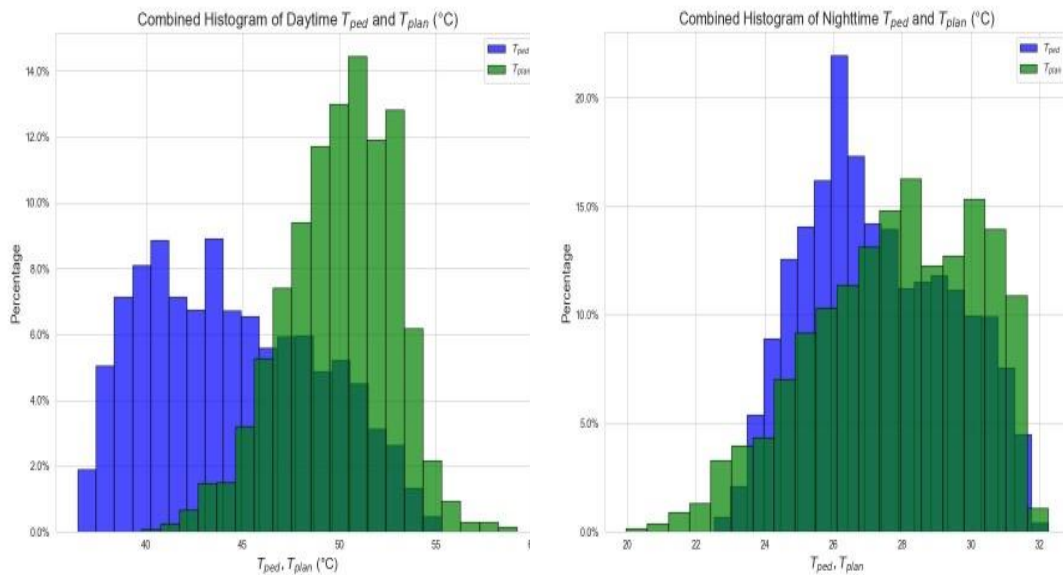


Figure A. 6 Histogram plots for a) Daytime T_{plan} and T_{ped} and b) Nighttime T_{plan} and T_{ped} for 50m x 50m domain of LCZ 5.

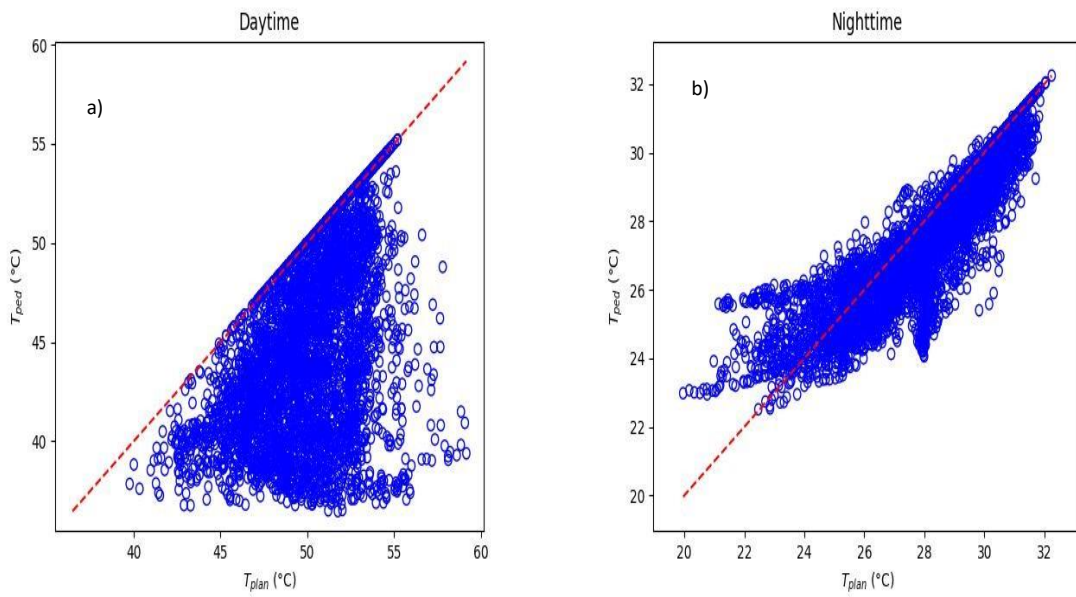


Figure A. 7. Scatter plots for a) Daytime T_{plan} and T_{ped} and b) Nighttime T_{plan} and T_{ped} for 50m x 50m domain of LCZ 5.

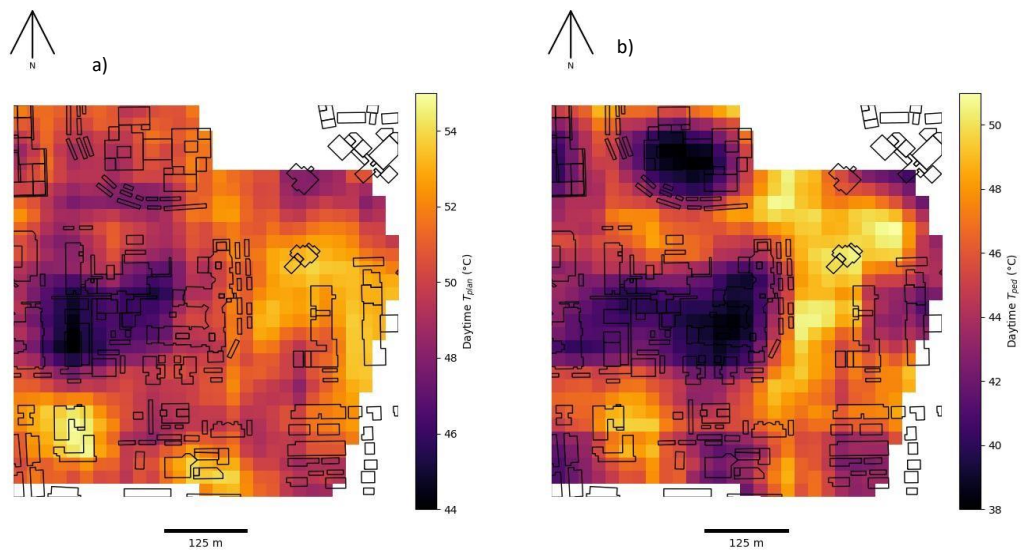


Figure A. 8. Images of a) Daytime T_{ped} and b) Daytime T_{plan} for 100m x 100m domains of LCZ 5.

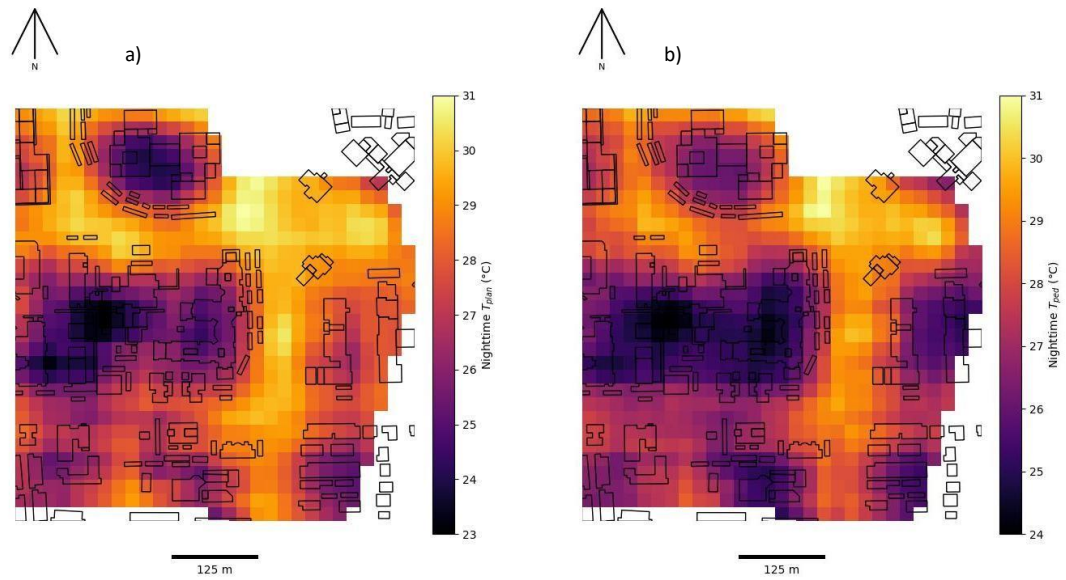


Figure A. 9. Images of a) Nighttime T_{ped} and b) Nighttime T_{plan} for 100m x 100m domains of LCZ 5.

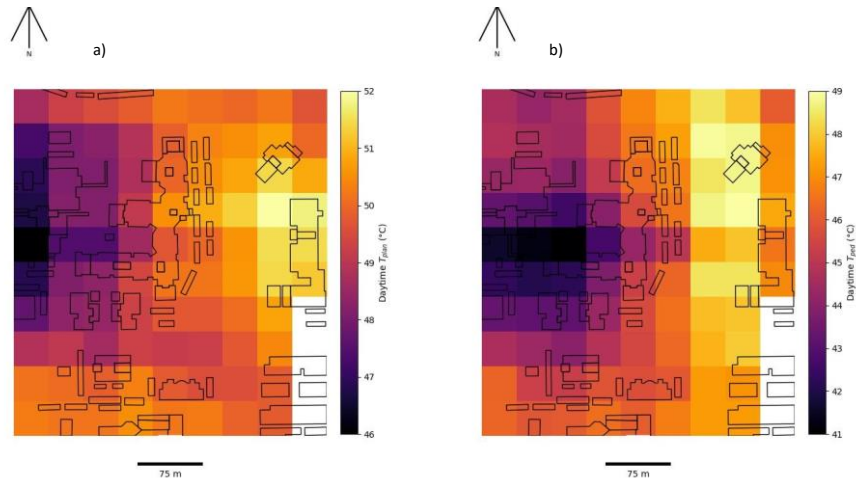


Figure A. 10. Images of a) Daytime T_{ped} and b) Daytime T_{plan} for 200m x 200m domains of LCZ 5.

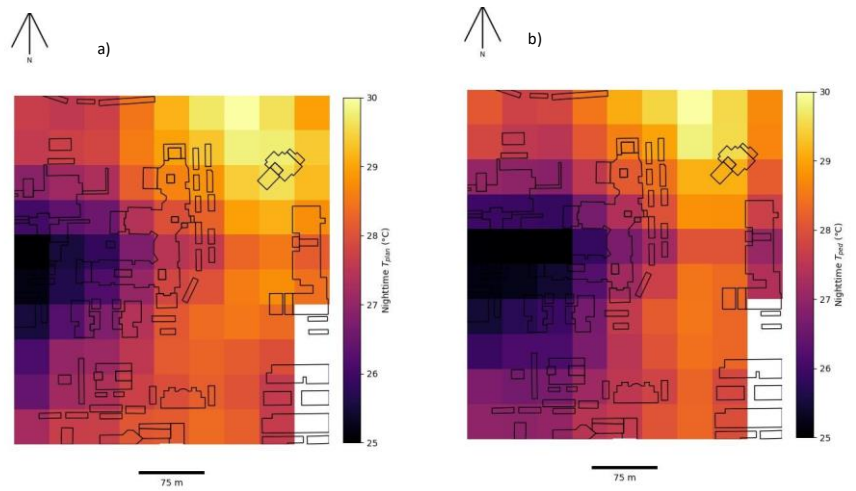


Figure A. 11. Images of a) Nighttime T_{ped} and b) Nighttime T_{plan} for 200m x 200m domains of LCZ 5.

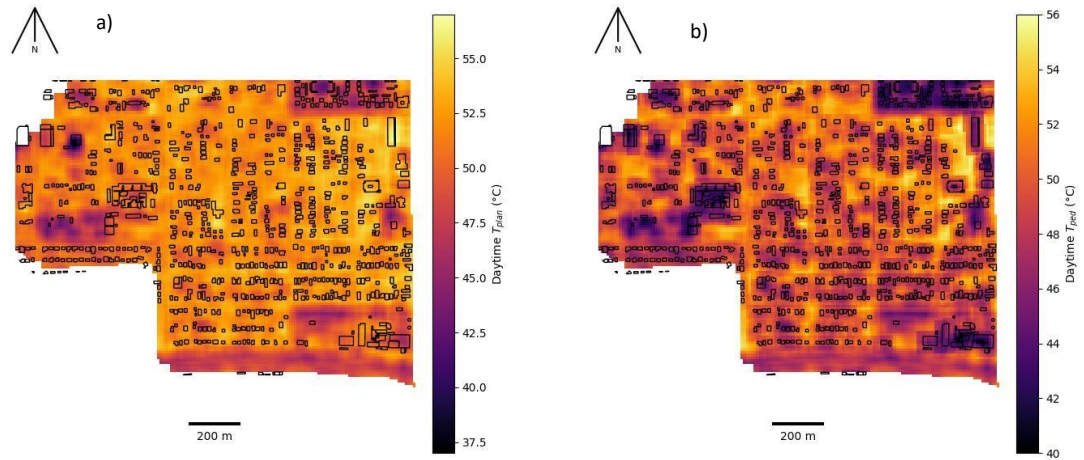


Figure A. 12. Images of a) Daytime T_{ped} and b) Daytime T_{plan} for 50m x 50m domains of LCZ 7.

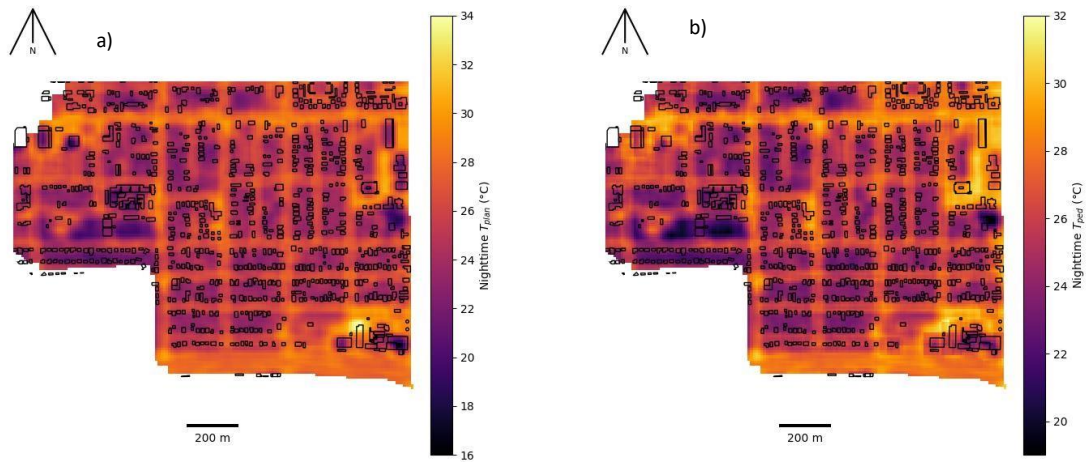


Figure A. 13. Images of a) Nighttime T_{ped} and b) Nighttime T_{plan} for 50m x 50m domains of LCZ 7.

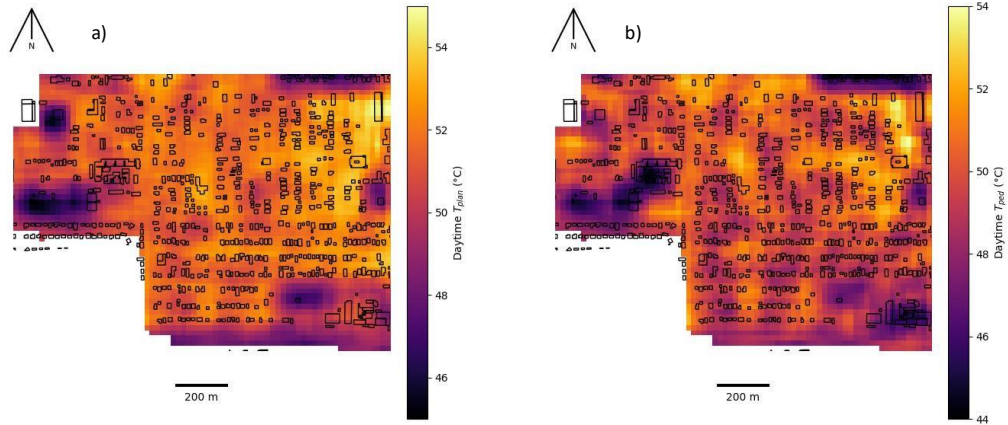


Figure A. 14. Images of a) Daytime T_{ped} and b) Daytime T_{plan} for 100m x 100m domains of LCZ 7.

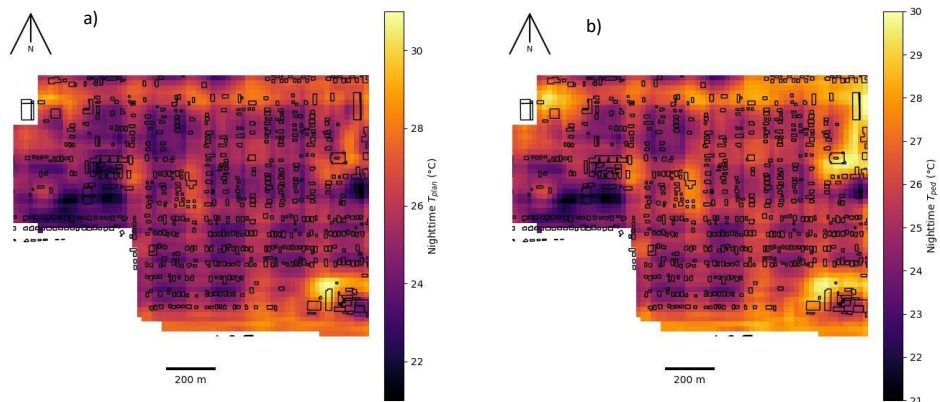


Figure A. 15. Images of a) Nighttime T_{ped} and b) Nighttime T_{plan} for 100m x 100m domains of LCZ 7.

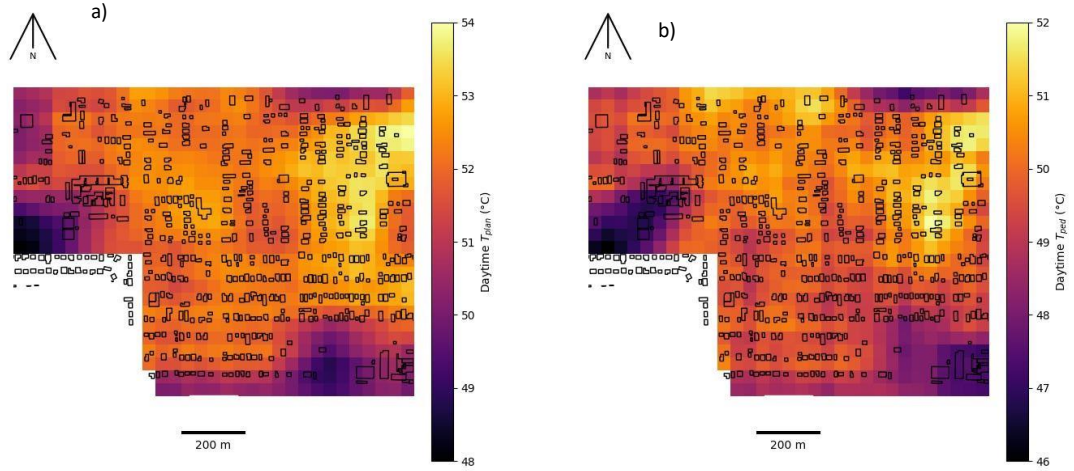


Figure A. 16. Images of a) Daytime T_{ped} and b) Daytime T_{plan} for 200m x 200m domains of LCZ 7.

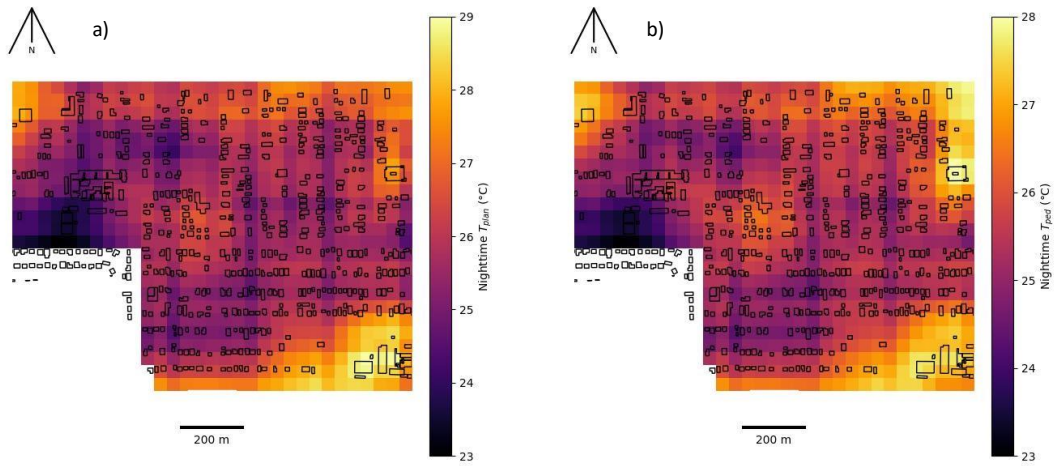


Figure A. 17. Images of a) Nighttime T_{ped} and b) Nighttime T_{plan} for 200m x 200m domains of LCZ 7.

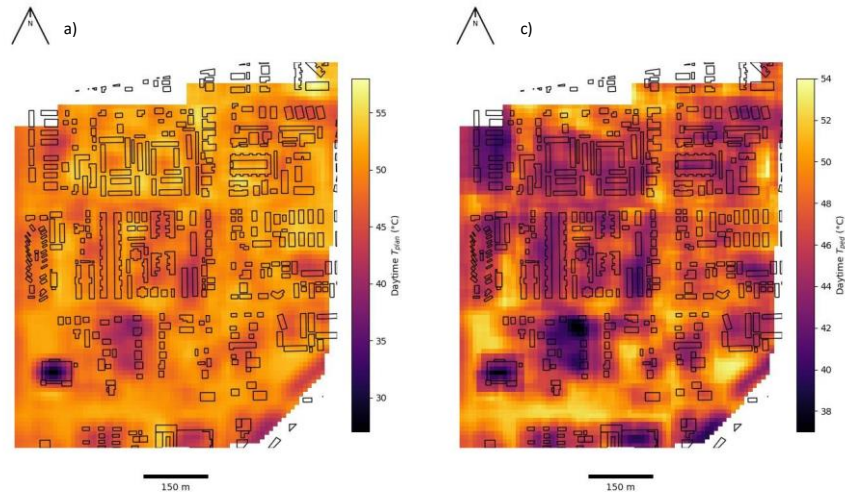


Figure A. 18. Images of a) Daytime T_{ped} and b) Daytime T_{plan} for 50m x 50m domains of LCZ 8.

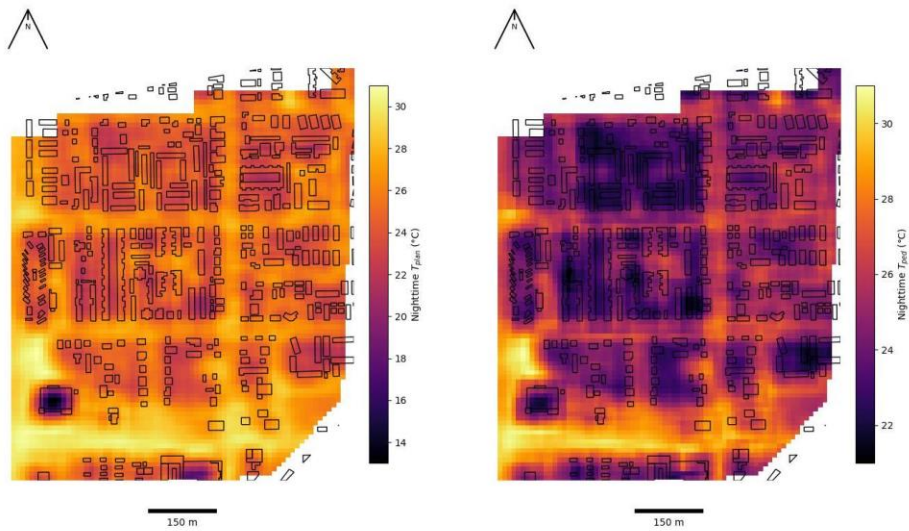


Figure A. 19. Images of a) Nighttime T_{ped} and b) Nighttime T_{plan} for 50m x 50m domains of LCZ 8.

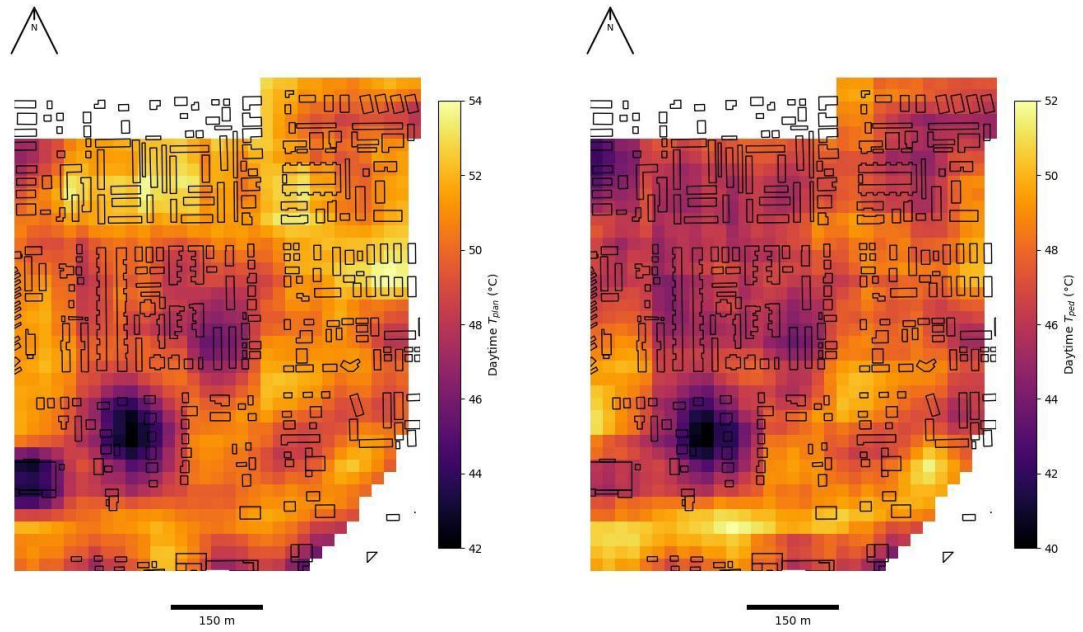


Figure A. 20. Images of a) Daytime T_{ped} and b) Daytime T_{plan} for 100m x 100m domains of LCZ 8.

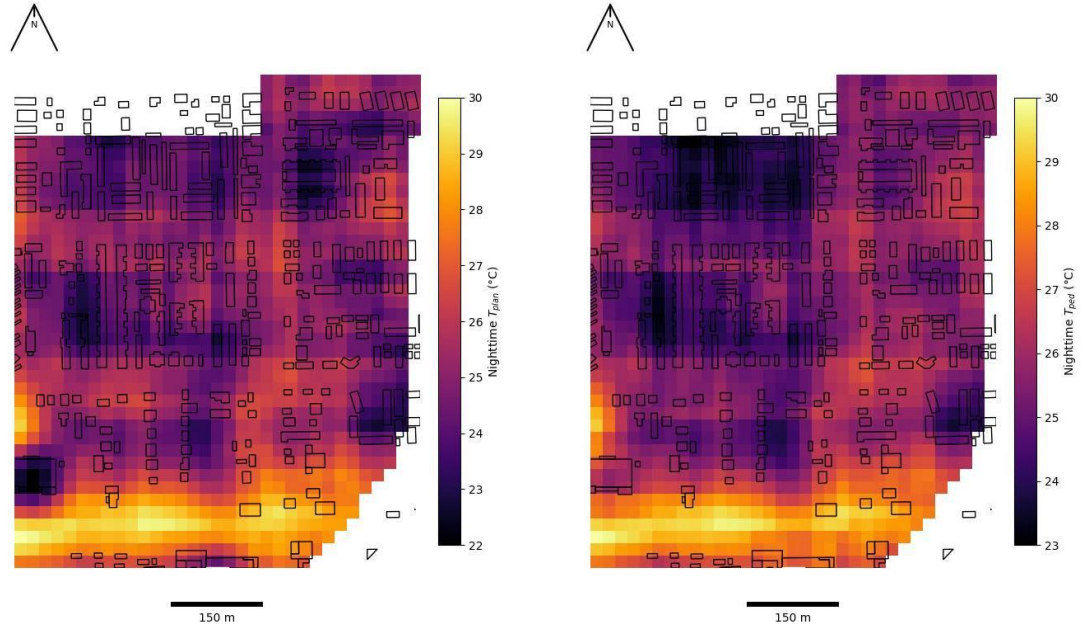


Figure A. 21. Images of a) Nighttime T_{ped} and b) Nighttime T_{plan} for 100m x 100m domains of LCZ 8.

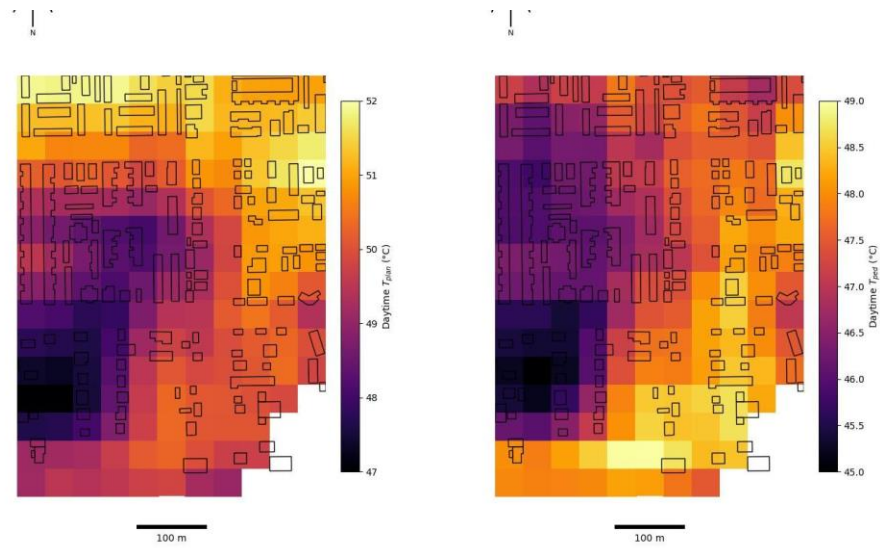


Figure A. 22. Images of a) Daytime T_{ped} and b) Daytime T_{plan} for 200m x 200m domains of LCZ 8.

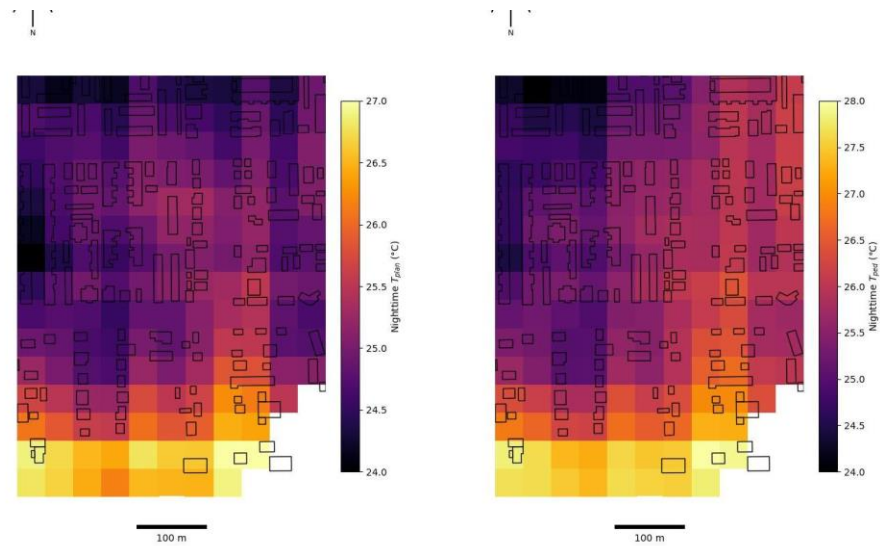


Figure A. 23. Images of a) Nighttime T_{ped} and b) Nighttime T_{plan} for 200m x 200m domains of LCZ 8.

A.7 Determining Shaded and Sunlit Walls for the Study Areas using Azimuth Angles and Overhang Calculations

Knowing the position of the sun or the azimuth angle of the sun helped to know the walls that are shaded and sunlit in Phoenix. Table 2.1 shows the azimuth angles at the time the thermal data was obtained for each LCZ. For example, in table 2.1, the azimuth angle for LCZ 5 is 125.4°. Because the sun illuminates a hemisphere, the hemisphere that will receive sunlight on July 13, 2011, at 11:00 AM local time in Phoenix at the azimuth angle of 125.4° is known by adding and deducting 90° from 125.4°.

Thus, the hemisphere angles are from 35.4 to 215.4. This means that the sunlit walls in LCZ 5 are Northeast (NE), East (E), Southeast (SE) and South (S) oriented walls, while walls oriented in the Southwest (SW), West (W) and Northwest (NW) will be shaded. As already explained, buildings in LCZ 5 with roof overhangs will have part of their walls oriented in the sunlit hemisphere be shaded, and thus it is necessary to adjust the wall temperatures from the model as fully sunlit to include the shaded part of those walls, while maintaining the modelled temperature values for walls oriented in the shaded hemisphere.

The shaded part of the sunlight facing walls could be calculated as follows:

Let $x(m)$ = length of the overhang

$y(m)$ = the length of the shaded part of the wall.

$w(m)$ = width of the building.

e = elevation angle

z = zenith angle

The length of the shaded part is calculated from the equation below;

$$\tan(z) = \frac{x}{y} \dots\dots\dots\text{Equation A. 9}$$

$$y = \frac{x}{\tan(z)} \dots\dots\dots\text{Equation A. 10}$$

Thus, the area of the shaded part:

$$a_s(\text{m}^2) = y \cdot z \dots\dots\dots\text{Equation A. 11}$$

To calculate the temperature of the shaded part, the modelled temperature of the wall oriented at the exact opposite of a sunlit wall is used as the temperature of the shaded part of the sunlit wall, as it was assumed that the most shaded wall is the wall oriented in the angle exactly opposite to the azimuth angle of the sunlit wall. For example, assuming a sunlit wall facing exactly at E (90°), the temperature of the W (270°) wall is used as the temperature of the shaded part of the E wall. This can be calculated as 9° 0+180° .

The temperature of the West wall can then be used to represent the temperature of the shaded wall as the West wall is colder at that azimuth angle, while the temperature of the east wall is maintained for the sunlit part of the wall. An area weighted temperature of the E wall can then be recalculated as follows:

$$T_e = \frac{a_s \cdot t_s + a_{su} \cdot t_{su}}{a_s + a_{su}} \dots\dots\dots\text{Equation A. 12}$$

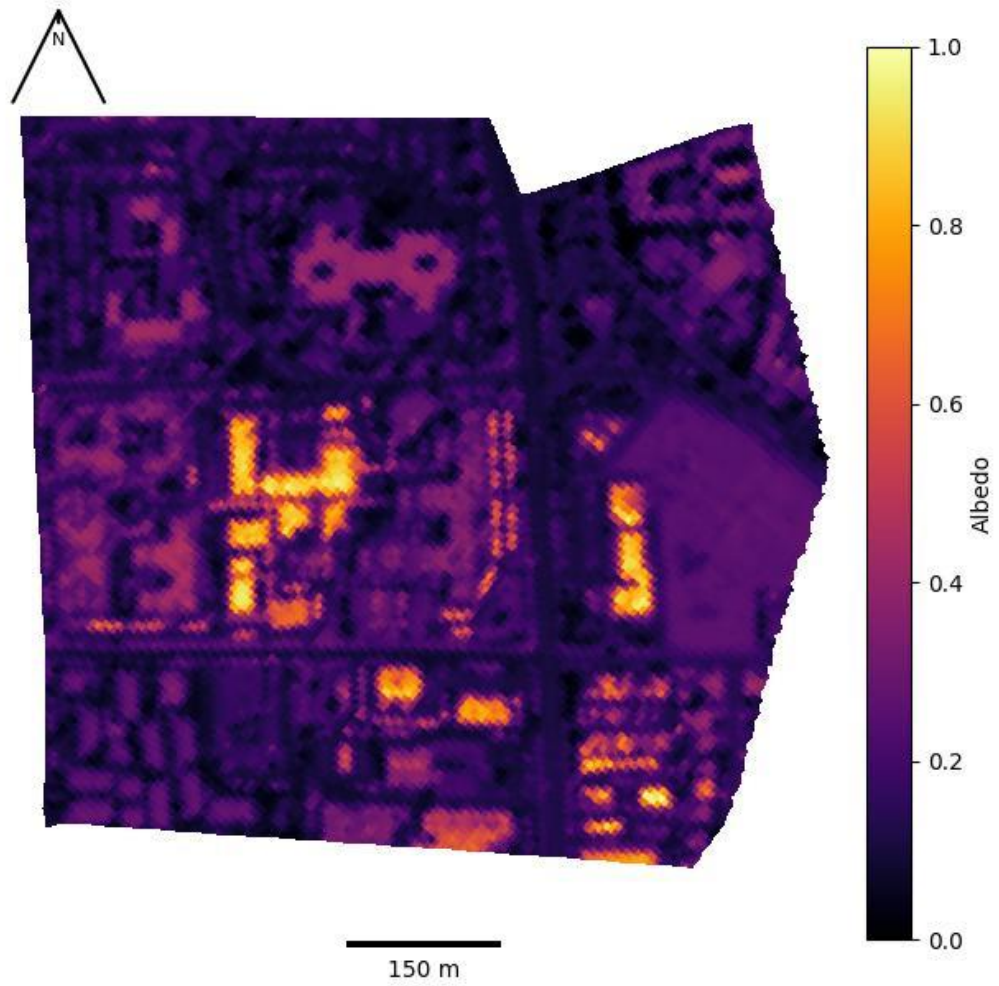
Where:

T_e = The area weighted temperature of the E wall.

a_s = Area of the shaded part of the E wall with its temperature t_s

a_{su} = area of the sunlit part of the E wall with its temperature t_{su}

This method was iterated for all sunlit walls for buildings with roof overhangs.

A.8 Graphical visualizations of albedo in each study area.**Figure A. 24. Albedo for LCZ 5.**

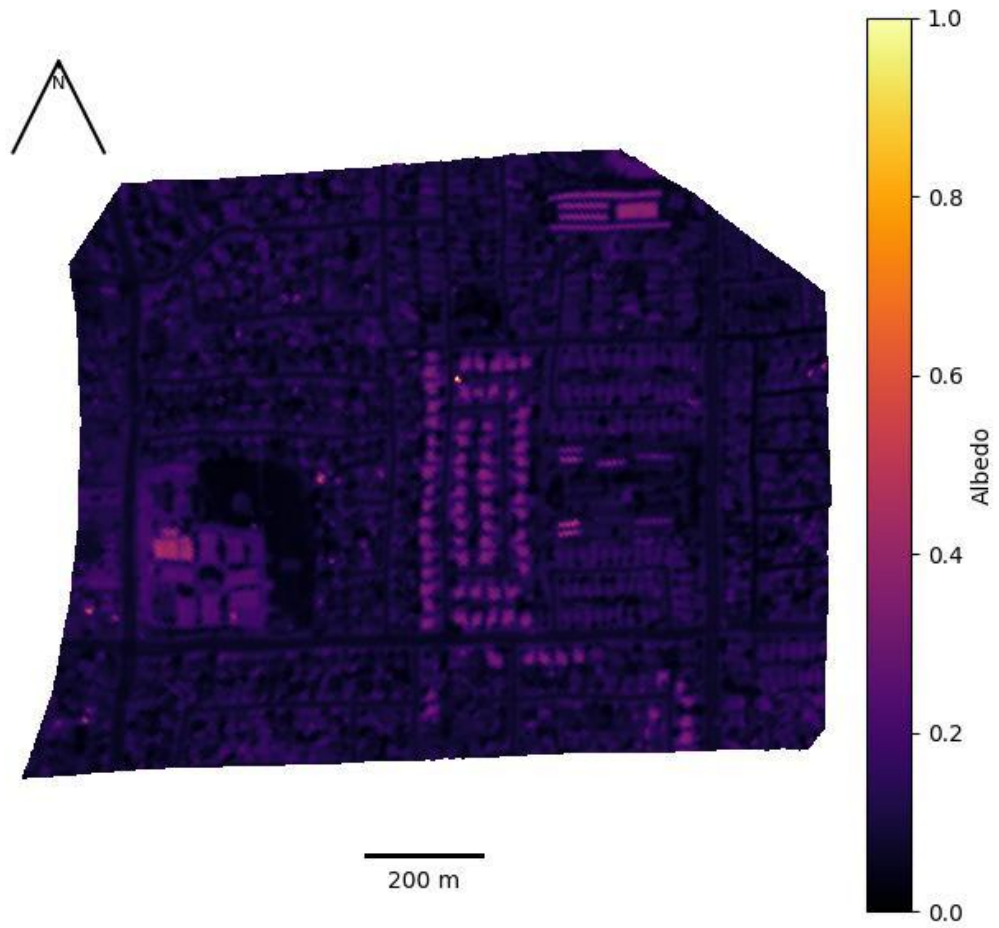


Figure A. 25. Albedo for LCZ 6.

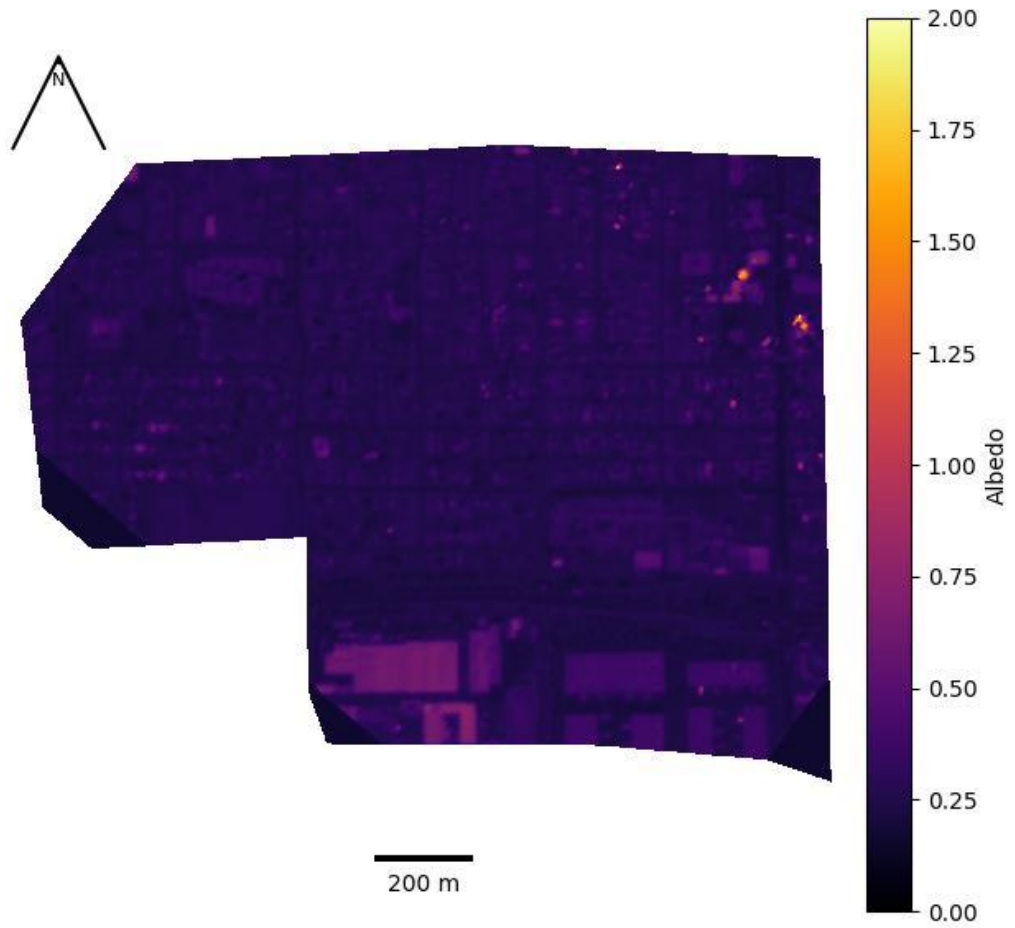


Figure A. 26. Albedo for LCZ 7.

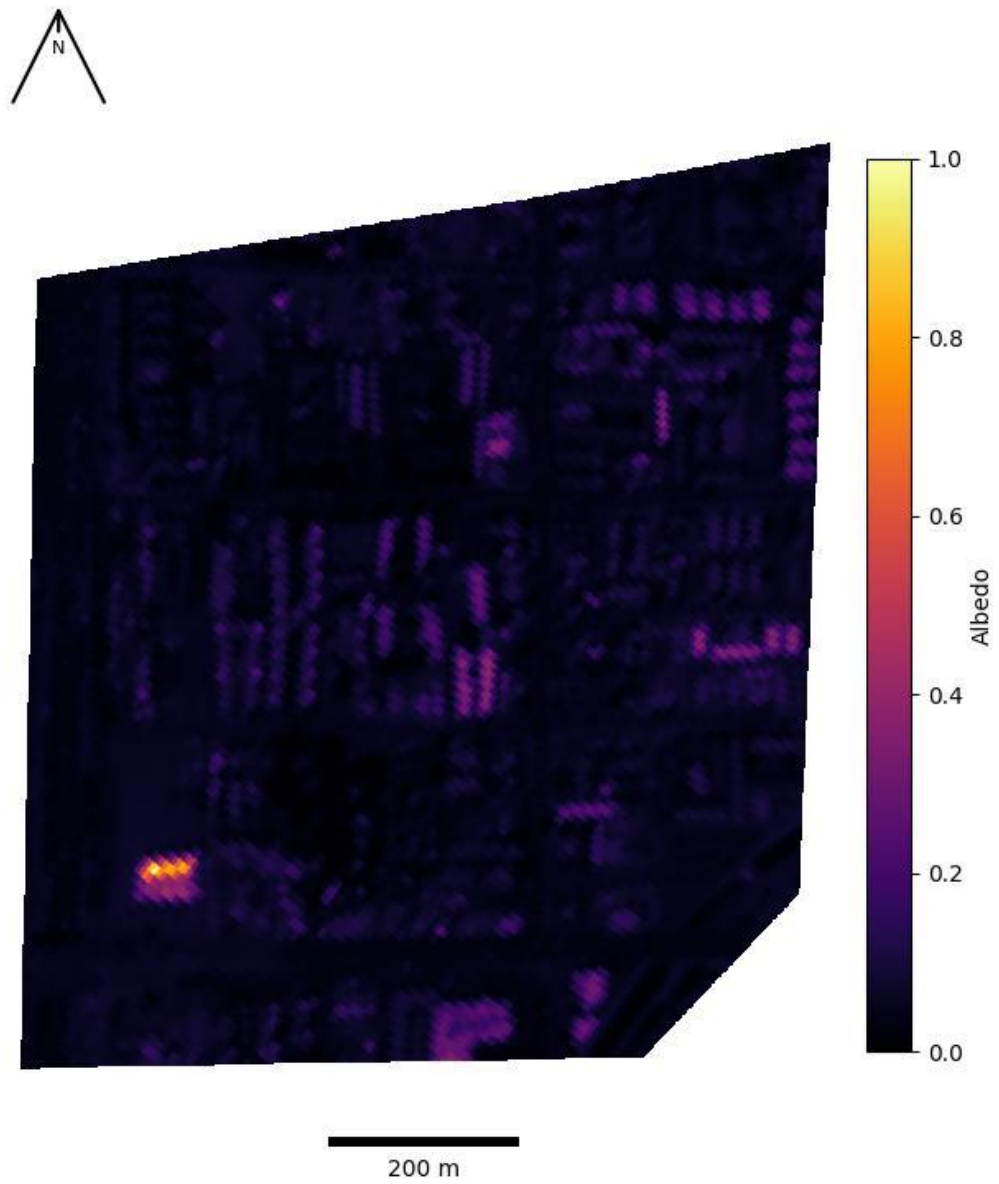


Figure A. 27. Albedo for LCZ 8

A.9 Input Parameters for LCZ 5 SA 1

The table below shows the input parameters used to obtain wall temperatures for LCZ 5 SA1. The parameters for all the other SA's are found in my [Github Link](#)

RADIATIVE PARAMETERS					
	ALBEDO				
roof	road	wall(min)	wall(max)	wall(step)	
0.28	0.18	0.35	0.55	0.05	
	EMISSIVITY				
roof	road	wall			
0.94	0.95	0.9			
	THERMAL PARAMETERS				
	ROOF				
	thickness	tk	cv		
Layer	m	$\text{Wm}^{-1}\text{K}^{-1}$	$\text{MJm}^{-3}\text{K}^{-1}$		
1	0.02	1.2	1.93		
2	0.04	0.7	0.88		

3	0.06	0.04	0.1		
4	0.09	0.85	0.84		
	ROAD				
	thickness	tk	cv		
Layer	m	$\text{Wm}^{-1}\text{K}^{-1}$	$\text{MJm}^{-3}\text{K}^{-1}$		
1	0.02	1.2	1.93		
2	0.05	1.73	2.1		
3	0.13	0.36	1.56		
4	0.24	0.3	1.28		
	WALL				
	thickness	tk	cv		
Layer	m	$\text{Wm}^{-1}\text{K}^{-1}$	$\text{MJm}^{-3}\text{K}^{-1}$		
1	0.03	1.98	1.42		
2	0.05	1.98	1.55		
3	0.2	0.78	0.86		
4	0.15	0.27	0.06		
	GEOMETRIC PARAMETERS				

elevation height (z_s)=	400			
longitude =	-112			
latitude =	33			
Total Land area (m^2) =				44216.22301
total building footprint area (m^2)=				13741
plan to area ratio (λ_p)=				0.31076829
mean building height (m) =				9.179167
mean building width (m) =				50.958333
building H/L =				0.180130834
building H/W =				0.142993534
reference height (z_{ref})= 2 x mean building height =				18.358334
Town roughness length (Town Z_0)=				0.9179167
Roof Roughness Length(Roof Z_0)				0.07
Road Roughness Length(Road Z_0)				0.08

Curriculum Vitae

Name: Derrick Kessie

Post-secondary University of Camerino

Education and Camerino, Italy

Degrees: 2017-2020 B.Sc.

The University of Western Ontario

London, Ontario, Canada

2021-2023

M.Sc.

Related Work Teaching Assistant

Experience **GIS Analyst, Ministry of Natural Resources and Forestry, Ontario**

Public Service April. 2023- present

- Leveraging Synthetic Aperture Radar (SAR) data in the development and deployment of GIS applications tailored for forest research and monitoring activities.
- Processing and analyzing SAR data using a combination of programming languages such as Python and SQL, effectively extracting vital information regarding forest structure, biomass, and health.

Graduate Teaching and Research Assistant, University of Western

Ontario. Sept. 2021- August 2022

- Lecturing undergraduate students during their laboratory study periods.
- Preparing Cartographic maps for tutorials
- Preparing lecture notes and presentation slides.
- Marking students' exams.

Geomatics technician (summer intern), Newmont Ghana 2017-2020

- Implementing LiDAR-based topographic survey processes
- Collect geospatial data satellite, aerial and photo imagery, Global Positioning System devices and survey equipment
- Manage and fuse digital geospatial data and products from a wide range of sources
- Generate and reproduce digital geospatial products